

University of Southampton Research Repository

Copyright © and Moral Rights for this thesis and, where applicable, any accompanying data are retained by the author and/or other copyright owners. A copy can be downloaded for personal non-commercial research or study, without prior permission or charge. This thesis and the accompanying data cannot be reproduced or quoted extensively from without first obtaining permission in writing from the copyright holder/s. The content of the thesis and accompanying research data (where applicable) must not be changed in any way or sold commercially in any format or medium without the formal permission of the copyright holder/s.

When referring to this thesis and any accompanying data, full bibliographic details must be given, e.g.

Matthew Stepney (2025) "The evolution of blue and red quasars at cosmic noon and beyond", University of Southampton, Faculty of Engineering and Physical Sciences, School of Physics and Astronomy, PhD Thesis.

University of Southampton

Faculty of Engineering and Physical Sciences School of Physics and Astronomy

The evolution of blue and red quasars at cosmic noon and beyond

by

Matthew Stepney

MPhys - Physics and Astrophysics with a Year of Research ORCiD: 0000-0002-7711-0537

A thesis for the degree of Doctor of Philosophy

November 2025

University of Southampton

Abstract

Faculty of Engineering and Physical Sciences School of Physics and Astronomy Doctor of Philosophy

The evolution of blue and red quasars at cosmic noon and beyond by Matthew Stepney

Observations show that all massive galaxies contain a supermassive black hole (SMBH) at their centre and, despite their vastly different spacial scales, SMBHs and their host galaxies appear to co-evolve. While most descriptions of this phenomenon invoke energy feed back from the SMBH during an active accretion phase, the exact nature of these feedback mechanisms are not fully understood. Accreting SMBHs or active galactic nuclei (AGN) come in many flavours - ranging in mass, luminosity, accretion rate and colour. The most luminous AGN are known as quasars, and given their immense power, quasars are the ideal laboratory for studying the role of AGN feedback in massive galaxy assembly. The primary aim of this thesis is to understand the role of energetic quasar-driven winds in depositing energy into their hosts, and hence, how these winds impact galaxy evolution at the peak epoch of both SMBH and galaxy growth - 1.0 $\lesssim z_{sys} \lesssim$ 4.0. By harnessing the power of large statistical samples from the Sloan Digital Sky Survey, I therefore investigate the redshift evolution of the outflow properties of luminous blue quasars. I leverage advanced spectroscopic analysis techniques to show that the primary driver of quasar-driven outflows is the mass and the accretion rate of the SMBH. The strongest outflows occur in quasars with $M_{BH} > 10^9~M_{\odot}$ and $L/L_{Edd} > 0.2$ at all redshifts, hence, there is no evidence to suggest a redshift evolution in the outflow properties of luminous blue quasars. This thesis also addresses the crucial question of whether dust enhances the efficiency of AGN feedback. I conduct a detailed investigation of the rest-UV/optical emission from a luminous, heavily reddened quasar (HRQ) at cosmic noon, with bolometric luminosity $L_{Bol} = 10^{48.16} \,\mathrm{erg \ s^{-1}}$ and $E(B-V) = 1.55 \,\mathrm{mag}$. The HRQ hosts strong multi-phase, multi-scale winds consistent with the trends identified in blue quasars between SMBH mass, accretion rate and outflow velocity - making it unclear whether dusty quasars host stronger winds than their blue counterparts. However, a full rest-UV to infrared SED analysis of 60 additional HRQs shows that their hot dust emission is suppressed. This suggests that strong AGN feedback processes are active in the red quasar phase and have cleared the inner regions of dust. Given also that excess rest-UV emission - likely scattered quasar light - is very common in HRQs, they likely mark a key evolutionary stage in SMBH and host galaxy growth. The results of this thesis cement the fact that studying AGN feedback is crucial to our understanding of galaxy evolution and highlight that only by studying diverse populations can we gain a complete understanding of the physics that drives these phenomena.

Contents

Li	st of 1	Figures	3	ix
Li	st of	Tables		xxi
D	eclara	ntion of	f Authorship	xxiii
A	cknov	wledge	ments	xxv
D	efinit	ions an	nd Abbreviations	xxix
1	Intr	oductio	on	1
	1.1	Thesis	s Structure	. 1
	1.2	Radia	tive transfer	. 4
		1.2.1	A quantum description of light	. 4
		1.2.2	Bound-free Interactions	
		1.2.3	Bound-bound Interactions	. 5
		1.2.4	Scattering	. 6
		1.2.5	Dust attenuation	
	1.3	Black	holes	. 10
	1.4		tion	
		1.4.1	The Eddington Limit	. 11
		1.4.2	Radiation-driven winds	
	1.5	Active	e Galactic Nuclei and quasars	. 13
		1.5.1	Unification	. 14
	1.6	Black	hole and galaxy co-evolution	. 15
		1.6.1	Cosmic history: Star formation and black hole growth	. 15
		1.6.2	AGN feedback	. 17
		1.6.3	Merger-driven co-evolution & red quasars	. 19
	1.7	Quasa	ars from large surveys	. 19
		1.7.1	Magnitudes and flux	. 21
		1.7.2	Spectral energy distributions	. 21
		1.7.3	Black hole masses	
		1.7.4	Outflows	. 24
2	Spe	ctrosco	pic reconstructions of blue SDSS quasars	27
	2.1	Introd	luction	. 28
	2.2	Samp	le Selection	. 30
	2.3	Impro	oving SDSS systemic redshift estimates	. 31

vi *CONTENTS*

		2.3.1	System	ic redshift dependence on rest-frame wavelength range .	37		
	2.4	Spectr	al Recon	structions with Mean Field Independent Component Anal-			
		ysis .			39		
	2.5	Concl	usions .		45		
3	The	redshi	ft evolut	ion of outflows in blue SDSS quasars	47		
	3.1	Introd	uction .		48		
	3.2	Metho	ods		50		
		3.2.1	Line pro	operties	50		
		3.2.2	Lumino	osities and black hole masses	50		
	3.3	Result	s		53		
		3.3.1	C IV em	ission	53		
			3.3.1.1	Matching the samples by quasar properties	53		
		3.3.2	He II en	nission	56		
		3.3.3	Compa	rison to Wu & Shen 2022	60		
	3.4	Discus	ssion		62		
		3.4.1	Probing	g the driver of outflows	62		
		3.4.2	Implica	tions at higher redshifts	66		
	3.5	Concl	usions .		70		
4	An i	n-dept	h view o	of a red quasar at cosmic noon.	73		
	4.1	_		*	74		
	4.2		ectral Observations & Data Reduction				
	4.3	-			80		
		4.3.1		ame UV Image Decomposition	80		
		4.3.2		l energy distribution	82		
			4.3.2.1	Reddened quasar + blue quasar light	82		
			4.3.2.2	Reddened quasar + star-forming host galaxy	85		
			4.3.2.3	Reddened quasar + blue quasar light + star-forming host			
				galaxy	88		
		4.3.3	Emissic	on and absorption line properties	89		
			4.3.3.1	Systemic redshift and star formation rate from [OII]	89		
			4.3.3.2	Black-hole mass, Eddington ratio and narrow-line re-			
				gion outflows	90		
			4.3.3.3	UV Emission and Absorption Line Features	94		
	4.4	Discus	ssion		98		
		4.4.1	Source	of the UV emission	98		
			4.4.1.1	A dual AGN system?	99		
			4.4.1.2	Leaked or scattered light from the primary quasar?	99		
			4.4.1.3	Associated Absorption Line Systems in ULASJ2315+0143	103		
			4.4.1.4	Star-forming host	103		
		4.4.2	Multi-p	phase winds in ULASJ2315+0143	104		
	4.5	Concl	_		107		
5	The	spectra	al energy	distributions of heavily reddened quasars	109		
-	5.1	_			110		
	5.2				112		
	<u>-</u>	5.2.1		netric data and sample selection	112		
				1			

CONTENTS vii

Rei	feren	ices		183
Ap	pend	dix B	The heavily reddened quasar "best-fit" SEDs	161
Ap	pend	dix A	The heavily reddened quasar photometric catalogue	155
	6.6	Concli	asions	154
	6.5		nation temperature dust in red quasars	153
	<i>(</i> -	6.4.2	Host galaxy signatures in red AGN populations	152
		6.4.1	Scattered light in red AGN populations	152
	6.4		sultra-violet emission in red AGN populations	151
	6.3		feedback in the red quasar phase	151
	6.2		rolution of blue quasars across cosmic time	150
	6.1		uction	150
6			ks and future prospects	149
	5.0	Concid	3510115	140
	5.6		asions	145
		5.5.2	Linking the UV and infrared SED properties of HRQs	143
		5.5.2	5.5.1.3 Balmer Absorption	140
			1 0	136 138
			5.5.1.1 Photometric selection: LRDs vs HRQs	133
		5.5.1	The source of the UV excess in red AGN	133
	5.5	Discus		133
		5.4.2	Sublimation temperature dust properties	129
			5.4.1.1 Rest-Ultraviolet line properties of ULASJ2200+0056	126
		5.4.1	Ubiquitous excess UV emission in HRQs	126
	5.4		S	126
		5.3.2	Dust-reddened quasar + scattered light model fit	118 119
		5.3.1	Dust-reddened quasar model fit	114
	5.3		ds	114
			Spectroscopic data	113
		5.2.2	-	

List of Figures

1.1	An illustration of Thomson scattering. The incident electromagnetic wave is depicted by the blue arrow moving mid-left to top-right. The perpendicular electric field associated with the incident radiation is depicted by the red arrows. The free electron is depicted in green, with the in-	
	duced oscillations depicted with green arrows running parallel with the incident electric field. The direction of motion of the free electron is depicted by the blue arrow moving top-right to bottom-right. The light blue shaded region depicts the scattering cone of the re-emitted electro-	
1.2	magnetic radiation. The deflection angle is given by ϕ An illustration detailing how a dust grain can extinct electromagnetic ra-	ϵ
	diation. The pink arrows represent the lines-of-sight of two perspective observers.	
	Credit: Li (2008), Fig.1	7
1.3	Empirically-derived dust extinction law curves normalised at 5500Å. Credit: Li <i>et al.</i> (2025), Fig.1	8
1.4	The effect of dust extinction on the continuum of a typical rest-UV/optical quasar spectrum at different values of $E(B-V)$. Increasing $E(B-V)$ results in increasing attenuation at all wavelengths, however, the bluer	
	wavelengths are most affected. Here, an $R_V = 3.1$ is assumed using an SMC-like extinction curve (Fig. 1.3; orange).	9
1.5	An unscaled representation of the AGN phenomenon, with the different sight lines that give rise the the various AGN populations high-lighted.	
	Credit: Beckmann & Shrader (2012), Fig.1	15
1.6	The cosmic history of star formation from far-UV and infrared measurements up to $z_{sys} \sim 8$. The distribution can be described by a Salpeter function position at $z_{sys} = 2$, i.e. cosmic week	
	function peaking at $z_{sys} \sim 2$ - i.e. cosmic noon. Credit: Madau & Dickinson (2014), Fig.9a	16
1.7	The black hole mass versus the central velocity dispersion σ_c (solid circles) or the rms velocity v_{rms} (open circles) of the host galaxy. Crosses represent lower limits in v_{rms} . The solid and dashed lines represent the "best-fits" in σ_c and v_{rms} , respectively.	
	Credit: Ferrarese & Merritt (2000), Fig.2	17
1.8	A schematic representing the various constituents of a "typical" AGN SED. We note that changes to the accretion rate, SMBH mass and/or	
	dust properties can significantly alter the observed SED of an AGN. Credit: Harrison (2014), Fig.1.2	22
1.9	Relationship between the C IV blueshift ($\Delta V = V_{50} - V_{peak}$) and the [O III] blueshift ($\Delta V = V_{10} - V_{peak}$) for a sample of luminous blue quasars.	
	Credit: Coatman <i>et al.</i> (2019), Fig.10	25

x LIST OF FIGURES

2.1	The CTV emission space for the $1.5 < z_{sys} < 3.5$ SDSS quasars. The blue distribution represents the non-BALs and the red distribution represents the BALs. Marginalised distributions of the CTV blueshift and EW are also shown. Density contours encircle 68, 50 and 25 per cent of the sample, respectively. Both populations exhibit the classic "banana" shape.	
2.2	Credit: Rankine <i>et al.</i> (2020), Fig.8	29
2.3	to producing accurate systemic redshifts	34
2.4	The difference between the systemic redshifts presented in DR16Q and their corresponding corrected redshifts, as a function of their corrected redshift. Quasar spectra with $\delta v > 0~{\rm kms^{-1}}$ have been blueshifted with respect to the initial SDSS systemic redshift estimates. We estimate $\langle \delta v \rangle \simeq -210 \pm 180~{\rm kms^{-1}}$	37
2.5	The velocity difference in systemic redshifts between those estimated by Rankine <i>et al.</i> (2020) and calculated using the same recipe and rest-frame wavelength range as this work. This is plotted as a function of the C IV blueshift for a random sample of $1000 \ 1.5 < z_{sys} < 2.65$ quasars of comparable luminosity to the $3.5 < z_{sys} < 4.0$ quasar population. At low C IV blueshifts, the cross-correlation algorithm has a tendency to overestimate the systemic redshift and therefore biases the C IV line centroids	3/
2.6	blue-ward of their true position	38
2.7	therefore permitted to have negative weights in the MCMC fitting The MFICA components, generated using the technique described in Allen <i>et al.</i> (2013), used to reconstruct quasar spectra whose $20 < C$ IV EW < 70 Å . Components "9" and "10" are correction components and	40
2.8	are therefore permitted to have negative weights in the MCMC fitting The MFICA components, generated using the technique described in Allen <i>et al.</i> (2013), used to reconstruct quasar spectra whose C IV EW > 70Å. Components "6" and "7" are correction components and are	41
	therefore permitted to have negative weights in the MCMC fitting	42

LIST OF FIGURES xi

2.9	Example quasar spectra from our sample at $3.5 < z_{sys} < 4.0$ with signal-to-noise of 30 (top), 20 (top-middle), 10 (bottom-middle) and 5 (bottom), with their corresponding mean-field independent component analysis reconstructions overlaid. We can see that the MFICA reconstructions have the effect of boosting the signal-to-noise of the SDSS spectra, and hence robust UV emission line analysis becomes achievable	44
3.1	The C IV emission space for both the $1.5 < z_{sys} < 3.5$ (red, Rankine et al., 2020; Temple et al., 2023) and $3.5 < z_{sys} < 4.0$ (blue) samples. Density contours encircle 68, 50 and 25 per cent of the sample, respectively. Marginalised distributions of the C IV blueshift and EW are also shown. While the distributions feature the same characteristic shape, the $3.5 < z_{sys} < 4.0$ sample is biased to higher C IV blueshift and lower C IV EW. The following criteria was applied to remove poorly fit spectra from both samples;	
	$\log_{10}(\text{C IV EW [Å]}) < -2.3077 \times 10^{-4} \times \text{C IV blueshift [km s}^{-1}] + 1.3231.$	54
3.2	The C IV emission space for the $3.5 < z_{sys} < 4.0$ sample (blue) and the L ₃₀₀₀ matched $1.5 < z_{sys} < 2.65$ quasars (red) from Temple <i>et al.</i> (2023).	
	Density contours encircle 68, 50 and 25 per cent of the sample, respectively.	55
3.3	The C IV emission space for the $3.5 < z_{sys} < 4.0$ sample (blue) and the M _{BH} and L/L _{Edd} matched $1.5 < z_{sys} < 2.65$ quasars (red) from Temple	
	et al. (2023). Density contours encircle 68, 50 and 25 per cent of the sam-	56
3.4	ple, respectively	56
	scaled accretion rate (bottom). The data is compressed into 17 equidistant bins, where we present the median and median absolute deviation (MAD) of each bin in the appropriate panels. We see a tendency for increasing C IV blueshifts with increasing systemic redshift, UV continuum luminosity and Eddington-scaled accretion rate. The trends with UV continuum luminosity and Eddington-scaled accretion rate can explain why we observe an increase in C IV blueshift as we tend to larger systemic redshifts. There is limited evidence of a strong trend between SMBH mass and C IV blueshift (bottom middle), with a slight tendency to lower C IV blueshifts as we approach the upper limit of our SMBH masses for the sample. There is limited evidence to suggest that the emission line used to estimate virial black hole masses will have any	- 77
2 -	significant impact on our results	57
3.5	The median observed He II EW in bins of C IV blueshift and C IV EW for the $3.5 < z_{sys} < 4.0$ sample. The He II EW is correlated with both C IV blueshift and C IV EW, with the most blueshifted C IV lines only observed when the He II EW is low. Conversely, the highest EW C IV lines are only observed when the He II EW is high	58
3.6	The He II EW as a function of systemic redshift (top) and UV continuum luminosity (bottom). The data is compressed into 17 equidistant bins, where we present the median and median absolute deviation (MAD) of each bin in the appropriate panels. We see a slight tendency for decreasing He II EWs with increasing systemic redshift. The trends with He II EW and UV continuum luminosity can therefore well explain the appar-	
	ent evolution with systemic redshift	59

xii LIST OF FIGURES

3.7	The He II EW measured from 20 high signal-to-noise composite stacked spectra overlaid on the C IV emission space. As in Fig. 3.5, the He II EW is correlated with both C IV blueshift and C IV EW, with the most blueshifted C IV lines only observed when the He II EW is low. Conversely, the highest EW C IV lines are only observed when the He II EW is high.	60
3.8	is high	
3.9	EW	61
3.10	is also significantly weaker than what is observed in Fig. 3.5 The median observed C IV blueshift (top), C IV EW (middle) and He II EW (bottom) in bins of SMBH mass and Eddington-scaled accretion rate for the 3.5 $< z_{sys} < 4.0$ sample overlaid on the M _{BH} - L/L _{Edd} plane at 1.5 $< z_{sys} < 2.65$ (grey, Temple <i>et al.</i> , 2023). Save for a clear flux limit, the 1.5 $< z_{sys} < 2.65$ and 3.5 $< z_{sys} < 4.0$ samples are well-matched in this space. We note that above L/L _{Edd} \sim 0.2 there is evidence of a clear trend between He II EW and SMBH mass. Below $\sim 10^9 M_{\odot}$, the quasars generally have stronger UV emission lines and weaker C IV blueshifts and above this threshold, the contrary is true	62
3.11	•	64
	true	65

LIST OF FIGURES xiii

3.12	The M_{BH} - L/L _{Edd} plane for the 3.5 < z_{sys} < 4.0 and corresponding UV luminosity matched 1.5 < z_{sys} < 2.65 samples (left) and the z_{sys} ~ 6 and corresponding UV luminosity matched 1.5 < z_{sys} < 2.65 samples (right). Density contours (left) encircle 68, 50 and 25 per cent of the sample, respectively. The cartoon ellipses (right) approximate the locations of the z_{sys} ~ 6 quasars (blue) and the 1.5 < z_{sys} < 2.65 quasars, when UV luminosity matched to the z_{sys} ~ 6 sample (red). When UV luminosity matching the 3.5 < z_{sys} < 4.0 sample to the 1.5 < z_{sys} < 2.65 quasars, the samples are consistent in the M_{BH} - L/L _{Edd} plane, explaining the results presented in Fig. 3.2 and Fig. 3.3. When UV luminosity matching the z_{sys} ~ 6 sample to the 1.5 < z_{sys} < 2.65 quasars, we see an inconsistency between the samples in the M_{BH} - L/L _{Edd} plane, with the z_{sys} ~ 6 objects biased towards higher L/L _{Edd} and lower M_{BH} than their 1.5 < z_{sys} < 2.65 counterparts	69
4.1	The full flux calibrated 1D spectrum of ULASJ2315+0143 is presented in the top panels of each exert (blue). In addition, the corresponding noise spectrum is presented in the lower panels (grey). Noise spikes marking the transition between arms at $\sim 5800 \text{Å}$ and $\sim 10,000 \text{Å}$ have been masked out, as too has a region of high noise redward of the H α emission. Prominent emission lines are marked by dashed vertical black lines and labelled accordingly	<i>7</i> 9
4.2	GALIGHT fitting results on the HSC <i>g</i> band image of ULASJ2315+0143. The first row shows the case when use a model incorporating only the Sérsic profiles. The second row shows the case when we include one point source in the model. The reconstructed images are shown by the second and first panel of the rows, respectively. In the second panel of second row, we also show the image after subtracting the point source model from the data. The third column shows the 2D normalised residual map of the fitting. The final column shows the 1D annulus light profiles for the data and the reconstructed model, with the fractional resid-	
4.3	ual shown in the bottom sub-panel	81
4.4	The reddened quasar + blue quasar light SED model (see Section 4.3.2) corner plots. In order left-to-right/top-to-bottom the marginalised distributions represent $\log_{10}\{\lambda L_{\lambda}(3000\mathring{A})\}$, $E(B-V)^{QSO}$, emline_type and f_{UV} . The corner plot illustrates that the model is well-converged and highlights the degeneracies between several model parameters	85
4.5	Same as Fig. 4.3, but instead the rest-frame UV is modelled by a star-forming galaxy, generated using BAGPIPES	87

xiv LIST OF FIGURES

4.6	J -Band spectrum for ULASJ2315+0143 with a dust correction, $E(B-V)^{\rm QSO}$ = 1.55, applied in grey and showing the [O II] doublet. The continuum is presented in navy blue, and the windows over which the continuum was fitted are denoted by the thick, lime-green lines. The final fit of the spectrum is presented in red. The smaller panel shows the continuum subtracted total fit in red. The broad components contributing to the total fit are presented in blue and the narrow components are presented in	
4.77	green	90
4.7	We present the H -Band spectrum for ULASJ2315+0143 with a dust correction, $E(B-V)^{QSO}=1.55$, applied in grey. The continuum is presented in navy blue, and the windows over which the continuum was fitted are denoted by the thick, lime-green lines. In addition, the combination of the continuum and iron template are presented in teal. The final fit of	
	the spectrum is presented in red. Noteworthy emission lines are marked	
	by thin black lines and labelled appropriately. The smaller panels are	
	labelled by the line/complex they represent. The continuum subtracted	
	total fit is presented in red, the broad components contributing to the	
	total fit are presented in blue and finally, the narrow components are	92
4.8	presented in green	93
4.9	Same as Fig. 4.7, but instead we present the K-band spectrum	93
4.9	correction applied	96
4.10	The UVB narrow absorption line features detected in the X-Shooter spec-	70
1.1 0	trum. The flux density normalised by the PyQSOFit pseudo-continuum	
	is presented in grey. The absorption model reconstructions are presented	
	in black. The species are labelled in each panel. We mark the various ve-	
	locity components with vertical lines in each panel	97
4.11	The X-Shooter spectrum of ULASJ2315+0143 is presented in grey, with	
	the broad-band photometry from UKIDSS and WISE overlaid in red. The	
	best-fit UV/optical SED, see Section 4.3.2, is extrapolated to mid-infrared	
	wavelengths (blue, solid), assuming $L_{2\mu m,Dust}/L_{2\mu m,QSO}=2.5$. The pho-	
	tometry is inconsistent with the SED model redward of the W1 filter.	
	The same SED model assuming $L_{2\mu m,Dust}/L_{2\mu m,QSO}=0.5$ (blue, dashed)	
	is more consistent with the photometry. Both SED models assume a hot	
	dust temperature of 1243K. This suggests that the ULASJ2315+0143 system contains less hot dust than the typical blue SDSS quasar, where $L_{2um,Dust}$ /	
		101
	$L_{2\mu m,QSO} \sim 1.0$ (remple et u., 2021a)	101

LIST OF FIGURES xv

	An illustration of our proposed geometry that best describes ULASJ2315 +043 focusing on the different scales associated with different features in the X-Shooter spectrum and the multi-wavelength observations of this source. On sub-pc scales we illustrate the BLR gas with blue clouds. Since the mid-infrared SED is devoid of hot dust (Fig. 4.11), we illustrate the missing/depleted torus with dotted black lines stretching to $\sim\!10$ pc. ALMA observations suggest that the ISM dust is on scales of $\sim\!15\text{-}20$ kpc based on the size of the millimetre continuum emission. NLR gas and star-forming regions are represented with green clouds and black stars respectively. The warm molecular gas is depicted with red clouds and the cold molecular gas is depicted with maroon clouds. A cartoon sight line, scattered from ISM dust and then subsequently absorbed by the warm and cold gas reservoirs, potentially giving rise to the AAL features in the UV spectrum, is illustrated by the dashed black arrow. The merging companion galaxy resides at 15 kpc and is illustrated to the left of the sketch. Blue, green and maroon arrows represent BLR, NLR and cold molecular gas flows respectively all of which exhibit significant velocity offsets relative to the systemic redshift	102
5.2	Example SED fits for HRQs where a UV excess is "confirmed" (top), "inconclusive" (middle) or "rejected" (bottom). The photometric data and associated uncertainties are presented in black. The best-fit SED model and photometry are presented by the blue line and triangles. The dust attenuated quasar component and photometry are presented by the orange line and triangles. In the "confirmed" case, there is clear evidence of a UV excess. In the "inconclusive" case, there is tentative evidence of a UV excess, but the wavelength coverage does not extend blue enough to constrain the model. In the "rejected" case, there is no evidence to support that the two-component model yields a better fit than a single-component reddened quasar SED. The "best-fit" SED for the HRQ VIKJ2258-03219 with no galaxy contribution (Panel A) and with $fragal = 0.05$ (Panel B). The photometric data and associated uncertainties are presented in black. The best-fit SED model and photometry are presented by the blue line and triangles. The dust attenuated quasar component and photometry are presented by the orange line and triangles. At near-infrared wavelengths the model is unable to reproduce the photometry in Panel A, suggestive of old stellar populations having a significant contribution to the SED in this region. Hence, the inclusion of a galaxy component in Panel B improves the fit.	119

xvi LIST OF FIGURES

5.3	The scattering fraction, F_{UV} , vs the <i>i</i> -band magnitude (top) and the $(i - K)_{\text{AB}}$ colour (bottom), calculated from the best-fit SED models for the	
	39 HRQs that exhibit a statistically significant UV excess. The HRQ selections are represented by dashed black lines in their respective panels.	
	The <i>i</i> -band magnitude does not appear correlated with F_{UV} , however, there is a strong anti-correlation between F_{UV} and the $(i - K)_{AB}$ colour.	
	It is likely that this colour selection prevents HRQs with higher scattering fractions from being selected	127
5.4	The SALT spectra of ULASJ2200+0056 in the C IV and He II emission re-	12,
	gions are presented in grey. The continua are presented in blue and the	
	final line reconstructions are presented in red. Both emission lines exhibit a FWHM $>> 1000~$ km s $^{-1}$ and are hence considered broad	128
5.5	We present the $(J - K)_{AB}$ colours of various QSOGEN SED models as a	120
	function of the systemic redshift. Our $(J - K)_{AB} = 1.6$ mag colour selec-	
	tion is illustrated by the black dashed line. We opt for an extinction E(B-V)OSQ 1 mag and a 2000 Å continuous luminosity long (NL (2000 Å))	
	V) ^{QSO} = 1 mag and a 3000Å continuum luminosity $log_{10}{\lambda L_{\lambda}(3000Å)}$ = 47 erg s ⁻¹ - consistent with the mean extinction observed in the 60 HRQs	
	for which an SED model was conducted. At $z_{\text{sys}} \geq 1.5$, the $(J - K)_{\text{AB}}$	
	colour is insensitive to the sublimation temperature dust amplitude. Be-	
E (low this redshift, the distribution is shaped by selection effects We present the $(W1 - W2)$ colours of various QSOGEN SED models as	130
5.6	a function of the systemic redshift. Our $(W1 - W2) = 0.85$ mag colour	
	selection is illustrated by the black dashed line. We opt for an extinction	
	$E(B-V)^{QSO} = 1 \text{ mag and a } 3000\text{Å continuum luminosity } \log_{10} \{\lambda L_{\lambda}(3000\text{Å})\}$	=
	47 erg s^{-1} - consistent with the mean extinction and luminosity observed in the 60 HRQs for which an SED model was conducted. The $(W1 - W2)$	
	colour selection appears to bias our sample towards HRQs with higher	
	sublimation temperature dust amplitudes	131
5.7	Histograms illustrating the ratio in luminosity between the sublimation	
	temperature dust blackbody and the tail of the UV continuum slope at $2\mu m$. The $z_{\text{sys}} \geq 1.5$ HRQ sample is presented in orange and the blue	
	SDSS quasars studied in Temple <i>et al.</i> (2021a) are presented in blue. The	
	HRQ histogram is systematically biased toward lower sublimation tem-	
	perature dust amplitudes, implying that there is less dust in the inner	
	regions of HRQs with respect to blue quasars at equivalent black-hole mass, luminosity and redshift	132
5.8	The optical continuum slope, β_{opt} , vs the UV continuum slope, β_{uv} , is	102
	presented for the 50 HRQs analysed in this work. The red shaded re-	
	gion represents the LRD parameter space and the dashed lines along the	
	boundary mark the LRD selection criteria, $\beta_{\rm opt} > 0$ and $-2.8 < \beta_{\rm uv} < -0.37$. While 47/50 HRQs host sufficiently red rest-optical continua,	
	only 4/50 host sufficiently blue rest-UV continua and would therefore	
	be considered LRDs by this formalism	134

LIST OF FIGURES xvii

5.9	We present a composite SED model for LRDs (Akins <i>et al.</i> , 2024), in blue. The best-fit SED model for the "LRD-Like" HRQ - VIKJ2230-2956 - is presented in beige. The noise-weighted composite SED model for HRQs is presented in coral. The best-fit SED model for an HRQ with no statistically significant UV excess - ULASJ0144+0036 - is presented in maroon. The SEDs were normalised in the <i>K</i> -band at the average HRQ redshift, $z_{\rm sys} = 2.12$. The Balmer Break is denoted by the dashed black line.	
	At rest-optical wavelengths, LRDs and HRQs have similar SED shapes, however, the SEDs diverge blueward of H β , with LRDs exhibiting bluer	
	continua than HRQs	135
5.10	SED fits for the HRQs; VIKJ2115-5913 (top) and ULASJ0144-0114 (bottom). The photometric data and associated uncertainties are presented in	
	black. The best-fit SED models using the Orion dust law are presented by	
	the blue lines and triangles. The best-fit SED models using the SMC-like	
	dust law used in QSOGEN are presented by the orange lines and triangles. In both cases, a multi-component model with an SMC-like dust extinc-	
	tion law is favoured (see the $\overline{\chi}^2_{\nu}$ statistics), despite VIKJ2243-3504 satis-	
	fying the LRD selection criteria. The Orion dust extinction law is flatter	
	than the dust law used in QSOGEN. While this can produce favourable fits at rest-UV wavelengths, it is too flat to reproduce the rest-optical	
	emission	137
5.11	The UV/optical inflection point wavelength as a function of E(B-V) ^{QSO}	
	for the HRQ sample. The violin plot represents the rest-UV/optical inflection point wavelengths for the HRQ sample. The 1^{st} , 2^{nd} and 3^{rd} quar-	
	tiles are represented by the box plot. The HRQ inflection points are in-	
	consistent with the Balmer Break, $\lambda_{\text{rest}} = 3645\text{Å}$, and the dispersion in	
	the distribution is large. Hence, a two-component model for HRQ SEDs is preferred over the Balmer Absorption models proposed for LRDs. The	
	positive correlation illustrates the flexibility of multi-component SED	
	models, showing that the SED inflection point can migrate red-wards	
E 10	1 0 0	139
3.12	We present the de-reddened $2.3\mu m$ to $0.51\mu m$ flux ratio, $F_{2,3}$, for the 47 HRQs whose redshifts $z_{\rm sys} \geq 1.5$ and $\overline{\chi_{\nu}^2} < 5.0$ (top). The Jun & Im	
	(2013) condition for dust-poor quasars is marked by the dashed black	
	line. The mean of the HRQ sample ($\langle F_{2,3} \rangle _{HRQ} = -0.27$) is marked by	
	the solid black line. The mean sublimation-temperature dust amplitude, $L_{Dust}/L_{Disk} _{2\mu m}$, per bin is plotted in the bottom panel and is shown to	
	increase with $F_{2,3}$	142
5.13	The rest-frame ultraviolet scattering fraction, F_{UV} , of an HRQ as a func-	
	tion of their dust extinctions, $E(B-V)$. We see evidence of a negative correlation suggesting that the more beautily extincted HPOs have	
	tive correlation, suggesting that the more heavily extincted HRQs have weaker UV continuum luminosities or larger scattering fractions	144
5.14	The rest-frame ultraviolet scattering fraction, F_{UV} , of an HRQ as a func-	
	tion of their sublimation temperature dust amplitudes, $L_{Dust}/L_{Disk} _{2\mu m}$.	
	We see evidence of a positive correlation, suggesting that the HRQs whose obscuring medium is distributed close to their sublimation temperature	
	radii host stronger UV continuum luminosities or larger scattering frac-	
	tions	145

xviii LIST OF FIGURES

Appendix B.1 The "best-fit" SED for the HRQ ULASJ0016-0038. The pho-	
tometric data and associated uncertainties are presented in black. The	
best-fit multi-component SED model and photometry are presented by	
the blue line and triangles. The dust attenuated quasar component and	
photometry are presented by the orange line and triangles	162
Appendix B.2 Same as Fig. B.1 but for the HRQ - ULASJ0041-0021	162
Appendix B.3 Same as Fig. B.1 but for the HRQ - ULASJ0123+1525	162
Appendix B.4 Same as Fig. B.1 but for the HRQ - ULASJ0141+0101	163
Appendix B.5 Same as Fig. B.1 but for the HRQ - ULASJ0144-0114	163
Appendix B.6 Same as Fig. B.1 but for the HRQ - ULASJ0144+0036. $\ \ldots \ \ldots$	163
Appendix B.7 Same as Fig. B.1 but for the HRQ - ULASJ0221-0019	
Appendix B.8 Same as Fig. B.1 but for the HRQ - ULASJ1002+0137	164
Appendix B.9 The "best-fit" SED for the HRQ ULASJ1234+0907. The pho-	
tometric data and associated uncertainties are presented in black. The	
best-fit single-component SED model and photometry are represented	
by the orange line and triangles	164
Appendix B.10 Same as Fig. B.9 but for the HRQ - ULASJ1415+0836	
Appendix B.11 Same as Fig. B.9 but for the HRQ - ULASJ1539+0557	
Appendix B.12 Same as Fig. B.1 but for the HRQ - ULASJ2200+0056	
Appendix B.13 Same as Fig. B.1 but for the HRQ - ULASJ2224-0015	
Appendix B.14 Same as Fig. B.1 but for the HRQ - ULASJ2312+0454	
Appendix B.15 Same as Fig. B.1 but for the HRQ - ULASJ2315+0143	
Appendix B.16 Same as Fig. B.9 but for the HRQ - VHSJ1117-1528	
Appendix B.17 Same as Fig. B.9 but for the HRQ - VHSJ1122-1919	
Appendix B.18 Same as Fig. B.9 but for the HRQ - VHSJ1301-1624	
Appendix B.19 Same as Fig. B.1 but for the HRQ - VHSJ1350-0503	168
Appendix B.20 Same as Fig. B.9 but for the HRQ - VHSJ1409-0830	
Appendix B.21 Same as Fig. B.1 but for the HRQ - VHSJ1556-0835	
Appendix B.22 Same as Fig. B.9 but for the HRQ - VHSJ2024-5623	
Appendix B.23 Same as Fig. B.1 but for the HRQ - VHSJ2028-4631	
Appendix B.24 Same as Fig. B.1 but for the HRQ - VHSJ2028-5740	169
Appendix B.25 Same as Fig. B.1 but for the HRQ - VHSJ2048-4644	
Appendix B.26 Same as Fig. B.1 but for the HRQ - VHSJ2100-5820	
Appendix B.27 Same as Fig. B.1 but for the HRQ - VHSJ2101-5943	170
Appendix B.28 Same as Fig. B.1 but for the HRQ - VHSJ2109-0026	171
Appendix B.29 Same as Fig. B.1 but for the HRQ - VHSJ2115-5913	171
Appendix B.30 Same as Fig. B.1 but for the HRQ - VHSJ2130-4930	171
Appendix B.31 Same as Fig. B.1 but for the HRQ - VHSJ2141-4816	172
Appendix B.32 Same as Fig. B.1 but for the HRQ - VHSJ2143-0643	172
Appendix B.33 Same as Fig. B.9 but for the HRQ - VHSJ2144-0523	172
Appendix B.34 Same as Fig. B.9 but for the HRQ - VHSJ2212-4624	173
Appendix B.35 Same as Fig. B.1 but for the HRQ - VHSJ2220-5618	173
Appendix B.36 Same as Fig. B.1 but for the HRQ - VHSJ2227-5203	173
Appendix B.37 Same as Fig. B.1 but for the HRQ - VHSJ2256-4800	174
Appendix B.38 Same as Fig. B.1 but for the HRQ - VHSJ2257-4700	174
Appendix B.39 Same as Fig. B.1 but for the HRQ - VHSJ2306-5447	174
Appendix B 40 Same as Fig. B 1 but for the HRO - VHSI2322-5240	175

LIST OF FIGURES xix

Appendix B.41 S	Same as Fig. 1	B.1 but for	the HRQ -	VHSJ2355-0	011	 175
Appendix B.42 S	Same as Fig. 1	B.1 but for	the HRQ -	VIKJ2205-31	132	 175
Appendix B.43 S	Same as Fig. 1	B.1 but for	the HRQ -	VIKJ2214-31	100	 176
Appendix B.44 S	Same as Fig. 1	B.1 but for	the HRQ -	VIKJ2228-32	205	 176
Appendix B.45 S	Same as Fig. 1	B.1 but for	the HRQ -	VIKJ2230-29	956	 176
Appendix B.46 S	Same as Fig. 1	B.1 but for	the HRQ -	VIKJ2232-28	344	 177
Appendix B.47 S	Same as Fig. 1	B.1 but for	the HRQ -	VIKJ2238-28	336	 177
Appendix B.48 S	Same as Fig. 1	B.1 but for	the HRQ -	VIKJ2241-30	006	 177
Appendix B.49 S	Same as Fig. 1	B.1 but for	the HRQ -	VIKJ2243-35	504	 178
Appendix B.50 S	Same as Fig. 1	B.1 but for	the HRQ -	VIKJ2245-35	516	 178
Appendix B.51 S	Same as Fig. 1	B.1 but for	the HRQ -	VIKJ2251-34	133	 178
Appendix B.52 S	Same as Fig. 1	B.1 but for	the HRQ -	VIKJ2256-31	14	 179
Appendix B.53 S	Same as Fig. 1	B.1 but for	the HRQ -	VIKJ2258-32	219	 179
Appendix B.54 S	Same as Fig. 1	B.1 but for	the HRQ -	VIKJ2306-30)50	 179
Appendix B.55 S	Same as Fig. 1	B.1 but for	the HRQ -	VIKJ2309-34	133	 180
Appendix B.56 S	Same as Fig. 1	B.1 but for	the HRQ -	VIKJ2313-29	904	 180
Appendix B.57 S	Same as Fig. 1	B.1 but for	the HRQ -	VIKJ2314-34	159	 180
Appendix B.58 S	Same as Fig. 1	B.1 but for	the HRQ -	VIKJ2323-32	222	 181
Appendix B.59 S	Same as Fig. 1	B.1 but for	the HRQ -	VIKJ2350-30)19	 181
Appendix B.60 S	Same as Fig. 1	B.1 but for	the HRQ -	VIKJ2357-30)24	 181

List of Tables

2.1	We present estimates of the average signal-to-noise, C IV EW and C IV blueshift for the 33 high signal-to-noise composite spectra used to correct the systemic redshifts of our sample. The signal-to-noise estimates are calculated assuming the individual spectra have a median continuum signal-to-noise ~ 5 . We also provide filenames for the composites, which are available as online only supplementary material, in addition to the total number of spectra used to construct them. 62,464 quasar spectra were used in total	32
3.1	The format of the table containing the emission line properties from our MFICA reconstructions. The table is available in a machine-readable format in the online journal	52
4.1	We present the various PypeIt user-level parameters used to optimise the reduction and extraction of the ULASJ2315+0143 X-Shooter spectrum. The numerous additional parameters, which do not feature in this table, were left at their default settings	77
4.2	Best-fit QSOGEN parameters for the SED fit shown in Fig. 4.3. Uncertainties represent the MCMC uncertainties	84
4.3	QSOGEN and BAGPIPES user-level parameters for the SED fit shown in Fig. 4.5. Uncertainties represent the MCMC uncertainties	88
4.4	Quasar emission line properties inferred from the ULASJ2315+0143 X-Shooter spectrum. Since the [O II] emission was used to determine z_{sys} , its V50 velocity is zero by definition. Here, the results pertaining to the [O III] emission refer to the λ 5008Å line	94
4.5	Summary of different velocity components of narrow associated absorption line systems (AALs) shown in Fig. 4.10. Velocity offsets are relative to the [O II] systemic redshift. We group velocity components whose offsets are consistent within the uncertainty on z_{sys}	98
5.1	The H α EWs taken from Banerji <i>et al.</i> (2012, 2015); Temple <i>et al.</i> (2019); Stepney <i>et al.</i> (2024) and their corresponding <i>emline_type</i> for the entire HRO sample. Where H α EWs are unavailable, we assume <i>emline_type</i> = 0	116

xxii LIST OF TABLES

5.2	The best-fit parameters for the 60 HRQs for which we conducted an SED			
fit with QSOGEN. Objects for which it was not possible to model the U				
	Excess are classified as "N/A". Objects for which a UV excess was con-			
	firmed, rejected or yielded inconclusive results are denoted as "Conf.",			
	"Rej." or "Inc." respectively. HRQs whose redshift $z_{\rm sys} < 1.5$ are mod-			
	elled with $fragal = 0.05$, otherwise $fragal = 0.00$ Uncertainties repre-			
	sent the MCMC uncertainties only, and are therefore likely to be under-			
	estimated	122		
5.3	The rest-UV emission line properties of the HRQ, ULASJ2200+0056	128		
Λ	andia A.1. The LIDO what are street for each of the (O courses calcuted in			
App	pendix A.1 The HRQ photometry for each of the 60 sources selected in			
	Banerji et al. (2012), Banerji et al. (2013), Banerji et al. (2015) and Temple			
	et al. (2019). Photometric bands whose uncertainties are set by the 10 per			
	cent floor (see Section 5.2) are presented in hold face	156		

Declaration of Authorship

I declare that this thesis and the work presented in it is my own and has been generated by me as the result of my own original research.

I confirm that:

- 1. This work was done wholly or mainly while in candidature for a research degree at this University;
- 2. Where any part of this thesis has previously been submitted for a degree or any other qualification at this University or any other institution, this has been clearly stated;
- 3. Where I have consulted the published work of others, this is always clearly attributed;
- 4. Where I have quoted from the work of others, the source is always given. With the exception of such quotations, this thesis is entirely my own work;
- 5. I have acknowledged all main sources of help;
- 6. Where the thesis is based on work done by myself jointly with others, I have made clear exactly what was done by others and what I have contributed myself;
- 7. Parts of this work have been published in *Monthly Notices of the Royal Astronomical Society* as:

"No redshift evolution in the rest-frame ultraviolet emission line properties of quasars from z = 1.5 to z = 4.0", **Matthew Stepney**, Manda Banerji, Paul C. Hewett, Matthew J. Temple, Amy L. Rankine et al., 2023, 10.1093/mnras/stad2060.

"A big red dot: scattered light, host galaxy signatures, and multiphase gas flows in a luminous, heavily reddened quasar at cosmic noon", **Matthew Stepney**, Manda Banerji, Shenli Tang, Paul C. Hewett et al., 2024, 10.1093/mnras/stae1970.

Signed: Date: 13th November 2025

Acknowledgements

There are a number of people without whom the work in this thesis would not be possible. Firstly, I need to thank my supervisor Manda. Thank you for letting me be your first Southampton student and curating a PhD experience that was perfectly tailored to my own interests and goals. Thank you for believing in me when I was, perhaps, unconvinced. Thank you for helping me navigate the balance between my research and teaching commitments, and finally, thank you for equipping me with all the necessary tools for a successful career in research beyond Southampton.

I must also thank the co-authors named in the declaration, whose collaboration and support undoubtedly resulted in stronger research. Thank you to Paul, whose insight into quasar spectra was invaluable, for sharing the MFICA components used to fit the SDSS quasar spectra and finally, for providing a reference which has set the stage for my onward journey in academia. Thanks to Matthew, for making my first international conference less daunting, building the qsogen package - with which I conducted my SED fits - and the countless science conversations. Thank you Amy, whose work on SDSS quasars paved the way for my first project and also for providing me with the opportunity to discuss my results in Edinburgh. Thanks to James, for all the useful science conversations, providing me with the opportunity to discuss my science at Oxford and understanding the life of a Southampton PhD student. I must also thank Shenli, Clare, Anna and Stephen for their useful comments on both papers and proposals, as well as Elham and Rashi for sharing food from their travels at group meetings.

My time in the department was made all the better thanks to Megan, Charlotte and Marcus. From pub-crawl thievery to crosswords, from geese-themed board games to bottomless brunch - it has truly been a joy. I would also like to thank Phil and Chris for helping with the big things (Why are my $\overline{\chi}_{\nu}^{2}$'s too small?) and the small things (What is the cheapest baked-good sold in the SUSU shop?).

Finally, I wish to acknowledge the support of my family and friends outside of Southampton. Thank you Mom and Dad for supporting me long before I chose to be an astronomer. Thank you Harriet and Ross for giving me a beautiful niece and reminding me that whenever the weather in Southampton was grim, it was always worse in Newcastle. Thank you to Ivo, Becca and Lucy - gallivanting through the Mediterranean is the highlight of my year, even if it costs Ivo an arm and the rest of us 100 Euros in Caipirinhas. Thank you to my housemate Liv, as well as Courtney, Alex, Jade, Joe and Abby for the unmeasurable fun over the last four years and finally, Southampton - it's been a long 8 years but it was definitely worth it.

	xxvii
To my family, friends and the city of Southampton	

Definitions and Abbreviations

 A_V V-band dust extinction L_{\odot} Solar luminosity unit

 $\lambda_{\rm Edd}$ Eddington-scaled accretion rate

 M_{\odot} Solar mass unit

z Redshift

 Z_{\odot} Solar metallicity unit

AGN Active Galactic Nuclei

ALMA Atacama Large Millimeter/submillimeter Array

ANDICAM A Novel Dual Imaging Camera

BLR Broad Line Region
CNR Central Nuclear Region

CTIAO Cerro Tololo Inter-American Observatory
DESI Dark Energy Spectroscopic Instrument

eBOSS/BOSS (extended) Baryon Oscillation Spectroscopic Survey

ERQ Extremely Red Quasar EW Equivalent Width

Hot DOG Hot Dust-Obscured Galaxy HRQ Heavily Reddened Quasar

ISM Interstellar Medium

JWST James Webb Space Telescope

LRD Little Red Dot

MFICA Mean-Field Independent Component Analysis

NLR Narrow Line Region

PCA Principle Component Analysis

SDSS Sloan Digital Sky Survey SMBH Super-Massive Black Hole

UKIDSS United Kingdom Infrared Deep Sky Survey

UKIRT United Kingdom Infrared Telescope

VLT Very Large Telescope

WISE Wide-field Infrared Sky Explorer

Chapter 1

Introduction

1.1 Thesis Structure

Energy feedback from active galactic nuclei (AGN) and their accreting supermassive black holes (SMBHs) can have a profound impact on their host galaxies (see review by; Heckman & Best, 2014). These feedback processes facilitate the co-evolution of the central SMBH and the host galaxy bulge, allowing both the black hole and the host galaxy to grow in tandem - despite their vastly different spatial scales (Ferrarese & Merritt, 2000; Gebhardt *et al.*, 2001; Kormendy & Ho, 2013). At present, the exact nature of these feedback processes are not fully understood. Hence, in this thesis, we leverage novel spectroscopic reconstruction and SED fitting techniques to tackle the crucial question of how energetic winds from SMBHs influence galaxy evolution across cosmic time.

In this thesis, we utilise both large statistical samples and detailed single-object investigations for our analysis. To gain the most holistic view of AGN feedback possible, we employ a multi-wavelength approach to study both blue and red quasar populations. We investigate how AGN-driven winds at different scales depend on fundamental properties - such as black hole mass and accretion rate - as well as whether the strength of these outflows evolve with redshift. In addition, we also explore whether the presence of dust can facilitate stronger, more energetic winds which propagate to galaxy-wide scales - reshaping the geometry of the AGN and moderating star-formation in the host galaxy. By studying diverse populations of AGN and carefully considering selection effects, we enable a more complete understanding of the complex physical processes that govern AGN feedback. The structure of the thesis is as follows;

In Chapter 1, we introduce the fundamental physics underpinning radiative transfer and black-hole accretion, examining their role in driving the AGN phenomenon. We then explore the geometry and composition of AGN before discussing evidence of their role in moderating the evolution of their host galaxies. Lastly, we review the key observational techniques used by astronomers to probe AGN physics, connecting the physical components of the AGN discussed earlier in the chapter to their characteristic emission signatures.

In Chapter 2, we implement a non-parametric spectroscopic reconstruction technique that utilises Mean-Field Independent Component Analysis (MFICA) to reconstruct blue quasar spectra from the Sloan Digital Sky Survey (SDSS). The use of MFICA enables more robust reconstructions of the $3.5 < z_{sys} < 4.0$ quasar spectra, which are of modest signal-to-noise, and ensures that a consistent methodology is used to analyse the blue SDSS quasar sample across the entire redshift range ($1.5 < z_{sys} < 4.0$), minimising selection effects. The high-redshift quasar sample is defined and a cross-correlation analysis is employed to measure accurate systemic redshifts from the rest-UV emission alone. A masking recipe for the removal of narrow absorption features is also described.

In Chapter 3, a robust analysis of the C IV and He II line morphologies using the spectroscopic reconstructions discussed in Chapter 2 is conducted. We employ the C IV line centroid and a sample of identically analysed SDSS quasars at $1.5 < z_{sys} < 3.5$ to investigate the redshift evolution of broad-line region outflows from $1.5 < z_{sys} < 4.0$. The use of a consistent methodology across the entire SDSS quasar population enables detailed discussions into how quasar-driven winds at different scales depend on fundamental properties such as cosmological redshift, black hole mass and accretion rate - largely free of selection effects. Hence, an analysis of the primary driver of quasar outflows, the nature of their evolution, and the implications of our results at higher redshifts is possible.

In Chapter 4, we conduct a detailed single-object study of a luminous red quasar undergoing a gas-rich merger at cosmic noon. We describe the reduction and analysis of the object's rich VLT-XShooter spectrum, employing Balmer emission and the rest-optical continuum to infer the physical properties of the quasar - such as SMBH mass and accretion rate. With a suite of line properties combined with the analysis of the quasar's full ultraviolet to near-infrared SED, we test whether the presence of dust is a fundamental driver of quasar outflows. Furthermore, we discuss how these multi-phase gas flows propagate beyond the torus and onto interstellar medium scales - using the hot dust emission and host galaxy signatures to gauge the impact of dust-driven winds on torus structure and star formation within the quasar host.

1.1. Thesis Structure 3

In Chapter 5, we investigate the full ultra-violet to near-infrared SED properties of a sample of 60 heavily reddened quasars. We discuss the selection of the photometric data and the construction of the SED model. We expand on our previous discussions on the source of the excess UV continuum emission observed in heavily reddened quasars, however, by expanding our previous work to larger sample sizes, we can determine whether the results from Chapter 4 are applicable to the heavily reddened quasar population as a whole. With such broad photometric coverage, it is possible to link the ultraviolet SED properties of heavily reddened quasars to the near-infrared enabling us to develop a framework by which we can describe the evolution of luminous red quasars as they transition into their blue counterparts. Finally, we detail our results in the context of JWST's newly emerging population of "Little Red Dots" as well as other dust-obscured quasar populations at cosmic noon - discussing the similarities and differences of the red AGN phase at different black hole mass and accretion rate.

In Chapter 6, we provide a final summary of the results detailed in this thesis, as well as a discussion of some potential directions for future research with the latest generation of ground- and space-based spectroscopic/imaging surveys. Vacuum wavelengths are employed throughout this thesis unless stated otherwise. We adopt a Λ CDM cosmology with $h_0 = 0.71$, $\Omega_{\rm M} = 0.27$ and $\Omega_{\Lambda} = 0.73$ when calculating quantities such as quasar luminosities. The first-person plural is adopted to match the usual style of scientific prose and does not imply any co-authorship beyond that indicated specifically in the text.

1.2 Radiative transfer

Radiative transfer describes the process by which a radiation field can transfer electromagnetic energy, generally taking the form of ionisation, absorption, emission and/or scattering (Chandrasekhar, 1950).

1.2.1 A quantum description of light

In the classical interpretation of light, electromagnetic energy is continuously transferred to matter via waves. It was Planck (1901) who identified that electromagnetic radiation should instead be described as discrete energy packets, which underpinned Einstein's "heuristic" description of the Photoelectric Effect.

The Photoelectric Effect was first observed by Hertz (1887), who detailed how ultra-violet (UV) light had the ability to transfer energy to bound electrons via electromagnetic waves. Having accumulated enough energy, the bound electrons became free, yielding a photocurrent. It was Hertz (1887)'s interpretation that a change in the *intensity* of the incident radiation should increase/decrease the energy of the free electrons. However, Lenard (1902) discovered that the energy of the electrons emitted via the Photoelectric Effect had no relationship to the intensity of the incident light.

Consequently, Einstein (1905b) proposed that quantised light - later popularised as *photons* by Lewis (1926) - were not infinitely divisible - but instead had discrete energies proportional to the frequency of the emission, expressed as;

$$E = h\nu \tag{1.1}$$

where E is the photon energy, v is the photon frequency, and h is what later became known as Planck's constant. In addition, Einstein (1905b) also proposed that photons have momenta. Photon momenta can be expressed via Eqn. 1.2 - proved experimentally by Compton (1923), where c is the velocity defined by Maxwell (1865).

$$p = \frac{E}{c} = \frac{h\nu}{c} \tag{1.2}$$

1.2.2 Bound-free Interactions

Since Einstein's quantised description of light states that photon energies are discrete, a photon must transfer *all* of it's energy to an electron for the interaction to be allowed by quantum mechanics (Planck, 1901; Einstein, 1905b). When a photon incident on a

given material exceeds the corresponding threshold frequency, *ionisation* occurs. In this *bound-free* interaction, the remaining photon energy is transferred to the kinetic energy of the newly free electron (Millikan, 1914). It is also possible for bound-free interactions to occur in reverse, whereby a free electron can *recombine* with an atom/ion. The result is a series of recombination lines as the electron cascades through the various energy levels in the atom/ion - (e.g. the Balmer Series; Baker & Menzel, 1938).

1.2.3 Bound-bound Interactions

Photons whose frequencies fall below the threshold frequency cannot induce a photocurrent (Einstein, 1905b). However, they may still be *absorbed* by bound electrons if the photon energy corresponds to the energy of an allowed¹ excited state. This is an example of a *bound-bound* interaction, the likelihood of which is dictated by the Einstein Coefficients (Einstein, 1916b). The newly excited electron will eventually decay to a less energetic state and the energy of the emitted photon will correspond to the difference between the two energy levels. The resulting emission will therefore have a single discrete frequency - known as *line emission*. Observing line emission in the spectra of astronomical sources is an effective tool for studying their composition, a technique we utilise throughout this thesis.

The mechanism by which an electron decays to a less energetic state can take the form of either spontaneous or stimulated emission. The preferred mode of decay is dependent on the emission rate of the particular species/transition and the physical properties of the plasma. We often refer to emission lines as either *permitted* or *forbidden*. Permitted lines are those transitions whose spontaneous emission rates are high and are therefore observed under usual laboratory conditions. Conversely, forbidden lines have low spontaneous emission rates and are therefore collisionally de-excited in high-density/laboratory environments before the electron has time to emit a photon through the forbidden transition. However, in less dense environments - such as nebulae or diffuse interstellar medium gas - the collision rate is low enough such that forbidden transitions can be observed (Bowen, 1927).

In this thesis, we adopt the standard naming convention of using a pair of square brackets to reflect whether a line transition is forbidden or a singular square bracket to reflect if a line transition is semi-forbidden. In addition, we use Roman Numerals to represent the ionisation state of a given species, where *I* represents the neutral atom and successive ionisations are represented by increasing the Roman Numeral by the appropriate number of ionisations - e.g. [O III] and C III] represent a forbidden doubly ionised Oxygen transition and a semi-forbidden doubly ionised Carbon transition, respectively.

¹by *allowed* we refer to any transition permitted by the transition rules proposed by Hund (1925).

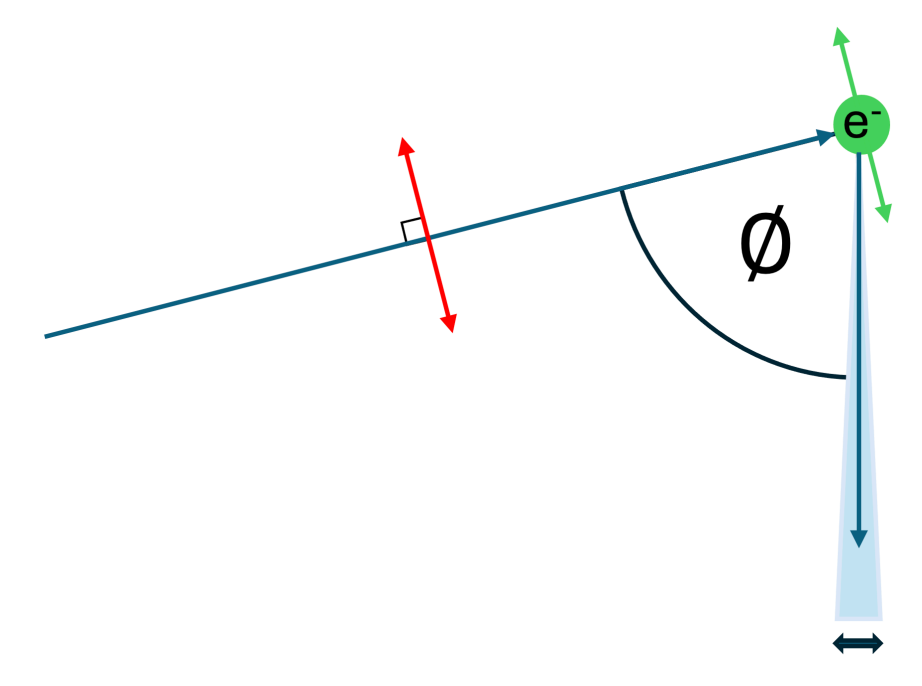


FIGURE 1.1: An illustration of Thomson scattering. The incident electromagnetic wave is depicted by the blue arrow moving mid-left to top-right. The perpendicular electric field associated with the incident radiation is depicted by the red arrows. The free electron is depicted in green, with the induced oscillations depicted with green arrows running parallel with the incident electric field. The direction of motion of the free electron is depicted by the blue arrow moving top-right to bottom-right. The light blue shaded region depicts the scattering cone of the re-emitted electromagnetic radiation. The deflection angle is given by ϕ .

1.2.4 Scattering

Charged particles - such as free electrons - also have the ability to *scatter* electromagnetic radiation in *free-free* interactions. Thomson scattering describes the low-energy limit where the scattering of light by charged particles is elastic, and therefore the frequency of the incident radiation remains unchanged (Thomson, 1906). The electric field component of the incident radiation accelerates the charged particle, resulting in oscillations perpendicular to the initial direction of motion of the incident beam. The scattered emission is then deflected along the new direction of motion of the charged particle - i.e. the vector summation of it's original path and the oscillations induced by the incident electric field (see Fig. 1.1). The likelihood of the interaction is represented by the Thomson cross-section, σ_T . Hence, the scattering intensity can be increased should the interaction be mediated by a larger cross-section.

1.2.5 Dust attenuation

Dust plays an important role in the structure and evolution of the Universe. In this thesis, we consider astrophysical dust to be any small solid particle found in the interstellar medium (ISM) of galaxies. Dust regulates the thermodynamics of ISM gas,

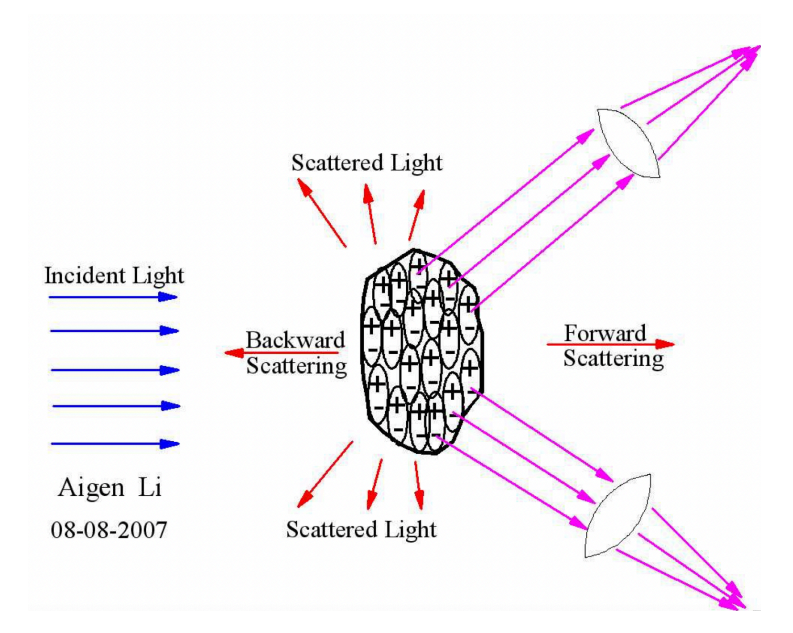


FIGURE 1.2: An illustration detailing how a dust grain can extinct electromagnetic radiation. The pink arrows represent the lines-of-sight of two perspective observers. Credit: Li (2008), Fig.1.

facilitating star and planet formation, however, the focus of this thesis is the ability of dust to reprocess electromagnetic radiation in *attenuation*² processes.

Trumpler (1930) found that the photometric distances to Milky Way open clusters were systematically overestimated compared to geometric distances based on angular size. The distance discrepancies suggest that light from distant stars gets scattered/absorbed by dusty material in the ISM. If we assume that a dust grain is comprised of many dipoles, when irradiated by incident light, these dipoles oscillate and elastically scatter the incident wave in all directions. Furthermore, the oscillating dipoles generate thermal energy which, in-turn, is absorbed by the dust grain (Bohren & Huffman, 1983). The stored thermal energy is eventually re-radiated at infrared wavelengths, accounting for approximately 30 per cent of all stellar emission in the Universe (Bernstein et al., 2002). We present an illustration of this process in Fig.1.2.

A key property of dust attenuation is that bluer wavelengths are preferentially extincted (Draine, 2003). From an astrophysical perspective, this means that the colours of distant galaxies - as well as the stars in the Milky Way - are *dust reddened*. The degree to which dust preferentially reddens a radiation field is described by an extinction curve. However, given that the level of extinction suffered by the incident light is dependent on the composition, size and shape of the dust grains, the functional form of an extinction curve varies depending on the specific properties of the obscuring medium.

²In this thesis, we interchangeably use the terms *attenuation* and *extinction* to refer to the scattering/absorption of electromagnetic radiation by dust.

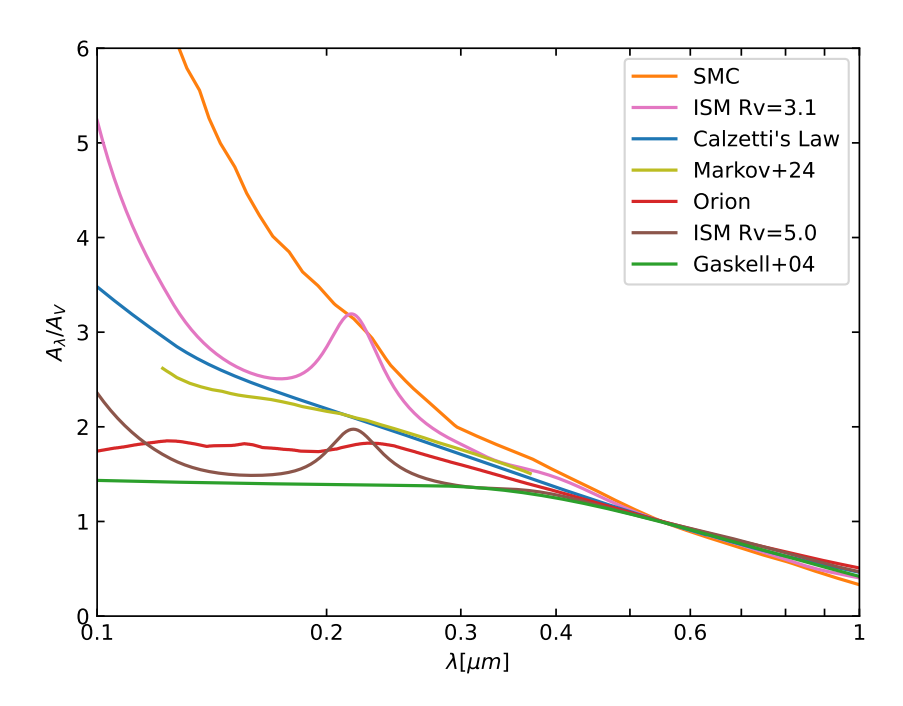


FIGURE 1.3: Empirically-derived dust extinction law curves normalised at 5500Å. Credit: Li *et al.* (2025), Fig.1.

Figure 1.3 illustrates the diversity in dust properties between the Milky Way, the Orion Nebula, the Small Magellanic Cloud (SMC) and starburst galaxies (e.g Calzetti *et al.*, 2000). Extinction curves lacking small dust grains (e.g. Fig. 1.3; green, red, brown) show weaker attenuation at bluer wavelengths compared to those with small grains (e.g. Fig. 1.3; orange, pink, blue). It was Stecher & Donn (1965) who first identified the $\lambda = 2175$ Å feature in the Milky Way extinction curve (Fig. 1.3; pink, brown), suggesting the cause was graphite crystals. In systems that lack the metallicity to produce carbonaceous dust, or host environments harsh enough to destroy dust grains, the $\lambda = 2175$ Å feature is less pronounced or missing entirely (Fig. 1.3; orange, blue). For this reason, dust-extinction laws employed to describe the attenuation of light from Active Galactic Nuclei (AGN) generally resemble that of the SMC (Czerny *et al.*, 2004; Temple *et al.*, 2021b).

Given that the degree to which AGN emission is attenuated by an obscuring medium is dependent on the functional form of the chosen dust extinction law, it is often helpful to discuss reddening in terms of the colour excess between **two** photometric bands - i.e. E(B-V), defined via Eqn. 1.3

$$A_{\lambda} = k(\lambda) \cdot E(B - V)$$

$$A_{V} = R_{V} \cdot E(B - V)$$
(1.3)

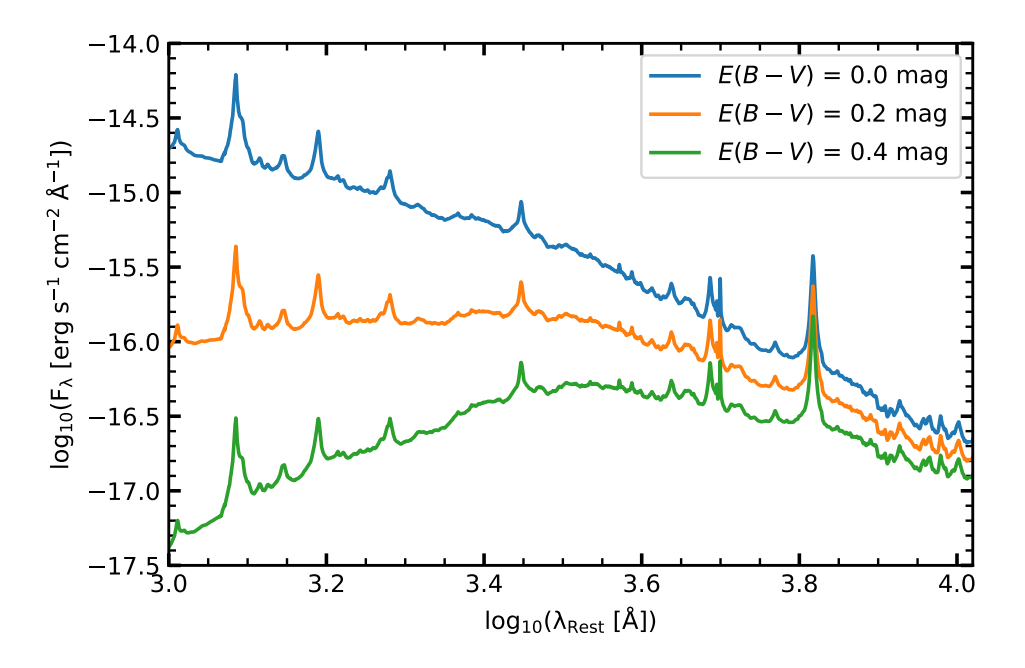


FIGURE 1.4: The effect of dust extinction on the continuum of a typical rest-UV/optical quasar spectrum at different values of E(B-V). Increasing E(B-V) results in increasing attenuation at all wavelengths, however, the bluer wavelengths are most affected. Here, an $R_V=3.1$ is assumed using an SMC-like extinction curve (Fig. 1.3; orange).

where A_{λ} is the wavelength-dependent extinction defined by a given extinction curve, $k(\lambda)$ is the wavelength-dependent total-to-selective extinction ratio (given by R_V in the V-band), and the E(B-V) is an estimate of the total extinction (Cardelli *et al.*, 1989) - it is assumed that $R_V=3.1$ throughout this thesis. Fig. 1.4 illustrates the effect of dust extinction on the continuum of a typical rest-UV/optical quasar spectrum at different values of E(B-V) - where larger values of E(B-V) result in more significant attenuation of the intrinsic quasar emission.

1.3 Black holes

At the turn of the 20th century, Einstein (1915) proposed the field equations of General Relativity and changed the landscape of physics. The field equations provide our most complete description of gravitation to date, describing gravity as a geometric property of the 4-dimensional *spacetime* manifold. More specifically, the Theory of General Relativity describes gravitation as the curvature of spacetime in the presence of energy or momentum (Einstein, 1916a) - which in-turn has significant astrophysical implications.

The first non-trivial solution to the field equations of General Relativity was discovered by Schwarzschild (1916) - whose solution describes the gravitational field around a spherically-symmetric point mass with zero angular momentum, embedded in an otherwise flat spacetime. Oppenheimer & Volkoff (1939) then used the field equations to prove that neutron stars with masses above the Tolman–Oppenheimer–Volkoff mass limit had no stable solutions, collapsing indefinitely toward the Schwarzschild (1916) solution. However, at what is now known as the Schwarzschild radius this point-like mass becomes singular, giving rise to some peculiar behaviour.

The surface subtended by the Schwarzchild radius was described by Oppenheimer & Volkoff (1939) as the point at which time stops. Finkelstein (1958) then extended this description to include the point-of-view of an *infalling* observer, describing the surface as a membrane that can only be traversed in one direction. We now refer to this surface as the *event horizon*, marking the boundary layer beyond which particles travelling at or below the speed of light would fail to escape the gravitational potential in finite time.

It is possible to derive an approximate expression for the Schwarzchild radius within a Newtonian framework. If we consider a particle of mass m acted upon by the gravitational potential of a black hole of mass M, the Schwarzchild radius can be inferred by equating the kinetic and potential energies of the particle when its velocity is equal to the speed of light c - i.e;

$$\frac{GMm}{R_s} = \frac{1}{2}mc^2 \longrightarrow R_s = \frac{2GM}{c^2} \tag{1.4}$$

where *G* represents the gravitational constant. In the mid-20th century, Kerr (1963) extended our understanding of Einstein's field equations, showing that they support point mass solutions with non-zero angular momenta. This discovery was significant given that all astrophysical black holes are thought to possess some level of spin since matter is unlikely to pass through the event horizon in perfect spherical symmetry. While these solutions also predict an event horizon, the radius of it's surface depends

1.4. Accretion 11

on the degree of spin experienced by the black hole, however, Eqn. 1.4 still serves as a useful approximation.

1.4 Accretion

In order for matter to be transported across the event horizon of a black hole, it's angular momentum must first be transported outward (Salpeter, 1964; Zel'dovich, 1964). Accretion disks - which are ubiquitous in astrophysics and found surrounding planets, stars and black holes - provide the turbulent viscosity required to dissipate energy from the infalling matter via dynamical friction (Shakura & Sunyaev, 1973).

In the case of black holes, the accretion process is extremely efficient. By employing a Newtonian description of gravity and our expression for the Schwarzchild radius (Eqn. 1.4), we can derive an upper limit to the accretion efficiency of a compact object. If we again assume that a particle of mass m is acted upon by the gravitational potential of a black hole of mass M, we can express the maximum energy output of accretion as;

$$\lceil E_{acc} \rceil = \frac{GMm}{Rs}
 = \frac{1}{2}mc^2$$
(1.5)

Hence, from the invariant mass equation (Einstein, 1905a,c), we know that the maximum energy output of accretion is equal to half of the rest-mass energy of the infalling particle. In practice, black-hole accretion is not 100 per cent efficient. Consequently, it is estimated that just 10 per cent of the rest-mass energy can be liberated via radiation before the accretion material passes over the event horizon (Soltan, 1982; Yu & Tremaine, 2002). However, accretion onto compact objects represents over an order of magnitude improvement in efficiency on stellar nucleosynthesis - which manages to liberate just 0.7 per cent of the hydrogen nuclei's rest-mass energy during nuclear fusion.

1.4.1 The Eddington Limit

Given that photons have momenta (as discussed in Section 1.2), when electromagnetic radiation is scattered, a radiative force is exerted on the scattering medium. It was Eddington (1925) who first identified that there was therefore a limiting luminosity at which an accreting body could emit before reaching radiative equilibrium. Let us consider a point source of mass M which emits isotropically at a luminosity L. The

outward force exerted on a particle of mass m at a radius r, due to radiation pressure, can then be expressed as;

$$F_{rad} = m \left(\frac{L\kappa}{4\pi r^2 c} \right) \tag{1.6}$$

Where κ is an opacity term. If we assume that the accreting material is comprised of pure ionised hydrogen, the opacity term can be expressed as the ratio between the Thomson cross-section and the mass of a proton³ - i.e. $\kappa = \sigma_t/m_p$. To determine the limiting luminosity L_{Edd} , we can therefore equate Eqn. 1.6 to the Newtonian expression for gravity, yielding;

$$m\left(\frac{L_{Edd}\kappa}{4\pi r^{2}c}\right) = m\left(\frac{GM}{r^{2}}\right) \longrightarrow L_{Edd} = \frac{4\pi GMm_{p}c}{\sigma_{T}}$$

$$\simeq 1.26 \times 10^{38} \left(\frac{M}{M_{\odot}}\right) \text{ erg s}^{-1}$$
(1.7)

1.4.2 Radiation-driven winds

It is often helpful to express the accretion rate of a black hole as its Eddington ratio;

$$\lambda_{Edd} = L/L_{Edd} \tag{1.8}$$

Under the assumptions that the emission is isotropic and the plasma is fully ionised, black holes whose luminosities exceed the Eddington Limit - i.e. $\lambda_{Edd} \gtrsim 1$ - will eject material via winds and therefore starve themselves of accretion fuel.

Since the Eddington luminosity has an opacity dependence, it can be modified if we introduce different plasma properties. For instance, should the plasma contain partially ionised gas, the absorption cross-section for photons at specific frequencies will exceed that of Thomson scattering (Murray *et al.*, 1995; Proga *et al.*, 2000). Given that the temperature of SMBH accretion disks are of order $\sim 10^5$ K, the radiation field is largely dominated by UV/optical emission. Hence, should the partially ionised gas support UV/optical line transitions, the Eddington Limit can be reduced by orders of magnitude (Stevens & Kallman, 1990).

This effect is known as *line driving* and depends on a delicate balance between the UV/optical flux and the far-UV/X-ray flux. Should the SED become too hard, the gas becomes overionised and therefore loses its ability to drive winds (Stevens & Kallman, 1990). In Chapter 3, we examine how black-hole mass, accretion rate, luminosity, and

³A generally good assumption for astrophysical plasmas

the ionising potential of the SED can influence line-driven disk winds. Similarly, in Chapters 4 & 5, we examine how these properties influence dust-driven winds - which arise when the opacity of the scattering medium is increased by the presence of dust at large enough radii such that the ionising continuum does not destroy the dust grains.

1.5 Active Galactic Nuclei and quasars

The study of Active Galactic Nuclei (AGN) began in the mid-20th century. Seyfert (1943) discovered high-excitation emission associated with the nuclei of several nearby spiral galaxies - which we now know as Seyferts. However, the detection of the first *quasar* would take another twenty years, with the publication of the Third Cambridge Catalogue of Radio Sources (3C; Edge *et al.*, 1959) laying the foundations for their discovery.

Schmidt (1963) discovered that the radio source - 3C273 - had a quasi-stellar (point-like) counterpart at rest-optical wavelengths. Furthermore, the optical emission spectrum of 3C273 hosted Balmer lines with large off-sets towards the red - defined by Eqn. 1.9;

$$1 + z_{sys} = \frac{\lambda_{\text{obs}}}{\lambda_{\text{rest}}} \tag{1.9}$$

where $\lambda_{\rm obs}$ and $\lambda_{\rm rest}$ are the observed and rest-frame wavelengths of a given spectral feature and $z_{\rm sys}$ is the corresponding systemic redshift. With a redshift $z_{\rm sys}=0.158$, Schmidt (1963) and 3C273 caught the attention of astronomers. Before long, optical counterparts had been detected for hundreds of the radio sources in the 3C catalogue - the most notable being 3C48, hosting an even more extreme redshift ($z_{\rm sys}=0.368$) than 3C273 (Greenstein, 1963).

With such large redshifts; 3C273, 3C48 and what we now know as *quasars* must be located on cosmological scales. Consequently, quasars became the most luminous non-transient sources in the known Universe, with luminosities in excess of $L \approx 10^{46}$ erg s⁻¹. In addition, 3C273 and 3C48 exhibit rapid variability at rest-optical wavelengths, suggesting that the emission region is no larger than just a few light-days. Owing to their extreme luminosities and compact emission regions, astronomers quickly concluded that quasars are powered by accreting super-massive black holes (SMBHs) - i.e. $M_{BH} \gtrsim 10^6~M_{\odot}$. It is now the consensus that all massive galaxies undergo an "active" phase, with the ubiquity of SMBH accretion first proposed by Lynden-Bell (1969).

1.5.1 Unification

The late- 20^{th} century witnessed a proliferation in the discovery of distinct AGN populations. For instance, Sandage (1965) was the first to identify a substantial population of radio-quiet AGN, which outnumber their radio-loud counterparts by at least an order of magnitude. Moreover, many AGN host broad ($\sigma > 1000 \text{ km s}^{-1}$) emission lines in species such as; C IV, Mg II and the Balmer Series - these are classified as Type 1 AGN. In contrast, other populations, such as Type 2 AGN, display only narrow-line emission.

The suite of emission line morphologies suggests that there exists a difference in the line-of-sight projected velocity structure of the emitting material. Hence, the different emission lines arise from different physical regions (Peterson, 2006). Broad emission lines arise from sub-parsec scale gas, where their large velocity dispersions are attributed to significant Doppler shifts caused by virial motion within the gravitational potential of the SMBH. By similar reasoning, narrow emission lines are thought to originate from kiloparsec-scale gas, consistent with their comparatively modest velocity dispersions. This stratified structure to the ionised gas has been confirmed via reverberation mapping (e.g. Clavel *et al.*, 1991; Peterson, 1993; Bentz *et al.*, 2008; Shen *et al.*, 2015; Yu *et al.*, 2021, see Section 1.7.3 for details) - with broad lines such as C IV situated on light-day to light-month scales.

Antonucci & Miller (1985)'s spectropolarimetry work demonstrated that, although broad emission lines are absent in the direct spectra of Type 2 AGN, they are detectable in polarized light. Evidence of obscured broad-line emission in Type 2 AGN prompted the development of a unified framework with which the diverse observational characteristics of AGN could be explained. The first AGN unification schemes (e.g. Antonucci, 1993; Urry & Padovani, 1995) invoked simple geometric arguments and the presence or absence of a radio jet to explain the observations postulating that all AGN can be broadly described by the components illustrated in Fig. 1.5.

In the Antonucci (1993) paradigm, AGN diversity arises from their axisymmetric geometry and hence, our observations are dependent on their on-sky orientations. For example, the dichotomy of Type 1 and Type 2 AGN can be considered an orientation effect. Consequently, Type 1 AGN describe orientations in which the broad-line region (BLR) gas is visible to an observer, whereas Type 2 AGN describe orientations in which the BLR emission is obscured by a dusty toroidal structure. However, there still remain many observations of AGN that are not well-understood. Hence, unifying these disparate AGN populations and understanding the physics that drives such diversity remains an active field in modern astronomy.

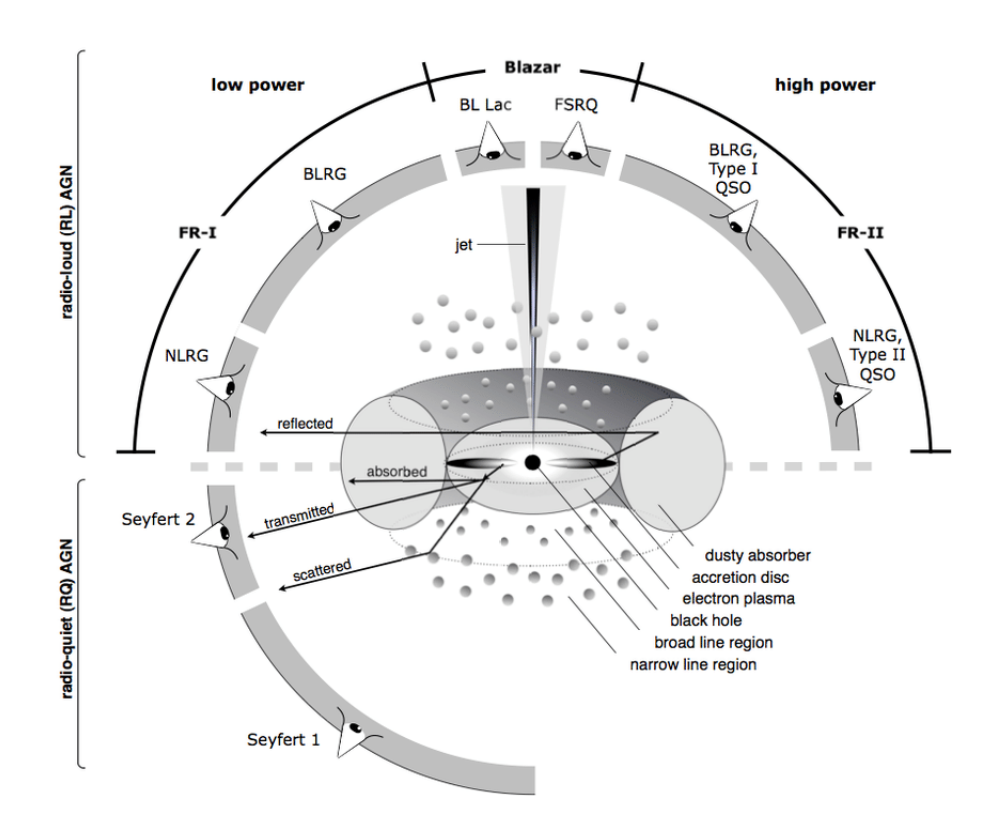


FIGURE 1.5: An unscaled representation of the AGN phenomenon, with the different sight lines that give rise the tre various AGN populations high-lighted. Credit: Beckmann & Shrader (2012), Fig.1.

More recent work builds on the Antonucci (1993) model by invoking evolutionary effects to unify all AGN. For instance, Giustini & Proga (2019) have developed a framework that incorporates an Eddington Ratio dependence, whereby the geometry and opacity of the accretion disk varies with accretion rate and hence, the properties of AGN can vary over time. Throughout this thesis, we will refer to luminous Type 1 broad-line AGN as "quasars". The evolution of the quasar geometry with both their physical and wind properties is therefore a key theme of the thesis, explored in Chapters 3, 4 & 5.

1.6 Black hole and galaxy co-evolution

1.6.1 Cosmic history: Star formation and black hole growth

It was Lilly *et al.* (1996) who identified that the co-moving luminosity density of the Universe increases with redshift from $0.3 < z_{\rm sys} < 1$. The Hubble Deep Field (HDF) pushed observations deeper into the cosmic history of the Universe, enabling Madau *et al.* (1996) to calculate the star formation rate densities (SFRDs) of galaxies up to $z_{\rm sys} \sim 4$ and discover a temporal evolution peaking at $z_{\rm sys} \sim 1-2$. Subsequent work

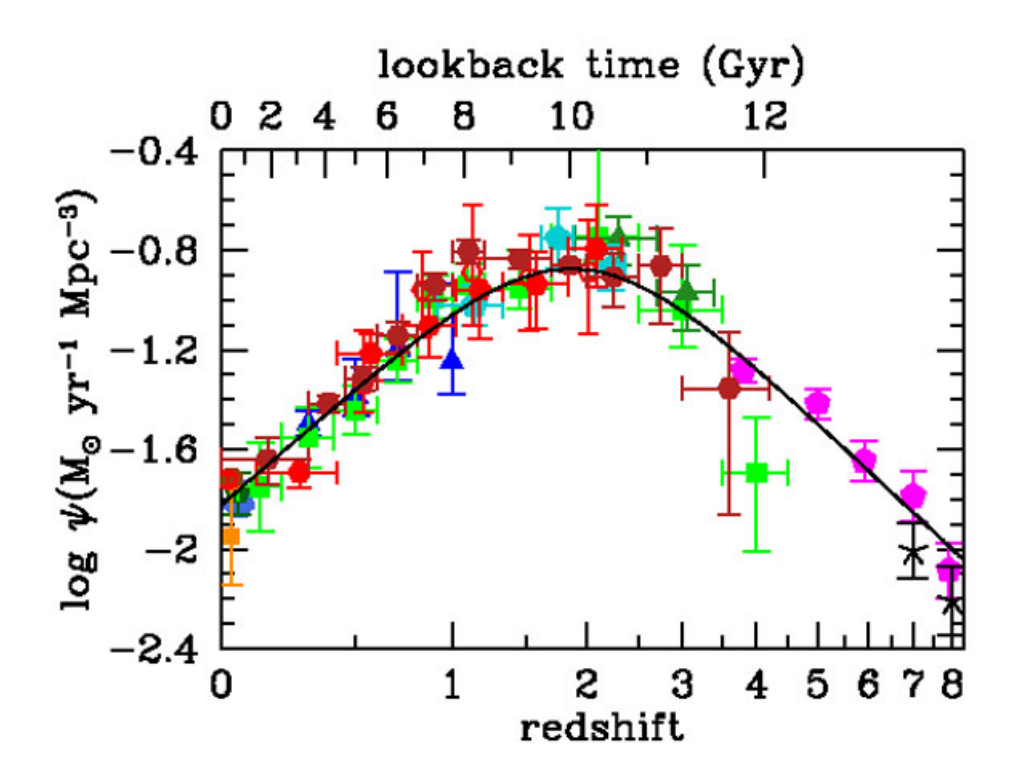


FIGURE 1.6: The cosmic history of star formation from far-UV and infrared measurements up to $z_{sys} \sim 8$. The distribution can be described by a Salpeter function peaking at $z_{sys} \sim 2$ -i.e. *cosmic noon*.

Credit: Madau & Dickinson (2014), Fig.9a.

(e.g. Madau *et al.*, 1998) utilised UV observations to trace the most recent periods of star formation in high-redshift galaxies. These observations confirmed that the SFRD peaks at $z_{sys} \sim 2$ before dropping dramatically at higher and lower redshifts - as illustrated in Fig. 1.6. Throughout this work, we refer to $z_{sys} \sim 2$ as *cosmic noon* - the epoch during which star formation reached its maximum.

Interestingly, the peak epoch of black hole growth also occurs at cosmic noon, with the number densities of the most massive SMBHs (i.e. $M_{BH} \gtrsim 10^9~M_{\odot}$) reaching their maximum at $z_{\rm sys} \sim 2$ before dropping exponentially. The number densities of lower-mass SMBHs appear to peak at later epochs ($z_{\rm sys} \sim 1-2$) even when adjusting for survey incompleteness (Kelly *et al.*, 2010). This delayed growth of lower-mass SMBHs (as well as galaxies) is generally referred to as "cosmic downsizing". Furthermore, the accretion rate density of black holes has been shown to closely trace the cosmic star formation history of the Universe (Shankar *et al.*, 2009). Given that the peak epoch of black hole growth coincides with the peak epoch of star formation, it is widely considered that the two processes are linked (see review article; Heckman & Best, 2014).

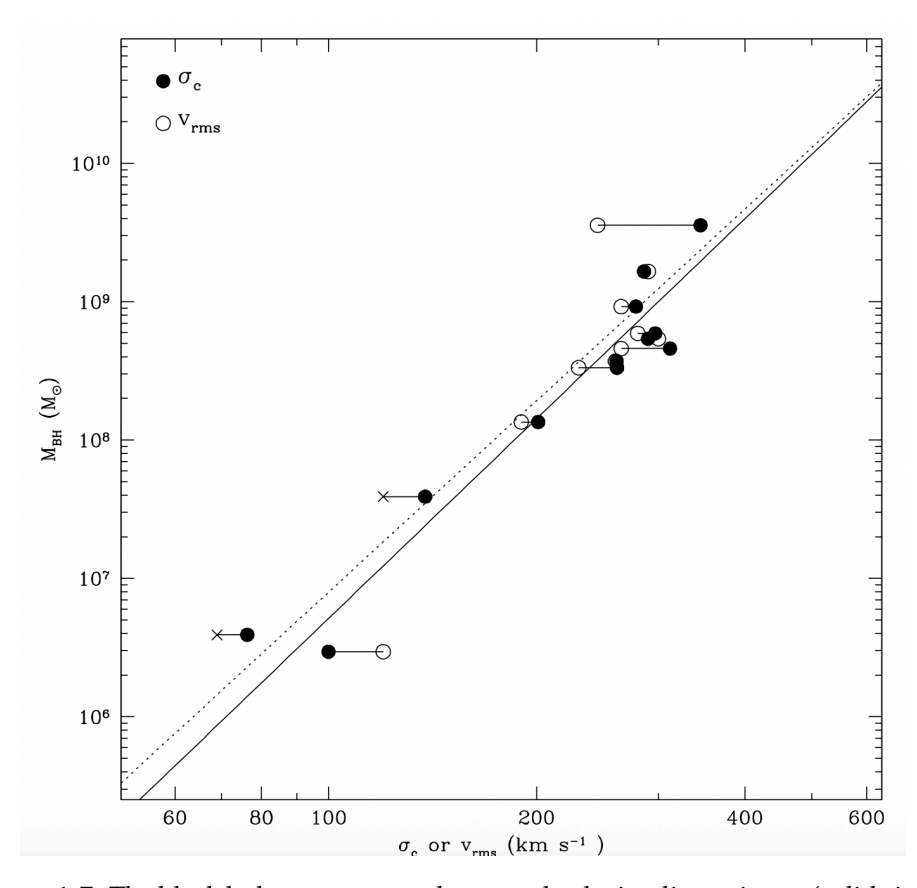


FIGURE 1.7: The black hole mass versus the central velocity dispersion σ_c (solid circles) or the rms velocity v_{rms} (open circles) of the host galaxy. Crosses represent lower limits in v_{rms} . The solid and dashed lines represent the "best-fits" in σ_c and v_{rms} , respectively. Credit: Ferrarese & Merritt (2000), Fig.2.

1.6.2 AGN feedback

The ubiquity of SMBHs was first observed by Magorrian *et al.* (1998) - identifying that almost all massive galaxies host a SMBH at their centre. In addition, the masses of these SMBHs are tightly correlated with the mass of their host galaxy bulge. Subsequent work has shown that SMBH masses also correlate with the stellar velocity dispersion of host galaxy bulges - well beyond the region in which the gravitational potential of the SMBH dominates (Ferrarese & Merritt, 2000; Gebhardt *et al.*, 2001; Kormendy & Ho, 2013). This empirical correlation, known as the $M-\sigma$ relation, is illustrated in Fig. 1.7.

The $M-\sigma$ relation supports the idea of symbiotic growth between SMBHs and their host galaxies. Co-evolution frameworks (e.g. Fabian, 2012; Alexander & Hickox, 2012; Harrison, 2017) often invoke AGN feedback to explain observations. In these frameworks, the energy of the AGN is injected into the ISM of the surrounding host, regulating the AGN fuelling process as well as star formation in the bulge. Cosmological simulations have also demonstrated that feedback processes are pivotal to explaining a multitude of other observables - e.g. the shape of the galaxy

luminosity and stellar mass functions (Cole *et al.*, 2001; Benson *et al.*, 2003; Huang *et al.*, 2003; Somerville *et al.*, 2008; Schaye *et al.*, 2015) as well as the observed morphologies and colours of present-day galaxies (Dubois *et al.*, 2016; Pillepich *et al.*, 2017). As a result, uncovering the nature of AGN feedback has become a central focus in present-day astrophysics.

AGN feedback is generally classified into two distinct "modes" - (i) radiative-mode feedback and (ii) kinetic-mode feedback. In current models of AGN feedback, this dichotomy is broadly attributed to the accretion rate - the radiative mode corresponds to high accretion rates and radiative efficiency, while the kinetic mode is associated with the converse (e.g. Giustini & Proga, 2019). However, this is likely a simplification, as multiple signatures of AGN feedback have been observed in both "modes".

Radiative mode feedback is characterised by powerful outflows and the photoionisation/excitation of the surrounding gas. These outflows are launched from the innermost regions of the AGN and transport energy and material away from the central engine (Silk & Rees, 1998; Fabian, 1999; King, 2003; Murray et al., 2005; Ishibashi & Fabian, 2022). Hence, AGN-driven outflows are detected across multiple gas phases and therefore extend well beyond the region in which the gravitational potential of the SMBH is dominant (Crenshaw et al., 2003; Rupke & Veilleux, 2011; Herrera-Camus et al., 2019; Fluetsch et al., 2021). However, while generally associated with radiatively efficient systems, outflows may also result from thermally driven winds - launched from radiatively inefficient systems due to effects of X-ray heating (e.g. Begelman et al., 1983). Kinetic mode feedback refers to the transfer of thermal energy from the AGN into the ISM of the host (Binney & Tabor, 1995; Churazov et al., 2000; Fabian et al., 2003), quenching star formation by inhibiting the condensation of the surrounding gas and dust. This mode of feedback is often associated with the presence of powerful radio jets (Fabian, 2012; Morganti et al., 2013; Heckman & Best, 2014), however, radio emission has also been observed in radiatively efficient systems (e.g. Fawcett et al., 2023, 2025).

The mechanism by which AGN feedback couples to the host galaxy's ISM is not fully understood. Recent literature proposes that we should consider the AGN phenomenon as an *event* rather than persistent astronomical objects (e.g. Schawinski *et al.*, 2015). Given that the "duty cycle" of an accretion event may be far shorter than that of star formation (Hickox *et al.*, 2014), estimating the impact of a single accretion event on galaxy evolution becomes challenging. Instead, the effects of feedback should be considered as the cumulative impact of multiple phases, each varying in their efficiency at coupling with the host. The coupling of feedback to the surrounding environment has a number of determining factors - such as the luminosity of the AGN, the orientation of the outflows and jets, the black hole spin and the "duty cycle" (Blandford & Znajek, 1977; Cicone *et al.*, 2014; García-Burillo *et al.*, 2021; Temple *et al.*, 2023). Given the complexity of the problem, a multi-wavelength approach is required

to gain the most holistic view of AGN feedback. This is the primary theme of the thesis, discussed comprehensively in Chapters 3, 4 & 5.

1.6.3 Merger-driven co-evolution & red quasars

It is likely that most massive galaxies have undergone at least one major merger to account for the mass distribution of massive galaxies in the local Universe (Conselice *et al.*, 2003; López-Sanjuan *et al.*, 2012). Such events are expected to be most frequent during cosmic noon (Bluck *et al.*, 2009; Man *et al.*, 2012) - a period marked by rapid black-hole growth and star formation, when galaxies were most gas-rich and their spatial densities were at their peak.

Many major merger simulations predict an *obscured quasar phase* (e.g. Di Matteo *et al.*, 2005; Hopkins *et al.*, 2008). In this paradigm, rapid gas inflow to the nucleus fuels a powerful quasar while simultaneously inducing a starburst. These starburst galaxies are shrouded in dust, appearing as either ultra-luminous infrared galaxies (ULIRGs) or sub-mm galaxies (SMGs) (Veilleux *et al.*, 2009; Simpson *et al.*, 2014). However, the same gas supply that fuels the star formation is also responsible for fuelling accretion onto the initially dust-obscured SMBH (Granato *et al.*, 2004; Di Matteo *et al.*, 2005; Hopkins & Elvis, 2009).

The presence of dust has the potential to make radiatively driven outflows more efficient (e.g. Costa *et al.*, 2018; Ishibashi *et al.*, 2017; Ishibashi & Fabian, 2022) while simultaneously reddening the quasar - as discussed in Section 1.2.5. Hence, powerful feedback processes in *red quasar*⁴ populations are expected to couple energy and momenta from the accreting SMBH to the host galaxy ISM, quenching star formation during a "blow-out" phase (Fabian, 2012; Harrison & Ramos Almeida, 2024). Testing this merger-induced "blow-out" framework is the primary focus of Chapters 4 & 5, where we attempt to better understand the role of the obscured quasar phase in the assembly of massive galaxies at $z_{sys} \sim 2-3$.

1.7 Quasars from large surveys

The 21^{st} century has witnessed a data explosion driven by large-area surveys in the optical regime. The Sloan Digital Sky Survey (SDSS; York *et al.*, 2000) was the first such survey, with the DR16Q catalogue containing \sim 750,000 quasars with redshifts; $0 < z_{sys} \lesssim 5.0$ (Lyke *et al.*, 2020). At present, the Dark Energy Spectroscopic Instrument (DESI; Alexander *et al.*, 2023) aims to increase quasar sample sizes to

⁴In this context, we define "red quasars" as any quasar whose continuum has been attenuated - be that by gas or dust extinction. There are, in-fact, numerous definitions of a "red quasar" which are discussed explicitly in Chapters 4 & 5

 \sim 3 \times 10⁶, extending large statistical samples to $z_{sys} \sim$ 6.0 with total sky densities approaching 200 deg⁻² (Yèche *et al.*, 2020). Such large samples have enabled the robust statistical analyses of high-redshift quasars, leveraging both photometric and spectroscopic data sets to investigate their rest-frame UV emission properties (e.g. Richards *et al.*, 2011; Baskin *et al.*, 2015; Rankine *et al.*, 2020; Temple *et al.*, 2023).

In addition to large optical surveys, there have been many campaigns that select AGN in the X-ray, utilising narrow "pencil-beam" surveys such as Chandra Deep Field-North (CDF-N; Vignali *et al.*, 2002) and Chandra Deep Field-South (CDF-S; Luo *et al.*, 2017) as well as wider/shallower campaigns such as the SWIFT AGN Clustering Survey (SACS; Dai *et al.*, 2015) and the eROSITA All-Sky Survey (eRASS1; Merloni *et al.*, 2024). Given that hard X-rays can penetrate even the densest gas columns ($N_H > 10^{22} \, cm^{-2}$), X-ray observations can provide a near complete census of the AGN population and are therefore complementary to UV/optical observations of red quasars (e.g. Lansbury *et al.*, 2020). Furthermore, their high penetration power enables the study of the very high redshift regime, placing high-redshift constraints on the quasar luminosity function which is key to understanding the evolution of galaxies in the early Universe (e.g. Barlow-Hall *et al.*, 2023).

Radio observations have also been used to identify AGN and quasars (e.g. Ching et al., 2017; Magliocchetti et al., 2018; Hardcastle et al., 2025) - indeed, as discussed in Section 1.5, the discovery of such objects is directly linked to the Third Cambridge Catalogue of Radio Sources (3C; Edge et al., 1959). Given that the radio regime traces synchrotron emission, it can be used to observe the true extent and power of vast radio jets (Jennison & Das Gupta, 1953; Fabian, 2012; Harrison et al., 2014), making the radio fundamental to our understanding of the impact of AGN on their host galaxies and environments (e.g. Binney & Tabor, 1995; Fabian et al., 2003). However, recent studies of red quasar populations suggest that many are "radio-intermediate" sources - whose radio emission originates from shocks caused by dusty outflows as they interact with the interstellar medium of the quasar host (e.g. Fawcett et al., 2020, 2025).

The latest and upcoming generation of astronomical surveys will utilise a multitude of selection techniques to push towards more diverse quasar populations. For instance, multi-wavelength selection techniques using both mid-infrared, near-infrared and optical observations have been used to target redder AGN than those observed by optically-selected surveys (e.g. Eisenhardt *et al.*, 2012; Glikman *et al.*, 2012; Banerji *et al.*, 2012, 2013, 2015; Assef *et al.*, 2015). In addition, the Vera Rubin Observatory's Legacy Survey of Space and Time (LSST; Ivezić *et al.*, 2019) will enable variability-based selections of AGN, pushing to the fainter end of the quasar luminosity function (Bauer *et al.*, 2023). This huge volume of data is set to revolutionise our understanding of AGN and galaxy evolution over the coming years.

1.7.1 Magnitudes and flux

The use of "magnitudes" to describe the apparent brightness of astronomical objects has ancient origins, however, the first formalised description is generally credited to Pogson (1856). In this formalism, a logarithmic scale is used to define the apparent brightness of a source - with 5 magnitudes corresponding to a factor of 100 difference in brightness - i.e;

$$m_{Pogson} = -5 \log_{100} \left(\frac{F}{F_0}\right)$$

$$= -2.5 \log_{10} \left(\frac{F}{F_0}\right)$$
(1.10)

where F is the integrated flux of a source through a given photometric filter and F_0 is the zero point - i.e. the equivalent integrated flux of a spectrum defined to have zero magnitude. In the AB system, the zero point is defined by a flat reference spectrum, hence, Eqn. 1.10 becomes;

$$m_{AB} = -2.5 log_{10} \left(\frac{\int \frac{\lambda}{hc} F_{\lambda} S_{i,\lambda} d\lambda}{\int \frac{\lambda}{hc} F_{AB,\lambda}^{0} S_{i,\lambda} d\lambda} \right)$$
(1.11)

where $S_{i,\lambda}$ is the filter transmission curve evaluated at a given wavelength, $F_{AB,\lambda}^0 = c\,F_{AB,\nu}^0/\lambda$, c is the velocity of light and $F_{AB,\nu}^0 = 3.631\times 10^{-20}$ erg s⁻¹ cm⁻² Hz⁻¹ (Equations 11 & 12; Girardi *et al.*, 2002). Throughout this thesis, we use AB magnitudes unless otherwise stated.

1.7.2 Spectral energy distributions

The AGN phenomenon produces a broad spectral energy distribution (SED), with different physical components dominating the emission at various wavelengths - an illustration of which is presented in Fig. 1.8. For a "typical" AGN - e.g. $\lambda_{Edd} \sim 0.1$, $M_{BH} \sim 10^{8-9}~M_{\odot}$ - the accretion disk can be considered optically thick and geometrically thin (Shakura & Sunyaev, 1973). As such, the disk is generally modelled by a multi-temperature Blackbody (e.g. Li *et al.*, 2005; Zimmerman *et al.*, 2005; Temple *et al.*, 2021b), peaking in the far-UV and producing a power-law continuum across the rest-UV/optical wavelengths (Cheney & Rowan-Robinson, 1981; Vanden Berk *et al.*, 2001; Davis *et al.*, 2007) - i.e. Fig. 1.8, blue. While the exact geometry and composition of the dusty torus remain uncertain, as discussed in Section 1.5.1, it is understood that the ionizing quasar continuum is absorbed by surrounding dust and re-emitted in the infrared (e.g. Antonucci, 1993). The sublimation temperature of the dust depends on

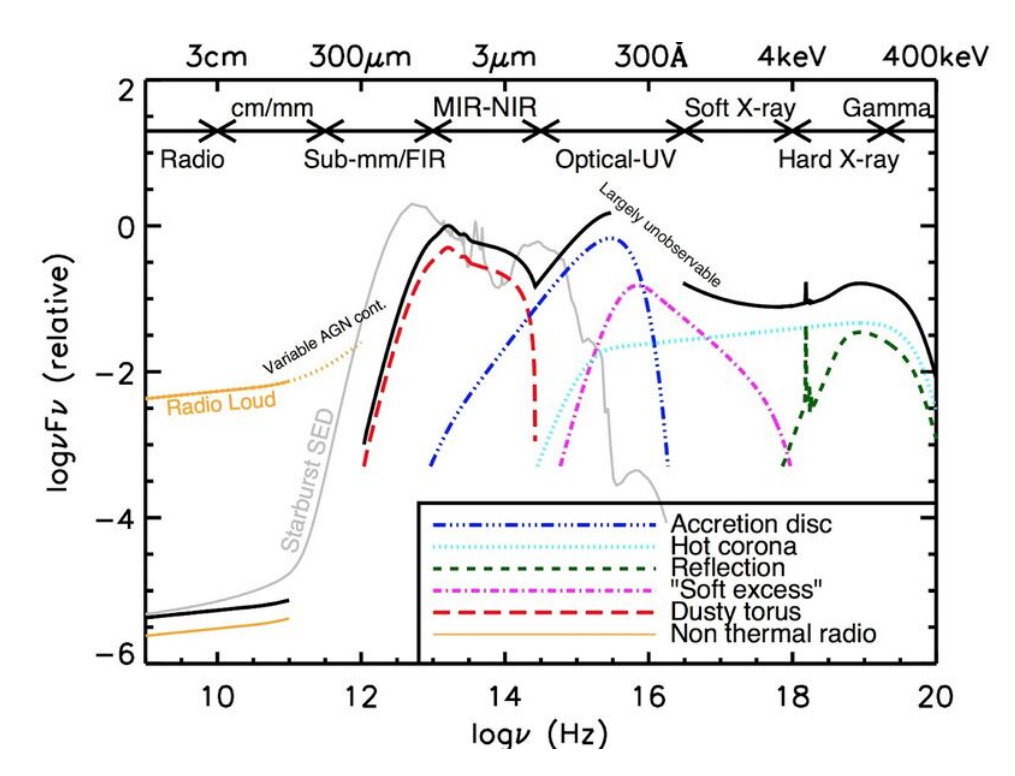


FIGURE 1.8: A schematic representing the various constituents of a "typical" AGN SED. We note that changes to the accretion rate, SMBH mass and/or dust properties can significantly alter the observed SED of an AGN. Credit: Harrison (2014), Fig.1.2.

the grain composition, with the innermost edge of the torus emitting at $\sim 2\mu m$ (Barvainis, 1987) and a greybody spectrum often used to describe cooler dust components (Fig. 1.8, red).

The hot corona (Fig. 1.8, cyan) dominates the X-ray regime and is comprised of a super-heated ($T \sim 10^9~K$) plasma close to the SMBH. This sea of hot electrons can therefore Compton up-scatter UV/optical photons emitted by the accretion disk to extremely high energies, producing a power-law continuum (Haardt & Maraschi, 1991; Fabian *et al.*, 2015). Finally, typical SED shapes for "radio-loud" and "radio-quiet" AGN are also presented in Fig. 1.8 (yellow) highlighting the presence or absence of radio jets, respectively. However, other sources of radio emission such as shocks caused by dusty outflows in red quasars are beginning to break this dichotomy, with many "radio-intermediate" sources now being discovered with LOFAR (Fawcett *et al.*, 2020, 2025).

Since AGN SEDs encode key information about the accretion physics of SMBHs, their interaction with the surrounding galactic environment, and the geometry and composition of circumnuclear dust, they serve as a powerful diagnostic tool for investigating AGN feedback and its role in massive galaxy assembly. In Chapters 4 & 5, we explore how quasar SEDs can be leveraged to gain a better insight into the red quasar phase and its significance in massive galaxy evolution.

1.7.3 Black hole masses

Given that black holes lack an intrinsic electromagnetic signature, studying the kinematics of material in orbit close to a SMBH remains one of the primary techniques for inferring black-hole masses. Under the assumption that the kinematics of the material is dominated by virial motions about the gravitational potential of the SMBH, we can attribute the widths of spectroscopic features to Doppler broadening and express the black-hole mass via Eqn. 1.12;

$$M = \frac{fv^2R}{G} \tag{1.12}$$

where v is the velocity of the material at a radius R and f represents the *virial factor* - used to empirically translate the chosen line diagnostic to a virial velocity. Therefore, the main challenge is to infer the spatial distribution of the material in orbit of the SMBH - i.e. estimate R - however, even in the local Universe, material near the event horizon of a SMBH is unresolvable by observations - with M87* and SgrA* being notable exceptions (Event Horizon Telescope Collaboration *et al.*, 2019, 2022).

In the Milky Way, high-resolution interferometry has been exploited to model the orbits of nearby stars to determine the mass of its SMBH (e.g. GRAVITY Collaboration *et al.*, 2022) - although, this method is not viable in AGN, where their emission is dominated by an accretion disk. Instead, we must utilise the kinematics of the ionised gas in the broad-line region to estimate the black-hole masses of AGN. The size of the BLR can also be inferred via high-resolution interferometry (e.g. GRAVITY Collaboration *et al.*, 2020, 2022), however, this requires that the BLR is sufficiently bright to yield a strong enough signal-to-noise. As such, this technique is generally limited to local AGN - with the exception of the luminous cosmic noon quasar SDSS J092034.17+065718.0, whose BLR has been velocity mapped with GRAVITY+ (Abuter *et al.*, 2024).

Another method of inferring black-hole masses, is reverberation mapping to determine the black-hole masses of AGN (e.g. Clavel *et al.*, 1991; Peterson, 1993; Kaspi *et al.*, 2000, 2005; Bentz *et al.*, 2008; Shen *et al.*, 2015; Yu *et al.*, 2021) - a technique that uses the time delay between stochastic variations in the AGN continuum and the broad emission-line response to estimate the size of the BLR. Reverberation mapping experiments have shown that the radius of the broad-line region correlates tightly with the optical continuum luminosity of an AGN. The so-called R_{BLR} -L relation is best described by a power-law, with a slope \sim 0.5, and can be used to estimate the masses of SMBHs from a single-epoch spectrum (Kaspi *et al.*, 2000, 2005; Bentz *et al.*, 2009). This is particularly important since multi-epoch observations of AGN are time-expensive, meaning reverberation mapping studies have targetted only modest sample sizes and do not yet extend to cosmic noon (although there are several

campaigns expected to address this in the era of LSST - e.g. TiDES-RM Swann *et al.* (2019)). We can therefore define the mass of a SMBH with Eqn. 1.13;

$$M = M_0 \left(\frac{L}{L_0}\right)^{0.5} \left(\frac{\sigma}{\sigma_0}\right)^2 \tag{1.13}$$

where σ denotes the velocity dispersion of a given emission line and L represents the monochromatic continuum luminosity at a nearby wavelength. The constants M_0 L_0 & σ_0 are calibration parameters specific to the emission line diagnostic employed. By extrapolating the R_{BLR} -L relation to higher luminosities it is also possible to estimate black-hole masses for high-redshift quasars, though such estimates typically carry substantial systematic uncertainties (~ 0.5 dex; Vestergaard & Peterson, 2006). The specific form of Eqn. 1.13 applied in Chapters 3 & 4, along with the corresponding uncertainties, are discussed in detail within their respective chapters.

1.7.4 Outflows

Quasar spectroscopy serves as an essential diagnostic tool for characterising outflow kinematics across multiple gas phases, however, in this thesis we focus on the ionised component of the gas. Should the line-of-sight of an observer intersect the streamline of an outflow, one would expect to observe blueshifted line emission due to the Doppler effect. Since the accretion disk of a Type 1 AGN is orientated in roughly the same plane as the sky and taken to be optically thick, the redshifted emission from any receding component to the outflow is obscured. Consequently, asymmetric line profiles with an excess in flux towards the blue are observed.

One such line is the high-ionisation (64eV) C IV $\lambda\lambda$ 1548, 1550 emission, often employed to trace pc-scale winds in the broad-line region gas, hosting line profiles skewed by up to 5000 km s⁻¹ relative to the systemic redshift (e.g. Richards *et al.*, 2011; Coatman *et al.*, 2016; Rankine *et al.*, 2020; Temple *et al.*, 2024). Additionally, in certain conditions, C IV has been known to host high-velocity broad absorption line (BAL) troughs, tracing material with outflow velocities \gtrsim 10,000 km s⁻¹ with respect to systemic (Rankine *et al.*, 2020).

In low-density ionised gas - e.g. $n_e \sim 10^3$ cm⁻³ - the forbidden [O III] $\lambda\lambda4960$, 5008 emission are commonly used to trace AGN-outflows (Baskin & Laor, 2005). Indeed, the [O III] emission frequently exhibit asymmetric line profiles skewed towards the blue (e.g. Boroson, 2005; Aoki *et al.*, 2005). Unlike the broad, high-velocity C IV emission, the [O III] typically displays much narrower line profiles, with Full-Width at Half-Maxima (FWHM) of order 1000 km s⁻¹ in luminous quasars. Consequently,

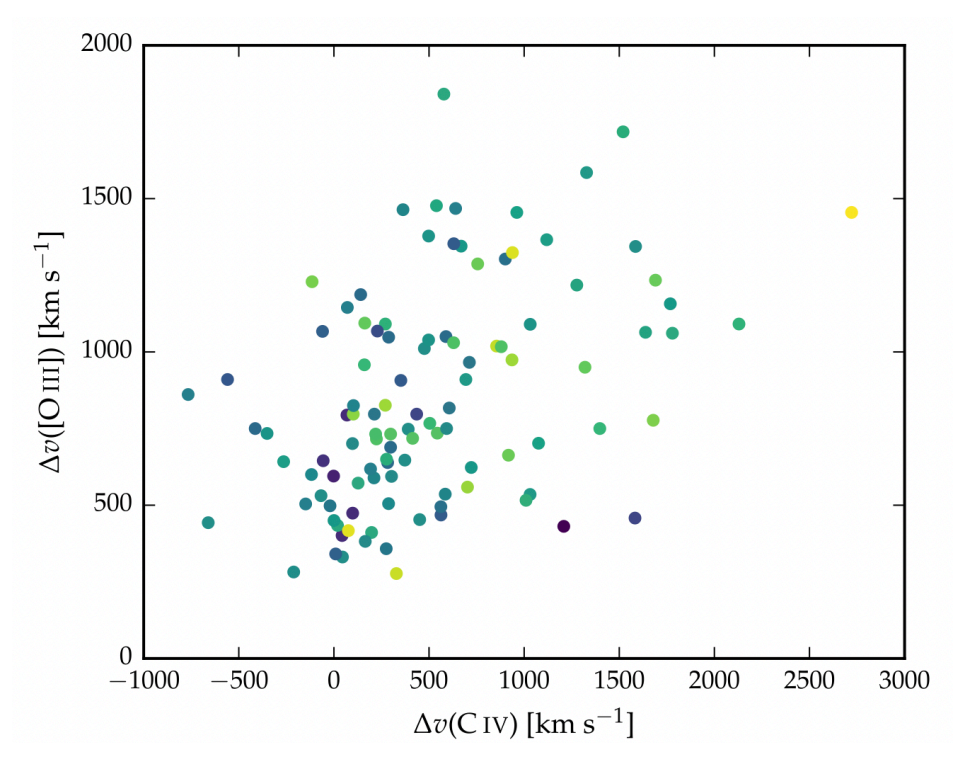


FIGURE 1.9: Relationship between the C IV blueshift ($\Delta V = V_{50} - V_{peak}$) and the [O III] blueshift ($\Delta V = V_{10} - V_{peak}$) for a sample of luminous blue quasars. Credit: Coatman *et al.* (2019), Fig.10.

blueshifted [O III] is generally interpreted as a signature of narrow-line region winds, extending to kiloparsec scales.

Recent work by Coatman *et al.* (2019) identified a correlation between the outflow velocities of multi-scale winds, independent of quasar luminosity and black-hole mass (Fig. 1.9). Should outflows launched on the parsec-scale propagate to the kiloparsec scale, quasar-driven winds are likely to interact with the host galaxy ISM. The implication is that radiative mode feedback is a crucial tool for developing the SMBH scaling relations we observe in present-day galaxies. Hence, in Chapters 3 & 4, we exploit both broad and narrow line diagnostics for the study of ionised gas flows and their role in facilitating AGN feedback.

Chapter 2

Spectroscopic reconstructions of blue SDSS quasars

"hmm... Their [re]construction should be exceedingly simple, I think"

The Nightmare Before Christmas

This Chapter is based on the article:

"No redshift evolution in the rest-frame ultraviolet emission line properties of quasars from $z_{sys} = 1.5$ to $z_{sys} = 4.0$ ", Matthew Stepney, Manda Banerji, Paul C. Hewett, Matthew J. Temple, Amy L. Rankine et al., 2023, MNRAS, Volume 524, Issue 4, July 2023, Pages 5497–551.

All work presented in this Chapter is my own, completed with guidance and support from my co-authors.

2.1 Introduction

The increase in the size of large spectroscopic samples of high-redshift ($z_{sys} > 1.5$) quasars, with rest-frame ultra-violet (UV) spectra has been rapid over the past decade. The Sloan Digital Sky Survey (SDSS) DR7 catalogue (Schneider *et al.*, 2010) enabled the study of $\sim 105,000$ rest-frame UV to optical quasar spectra, from which Shen *et al.* (2011) constructed a comprehensive catalogue of line properties. With subsequent SDSS data releases and the introduction of the BOSS spectrograph, the SDSS DR16Q catalogue now contains over 750,000 quasars (Lyke *et al.*, 2020), marking a near order of magnitude increase from DR7. Looking to ongoing and upcoming quasar surveys, these numbers are continuing to rapidly increase and push to less optically luminous populations, as well as increasing the numbers at high-redshifts - e.g. the Dark Energy Spectroscopic Instrument (DESI; Alexander *et al.* 2022), which has an expected quasar target density of $\gtrsim 5 \times$ that in SDSS DR7.

The emergence of large statistical samples of quasars at cosmic noon has enabled astronomers to robustly characterise their emission properties. For instance, there exists an anti-correlation between the C IV $\lambda\lambda$ 1548, 1550 equivalent width and line blueshift (Hereafter: the "C IV emission space"; Richards *et al.*, 2011, Fig. 2.1). This relationship is seen to persist in both BAL and non-BAL quasars (e.g. Rankine *et al.*, 2020) and has been shown to be linked to their broader SED properties - such as the ionising potential of the SED (e.g. Temple *et al.*, 2024, see Chapter 3 for a complete discussion). Furthermore, as discussed in Chapter 1, blueshifted C IV can also be used to trace the prevalence of outflows in the broad-line region. Many studies of AGN feedback at $z_{sys}=5-7$ suggest that broad-line region outflows are far stronger in early quasar populations than at cosmic noon (e.g. Mortlock *et al.*, 2011; Man *et al.*, 2019; Schindler *et al.*, 2020). Hence, any evolution of the trends observed in the C IV emission space with redshift can help explain the role of AGN feedback in massive galaxy evolution.

Due to their relatively low signal-to-noise ratios, there exists thousands of SDSS quasar spectra at $3.5 < z_{sys} < 4.0$ that remain difficult to robustly incorporate into the C IV emission space - e.g. the median continuum signal-to-noise of the SDSS sample at $z_{sys} \sim 2$ is ~ 6.4 (Rankine *et al.*, 2020), compared to ~ 4.9 at $3.5 < z_{sys} < 4.0$. However, harnessing these spectroscopic data is crucial to enable robust studies of the rest-frame UV line properties of high-redshift quasars and bridge the gap between cosmic noon and the very high-redshift Universe, without the need to rely solely on sample averages (e.g. Meyer *et al.*, 2019). The primary aim of this chapter is therefore to reconstruct these lower signal-to-noise SDSS quasar spectra at high redshift, to enable a robust investigation into the redshift evolution of their rest-UV emission-line properties across large statistical samples.

2.1. Introduction 29

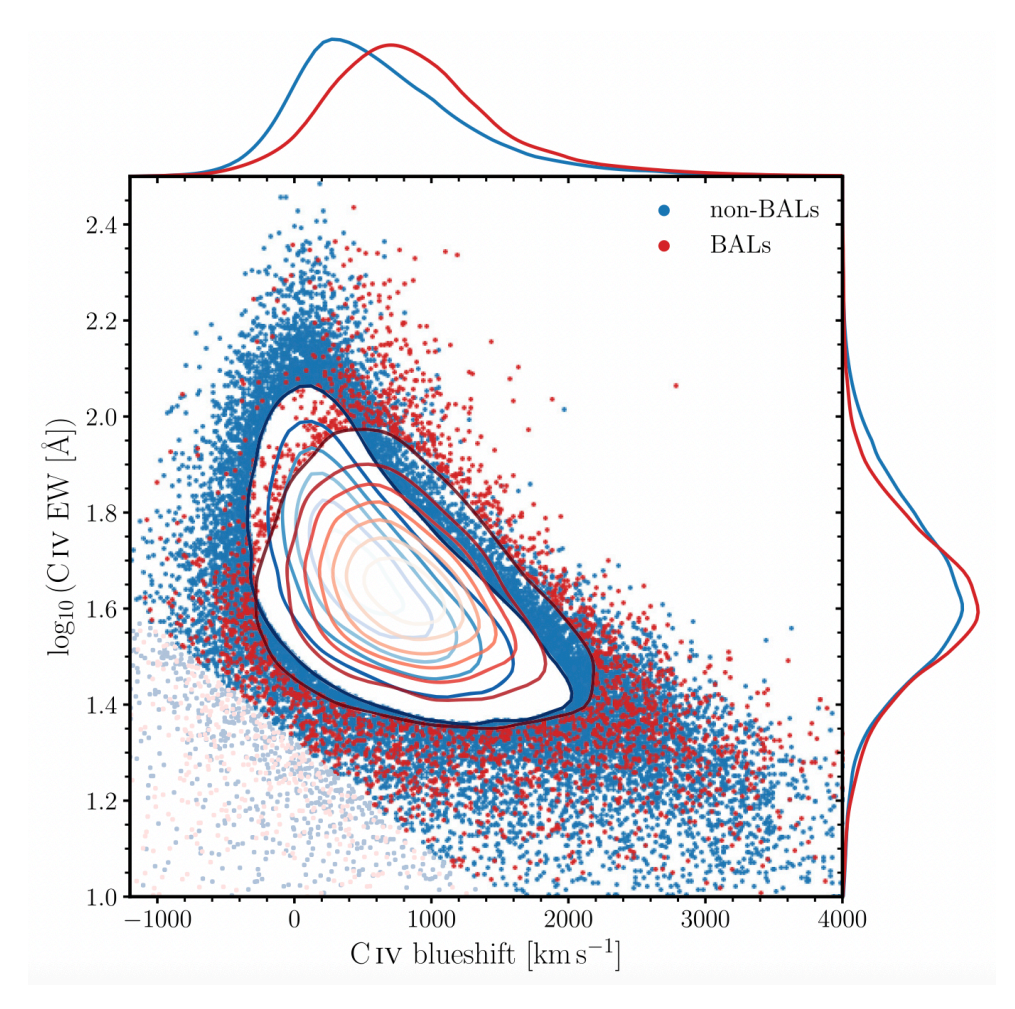


FIGURE 2.1: The C IV emission space for the $1.5 < z_{sys} < 3.5$ SDSS quasars. The blue distribution represents the non-BALs and the red distribution represents the BALs. Marginalised distributions of the C IV blueshift and EW are also shown. Density contours encircle 68, 50 and 25 per cent of the sample, respectively. Both populations exhibit the classic "banana" shape.

Credit: Rankine et al. (2020), Fig.8.

Throughout this work, our lower redshift comparison sample on which we base our results is drawn from Rankine *et al.* (2020), covering the redshift range $1.5 < z_{sys} < 3.5$. Objects whose redshifts cover $1.5 < z_{sys} < 2.65$ have also been analysed by Temple *et al.* (2023), meaning they have robust SED properties available. To minimise bias, it is crucial that the high-redshift quasar sample is treated identically to the cosmic noon reference quasars. To ensure this, we therefore explore the same non-parametric approach to spectral reconstruction already exploited in Rankine *et al.* (2020), called Mean-field Independent Component Analysis (MFICA).

In addition to accurate spectroscopic reconstructions, robust line-property measurements will require the availability of accurate systemic redshifts estimates for the high-redshift quasars. Given the limited spectral coverage above $z_{sys} \sim 3.5$ in SDSS, the SDSS pipeline becomes increasingly dependent on the C IV emission line - which is seldom at systemic - to inform the redshift estimates. Calculating revised

systemic redshifts for the high-redshift quasar sample is another central objective of this chapter. At $z_{sys} < 4.0$, the C III] λ 1908 complex is within the observed wavelength coverage of SDSS, hence, we can improve the systemic redshift estimates from the SDSS pipeline using the rest-UV spectra alone. This is crucial because while rest-frame optical emission lines or, even better, host galaxy ISM lines are the gold standard for systemic redshifts, they require either NIR spectroscopic follow-up or ALMA follow-up, which is not feasible for samples of thousands of quasars.

The structure of this chapter is as follows. In Section 2.2 we present the selection of the $3.5 < z_{sys} < 4.0$ quasar sample from SDSS. The subsequent post-processing is then explored in Section 2.3. Finally, in Section 2.4 we describe the spectral reconstruction recipe used to reproduce essentially "noise-free" SDSS quasar spectra, from which robust line properties can be calculated.

2.2 Sample Selection

Our quasar sample is drawn from the final installment of the Sloan Digital Sky Survey IV (SDSS-IV) quasar catalogue, otherwise referred to as the sixteenth data release of the extended Baryon Oscillation Spectroscopic Survey (eBOSS; Dawson *et al.*, 2016). The catalogue, which we will refer to as DR16Q, is comprised of 750,414 quasars, including the ~526,000 known quasars from SDSS-I/II/III and a further 225,082 quasars new to SDSS catalogues (Lyke *et al.*, 2020). We select a sample of 2775 non-BAL quasars (BAL probability \leq 0.7) in the redshift range $3.5 < z_{sys} < 4.0$ from the DR16Q quasar catalogue, which have a median signal-to-noise \geq 3.0 per pixel in the rest-frame interval 1265-1950Å. Above $z_{sys} > 4$ the numbers of quasars in DR16Q are relatively small precluding a statistical analysis of their UV line demographics. Furthermore at $z_{sys} > 4$ the C III] emission line complex redshifts out of the SDSS observed wavelength range, which means systemic redshift estimates based solely on rest-frame UV spectra, becomes increasingly unreliable (Hewett & Wild, 2010; Wu & Shen, 2022). We therefore restrict our sample to $3.5 < z_{sys} < 4.0$.

We follow a routine similar to that described by Hewett & Wild (2010) and later adopted by Coatman et al. (2016, 2017) and Rankine et al. (2020) to remove narrow absorption features and sky line residuals from the spectra. First, we define a 61-pixel median filtered pseudo-continuum. We then exclude any pixels that fall within 6Å of the strong night-sky emission lines at 5578.5Å and 6301.5Å. Pixels that fall below 2σ of the pseudo-continuum are regarded as narrow line absorption features and hence removed from the spectrum with a grow radius of two pixels. The removed pixels are consequently replaced by their corresponding pixel in the pseudo-continuum spectrum.

2.3 Improving SDSS systemic redshift estimates

The accuracy to which the SDSS pipeline estimates the systemic redshift of quasars has greatly improved since DR7 (Shen *et al.*, 2011). The DR16Q catalogue includes a number of redshift estimates for each quasar (Lyke *et al.*, 2020) e.g. automated classifications from the SDSS spectroscopic pipeline, visual inspection estimates (which reveal that only 2.1% of the automated classifications result in a catastrophic failure) and redshifts based on principal component analysis (PCA) (Lyke *et al.*, 2020). Accurate systemic redshifts are crucial to our study and we therefore calculate updated systemic redshifts for our sample of high-redshift quasars.

A visual inspection of all 2775 3.5 $< z_{sys} <$ 4.0 non-BAL quasar spectra shows that 244 quasars do not show clear broad emission line features and we therefore consider these objects to be misclassified, leaving 2,531 quasars remaining. This number represents a larger fraction of misclassified objects than those found among all SDSS quasar targets (Lyke *et al.*, 2020). We define $z_{\rm SDSS}$ as the 'primary' redshift presented in DR16Q, defined by either visual inspection or automated classifications. For our sample, $z_{\rm SDSS} = z_{\rm VI}$ for 2,527 quasars and $z_{\rm SDSS} = z_{\rm AUTO}$ for the remaining 4 objects. Nevertheless, these redshift estimates do not as yet account for the systematic velocity offsets between different quasar emission lines as a function of the UV emission line morphologies. This becomes increasingly true at high redshifts, where the C IV $\lambda\lambda$ 1548, 1550 emission line begins to dominate the redshift estimates.

To improve the systemic redshift estimates, we adopt a filtering and 'cross-correlation' scheme as described in section 4.2 of Hewett & Wild (2010). There are two key differences compared to Hewett & Wild (2010). First, we employ 33 high signal-to-noise composite spectra. The composite spectra are generated using median stacks of individual SDSS quasar spectra whose systemic redshifts are calculated using the $1600-3000\text{\AA}$ wavelength region, including the C III] emission complex and the Mg II $\lambda\lambda$ 2706, 2804 emission line. The 33 composite spectra span the full range of C IV emission morphologies in equivalent-width and blueshift space, as illustrated in Fig. 2.2. The properties of the composite spectra are summarised in Table 2.1. Second, the cross-correlation between each template and an individual quasar spectrum is performed with the quasar redshift as a free parameter. Finally, we create a bespoke template from the weighted mean of the seven composite spectra with the largest cross-correlation values, using the cross-correlation coefficients as the weights, and perform one last cross-correlation with the individual spectrum, again with the redshift as a free parameter.

Table 2.1: We present estimates of the average signal-to-noise, C IV EW and C IV blueshift for the 33 high signal-to-noise composite spectra used to correct the systemic redshifts of our sample. The signal-to-noise estimates are calculated assuming the individual spectra have a median continuum signal-to-noise ~ 5 . We also provide filenames for the composites, which are available as online only supplementary material, in addition to the total number of spectra used to construct them. 62,464 quasar spectra were used in total.

Filename	No. of Spectra	Signal-to-noise	C IV EW [Å]	C IV blueshift [km s ⁻¹]
mc_00000500_hew500.fits	500	110	113	197
mc_00000500_lew500p1.fits	5460	370	33.5	404
mc_00000500_lew500p2.fits	5461	370	46.3	336
mc_00000500_lew500p3.fits	5461	370	58.8	336
mc_00000500_lew500p4.fits	5459	370	76.8	266
mc_00000500_lew500.fits	500	110	21.7	404
mc_05001000_hew500.fits	500	110	83.6	680
mc_05001000_lew500p1.fits	3942	310	28.1	887
mc_05001000_lew500p2.fits	3942	310	35.0	887
mc_05001000_lew500p3.fits	3942	310	42.7	818
mc_05001000_lew500p4.fits	3942	310	55.9	749
mc_05001000_lew500.fits	500	110	20.7	818
mc_10001500_hew500.fits	500	110	58.1	1162
mc_10001500_lew500p1.fits	2402	250	26.4	1369
mc_10001500_lew500p2.fits	2403	250	31.2	1369
				Continued on next page

Table 2.1 – continued from previous page

Filename	No. of Spectra	Signal-to-noise	C IV EW [Å]	C IV blueshift [km s ⁻¹]
mc_10001500_lew500p3.fits	2403	250	39.3	1300
mc_10001500_lew500.fits	500	110	19.8	1300
mc_15002000_hew500.fits	500	110	39.8	1712
mc_15002000_lew500p1.fits	841	150	23.4	1781
mc_15002000_lew500p2.fits	840	150	26.6	1850
mc_15002000_lew500p3.fits	842	150	30.2	1850
mc_15002000_lew500.fits	500	110	19.9	1781
mc_20002500_010025.fits	799	140	20.6	2330
mc_20002500_025050.fits	674	130	28.4	2330
mc_25003000_all.fits	744	140	20.3	2809
mc_30006000_all.fits	577	120	18.1	3219
mc_m05000000_hew500.fits	500	110	111	-148
mc_m05000000_lew500p1.fits	1647	200	39.9	-78.8
mc_m05000000_lew500p2.fits	1647	200	53.7	-78.8
mc_m05000000_lew500p3.fits	1647	200	67.4	-78.8
mc_m05000000_lew500p4.fits	1647	200	80.4	-148
mc_m05000000_lew500.fits	500	110	27.1	-148
mc_m10000500_all.fits	742	140	54.9	-562

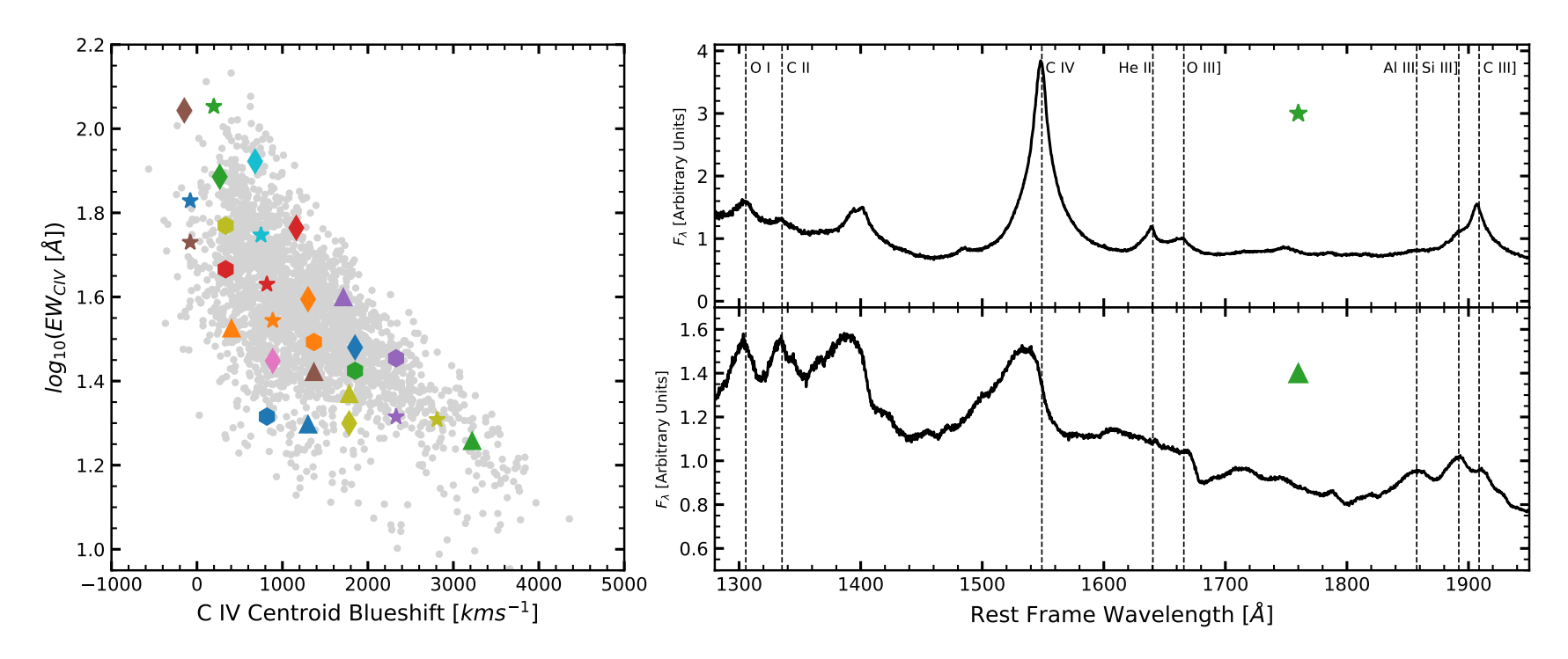


FIGURE 2.2: The left-hand panel shows the C IV blueshift versus equivalent width for the $3.5 < z_{sys} < 4.0$ quasar sample with the locations of the 33 high signal-to-noise templates used in the cross-correlation algorithm to calculate systemic redshifts. The spectra for templates at the extremes of the C IV emission space are also presented on the right. The high C IV EW and low C IV blueshift template (top right) features a strong symmetric C IV line profile. Conversely, the low C IV EW and high C IV blueshift template (bottom right) features both a weak and asymmetric C IV line profile and stronger Si III] relative to C III]. Accounting for these systematic changes in the SEDs as a function of the C IV line properties is critical to producing accurate systemic redshifts.

Figure 2.2 (right) depicts two templates from the top-left and bottom-right of the C IV emission space shown in Fig. 2.2 (left). The main difference in our approach to the estimation of systemic redshifts employing the C IV emission line is the use of templates that span the full range of emission line morphologies. The SDSS scheme employing their principal component analysis five-components, for example, does not have the capability to reproduce the full range of quasar UV SEDs, particularly at the extremes of the CIV emission-line space. We present composite spectra for objects with systemic redshift corrections -800 km s⁻¹ < δv < -600 km s⁻¹ or 600 km s⁻¹ | δv < 800 km s⁻¹ in Fig. 2.3.

Figure 2.3 illustrates that the systemic redshifts have dramatically improved with respect to the initial SDSS estimates. The centroids of the semi-forbidden Si III] λ 1892 and C III] emission are more consistent with the rest-frame wavelengths, after a correction to the systemic redshift was applied (Fig. 2.3 blue). This is in contrast with the C IV emission since semi-forbidden lines are produced at larger radii and should therefore not be present in outflows. We also note a similar effect in the higher energy O I] λ 1306, C II] λ 1335 and Si IV] λ 1398 emission lines as well as the He II λ 1640 and O III] λ 1665 complex.

We compare the systemic redshifts presented in DR16Q with the corrected redshifts, from this work, in Fig. 2.4. We find that 781 objects require systemic redshift corrections in excess of 500 km s⁻¹, 244 of which are in excess of 1000 km s⁻¹, corresponding to \sim 31 per cent and \sim 10 per cent of the sample, respectively. We find tentative evidence that suggests a bias towards lower systemic redshifts within the SDSS pipeline, most likely a result of the tendency of the C IV emission to exhibit blueshifts with respect to systemic. However, we find no evidence to suggest a bias in δv with systemic redshift.

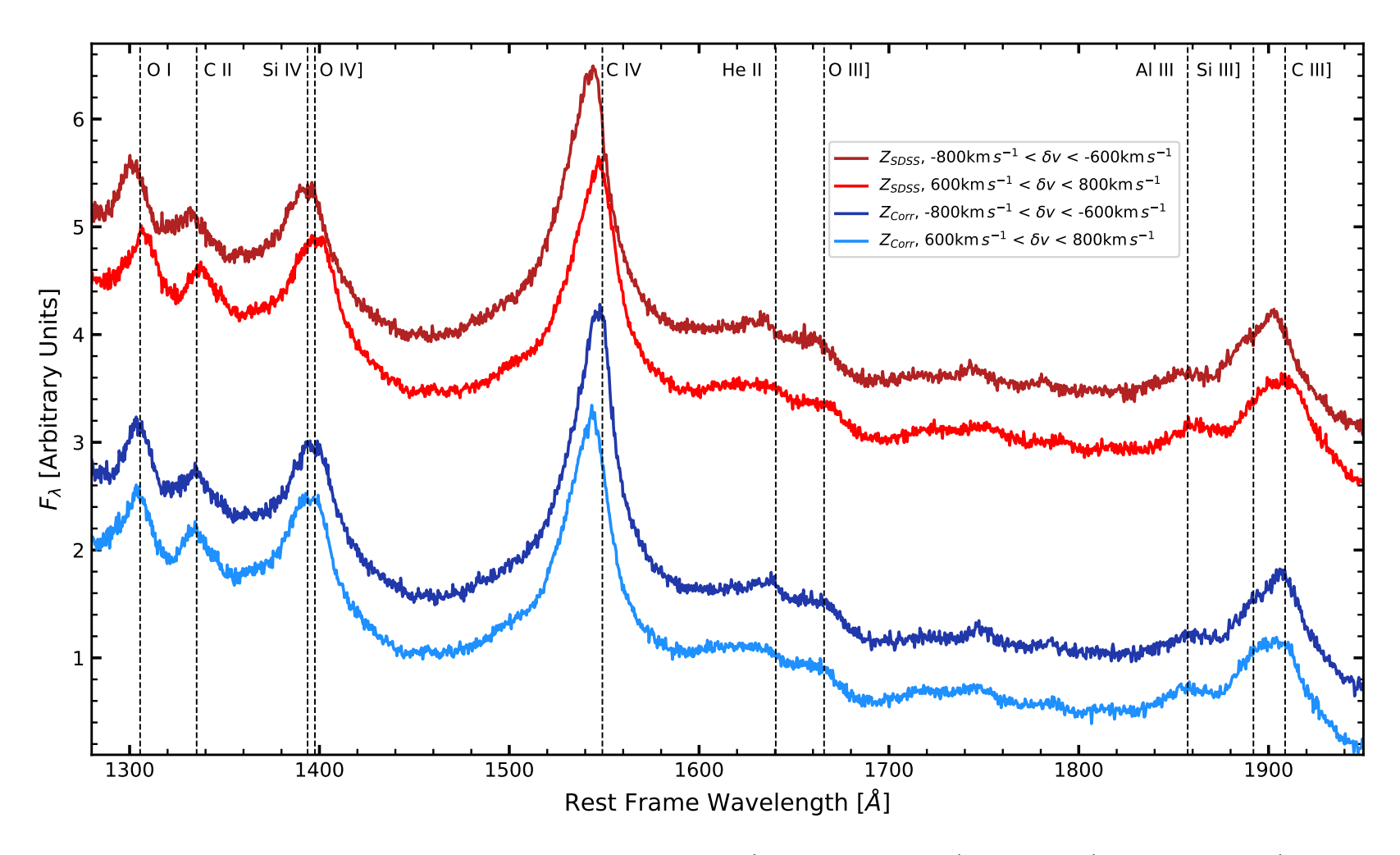


FIGURE 2.3: Composites of quasar spectra with redshift corrections -800 km s $^{-1}$ < δv < -600 km s $^{-1}$ or 600 km s $^{-1}$ < δv < 800 km s $^{-1}$. We present composites before a redshift correction is applied (red) and afterwards (blue). The corrected composites (blue) align with the lower ionisation lines, such as O I, C II, Si IV] and O IV far more convincingly than when the original SDSS systemic redshifts are used.

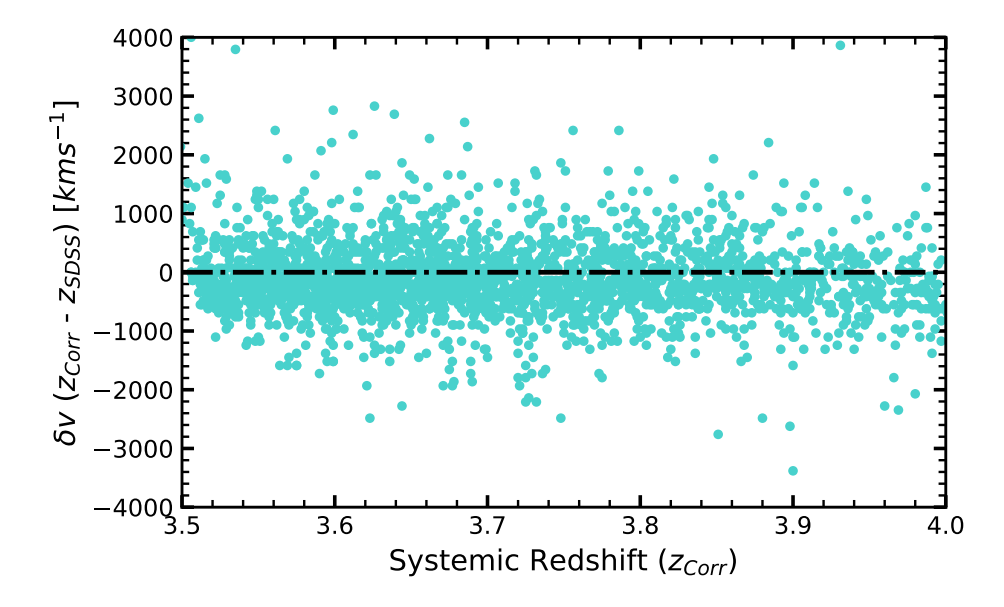


FIGURE 2.4: The difference between the systemic redshifts presented in DR16Q and their corresponding corrected redshifts, as a function of their corrected redshift. Quasar spectra with $\delta v > 0~{\rm km\,s}^{-1}$ have been blueshifted with respect to the initial SDSS systemic redshift estimates. We estimate $\langle \delta v \rangle \simeq -210 \pm 180~{\rm km\,s}^{-1}$.

2.3.1 Systemic redshift dependence on rest-frame wavelength range

A key aim of this work is to ensure that quasar samples across the entire redshift range, $1.5 < z_{sys} < 4.0$, have been analysed with the same methodologies for line-fitting and inference of quasar physical properties. However, at high-redshifts of $3.5 < z_{sys} < 4.0$, the SDSS spectrum covers a more limited rest-frame wavelength range compared to quasars at $1.5 < z_{sys} < 2.65$. In this chapter we truncated the $3.5 < z_{sys} < 4.0$ spectra at 2000Å before estimating systemic redshifts and reconstructing the line profiles, due to the poor signal-to-noise quality towards the red-most end of the SDSS observed wavelength range.

To assess the impact of the restricted wavelength range on systemic redshift estimates, we first construct a luminosity-matched control sample drawn from Rankine *et al.* (2020) for which SED properties have already been calculated by Temple *et al.* (2021a) for a full discussion on how SED properties are calculated see Section 3.2.2, Chapter 3. We use a minimisation recipe which matches our $3.5 < z_{sys} < 4.0$ quasars to their "nearest neighbour" in the $1.5 < z_{sys} < 2.65$ control sample. We then construct a random sample of $1000 \ 1.5 < z_{sys} < 2.65$ luminosity-matched quasars and truncated the spectra at $2000 \ \text{Å}$. Finally, we ran our cross-correlation algorithm on these quasars to calculate systemic redshifts. These are then compared to the redshifts estimated by Rankine *et al.* (2020) over the wider wavelength range in Fig. 2.5.

The redshift difference is systematic as a function of the C IV blueshift below blueshifts of $\sim 1000~\rm km\,s^{-1}$. The algorithm has a tendency to slightly overestimate systemic

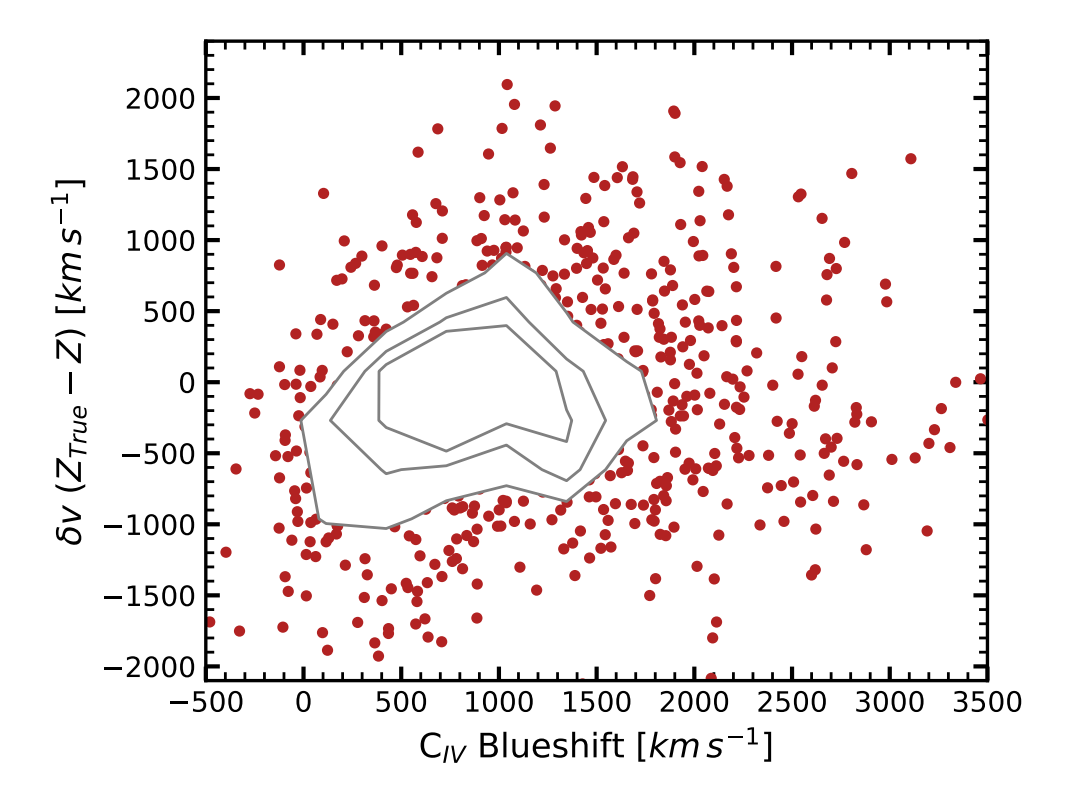


FIGURE 2.5: The velocity difference in systemic redshifts between those estimated by Rankine *et al.* (2020) and calculated using the same recipe and rest-frame wavelength range as this work. This is plotted as a function of the C IV blueshift for a random sample of 1000 1.5 $< z_{sys} <$ 2.65 quasars of comparable luminosity to the 3.5 $< z_{sys} <$ 4.0 quasar population. At low C IV blueshifts, the cross-correlation algorithm has a tendency to overestimate the systemic redshift and therefore biases the C IV line centroids blue-ward of their true position.

redshifts for objects whose C IV blueshift $\leq 500 \, \mathrm{km \, s^{-1}}$. This is due to the presence of narrow associated absorbers that predominantly affect the C IV lines at low blueshift but which are at low enough signal-to-noise to not be detected by our narrow absorption masking procedure. Furthermore, at these wavelengths, we also lose access to the Mg II $\lambda 2800$ emission line for calculation of z_{sys} , which is not usually affected by narrow associated absorption. As a result, symmetric C IV line profiles with the majority of their flux at velocities close to the systemic redshift are most affected by the bias, whereas high C IV blueshift spectra remain relatively unaffected. We fully consider how this bias affects results and conclusions on the potential redshift evolution of the rest-UV line properties in Chapter 3.

2.4 Spectral Reconstructions with Mean Field Independent **Component Analysis**

As discussed in Section 2.1, a key objective of this work is to compare the emission line properties of the $3.5 < z_{sys} < 4.0$ quasars to lower redshift quasars at $1.5 < z_{sys} < 3.5$ using exactly the same methods to analyse and fit the quasar spectra. This avoids biases in the measured line properties due to the different line-fitting procedures employed for quasars at different redshifts.

Our lower redshift comparison sample of quasars used throughout this work is drawn from Rankine et al. (2020) and Temple et al. (2023), covering the redshift range $1.5 < z_{sys} < 3.5$. The rest-frame UV line demographics for quasars with $1.5 < z_{sys} < 2.65$ and where the Mg II emission line is available for robust SMBH mass measurements, has been studied in detail by Temple et al. (2023). Analogous to Rankine et al. (2020) we therefore employ a technique called Mean-Field Independent Component Analysis (MFICA; Højen-Sørensen et al. 2002) to provide essentially noise-free reconstructions of each observed spectrum through a linear combination of 7-10 component spectra (see section 4.2 of Rankine et al. 2020 for more details). The component spectra are the same as those used by Rankine et al. (2020) at $1.5 < z_{sys} < 3.5$. They were generated using a sample of $\sim 4000 \, 1.5 < z_{sys} < 3.5$ spectra at intermediate C IV EWs, 20-40Å, and a further two samples of ~ 2000 $1.5 < z_{sys} < 3.5$ spectra with C IV EW > 40Å and < 20Å.

The scheme for deriving MFICA-components for use on astronomical data is described in Allen et al. (2013). Three sets of components were necessary to account for the extensive array of C IV emission line morphologies seen in the sample. For a visualisation of the three sets of MFICA components see Fig. 2.6, Fig. 2.7 and Fig. 2.8. The objects whose C IV EW < 20Å were fit using the components depicted in Fig. 2.6, the objects whose C IV EW are between 20-70Å were fit using the components depicted in Fig. 2.7, and the remainder of the spectra were reconstructed using the components depicted in Fig. 2.8. The C IV EW thresholds were calculated by minimising the χ^2_{ν} of the reconstructions, however, spectra in the overlapping regions of equivalent width generally have a similar quality fit with either set of MFICA components.

The MFICA components are highly effective for our purpose, however, the exact form of the components is not important. Rather, the key requirement is that the components can be combined to produce accurate reconstructions of the quasar spectra. Alternative approaches using principal component analysis or non-negative matrix factorization should also work well.

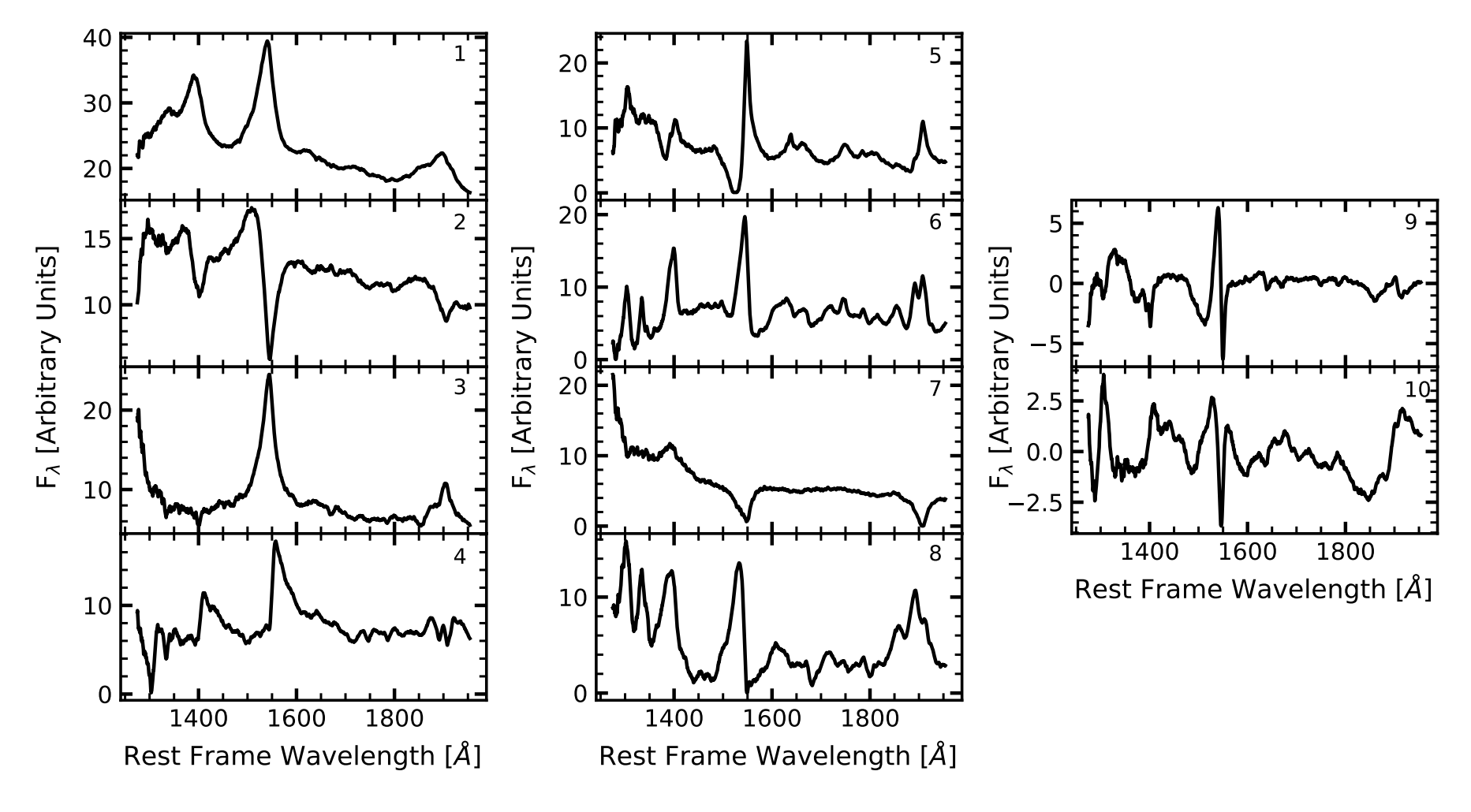


FIGURE 2.6: The MFICA components, generated using the technique described in Allen *et al.* (2013), used to reconstruct quasar spectra whose C IV EW < 20Å. Components "9" and "10" are correction components and are therefore permitted to have negative weights in the MCMC fitting.

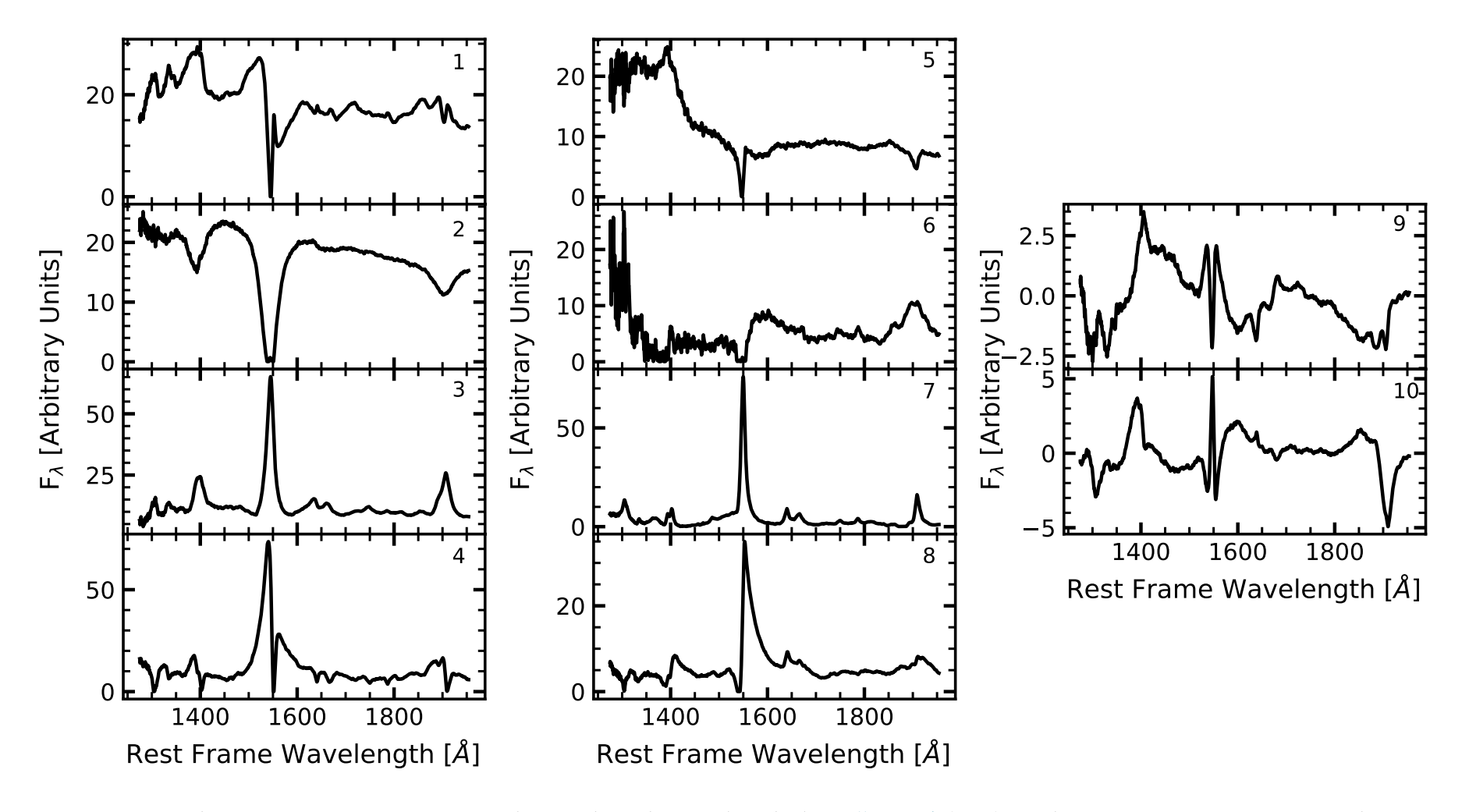


FIGURE 2.7: The MFICA components, generated using the technique described in Allen *et al.* (2013), used to reconstruct quasar spectra whose 20 < C IV EW < 70Å. Components "9" and "10" are correction components and are therefore permitted to have negative weights in the MCMC fitting.

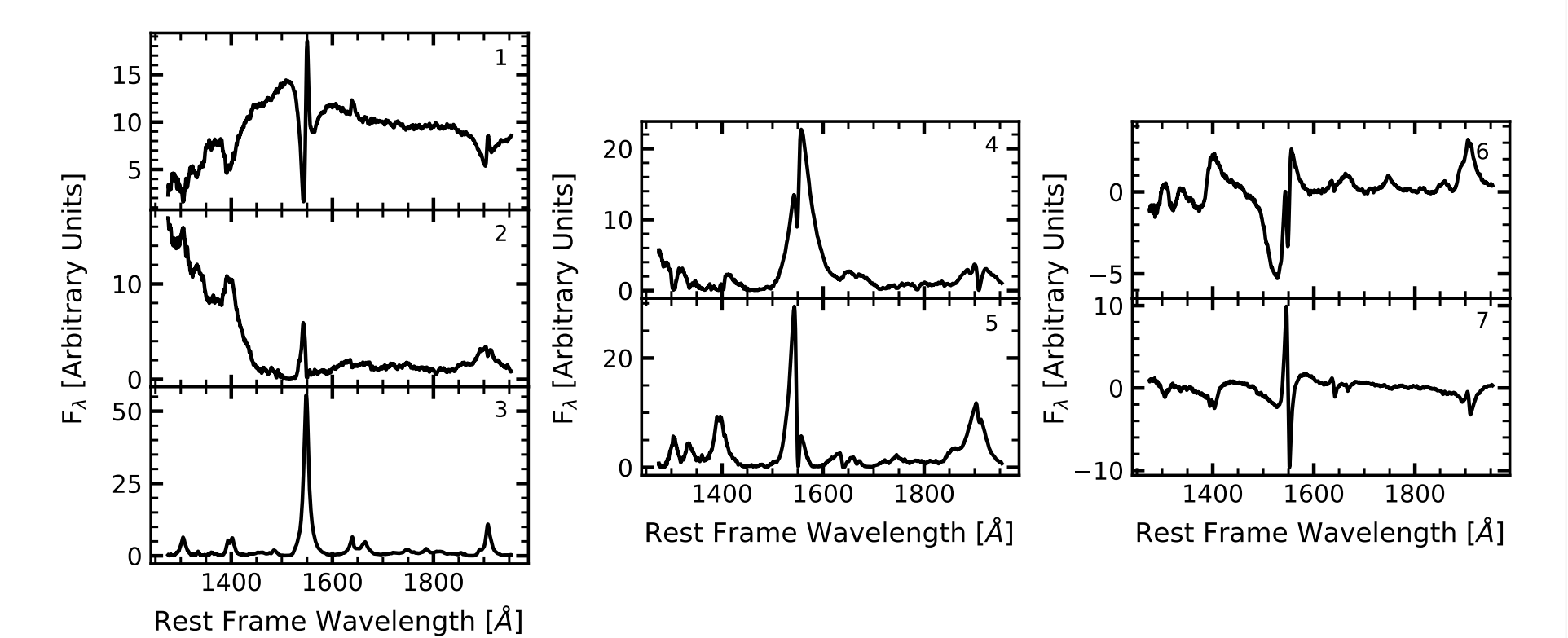


FIGURE 2.8: The MFICA components, generated using the technique described in Allen *et al.* (2013), used to reconstruct quasar spectra whose C IV EW > 70Å. Components "6" and "7" are correction components and are therefore permitted to have negative weights in the MCMC fitting.

Spectrophotometric calibration effects introduce both a blue excess and red decrement to the BOSS spectra (Dawson et al., 2012; Pâris et al., 2012). Consequently, we observe a $\pm 10\%$ multiplicative factor in the spectrophotometry as well as an additional effect introduced by the varying dust extinction towards each quasar. Since we aim to reconstruct the quasar spectra with linear combinations of fixed components, any wavelength dependent multiplicative factor needs to be removed, hence we implement a "morphing" recipe to standardise the shape of the quasar spectra. For a full description of the morphing recipe see section 4.1 of Rankine et al. (2020). The reference quasar SED used to "morph" the quasar spectra is a model quasar spectrum, discussed extensively in Maddox et al. (2012) and Temple et al. (2021b)¹.

We use the EMCEE Python package² (Foreman-Mackey et al., 2013) for the MFICA spectral reconstructions. The EMCEE package is a Python implementation of the affine-invariant ensemble sampler for Markov-Chain Monte Carlo (MCMC) simulations, proposed by Goodman & Weare (2010). We permit the EMCEE package to explore an N-Dimensional, Gaussian likelihood function, where N represents the number of MFICA components (N=7 for the high C IV EW set and N=10 otherwise), and apply uniform priors to the component weights. Typical example spectra, with various signal-to-noise characteristics are presented in Fig. 2.9 together with their MFICA reconstructions, which are representative of the whole sample.

A key result of this work is that the $1.5 < z_{sys} < 3.5$ MFICA components can successfully reconstruct the $3.5 < z_{sys} < 4.0$ spectra with a range of signal-to-noise ratios. The MFICA has the effect of boosting the signal-to-noise characteristics of the SDSS spectra affording us the opportunity to analyse weaker UV emission lines such as He II λ 1640. We have checked that different realisations of the spectra perturbed consistent with the Gaussian noise on each spectrum, result in essentially identical MFICA reconstructions. Although the component weights themselves change, the line properties derived from the reconstructions are unchanged by the noise on each spectrum. A further advantage of MFICA over parametric fitting of emission lines is the ability to accurately reproduce asymmetric emission line features, resulting in more robust reconstructions of the blue wing often observed in the C IV emission crucial for our work in Chapter 3.

¹https://github.com/MJTemple/qsogen

²https://github.com/dfm/emcee

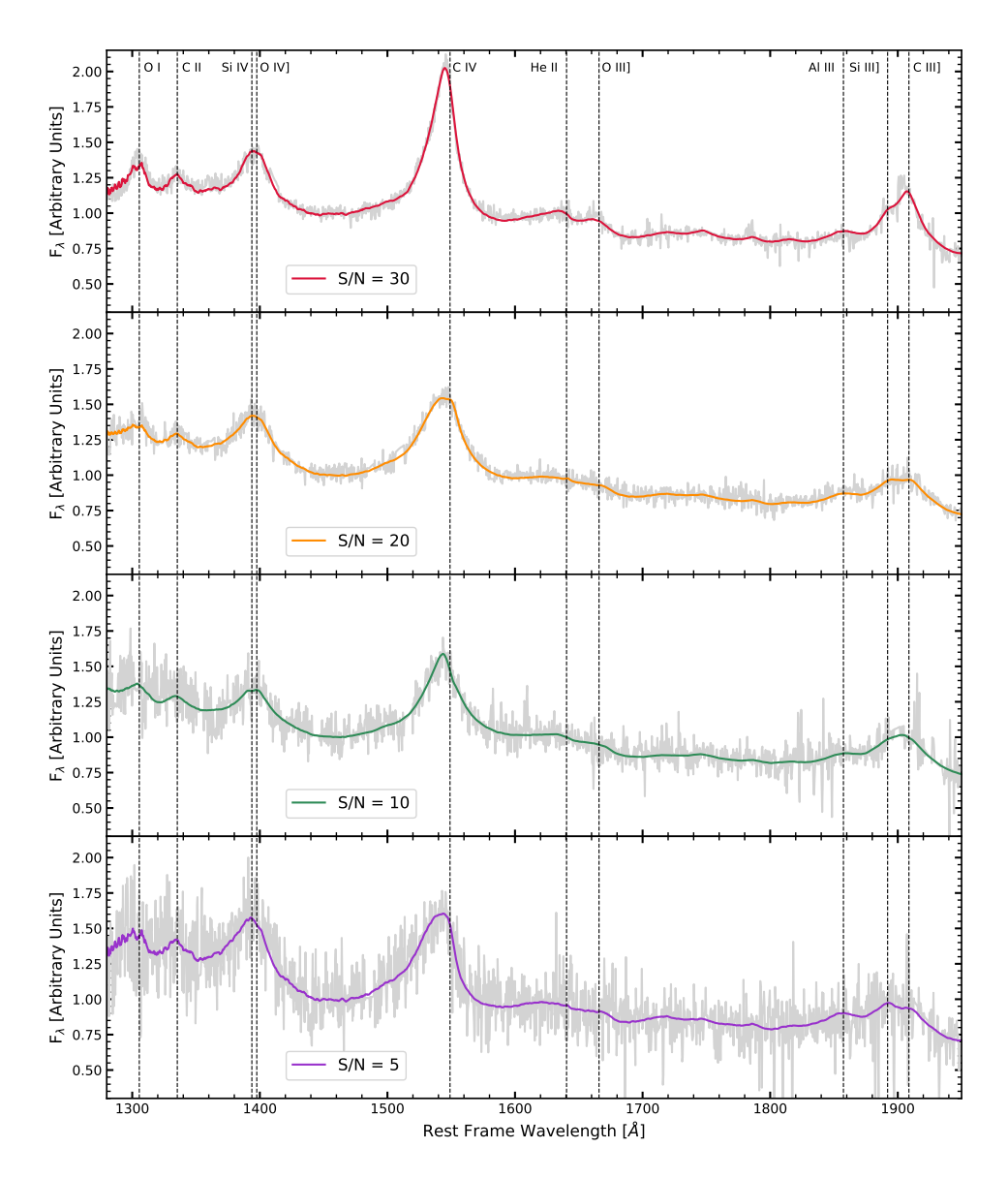


FIGURE 2.9: Example quasar spectra from our sample at $3.5 < z_{sys} < 4.0$ with signal-to-noise of 30 (top), 20 (top-middle), 10 (bottom-middle) and 5 (bottom), with their corresponding mean-field independent component analysis reconstructions overlaid. We can see that the MFICA reconstructions have the effect of boosting the signal-to-noise of the SDSS spectra, and hence robust UV emission line analysis becomes achievable.

2.5. Conclusions 45

2.5 Conclusions

We have reconstructed the rest-frame UV spectra of 2,531 3.5 $< z_{sys} < 4.0$ quasars from the SDSS DR16Q catalogue and corrected their systemic redshifts.

- We used high signal-to-noise template spectra of quasars at $1.5 < z_{sys} < 3.5$ and a cross-correlation algorithm to calculate updated systemic redshifts for the $3.5 < z_{sys} < 4.0$ quasars. The templates take into account the known systematic velocity offsets between different emission lines as a function of quasar properties as well as the diversity of the C IV emission line morphologies. This enables accurate systemic redshift estimates using just the rest-frame UV, a technique that can now be applied to quasars at even higher redshifts.
- We find tentative evidence that suggests a bias towards lower systemic redshifts within the SDSS pipeline, most likely a result of the reduced wavelength coverage at $z_{sys} > 3.5$ and the tendency of the C IV emission to exhibit line blueshifts. However, we find no evidence to suggest there is a bias in the velocity correction between the SDSS pipeline redshifts and the redshifts calculated in this work (i.e. δv Fig. 2.4) as a function of systemic redshift.
- We use Mean Field Independent Component Analysis (MFICA) to produce high signal-to-noise reconstructions of the individual quasar spectra from which we can measure non-parametric emission line properties.

Chapter 3

The redshift evolution of outflows in blue SDSS quasars

"Evolution. It's kind of scary, isn't it?"

Galaxy Quest

This Chapter is based on the article:

All work presented in this Chapter is my own, completed with guidance and support from my co-authors.

[&]quot;No redshift evolution in the rest-frame ultraviolet emission line properties of quasars from $z_{sys} = 1.5$ to $z_{sys} = 4.0$ ", **Matthew Stepney**, Manda Banerji, Paul C. Hewett, Matthew J. Temple, Amy L. Rankine et al., 2023, MNRAS, Volume 524, Issue 4, July 2023, Pages 5497–551.

3.1 Introduction

Thanks to large spectroscopic data-sets - such as the SDSS sample discussed in Chapter 2 - we are now able to conduct statistical studies of rest-frame UV quasar spectra, explore the diversity in their emission line properties and study correlations between the continuum and various emission lines (e.g. Sulentic et al. 2007; Richards et al. 2011; Rankine et al. 2020; Rakshit et al. 2020; Brodzeller & Dawson 2022; Wu & Shen 2022; Rivera et al. 2022). Characterising the emission line properties also enables single-epoch virial black hole mass estimates for large samples, allowing an exploration of how the UV spectral properties connect to fundamental physical properties of the quasars such as bolometric luminosity, black hole mass and Eddington-scaled accretion rate (e.g, Temple et al., 2023). The widely observed blueshifts seen in the C IV $\lambda\lambda$ 1548, 1550 emission lines of high-redshift, high-luminosity quasars are often interpreted as a signature of outflowing gas in the quasar broad line region (BLR; Baskin et al. 2015). Statistical studies of UV quasar spectra then enable these outflows to be linked to other quasar properties. For example, the observed anti-correlation between the C IV blueshift and He II $\lambda 1640$ equivalent width (EW) (Baskin et al., 2013; Rankine et al., 2020) can be interpreted as a link between the spectral energy density (SED) of the quasar and BLR outflow velocity (Temple et al., 2023).

In parallel to these developments in characterising the demographics of quasars at "cosmic noon" (1.5 $\lesssim z_{sys} \lesssim$ 3.5), the number of quasars at the highest redshifts ($z_{sys} \gtrsim$ 5) has also grown considerably in the last decade (e.g, Bañados *et al.*, 2016; Jiang *et al.*, 2016; Wang *et al.*, 2019; Fan *et al.*, 2022). A sizeable subset of these also have single-epoch black hole masses measured from rest-frame optical spectra (e.g. De Rosa *et al.* 2014; Mazzucchelli *et al.* 2017; Schindler *et al.* 2020; Farina *et al.* 2022). These high-redshift quasars are now being targeted as part of ongoing wide-field spectroscopic surveys such as DESI, which has recently confirmed \sim 400 new quasars at $4.7 < z_{sys} < 6.6$ (Yang *et al.*, 2023). These numbers are only expected to increase further with new observations from the 4-metre Multi-Object Spectroscopic Telescope (4MOST; Merloni *et al.* 2019).

The discovery of the first quasar at $z_{sys} > 7$ (Mortlock *et al.*, 2011) showed that its rest-frame UV spectrum was very similar to lower redshift quasars, of similar luminosity, but that the C IV blueshift was significantly larger than the other known $z_{sys} > 2$ quasars. With larger samples becoming available at high-redshifts, there have been suggestions that high-redshift quasars might in general display stronger C IV blueshifts (e.g, Meyer *et al.*, 2019; Schindler *et al.*, 2020), as well as higher broad absorption line fractions and velocities (e.g, Bischetti *et al.*, 2022, 2023). However, these samples are still small enough that these results might be affected by limited sample statistics (e.g, Reed *et al.*, 2019; Yang *et al.*, 2021). While there is an indication that there

3.1. Introduction 49

could be a real evolution in the rest-frame UV line properties driven by fundamental differences in the super massive black hole (SMBH) population at the highest redshifts, neither the line properties nor the physical properties of quasars have been measured consistently across the entire range in redshift (1.5 $\lesssim z_{sys} \lesssim$ 7.0).

In the line-driven disc wind paradigm, ionised gas opaque to the UV continuum photons emitted by the accretion disc, trace the streamlines of outflows (Stevens & Kallman, 1990; Murray & Chiang, 1995; Proga *et al.*, 2000) and hence the C IV blueshift becomes a diagnostic for the outflow velocity. By implication, the observed increase in C IV blueshift in the highest redshift quasars at $z_{sys} \gtrsim 6$ suggests that quasar winds are potentially evolving very rapidly on time-scales of $\sim 200-300$ Myrs (Meyer *et al.*, 2019). Thus far, the statistical studies of the rest-frame UV line properties, of quasars, have mostly focused on lower redshifts where we have samples of several hundred thousand spectra. In particular, below z_{sys} =2.65 the Mg II λ 2800 emission line is present in the SDSS spectrum, which enables the UV line properties to be linked to black hole mass. However, in lieu of the results at the highest redshifts, it is worth extending the studies of the evolution of the rest-frame UV spectra by even a few hundred Myr while also ensuring sufficient sample statistics. We therefore focus on quasars at redshifts $3.5 < z_{sys} < 4.0$ in this chapter.

At $z_{sys} \gtrsim 2.7$ the SDSS wavelength coverage means the Mg II emission line, widely used as a reliable single-epoch virial black hole mass estimator, is redshifted out of the observed spectrum, and hence we must turn to C IV for SMBH masses. A further aim of this work is to determine whether changing the SMBH mass estimator, compared to e.g. the $1.5 < z_{sys} < 2.65$ samples, has an impact on the observed trends in UV line properties with SMBH mass and Eddington-scaled accretion rate (e.g, Temple *et al.*, 2023). By measuring robust blueshifts from only the rest-frame UV spectra, and doing so at modest signal-to-noise, as well as demonstrating that the trends in these line properties are not sensitive to the SMBH mass estimator, we potentially open the door to studies of the evolution in UV line properties for much larger statistical samples out to high-redshifts e.g. those being assembled with DESI and 4MOST.

Having already discussed the selection of the $3.5 < z_{sys} < 4.0$ sample and its subsequent post-processing in Chapter 2, the structure of this chapter is as follows. In Section 3.2 we describe the recipe used to determine the emission line properties and physical properties of the quasar sample. Our key results are compared to the Rankine *et al.* (2020); Temple *et al.* (2023) $1.5 < z_{sys} < 3.5$ samples in Section 3.3, before discussing their implications in the context of the redshift evolution of quasar-driven outflows in Section 3.4.

3.2 Methods

Having already applied the techniques explored in Chapter 2 to process the spectral data from the SDSS DR16Q catalogue, in this section we discuss how both the line properties and physical properties of the quasar sample are calculated.

3.2.1 Line properties

A central aim of this work is to assess whether there is any redshift evolution in the rest-frame UV emission line properties from $1.5 < z_{sys} < 4.0$. To determine the C IV EW and blueshift, we first define a power-law continuum, $f(\lambda) \propto \lambda^{-\alpha}$. We then follow the non-parametric approach discussed by Coatman *et al.* (2016, 2017), whereby the median values of F_{λ} in the two wavelength regions 1445–1465Å and 1700–1705Å are used to determine the power-law approximation. Then, C IV EW measurements are made via numerical integration. Due to the well known asymmetry of the C IV emission line (Richards *et al.*, 2011), we define the blueshifts as the difference between the line centroid and rest-frame wavelength:

$$V_{50} = c(\lambda_r - \lambda_{50})/\lambda_r \ [\text{km s}^{-1}]$$
 (3.1)

where c is the velocity of light, λ_{50} is the rest-frame wavelength that bisects the 50th percentile line flux and λ_r is the rest-frame wavelength of a given emission feature - e.g. 1549.48Å for the C IV doublet. We note that several papers in the literature exploring the UV emission line properties of high-redshift quasars (e.g. Meyer *et al.* 2019; Schindler *et al.* 2020) use the observed wavelength corresponding to the peak of the line to define the C IV blueshift. This is often necessary at low signal-to-noise but does not fully capture the often significant flux in the blue wing of the C IV emission line.

3.2.2 Luminosities and black hole masses

We infer rest-frame monochromatic continuum luminosities λL_{λ} at $\lambda = 3000 \text{Å}$ and 1350 Å (hereafter L_{3000} and L_{1350} , respectively) using the PSF magnitudes from SDSS photometry reported in the Lyke *et al.* (2020) DR16Q catalogue. The SDSS photometry is corrected for Galactic dust extinction using the reddening law presented by Schlafly & Finkbeiner (2011) and the quasar-specific pass-band attenuations described in section 3.1.4 of Temple *et al.* (2021b). For each object, we then fit a quasar SED model (Temple *et al.*, 2021b) to the extinction-corrected photometry using the improved spectroscopic redshifts described in Section 2.3, with the quasar luminosity and

3.2. Methods 51

continuum reddening E(B-V) as the only free parameters. The E(B-V) accounts for the (slight) variations observed in ultraviolet continuum slope and allows a robust estimation of the rest-frame L_{3000} , which in turn allows us to estimate bolometric luminosities in the same way for our $z_{sys} > 3.5$ and $z_{sys} \approx 2$ samples. We exclude pass-bands with rest-frame wavelengths $\lambda < 1215$ Å, which results in the use of data from the riz pass-bands for our $z_{sys} > 3.5$ sample, and the griz pass-bands for our $1.5 < z_{sys} < 2.65$ comparison sample from Rankine $et\ al.\ (2020)$.

As the Mg II λ 2800 emission line is absent from SDSS spectra at redshifts $z_{sys} \gtrsim 2.7$, we estimate SMBH masses for our $3.5 < z_{sys} < 4.0$ sample using the FWHM of the C IV emission. Due to the asymmetric wing, blue-ward of the C IV peak emission, we apply a correction to the (FWHM)_{C IV} derived from the correlation between the FWHM of the C IV and H β emission lines - see Equation 5 and section 4.3 of Coatman *et al.* (2017) for further details.

$$(FWHM)_{C \text{ IV,Corr.}} = \frac{(FWHM)_{C \text{ IV}}}{(0.36 \pm 0.03) \left(\frac{C \text{ IV blueshift}}{10^3 \text{km s}^{-1}}\right) + (0.61 \pm 0.04)}$$
(3.2)

The functional form of Eqn. 3.2 leads to inappropriate mass estimates for objects with modest (or indeed negative) blueshifts, hence we only apply the correction on those objects whose C IV blueshift is $>500 \, \mathrm{km \, s^{-1}}$ (Figure 6; Coatman *et al.*, 2017). We correct the (FWHM)_{C IV} under the assumption that the C IV blueshift = $500 \, \mathrm{km \, s^{-1}}$, for the quasars that fall short of this threshold although the results would be qualitatively unchanged if no correction was applied to quasars with blueshifts of $<500 \, \mathrm{km \, s^{-1}}$. The mass estimates are then calculated using Eq. 3.3:

$$(M_{bh})_{C \text{ IV,Corr.}} = 10^{6.71} \left(\frac{(\text{FWHM})_{C \text{ IV,Corr.}}}{10^3 \text{kms}^{-1}} \right)^2 \left(\frac{\lambda L_{\lambda}(1350A)}{10^{44} \text{erg s}^{-1}} \right)^{0.53}$$
(3.3)

To determine the Eddington-scaled accretion rates of our sample, we use the 3000Å rest-frame luminosities and C IV derived SMBH masses. We apply the bolometric correction $BC_{3000} = 5.15$ (Shen *et al.*, 2011; Rankine *et al.*, 2020) to convert the rest-frame 3000Å luminosities to bolometric luminosities from which we calculate the Eddington-scaled accretion rates for our sample. A catalogue of all line properties derived from these spectra is available via the journal 1 . Details of the catalogue are presented in Table 3.1.

¹https://academic.oup.com/mnras/article/524/4/5497/7223474

TABLE 3.1: The format of the table containing the emission line properties from our MFICA reconstructions. The table is available in a machine-readable format in the online journal.

Header	Units	Description
SPEC_FILE	-	SDSS spec file name
RA	Degrees	Right Ascension
DEC	Degrees	Declination
REDSHIFT	$[-,-,km s^{-1}]$	Z _{SDSS} , Z _{Corrected} , Velocity shift
LOG_L1350	$\log_{10}(\operatorname{erg}\operatorname{s}^{-1})$	Monochromatic continuum luminosity at 1350Å
LOG_L3000	$\log_{10}(\text{erg s}^{-1})$	Monochromatic continuum luminosity at 3000Å
LOG_MBH_CIV_COATMAN	$\log_{10}(\mathrm{M}_{\odot})$	C IV derived MBH ^a
LOG_LAMBDA_EDD		Eddington-scaled accretion rate
C.IV	$[Å, km s^{-1}, km s^{-1}, km s^{-1}]$	C IV: EW, Centroid blueshift, FWHM and FWHM $_{\text{Coat.Corr}}^a$
HE_II	Å	He II: EW

^a The C IV FWHM Coatman *et al.* (2017) correction has been applied.

3.3. Results 53

3.3 Results

In this section we present the C IV and He II line properties for the $3.5 < z_{sys} < 4.0$ quasar sample and compare to quasars at $1.5 < z_{sys} < 3.5$ from the literature.

3.3.1 C IV emission

Figure 3.1 shows the distribution of the C IV blueshifts and equivalent widths in the $3.5 < z_{sys} < 4.0$ sample as well as the $1.5 < z_{sys} < 3.5$ sample from Rankine *et al.* (2020) and Temple *et al.* (2023). The Rankine *et al.* (2020) sample utilises SDSS DR14 so we supplement the sample with a small number of additional quasars in the same redshift range from DR16Q. Consistent with the findings of Richards *et al.* (2011); Coatman *et al.* (2016, 2017); Rankine *et al.* (2020), we observe an anti-correlation between the C IV blueshift and C IV EW of the emission lines. Stronger emission lines are generally symmetric and show modest C IV blueshifts while weaker lines exhibit a range of blueshifts with a clear tail extending to very high blueshifts of several 1000 km/s. While we find that both the $1.5 < z_{sys} < 3.5$ and $3.5 < z_{sys} < 4.0$ samples have the same characteristic distribution in the C IV emission space, as expected, the $3.5 < z_{sys} < 4.0$ objects do not populate the same region as the $1.5 < z_{sys} < 4.0$ quasars are biased towards lower C IV EWs and the $3.5 < z_{sys} < 4.0$ quasars also show a tail extending to much higher C IV blueshifts.

3.3.1.1 Matching the samples by quasar properties

To ensure a fair comparison between $3.5 < z_{sys} < 4.0$ and cosmic noon, we match our $3.5 < z_{sys} < 4.0$ quasars to the $1.5 < z_{sys} < 2.65$ DR16Q sample from Temple *et al.* (2023), by choosing the nearest $1.5 < z_{sys} < 2.65$ quasar to each $3.5 < z_{sys} < 4.0$ quasar in a variety of quasar physical properties. Specifically we match in turn by 3000Å continuum luminosity and *both* SMBH mass and Eddington-scaled accretion rate. For the lower redshift sample the SMBH masses are derived from the Mg II emission line, while at higher redshifts of $z_{sys} > 2.65$ they are derived instead using C IV. A key aim of this work is to investigate how changing the SMBH mass estimator potentially affects the dependence of UV line properties on SMBH mass and accretion rate.

We observe good agreement in the C IV emission line properties when matching the $3.5 < z_{sys} < 4.0$ sample to the $1.5 < z_{sys} < 2.65$ quasars in L_{3000} or both M_{BH} and L/L_{Edd} . The distributions are illustrated in Fig. 3.2 and Fig. 3.3 respectively. In both cases, the marginalised distributions in C IV EW are in good agreement between $1.5 < z_{sys} < 2.65$ and $3.5 < z_{sys} < 4.0$. The high C IV blueshift tail of the

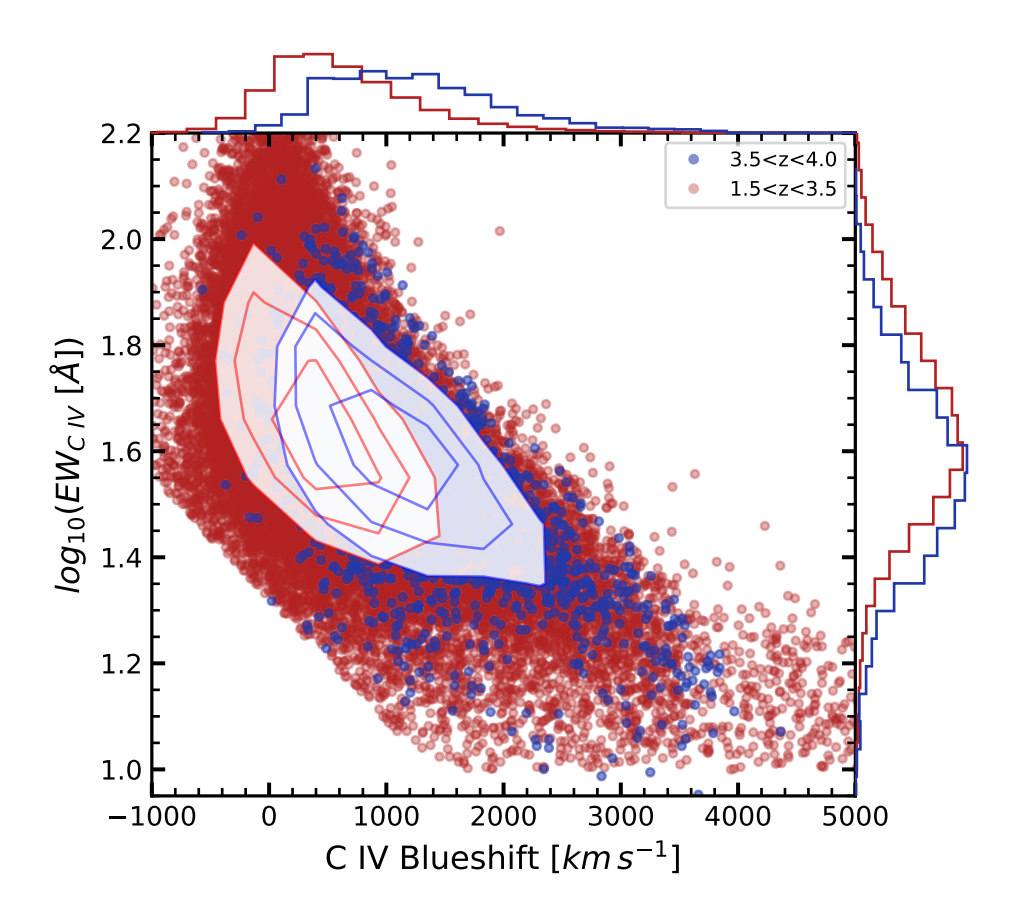


FIGURE 3.1: The C IV emission space for both the $1.5 < z_{sys} < 3.5$ (red, Rankine et al., 2020; Temple et al., 2023) and $3.5 < z_{sys} < 4.0$ (blue) samples. Density contours encircle 68, 50 and 25 per cent of the sample, respectively. Marginalised distributions of the C IV blueshift and EW are also shown. While the distributions feature the same characteristic shape, the $3.5 < z_{sys} < 4.0$ sample is biased to higher C IV blueshift and lower C IV EW. The following criteria was applied to remove poorly fit spectra from both samples;

 $\log_{10}(\text{C IV EW [Å]}) < -2.3077 \times 10^{-4} \times \text{C IV blueshift [km s}^{-1}] + 1.3231.$

 $3.5 < z_{sys} < 4.0$ sample is much more consistent with the $1.5 < z_{sys} < 2.65$ quasars when matching in either L₃₀₀₀ or *both* M_{BH} and L/L_{Edd}, compared to the marginalised distributions presented in Fig. 3.1. However, the number of objects with C IV blueshift $\leq 500 {\rm km \, s^{-1}}$ tails off more rapidly at $3.5 < z_{sys} < 4.0$.

In Chapter 2, we demonstrate that truncating the $1.5 < z_{sys} < 2.65$ spectra to the same rest-frame wavelength coverage as our $3.5 < z_{sys} < 4.0$ spectra (i.e. $\lambda < 2000\text{\AA}$) results in a slight over-estimation of z_{sys} at lower C IV blueshifts. The implication for the results presented in Fig. 3.2 and Fig. 3.3 is that the position of the line centroid is shifted blue-ward, hence the number of objects with C IV blueshift $\leq 500 \text{km s}^{-1}$ tails off more rapidly at $3.5 < z_{sys} < 4.0$ compared to the lower redshift quasar population. Conversely, the high C IV blueshift tail is less affected by this systemic redshift bias, since the narrow associated absorbers generating the effect are commonly found close

3.3. Results 55

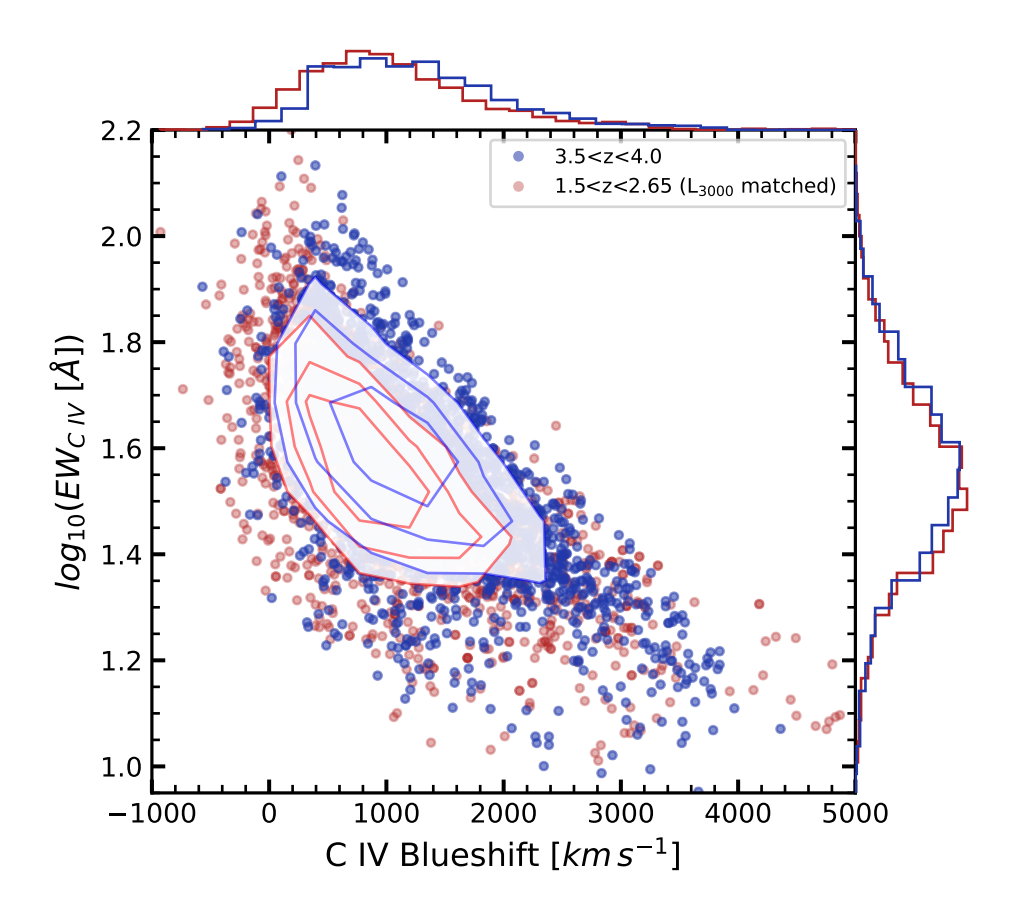


FIGURE 3.2: The C IV emission space for the $3.5 < z_{sys} < 4.0$ sample (blue) and the L₃₀₀₀ matched $1.5 < z_{sys} < 2.65$ quasars (red) from Temple *et al.* (2023). Density contours encircle 68, 50 and 25 per cent of the sample, respectively.

to systemic, explaining the discrepancies observed in the 1-D marginalised C IV blueshift histograms presented in both Fig. 3.2 and Fig. 3.3.

While the C IV emission line properties appear to be consistent across the entire redshift range investigated, it is important to note that the SMBH mass estimates at $1.5 < z_{sys} < 2.65$ were derived from the Mg II emission line (Temple *et al.*, 2023). As discussed in Section 3.2.2, the SMBH masses for the $3.5 < z_{sys} < 4.0$ sample are derived from the C IV emission with an associated correction to the FWHM to account for the line asymmetry (Coatman *et al.*, 2017). This could potentially lead to biases in the results presented in Fig. 3.3.

In Fig. 3.4 we investigate how the C IV blueshift evolves with redshift, luminosity, black hole mass and accretion rate. The C IV blueshift increases with systemic redshift (top). However, when one accounts for the trends in blueshift with UV luminosity (top middle) and Eddington-scaled accretion rate (bottom), this trend can be explained by the higher luminosities probed at high redshifts due to the flux limits of the SDSS. Furthermore, when one considers the redshift evolution of the quasar luminosity function (QLF), whereby the number density of the brightest quasars exponentially decreases beyond $z_{sys} \gtrsim 3.5$ (Fig. 7; Kulkarni *et al.*, 2019), the increase in C IV blueshift

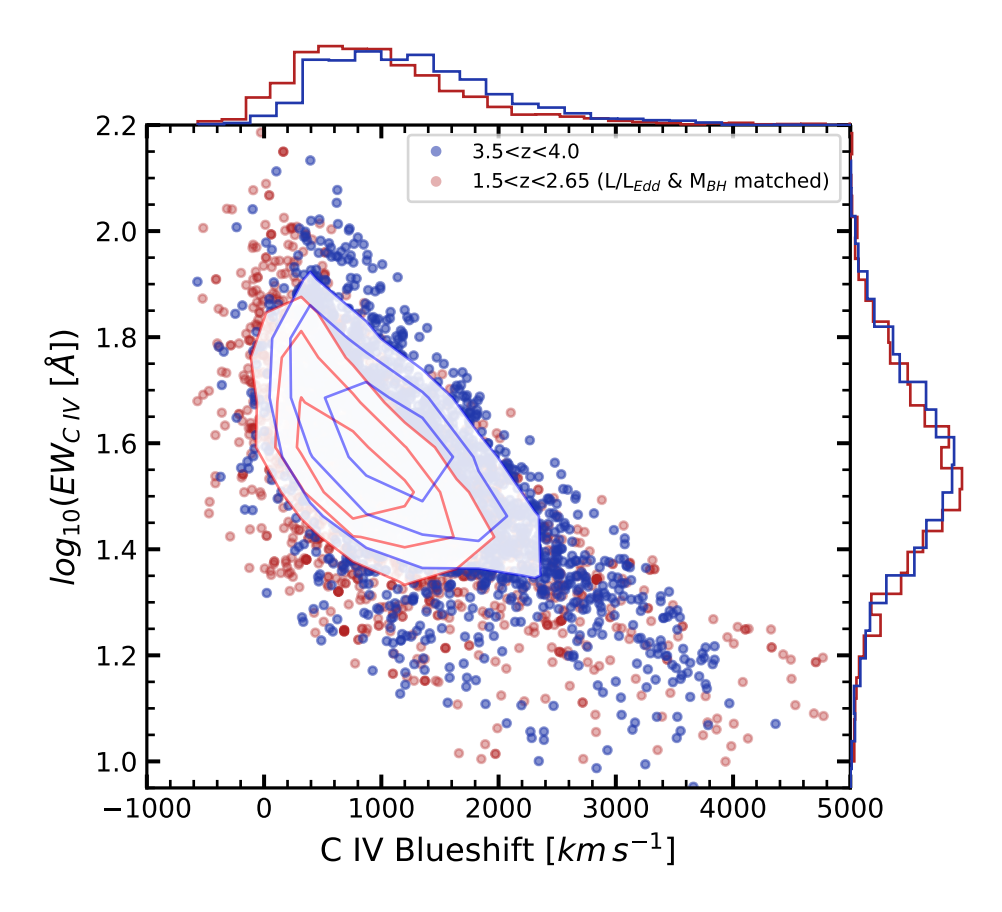


FIGURE 3.3: The C IV emission space for the $3.5 < z_{sys} < 4.0$ sample (blue) and the M_{BH} and L/L_{Edd} matched $1.5 < z_{sys} < 2.65$ quasars (red) from Temple *et al.* (2023). Density contours encircle 68, 50 and 25 per cent of the sample, respectively.

at $z_{sys} \sim 3-3.5$ (top) is consistent with the fact that we only see the most luminous quasars at these redshifts in a flux-limited sample. We also observe limited evolution in the C IV blueshift as a function of SMBH mass (bottom middle) with a slight tendency for C IV blueshifts to decrease with increasing SMBH masses. In addition, we observe no significant change to the trends in Fig. 3.4, when we measure the black hole masses from the Mg II emission versus the C IV emission line with a blueshift dependent correction applied to the C IV FWHM (Section 3.2; Coatman *et al.* 2017).

3.3.2 He II emission

The He II line (illustrated in Fig. 2.9) is generated by the direct recombination of He III ions to He II (with some covering factor dependence) and is therefore a "clean" measurement of the number of photons above 54.4 eV (Section 2c; Mathews & Ferland, 1987). Hence, provided that the He II line properties can be robustly measured, the He II emission is a better indicator of the ionisation potential of the soft X-ray photons than C IV (Timlin *et al.*, 2021; Temple *et al.*, 2023). Figure 3.5 illustrates how the He II line properties change across the C IV emission space. We recover the

3.3. Results 57

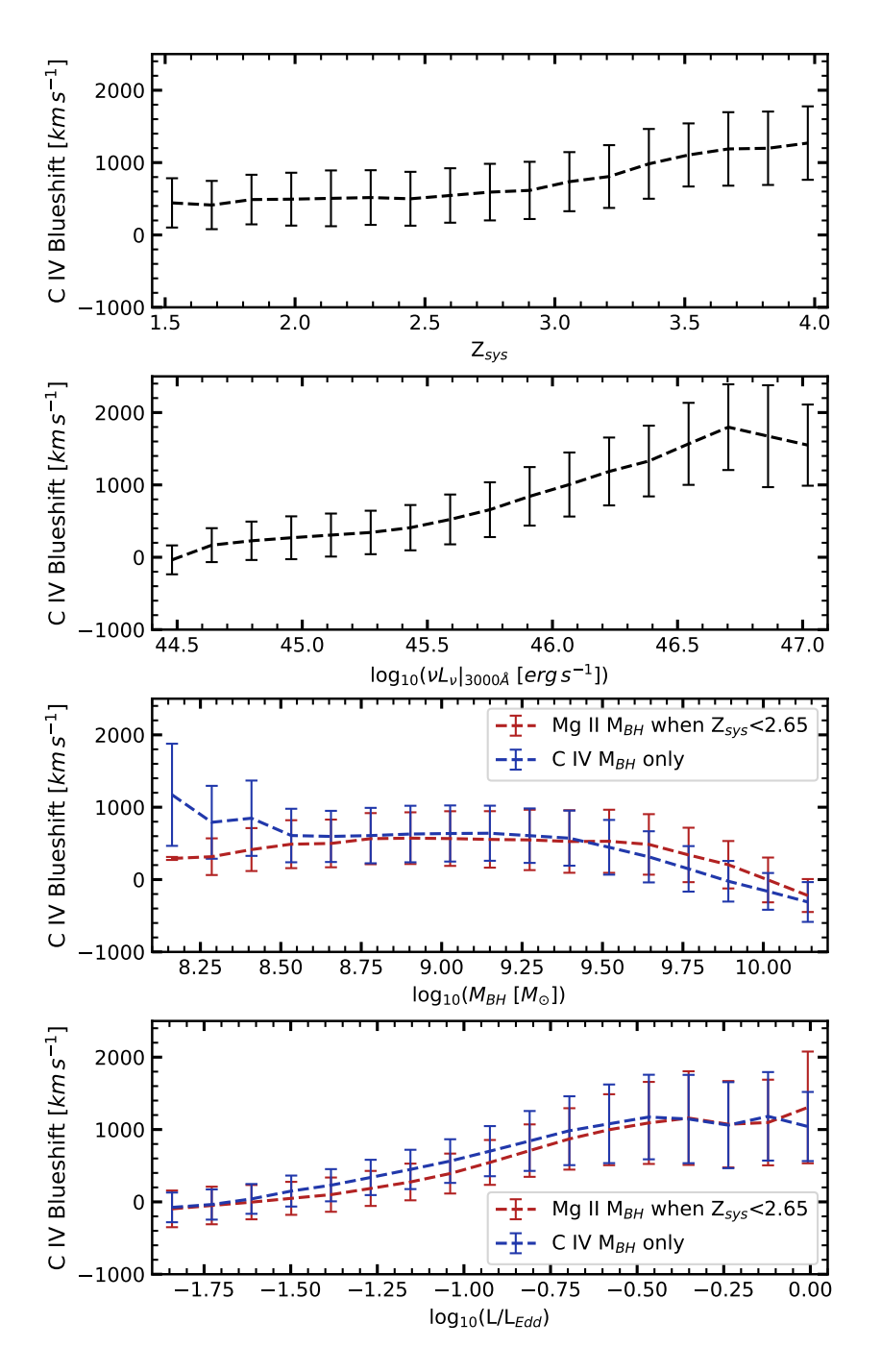


FIGURE 3.4: The C IV blueshift as a function of systemic redshift (top), UV continuum luminosity (top-middle), SMBH mass (bottom-middle) and Eddington-scaled accretion rate (bottom). The data is compressed into 17 equidistant bins, where we present the median and median absolute deviation (MAD) of each bin in the appropriate panels. We see a tendency for increasing C IV blueshifts with increasing systemic redshift, UV continuum luminosity and Eddington-scaled accretion rate. The trends with UV continuum luminosity and Eddington-scaled accretion rate can explain why we observe an increase in C IV blueshift as we tend to larger systemic redshifts. There is limited evidence of a strong trend between SMBH mass and C IV blueshift (bottom middle), with a slight tendency to lower C IV blueshifts as we approach the upper limit of our SMBH masses for the sample. There is limited evidence to suggest that the emission line used to estimate virial black hole masses will have any significant impact on our results.

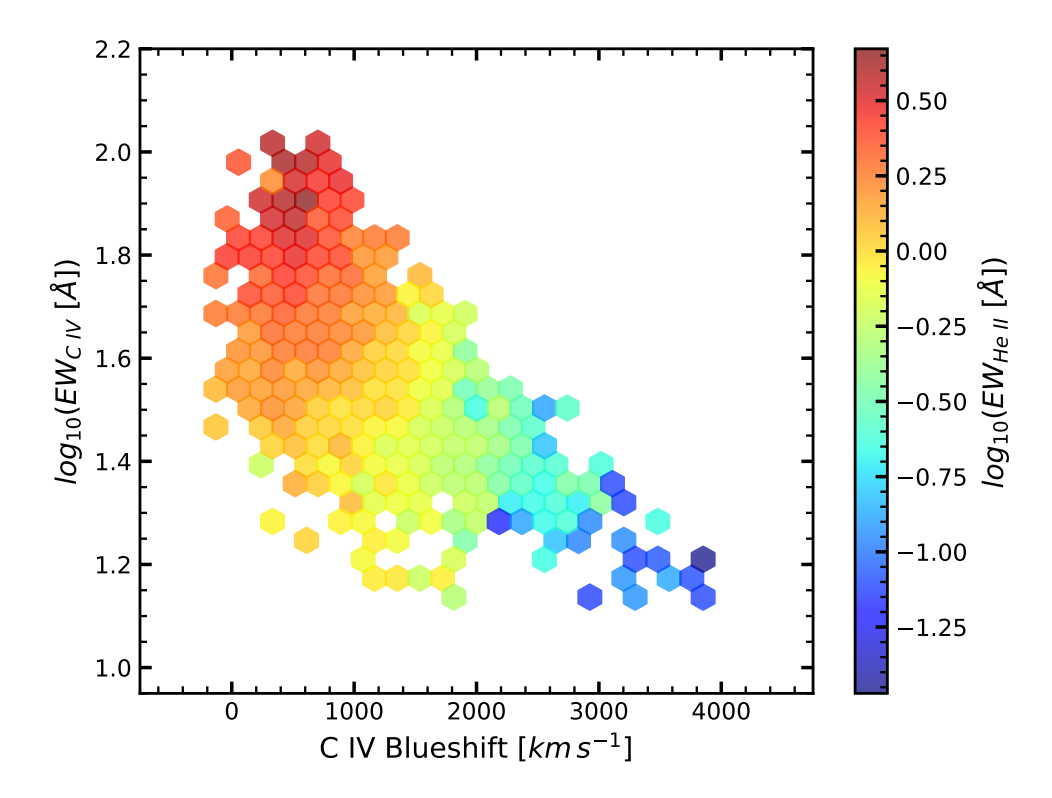


FIGURE 3.5: The median observed He II EW in bins of C IV blueshift and C IV EW for the 3.5 $< z_{sys} < 4.0$ sample. The He II EW is correlated with both C IV blueshift and C IV EW, with the most blueshifted C IV lines only observed when the He II EW is low. Conversely, the highest EW C IV lines are only observed when the He II EW is high.

same trends as those uncovered by Baskin *et al.* (2013) and Rankine *et al.* (2020) at lower redshifts. Figure 3.5 illustrates a clear anti-correlation between the He II EW and the C IV blueshift as well as an additional correlation between the He II and C IV EWs.

Under the assumption that the He II EW is a good proxy for the ionising flux at 54.4 eV (see Section 3.4.1 for full discussion), this result is consistent with the hypothesis that UV line-driven outflows give rise to the blueshift observed in the C IV emission of quasars. A soft SED is a prerequisite for the strong blueshifting observed in the CIV emission and over-ionisation of the outflowing material leads to weaker C IV blueshifts. In Fig. 3.6 we present the evolution of the He II EW as a function of both systemic redshift and UV continuum luminosity. We observe no convincing evidence of an evolution in the He II EW with systemic redshift, save for a slight tendency to lower He II EW at $3.5 < z_{sys} < 4.0$. However, this tendency is well accounted for when one considers the trend in He $\scriptstyle\rm II$ EW with UV continuum luminosity, whereby the He $\scriptstyle\rm II$ EW decreases with luminosity and therefore with systemic redshift as a result of the sampling bias at $z_{sys} \gtrsim 3.5$. Since the relation presented in Fig. 3.5 is observed in quasars across the entire redshift range, $1.5 < z_{sys} < 4.0$, and the He II EW demonstrates little to no evolution with systemic redshift in Fig. 3.6, we can conclude that the SED properties of quasars remain consistent across the entire $1.5 < z_{sys} < 4.0$ redshift range.

3.3. Results 59

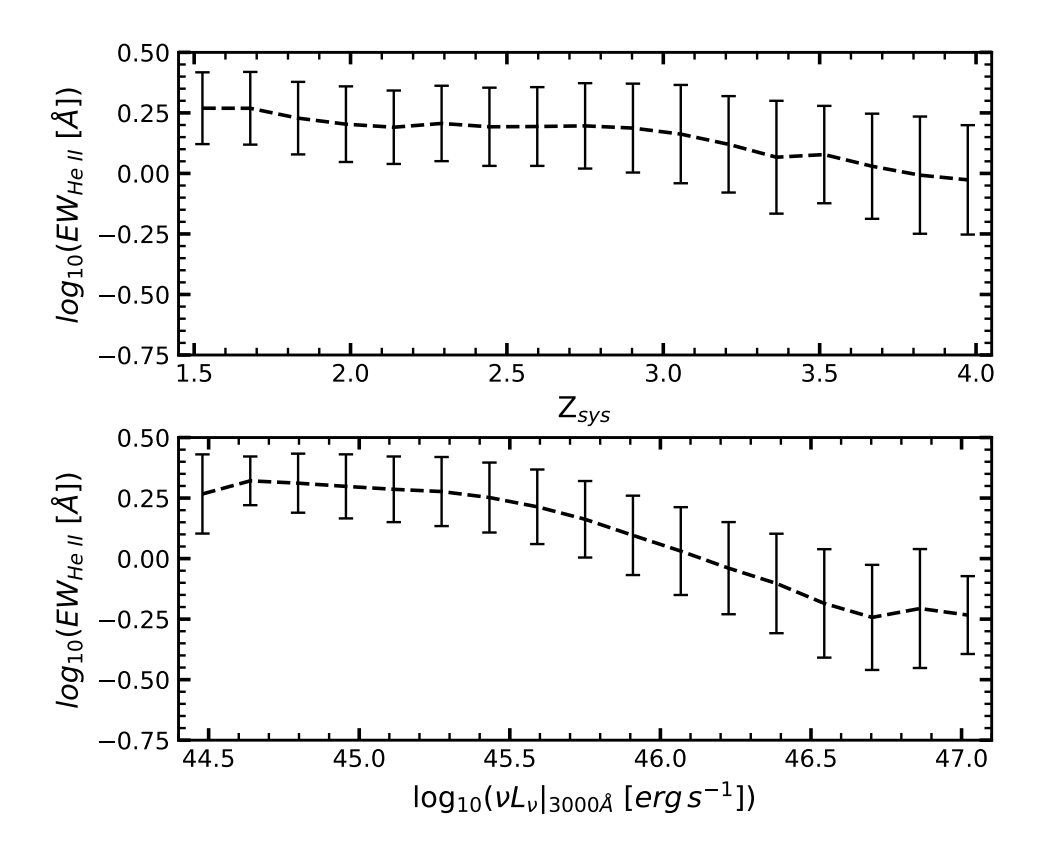


FIGURE 3.6: The He II EW as a function of systemic redshift (top) and UV continuum luminosity (bottom). The data is compressed into 17 equidistant bins, where we present the median and median absolute deviation (MAD) of each bin in the appropriate panels. We see a slight tendency for decreasing He II EWs with increasing systemic redshift. The trends with He II EW and UV continuum luminosity can therefore well explain the apparent evolution with systemic redshift.

To ensure the MFICA reconstructions identify meaningful signal in the low EW He II emission, we construct high signal-to-noise composite stacked spectra from 20 different regions in the C IV emission space. We then measure the line properties from the composites directly, rather than using MFICA reconstructions, and recreate Fig. 3.5 in Fig. 3.7. We find that identical trends in the He II EW and both C IV EW and blueshift are recovered. This confirms that through use of MFICA, we are able to robustly reconstruct the He II emission line, even at the relatively modest signal-to-noise ratios of the individual spectra in the $3.5 < z_{sys} < 4.0$ sample.

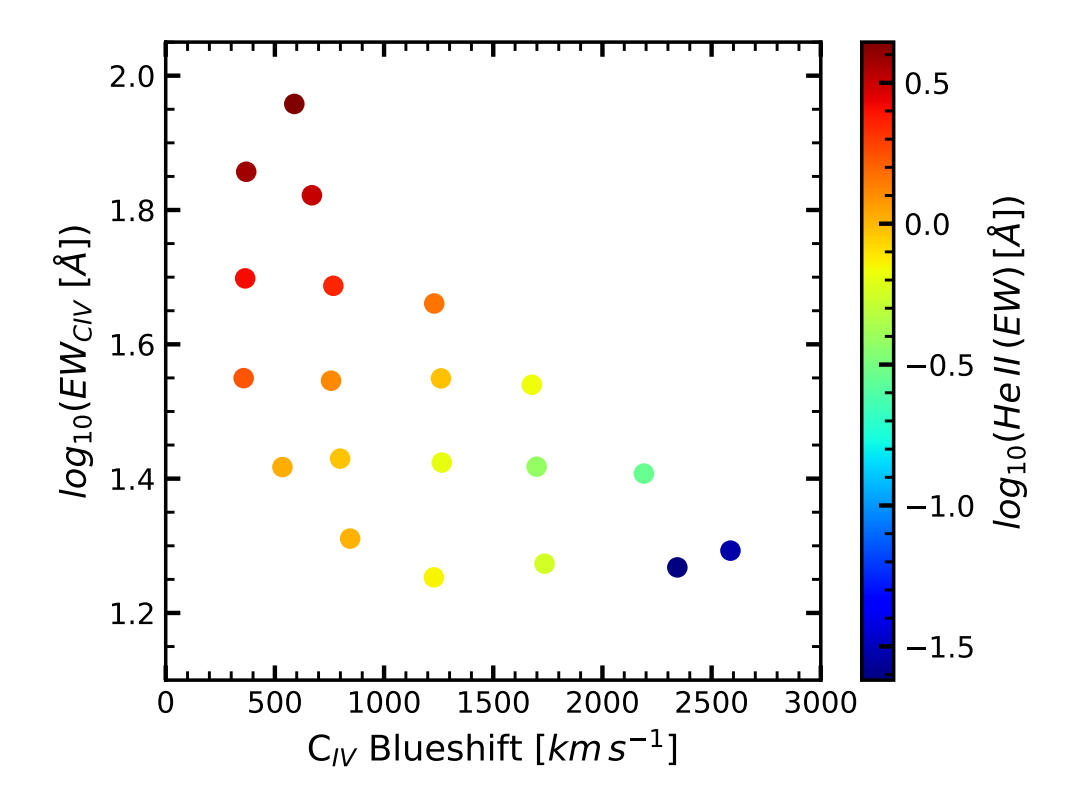


FIGURE 3.7: The He II EW measured from 20 high signal-to-noise composite stacked spectra overlaid on the C IV emission space. As in Fig. 3.5, the He II EW is correlated with both C IV blueshift and C IV EW, with the most blueshifted C IV lines only observed when the He II EW is low. Conversely, the highest EW C IV lines are only observed when the He II EW is high.

3.3.3 Comparison to Wu & Shen 2022

Here we discuss a comparison between our work and catalogues where line properties are determined via parametric fitting. Recently Wu & Shen (2022) have published a catalogue of quasar continuum and emission line properties for the $\sim 750,000$ quasars in DR16Q, including updated systemic redshifts for the quasars. Here we explicitly compare our line properties to theirs. We match the 2,531 quasars at $3.5 < z_{sys} < 4.0$ analysed in this paper to the Wu & Shen (2022) catalogue by position and extract the appropriate rest-frame UV line properties for the comparison.

Precision measurements of the C IV emission line properties was not a primary aim of Wu & Shen (2022). Hence a composite Gaussian fitting recipe was adopted to model the emission line profile. The C IV emission space for the $3.5 < z_{sys} < 4.0$ sample is presented in Fig. 3.8. While the marginalised distributions in C IV blueshift are consistent with ours, the marginalised distributions in C IV EW suggest that the Wu & Shen (2022) catalogue is biased to lower C IV EW when compared to this work. Since the low C IV EW line profiles are poorly approximated by parametric fitting recipes, the characteristic tail to high blueshifts in the C IV emission space is not as evident when one uses the Wu & Shen (2022) measurements.

3.3. Results 61

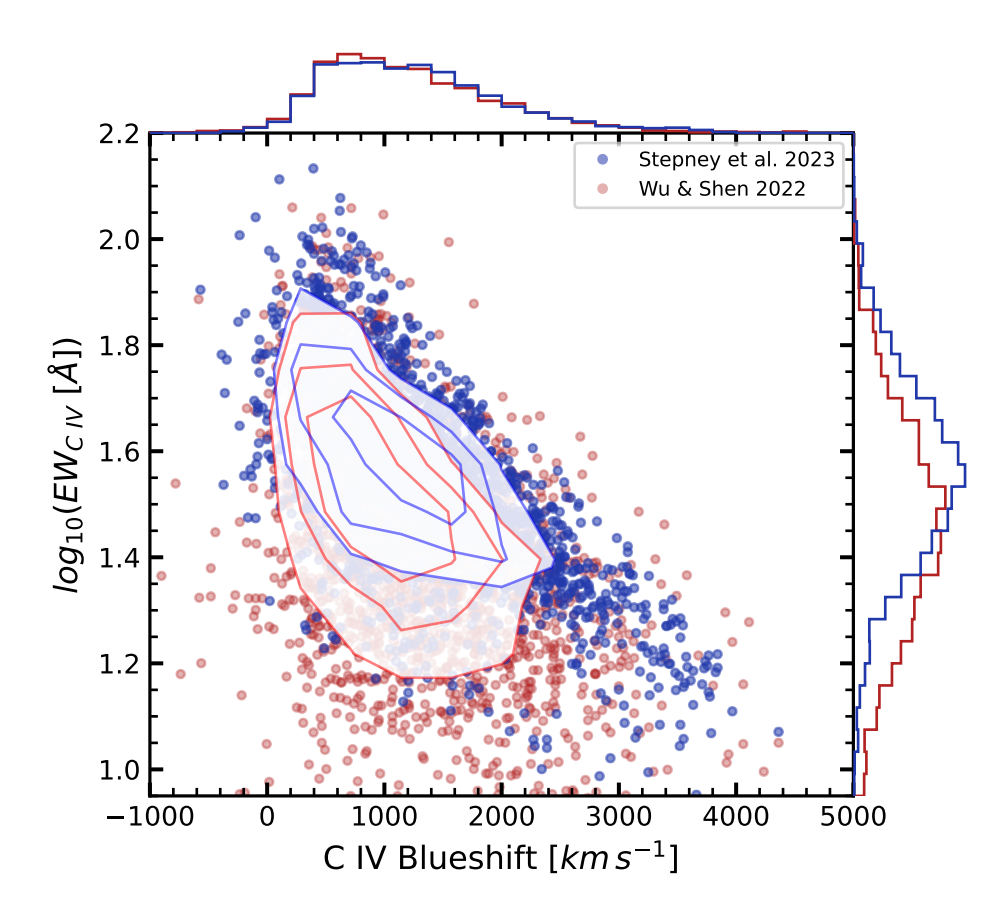


FIGURE 3.8: The C IV emission space for the $3.5 < z_{sys} < 4.0$ sample, using line properties derived from Wu & Shen (2022) (red) and this work (blue). C IV blueshifts are calculated from line centroids in both distributions. Density contours encircle 68, 50 and 25 per cent of the sample, respectively. Marginalised distributions of the C IV blueshift and EW are also shown. The distributions do not feature the same characteristic shape in C IV emission space, with the Wu & Shen (2022) objects biased to lower C IV EW.

A key result of our chapter is the correlation presented in Fig. 3.5. The existence of a correlation between the He II EW and both C IV EW and blueshift could suggest that the C IV emission is tracing outflows and that these are radiatively driven with an explicit dependence on the ionising SED. In Fig. 3.9 we present the same results using the Wu & Shen (2022) measurements. In addition to the bias towards lower C IV EW, the He II EW measurements appear systematically larger than those measured in this work. This difference can, in part, be attributed to the way in which the He II continuum is defined. Finally, while the correlation between He II EW and C IV EW persists, in Fig. 3.9, the anti-correlation between He II EW and C IV blueshift is significantly weaker. This highlights the strength of the MFICA technique in recovering robust He II EWs and C IV blueshifts for high-redshift quasar spectra.

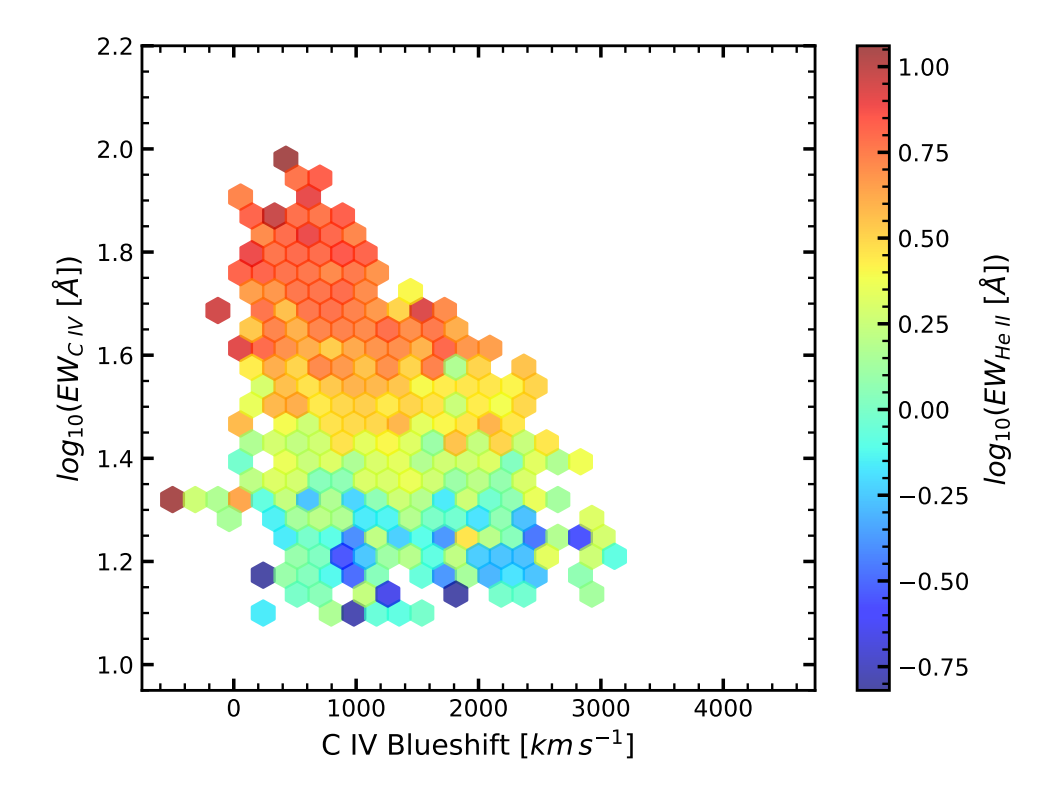


FIGURE 3.9: The median observed He II EW in bins of C IV blueshift and C IV EW for the 3.5 $< z_{sys} < 4.0$ sample, using line properties derived from Wu & Shen (2022). The He II EW is correlated with C IV EW, however, the He II EW measurements are systematically overestimated when compared to this work. The correlation between the He II EW and the C IV blueshift is also significantly weaker than what is observed in Fig. 3.5.

3.4 Discussion

3.4.1 Probing the driver of outflows

We have explored trends in the rest-frame UV emission line properties of quasars at $1.5 < z_{sys} < 4.0$, analysed using the same methodology across the full redshift range. As shown in Fig. 3.2 and Fig. 3.3, we find that the C IV emission line properties, and in particular the high-blueshift tail at $3.5 < z_{sys} < 4.0$ and $1.5 < z_{sys} < 2.65$ are best matched when matching the quasar samples in either UV luminosity or equivalently both SMBH mass and Eddington-scaled accretion rate. In Fig. 3.5 we demonstrated that there is a strong and systematic trend between the C IV blueshift and the He II EW in $3.5 < z_{sys} < 4.0$ quasars, which is qualitatively very similar to the trend found in the $1.5 < z_{sys} < 3.5$ population by e.g. Rankine et al. (2020). The result is broadly consistent with a paradigm where the C IV blueshift is tracing a radiation line-driven wind with the ability to launch a wind anti-correlating with the number of high-energy ionizing photons above 54eV (Baskin et al., 2015). We will therefore proceed from hereon under the assumption that the C IV emission line properties encode information about the strength of a radiation line-driven wind. A key question

3.4. Discussion 63

of interest is how the wind properties then relate to fundamental properties of the quasar such as UV luminosity, SMBH mass and Eddington-scaled accretion rate. Recently, Temple *et al.* (2023) have looked at this exact question using a sample of \sim 190,000 SDSS quasars at 1.5 < z_{sys} < 2.65. We can therefore extend the Temple *et al.* (2023) analysis to explicitly ask if the same fundamental properties drive trends in quasar UV emission line properties at 3.5 < z_{sys} < 4.0.

Figure 3.10 illustrates the MBH - L/L_{Edd} plane, for both the 1.5 < z_{sys} < 2.65 and 3.5 < z_{sys} < 4.0 samples, with trends in C IV blueshift, C IV EW and He II EW at 3.5 < z_{sys} < 4.0 overlaid. As expected, we observe a clustering at 3.5 < z_{sys} < 4.0 in the top right-hand corner of the parameter space and the 3.5 < z_{sys} < 4.0 sample is biased to higher black hole masses and Eddington-scaled accretion rates compared to 1.5 < z_{sys} < 2.65, due to the flux limits of the SDSS survey. Crucially though, and in contrast to quasars at even higher redshifts as we discuss later, the 3.5 < z_{sys} < 4.0 sample overlaps considerably with the 1.5 < z_{sys} < 2.65 sample in SMBH mass and Eddington-scaled accretion rate.

As is the case in the $1.5 < z_{sys} < 2.65$ sample, we observe the strongest outflows above $L/L_{Edd} \ge 0.2$ and MBH $\ge 10^9 M_{\odot}$. Indeed, the trends in C IV blueshift, C IV EW and He II EW are consistent with the $1.5 < z_{sys} < 2.65$ sample results, presented in Temple et al. (2023), suggesting that the underlying drivers of these UV line properties do not evolve with redshift. We also investigate trends in the M_{BH} - L_{3000} plane in Fig. 3.11. The flux limit of the $3.5 < z_{sys} < 4.0$ sample is evident at $\nu L \nu|_{3000\text{\AA}} \sim 45.5\,\mathrm{erg\,s^{-1}}$, the threshold above which quasar feedback is considered to be effective (Zakamska & Greene, 2014). The trends in line properties in the M_{BH} - L_{3000} plane are also consistent with those seen in 1.5 $< z_{sys} <$ 2.65 quasars by Temple *et al.* (2023). A key result of our work is therefore explicitly demonstrating that redshift is not a fundamental parameter in determining quasar UV emission line (and by implication outflow) properties and that these properties are instead governed by SMBH mass and accretion rate. Moreover, the results are not sensitive to the emission line used for the SMBH mass estimates, which demonstrates that with large enough statistical samples global trends of UV line properties with SMBH mass and accretion rate can be recovered even when one uses C IV lines for SMBH mass estimates (e.g, Fig. 3.4).

Giustini & Proga (2019) have proposed that accreting black holes with a mass, MBH $\geq 10^8 M_{\odot}$, and an Eddington-scaled accretion rate, L/L_{Edd} ≥ 0.25 are expected to facilitate strong radiation-driven winds. Conversely, objects whose Eddington-scaled accretion rate falls below this threshold will likely produce failed line-driven disc winds, or in extreme cases, the outflowing material is magnetically-driven, and the feedback kinetic. Temple *et al.* (2023) find that the observations at $1.5 < z_{sys} < 2.65$ are in good agreement with the proposed framework, only measuring significant C IV blueshifts ($\geq 1000 \, \mathrm{km \, s^{-1}}$), at $1.5 < z_{sys} < 2.65$, when objects are both strongly-accreting and high mass. We confirm that at $3.5 < z_{sys} < 4.0$, the C IV

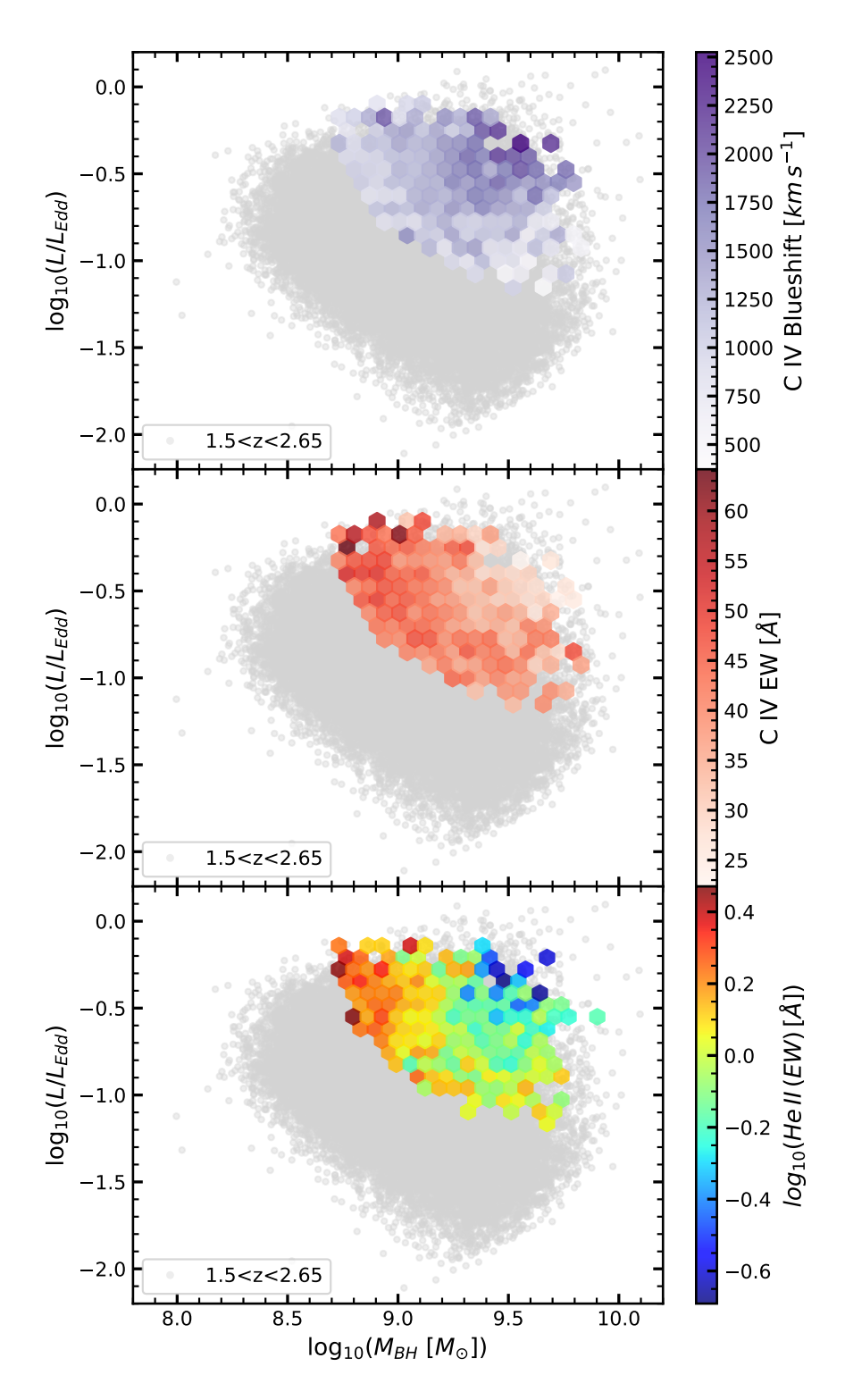


FIGURE 3.10: The median observed C IV blueshift (top), C IV EW (middle) and He II EW (bottom) in bins of SMBH mass and Eddington-scaled accretion rate for the 3.5 < z_{sys} < 4.0 sample overlaid on the M_{BH} - L/L_{Edd} plane at 1.5 < z_{sys} < 2.65 (grey, Temple et al., 2023). Save for a clear flux limit, the 1.5 < z_{sys} < 2.65 and 3.5 < z_{sys} < 4.0 samples are well-matched in this space. We note that above L/L_{Edd} \sim 0.2 there is evidence of a clear trend between He II EW and SMBH mass. Below $\sim 10^9 M_{\odot}$, the quasars generally have stronger UV emission lines and weaker C IV blueshifts and above this threshold, the contrary is true.

3.4. Discussion 65

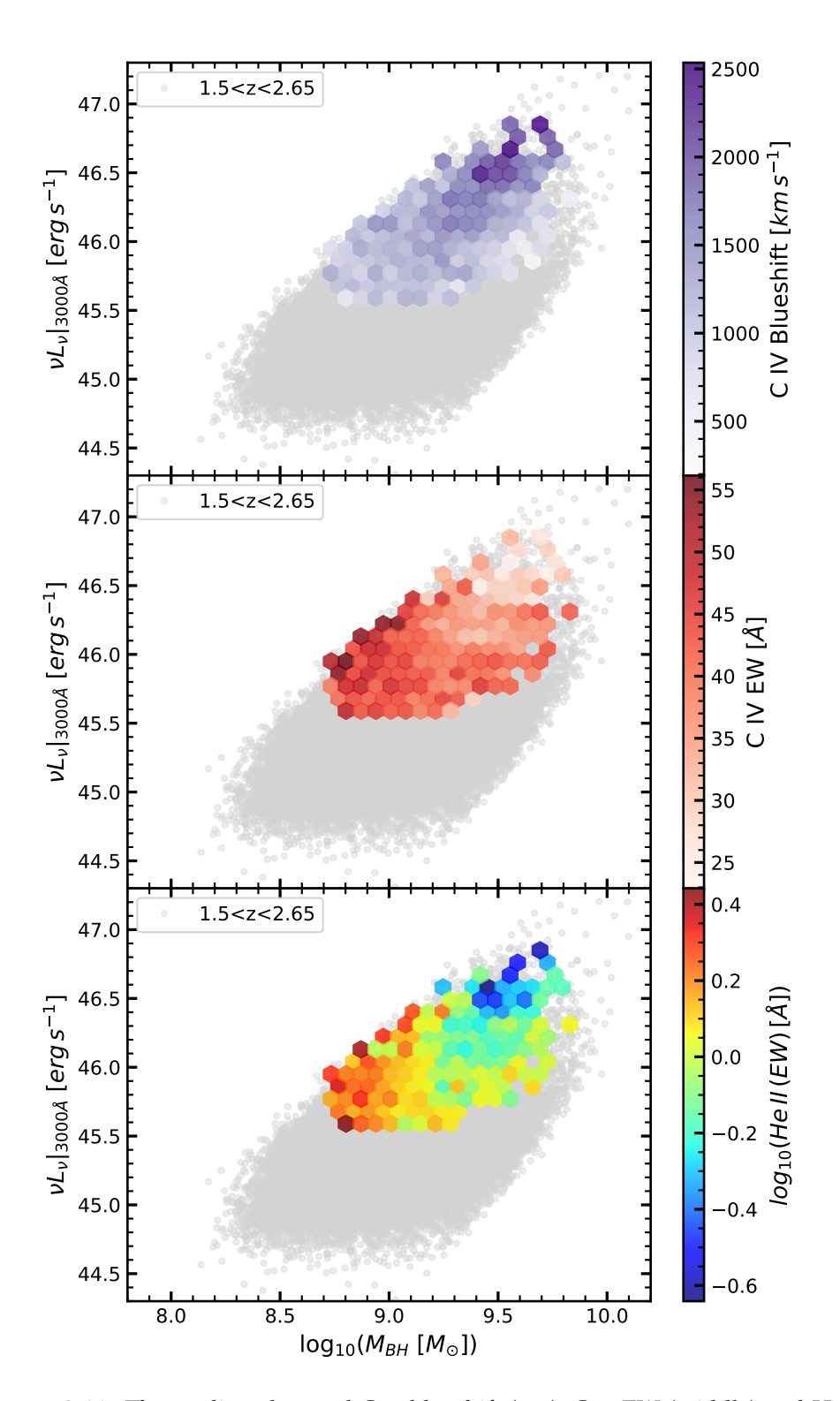


FIGURE 3.11: The median observed C IV blueshift (top), C IV EW (middle) and He II EW (bottom) in bins of SMBH mass and 3000Å UV continuum luminosity for the 3.5 < z_{sys} < 4.0 sample overlaid on the M_{BH} - L_{3000} plane at 1.5 < z_{sys} < 2.65 (grey, Temple *et al.*, 2023). A clear flux limit is observed at $\nu L \nu|_{3000 \text{Å}} \sim 45.5 \, \text{erg s}^{-1}$ in the 3.5 < z_{sys} < 4.0 sample. Apart from that the 1.5 < z_{sys} < 2.65 and 3.5 < z_{sys} < 4.0 samples are well-matched in this space. Below $\sim 10^9 \, M_{\odot}$ the quasars have stronger UV emission lines and smaller C IV blueshifts. Above this threshold, the contrary is true.

blueshift is again strongly dependent on the mass and accretion rate in much the same way as for the $1.5 < z_{sys} < 2.65$ population and that at high accretion rates and lower SMBH masses, the ionising potential above 54.4 eV, as traced by the He II EW, prevents strong disc winds from being launched.

Fundamentally, the similarity in the trends in UV emission line properties with luminosity, mass and accretion rate between $1.5 < z_{sys} < 2.65$ and $3.5 < z_{sys} < 4.0$, strongly suggests that the same accretion and wind-driving mechanisms are at play across the entire $1.5 < z_{sys} < 4.0$ redshift range. We will now discuss the implication of these results for studies of quasar winds and outflows at even higher redshifts, where there have been claims that the UV emission line properties do indeed show some evolution (Meyer *et al.*, 2019; Schindler *et al.*, 2020; Yang *et al.*, 2021; Farina *et al.*, 2022).

3.4.2 Implications at higher redshifts

Previous studies of quasars at the highest redshifts of $z_{sys} \gtrsim 6$ have concluded that their emission line properties, and in particular C IV blueshifts are on average higher than quasars at lower redshifts even when the samples are matched in UV luminosity. We now consider quasar samples at $z_{sys} \sim 4.8$ from Trakhtenbrot *et al.* (2011) and at $z_{sys} \gtrsim 6$ from Schindler *et al.* (2020) for explicit comparison to our work.

As has been done in the literature, we construct a control sample of $1.5 < z_{sys} < 2.65$ quasars drawing from the sample in Temple et al. (2023), and matching to the high-redshift samples in UV luminosity. In Fig. 3.2 we found that matching the $3.5 < z_{sys} < 4.0$ and $1.5 < z_{sys} < 2.65$ samples in UV-luminosity resulted in a good agreement in the C IV emission properties. The left-hand panel of Fig. 3.12 illustrates that the UV luminosity matching across the two redshift bins, results in a broadly consistent mapping to the M_{BH} - L/L_{Edd} plane, which we have already determined in Section 3.4.1 are the fundamental parameters driving trends in C IV blueshift. However, when we consider the Trakhtenbrot et al. (2011) and Schindler et al. (2020) quasars at $z_{sys} \sim 5 - 7$, the UV-luminosity matched control samples no longer map onto the same region of the M_{BH} - L/L_{Edd} plane as the high-redshift quasars, as illustrated in the right-hand panel of Fig. 3.12. This is perhaps unsurprising when one considers the degeneracy in matching quasar samples through their luminosities, i.e, samples with low Eddington-scaled accretion rates and high SMBH masses will populate the same region of the luminosity distribution as samples with high Eddington-scaled accretion rates and low SMBH masses.

As there are relatively small numbers of $z_{sys} \sim 5-7$ quasars and they are observed at higher Eddington-scaled accretion rates and lower SMBH masses, a region that isn't populated well by the $1.5 < z_{sys} < 2.65$ sample used as a control, UV-luminosity matching is ineffective in selecting a control sample of quasars with a similar SMBH

3.4. Discussion 67

mass and Eddington-scaled accretion rate distribution as the quasars found at $1.5 < z_{sys} < 2.65$. Indeed, Farina *et al.* (2022) do find that the $z_{sys} > 6$ quasars have systematically higher Eddington-scaled accretion rates compared to a UV-luminosity matched control sample at lower redshifts. Regardless of whether this is an intrinsic property of the highest redshift quasar population or a selection bias in the observed samples, this could in part explain the observed discrepancies in the C IV blueshifts between $1.5 < z_{sys} < 2.65$ and $z_{sys} \gtrsim 6$ quoted in the literature.

It is curious then, when exploring the trends in Fig. 3.10, that an extrapolation of these trends would imply that the lower mass, higher Eddington-scaled accretion rate quasars at $z_{sys} > 6$ should have higher He II EWs and therefore smaller C IV blueshifts compared to the luminosity-matched control at $1.5 < z_{sys} < 2.65$, contrary to what is observed. Unfortunately the He II EWs have not been measured for the highest redshift quasars, which precludes any direct comparison to the $3.5 < z_{sys} < 4.0$ sample analysed here. In the case of the $3.5 < z_{sys} < 4.0$ sample, our use of the novel MFICA technique has enabled us to extract information about the He II EWs even for spectra of modest signal-to-noise. While we do not have information on the He II properties at the highest redshifts, several papers have looked at the X-ray properties of the highest redshift quasars and confirmed the well-known correlation between $\alpha_{\rm OX}$, the UV-to-Xray SED slope, and the UV luminosity. Higher luminosity quasars have proportionally lower X-ray flux and therefore softer ionising SEDs with no apparent evolution in $\alpha_{\rm OX}$ with redshift (Nanni *et al.*, 2017; Pons *et al.*, 2020).

If the trends illustrated in Fig. 3.10 do break down for the $z_{sys} \sim 6$ population, this might point to a change in the underlying mechanisms driving the C IV blueshift. Meyer *et al.* (2019) have speculated about the role of orientation and obscuration in explaining the apparent lack of $z_{sys} > 6$ quasars with modest blueshifts. In a flux-limited sample probing only the highest UV-luminosity sources, quasars that are viewed more edge-on and/or more obscured would preferentially drop out of the sample. If the wind geometry is polar, these missing quasars would also be those at more modest blueshifts, thus explaining the bias to high blueshifts at $z_{sys} > 6$. Our work now explicitly demonstrates that despite sampling higher UV-luminosity sources at $3.5 < z_{sys} < 4.0$, there is no such bias in their C IV emission line properties relative to $z_{sys} \sim 2$, which could imply that the geometry and obscured fraction of quasars dramatically changes from $z_{sys} \sim 4$ to $z_{sys} \gtrsim 6$. Alternatively, it might be inappropriate to extrapolate the trends in Fig. 3.10 to the super-Eddington regime given the inner accretion disc transitions from geometrically thin and optically thick to a slim disc as radiation pressure causes the disc to "puff up" (Giustini & Proga, 2019).

It is also important to highlight that when illustrating trends in Fig. 3.12, all the SMBH masses, luminosities and Eddington-scaled accretion rates for the Trakhtenbrot *et al.* (2011) sample were re-derived using Eqns 3.2 and 3.3. Although we currently take the equivalent properties for the $z_{sys} \gtrsim 6$ quasars directly from Schindler *et al.* (2020), our

results would remain unchanged if we used the continuum luminosities and FWHM of the emission lines from that paper to re-derive black hole masses and Eddington-scaled accretion rates for the $z_{sys} > 6$ sample. Considerable care has also been taken in this work to ensure that the $3.5 < z_{sys} < 4.0$ and $1.5 < z_{sys} < 2.65$ samples have employed the same methodologies for calculating quasar systemic redshifts and measuring UV line properties. This was beyond the scope of the current work for the quasar samples analysed at higher redshifts and might result in biases when comparing to the lower redshift population (see e.g. Section 3.3.3).

A key conclusion of our study is that, under the premise that the C IV emission line blueshift is tracing the velocity of radiatively driven disc winds, the fundamental parameters that govern the blueshift are the SMBH mass and Eddington-scaled accretion rate. We have shown that quasars at the highest redshifts do not map on to the SMBH mass Eddington-scaled accretion rate plane occupied by similarly luminous quasars at lower redshifts. A more complete sampling of this plane is clearly needed at $z_{sys} > 6$ to determine whether the observed evolution in UV-line properties is due to an intrinsic difference in the masses and accretion rates of the first quasars, or conversely, if different mechanisms are at play in driving the observed C IV blueshift compared to quasars at $1.5 < z_{sys} < 4.0$. This is now becoming possible with the launch of the JWST which will enable lower mass, lower accretion rate quasars to be found in the very early Universe, as well as robustly measuring black hole masses and accretion rates for known $z_{sys} > 6$ quasars using Balmer lines, which suffer considerably less from systematic biases.

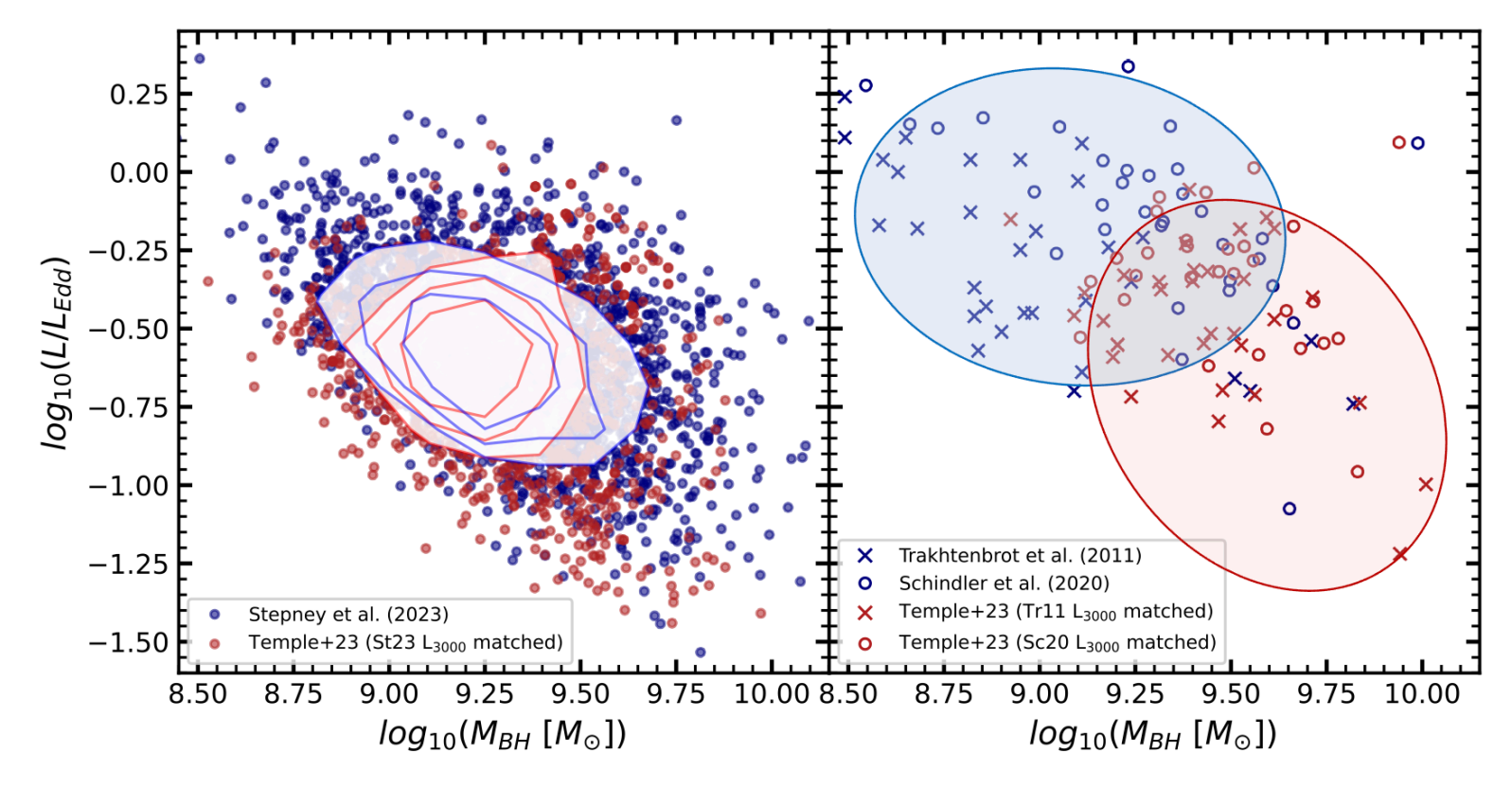


FIGURE 3.12: The M_{BH} - L/L_{Edd} plane for the $3.5 < z_{sys} < 4.0$ and corresponding UV luminosity matched $1.5 < z_{sys} < 2.65$ samples (left) and the $z_{sys} \sim 6$ and corresponding UV luminosity matched $1.5 < z_{sys} < 2.65$ samples (right). Density contours (left) encircle 68, 50 and 25 per cent of the sample, respectively. The cartoon ellipses (right) approximate the locations of the $z_{sys} \sim 6$ quasars (blue) and the $1.5 < z_{sys} < 2.65$ quasars, when UV luminosity matched to the $z_{sys} \sim 6$ sample (red). When UV luminosity matching the $3.5 < z_{sys} < 4.0$ sample to the $1.5 < z_{sys} < 2.65$ quasars, the samples are consistent in the M_{BH} - L/L_{Edd} plane, explaining the results presented in Fig. 3.2 and Fig. 3.3. When UV luminosity matching the $z_{sys} \sim 6$ sample to the $1.5 < z_{sys} < 2.65$ quasars, we see an inconsistency between the samples in the M_{BH} - L/L_{Edd} plane, with the $z_{sys} \sim 6$ objects biased towards higher L/L_{Edd} and lower M_{BH} than their $1.5 < z_{sys} < 2.65$ counterparts.

3.5 Conclusions

We have analysed the rest-frame UV spectra of 2,531 3.5 $< z_{sys} < 4.0$ quasars from the SDSS DR16Q catalogue and studied the evolution of the rest-frame UV properties of quasars in the redshift range $1.5 < z_{sys} < 4.0$.

- Using the MFICA reconstructions, we recover the same trends in C IV EW and C IV blueshift as those reported at $1.5 < z_{sys} < 2.65$. We find that there is no evidence for evolution in the C IV blueshifts and EWs between $1.5 < z_{sys} < 2.65$ and $3.5 < z_{sys} < 4.0$ when matching the quasars in either UV continuum luminosity, L₃₀₀₀, or *both* SMBH mass and Eddington-scaled accretion rate.
- The use of MFICA enables us to reconstruct the He II emission line profile even in modest signal-to-noise spectra. We recover the well-known correlation between the He II and C IV EWs as well as an anti-correlation between the He II EW and C IV blueshift. Under the assumption that the C IV blueshift traces broad line region outflows, we conclude that the quasar SED and more specifically the ionising flux above 54eV is a key determinant of the ability to launch outflows. Moreover, there is a common SED-dependent mechanism for quasar-driven outflows at play in quasars over the entire redshift range $1.5 < z_{sys} < 4.0$.
- We examine how the rest-frame UV line properties depend on fundamental properties of the quasars namely L_{3000} , M_{BH} and L/L_{Edd} . The $3.5 < z_{sys} < 4.0$ quasars are more luminous than the $1.5 < z_{sys} < 2.65$ quasars but show the same trends in their emission line properties with SMBH mass and Eddington-accretion rate as their lower redshift counterparts. As reported by Temple *et al.* (2023), significant C IV blueshift measurements require *both* $L/L_{Edd} \ge 0.2$ and $M_{BH} \ge 10^9 M_{\odot}$. Likewise, when $L/L_{Edd} \ge 0.2$, we observe a clear evolution in the He II EW, with higher SMBH mass objects presenting both weaker He II emission and larger C IV blueshifts.
- We explicitly show that matching quasars at $3.5 < z_{sys} < 4.0$ to those at $1.5 < z_{sys} < 2.65$ based on their UV continuum luminosity, ensures a consistent mapping of quasars in both redshift bins on to the M_{BH} L/L_{Edd} plane. However, when considering the much smaller sample of quasars at $z_{sys} \sim 5-7$ where UV-emission line properties have been measured, the UV-luminosity matched $1.5 < z_{sys} < 2.65$ samples are biased to higher SMBH mass and lower Eddington-scaled accretion rates than observed at the highest redshifts. If SMBH mass and Eddington-scaled accretion rate are indeed the fundamental parameters driving the C IV blueshift, this might at least partially explain the observed evolution of C IV blueshift seen in the highest redshift quasars. We therefore conclude that matching quasar samples in different redshift bins using

3.5. Conclusions 71

the UV continuum luminosity is only viable when one can also achieve a reasonable match in *both* the SMBH mass and Eddington-scaled accretion rate.

• We hypothesise a number of explanations for the inconsistent distributions in the M_{BH} - L/L_{Edd} plane between $1.5 < z_{sys} < 4.0$ and $z_{sys} \sim 5-7$. Farina *et al.* (2022) find that quasars at $z_{sys} \gtrsim 6$ have a tendency towards higher Eddington-scaled accretion rates and lower SMBH masses than their $1.5 < z_{sys} < 2.65$ UV luminosity-matched counterparts. Interestingly, if the relationship between the He II EW and the M_{BH} - L/L_{Edd} plane persists to $z_{sys} \sim 5-7$, we would expect objects with higher Eddington-scaled accretion rates and lower SMBH masses to exhibit weaker C IV blueshifts. This trend is contrary to the observations at $z_{sys} \gtrsim 6$, for which we suggest two possible explanations. One possibility is that the relationships between the M_{BH} , L/L_{Edd} and the UV emission line properties, at $1.5 < z_{sys} < 4.0$, do not hold at higher redshifts where the Eddington ratios appear higher, and hence the mechanisms driving outflows at $z_{sys} \gtrsim 6$ are intrinsically different. Alternatively, the different line-fitting methodologies used to analyse the quasar samples at $z_{sys} \gtrsim 6$ may prevent a direct comparison to the UV emission line properties at more modest redshifts.

Chapter 4

An in-depth view of a red quasar at cosmic noon.

"It was big, it was red, it was beautiful..."

The Adventures Of Ichabod And Mr. Toad

This Chapter is based on the article:

All work presented in this Chapter is my own, completed with guidance and support from my co-authors, unless otherwise stated.

[&]quot;A big red dot: scattered light, host galaxy signatures, and multiphase gas flows in a luminous, heavily reddened quasar at cosmic noon", Matthew Stepney, Manda Banerji, Shenli Tang, Paul C. Hewett et al., 2024, MNRAS, Volume 533, Issue 3, August 2024, Pages 5497-5513

4.1 Introduction

In Chapter 1, we discussed how feedback processes are pivotal to explaining a multitude of observables, such as the $M-\sigma$ relation, the shape of the galaxy luminosity function and the observed morphologies and colours of present-day galaxies (e.g. Magorrian *et al.*, 1998; Cole *et al.*, 2001; Dubois *et al.*, 2016). Moreover, red quasars, which show dust extinction affecting the quasar UV continuum, represent a unique opportunity to study AGN feedback, given that they correspond to a short-lived "blow-out" phase in massive galaxy formation (Urrutia *et al.*, 2008; Banerji *et al.*, 2012, 2015; Glikman *et al.*, 2012, 2015; Assef *et al.*, 2015; Calistro Rivera *et al.*, 2021).

A variety of different methods have been used to select red quasars with varying levels of extinction including optical (e.g. Klindt et al., 2019; Fawcett et al., 2020), near infra-red (e.g. Glikman et al., 2012; Banerji et al., 2015) and mid infra-red (e.g. Eisenhardt et al., 2012; Assef et al., 2015) colour selections. Many red quasars are found to reside in major mergers (e.g. Urrutia et al., 2008; Glikman et al., 2015; Banerji et al., 2021). Powerful feedback signatures have also been detected in several of these populations although it is debated whether these feedback processes are more efficient in the obscured quasar phase relative to the unobscured quasar phase. For example, extreme broad line region (BLR) and narrow line region (NLR) outflows have been reported among populations of Extremely Red Quasars (ERQs; Hamann et al. 2017; Perrotta et al. 2019; Gillette et al. 2024), with their kinetic power exceeding that of blue quasars at comparable luminosities (Zakamska et al., 2016; Perrotta et al., 2019). The correlation between dust extinction and radio emission in the mildly obscured red quasars in SDSS and the even redder quasars in DESI have been interpreted as evidence for low-power radio jets or winds causing shocks in a dusty environment (Fawcett et al., 2023). On the other hand some studies have found very similar ionised gas outflow properties between red and blue quasars when the two samples are matched in luminosity and redshift (e.g. Temple et al., 2019; Fawcett et al., 2022). Spatially resolved observations of multi-phase outflows in red quasars are also now starting to uncover the complex gas dynamics in these systems (e.g. Wylezalek et al. 2022; Veilleux et al. 2023).

Ground-based surveys of the most luminous obscured quasars at $z \sim 1-4$ suggest they could dominate the number densities at the highest intrinsic luminosities implying that this population of previously unstudied AGN may account for some of the most luminous and massive accreting black holes at cosmic noon (Assef *et al.*, 2015; Banerji *et al.*, 2015). More recently an abundant population of Little Red Dots (LRDs) observed with *JWST* has emerged, many of which are postulated to be obscured AGN, hundreds of times more common than UV-bright AGN at the faint end of the luminosity function (Onoue *et al.*, 2023; Kocevski *et al.*, 2023; Kocevski *et al.*,

4.1. Introduction 75

2024; Greene *et al.*, 2024). Therefore the obscured phase of supermassive black hole growth also appears to be increasingly important at lower luminosities, and in the high-redshift Universe.

Intriguingly, despite their red colour selection, several of the red quasar populations appear to show excess emission at rest-frame UV wavelengths that is inconsistent with an AGN SED affected by dust extinction (e.g. Assef et al., 2015; Wethers et al., 2018; Noboriguchi et al., 2019; Assef et al., 2020, 2022; Kocevski et al., 2023; Greene et al., 2024; Williams et al., 2024; Pérez-González et al., 2024; Matthee et al., 2024; Kocevski et al., 2024). In the population of Hot Dust Obscured Galaxies (HotDOGs) polarisation studies attribute the UV excess to a scattered light component from the heavily cocooned AGN (Assef et al., 2020). In ERQs, the extreme column densities $(N_H \gtrsim 10^{24} \, cm^{-1})$ reported are suggestive of a dense circumnuclear gas cloud suppressing the accretion disk emission (Goulding et al., 2018). Spectropolarimetry studies of this population also suggest scattering from equatorial dusty disk-winds as the primary cause of their UV emission (Alexandroff et al., 2018). Furthermore, ~ 20 per cent of the broad-line AGN recently observed with JWST are both obscured and feature relatively blue colours in the rest-frame UV, with many more unconfirmed AGN candidates demonstrating similar photometry (Kocevski et al., 2023; Matthee et al., 2024; Greene et al., 2024; Kocevski et al., 2024). The broadband UV excess can be explained by a scattered light component or emission from unobscured star-forming regions in the AGN host galaxy (Greene et al., 2024) and spectroscopic observations would help to discriminate between these scenarios.

In this chapter we study the heavily reddened quasar ULASJ2315+0143, at $z\sim$ 2.56. Heavily reddened quasars (HRQs) are one class of red quasars selected based on their red near infra-red colours. Over 60 HRQs have been selected using near and mid-infrared colour selections using data from the UKIDSS, VISTA and WISE surveys (Banerji et al., 2012, 2013, 2015; Temple et al., 2019). They cover a redshift range $0.7 \lesssim z \lesssim 2.7$ and have measured dust extinctions of $0.5 \lesssim E(B-V) \lesssim 3.0$. In the X-ray, HRQs are amongst the most powerful quasars known, with a median $\langle L_{2-10kev} \rangle = 10^{45.1} \, erg \, s^{-1}$ (Lansbury et al., 2020). As expected from the heavy attenuation observed in the rest-frame optical, HRQs have large gas column densities $N_H \sim 10^{22-23} \, cm^{-2}$, suggestive of a blow-out phase given their high Eddington-scaled accretion rates (Lansbury et al., 2020). Atacama Large Millimeter/submillimeter Array (ALMA) observations have revealed diverse gas fractions, gas morphologies and ISM properties in HRQs (Banerji et al., 2017, 2018, 2021). Finally, deep broad-band optical photometry of a sub-sample of 17 HRQs reveals that at least 10 feature blue colours in the rest-frame UV inconsistent with the dust-reddened quasar SED in the rest-frame optical. The UV-excess potentially originates from relatively unobscured star-forming host galaxies with average $SFR_{UV} = 130 \pm 95 M_{\odot} yr^{-1}$ (Wethers et al., 2018). However, spectroscopic data in the rest-frame UV is required to confirm this hypothesis.

We selected ULASJ2315+0143 for follow-up with X-Shooter due to its detection at rest-frame UV wavelengths across multiple bands in the HyperSuprimeCam (HSC) survey as well as the rich array of multi-wavelength observations already assembled for this source. X-ray data suggests that the inner regions of ULASJ2315+0143 are dominated by a powerful accreting SMBH ($L_{2-10 \, keV} = 3 \times 10^{45} \, erg \, s^{-1}$) with moderately high gas column densities ($N_H \sim 10^{22} \, cm^{-2}$), making it the ideal candidate for studying radiation-driven winds (Lansbury et al., 2020). At longer wavelengths, ULASJ2315 +0143 has been confirmed to be undergoing a gas-rich major merger via ALMA observations of the warm molecular gas as traced by CO(3-2) (Banerji et al., 2021). Further CO(1-0) observations from the Very Large Array (VLA) confirm that the merging galaxies reside within an extended reservoir of cold molecular gas, spatially offset from the merging pair and redshifted with respect to the CO(3-2) observations (Banerji et al., 2018). In addition, ALMA observations of the dust continuum suggest a total star formation rate of $\sim 680\,M_\odot\,yr^{-1}$, consistent with a merger-induced starburst. In the rest-frame optical, ULASJ2315+0143 is amongst the reddest of the HRQ sample and hence exhibits the most unambiguous evidence of excess rest-frame UV emission (Wethers et al., 2018). Owing to its broad wavelength coverage, the analysis of the X-Shooter spectrum will enable the detailed study of ULASJ2315+0143 across the entire rest-frame UV to optical wavelength region, leading to a better understanding of the UV excess emission and probing key diagnostic emission and absorption features that enable the study of multi-phase and multi-scale winds.

This chapter is organised as follows: Section 4.2 details the observations and reduction of the X-Shooter spectrum. In Section 4.3 we model the spectral energy distribution and analyse the emission and absorption line properties. We discuss our results in Section 4.4 in the context of other red AGN populations. Our conclusions are presented in Section 4.5.

4.2 Spectral Observations & Data Reduction

We observed ULASJ2315+0143 (RA=348.9842, Dec=1.7307) with the X-Shooter spectrograph on the Very Large Telescope (VLT). X-Shooter is an Echelle spectrograph installed on the UT2 telescope at the VLT (Vernet *et al.*, 2011). It is comprised of three arms; the Ultra-Violet/Blue (UVB), the Visible (VIS) and the near-infrared (NIR). The combined wavelength coverage of X-Shooter ranges from \sim 3100-24000Å, enabling the study of both the rest-frame UV and rest-frame optical emission of ULASJ2315+0143 at $z\sim2.5$. The spectra were obtained using a 2x2 binning to minimise read-out noise. Slit widths were set to 1.3 arc-seconds for the UVB and 1.2 arc-seconds for both the VIS and NIR arms, yielding a spectral resolution R=4100, 6500, 4300, for the UVB, VIS and NIR arms, respectively. The target was observed for \sim 9 hours based on its broadband SED (Wethers *et al.*, 2018) and to ensure sufficient signal-to-noise ratio

TABLE 4.1: We present the various PypeIt user-level parameters used to optimise the reduction and extraction of the ULASJ2315+0143 X-Shooter spectrum. The numerous additional parameters, which do not feature in this table, were left at their default settings.

UVB/VIS		
Primary block	Secondary Block	Parameter
reduce	findobj	snr_thresh = 3.0
reduce	findobj	ech_find_max_snr = 1.0
reduce	findobj	ech_find_min_snr = 0.1
reduce	findobj	ech_find_nabove_min_snr = 2.0
calibrations	wavelengths	rms_threshold = 2.0
calibrations	tilts	sig_neigh = 5.0
calibrations	tilts	tracethresh = 5.0
calibrations	slitedges	tracethresh = 7.0
NIR		
Primary block	Secondary Block	Parameter
reduce	N/A	trim_edge = 1,1
reduce	findobj	find_trim_edge = 1,1
reduce	findobj	snr_thresh = 5.0
reduce	findobj	ech_find_max_snr = 1.0
reduce	findobj	ech_find_min_snr = 0.1
reduce	findobj	ech_find_nabove_min_snr = 2.0
reduce	skysub	no_local_sky = True
reduce	skysub	global_sky_std = False
reduce	extraction	use_2dmodel_mask = False
calibrations	wavelengths	rms_threshold = 1.1
calibrations	tilts	sig_neigh = 5.0
calibrations	tilts	tracethresh = 5.0
calibrations	slitedges	tracethresh = 7.0

(S/N) across the entire wavelength range covered by X-Shooter. To aid scheduling, these observations were split into roughly one hour long observing blocks and a standard ABBA nodding pattern was adopted for the purposes of sky subtraction in the NIR arm.

We employ PypeIt v1.14.0¹, a Python package for semi-automated reduction of astronomical slit-based spectroscopy (Prochaska *et al.*, 2020; Prochaska *et al.*, 2020), for the spectral reduction. Some user-level parameters had to be adjusted from their default values and these are detailed in Table 4.1. Wavelength calibrations in the X-Shooter UVB/VIS arms were conducted by matching arc lines from Thorium-Argon (ThAr) lamps to the inbuilt ThAr arc line catalogue stored within PypeIt. For the NIR arm, wavelength calibrations were conducted using the OH sky line transitions from the spectrum itself. Pypeit's extraction algorithm is based on Horne (1986). A third order polynomial fit is attempted across all orders in a given exposure. Echelle objects are retained if the S/N of the trace exceeds a certain threshold value in all orders, or if

¹https://github.com/pypeit/PypeIt/tree/1.14.0

the S/N of the trace exceeds the minimum S/N threshold over a user-defined number of orders (See Table 4.1 for details). The standard star trace is used as a crutch for the polynomial fit for those orders that do not exceed the minimum S/N requirement.

The relative flux calibration was conducted within PypeIt. The spectrum was then normalised to the cModel magnitudes of the quasar from Hyper Suprime-Cam (HSC) in the g, i and z bands and the United Kingdom Infrared Deep Sky Survey (UKIDSS) magnitudes in the H and K-bands (Banerji et al., 2015) using Eqn. 1.11². Hence, we renormalise the UVB, VIS and NIR spectra of ULASJ2315+0143 by a multiplicative factor of 0.44, 2.17 and 0.22, respectively. Calibration to the Dark Energy Camera photometry for this source yields $\Delta g = 0.06 \, mag$ (Wethers et al., 2018), hence we estimate a \sim 6% uncertainty in the flux calibration.

Figure 4.1 depicts the full flux calibrated 1D X-Shooter spectrum of ULASJ2315+0143 , as well as the corresponding noise spectrum. As expected from the red NIR colour of ULASJ2315+0143 ((H-K)>1.4; Banerji *et al.* 2015), the NIR spectral shape (middle/bottom; Fig. 4.1) is consistent with significant dust attenuation toward the quasar continuum. To calculate the continuum signal-to-noise (S/N_{cont}) in each arm of the spectrograph, we use Eqn. 4.1.

$$S/N_{cont} = S/N \times \frac{pix}{\lambda} \tag{4.1}$$

where S/N is the median signal to noise in a given continuum interval, pix is the number of pixels in said interval, and λ is the corresponding wavelength coverage. The median continuum S/N in the intervals [16000,17000]Å and [21000, 22000]Å are $\sim 13 \text{Å}^{-1}$ and $\sim 12 \text{Å}^{-1}$, respectively. We observe narrow emission lines, including $[OII] \lambda\lambda 3726, 3729$ and $[OIII] \lambda\lambda 4960, 5008$ in the NIR spectrum. However, there is no discernible signal from either [Ne III] $\lambda 3869$ or [Ne V] $\lambda 3426$. We see several broad Balmer lines in the NIR, including the H γ λ 4342, H β λ 4863 and H α λ 6565 emission. The median continuum S/N in the interval [6000,10000]Å is $\sim 1 \text{Å}^{-1}$ (top/right; Fig. 4.1). When rebinned by a factor of ten, the median continuum S/N \sim 0.2Å $^{-1}$ - i.e. the S/N increased by less than the binning factor and hence the flux in this region is dominated by noise. The median continuum S/N in the interval [4600,4900]Å (top/left; Fig. 4.1) is $\sim 15 \text{Å}^{-1}$. The rest-UV emission is inconsistent with the attenuation observed at redder wavelengths. We see broad Lyα, N V and C IV emission features on a blue UV continuum. We also observe a strong narrow component to the Ly α emission as well as absorption around the Ly α and C IV emission line profiles. These spectral features are fully explored in Section 4.3.3.

 $^{^2}$ We use CTIAO's ANDICAM transmission curves for the g, i and z bands and UKIRT's UKIDSS transmission curves for the H and K bands, available via the SVO Filter Profile Service (Rodrigo et al., 2012; Rodrigo & Solano, 2020).

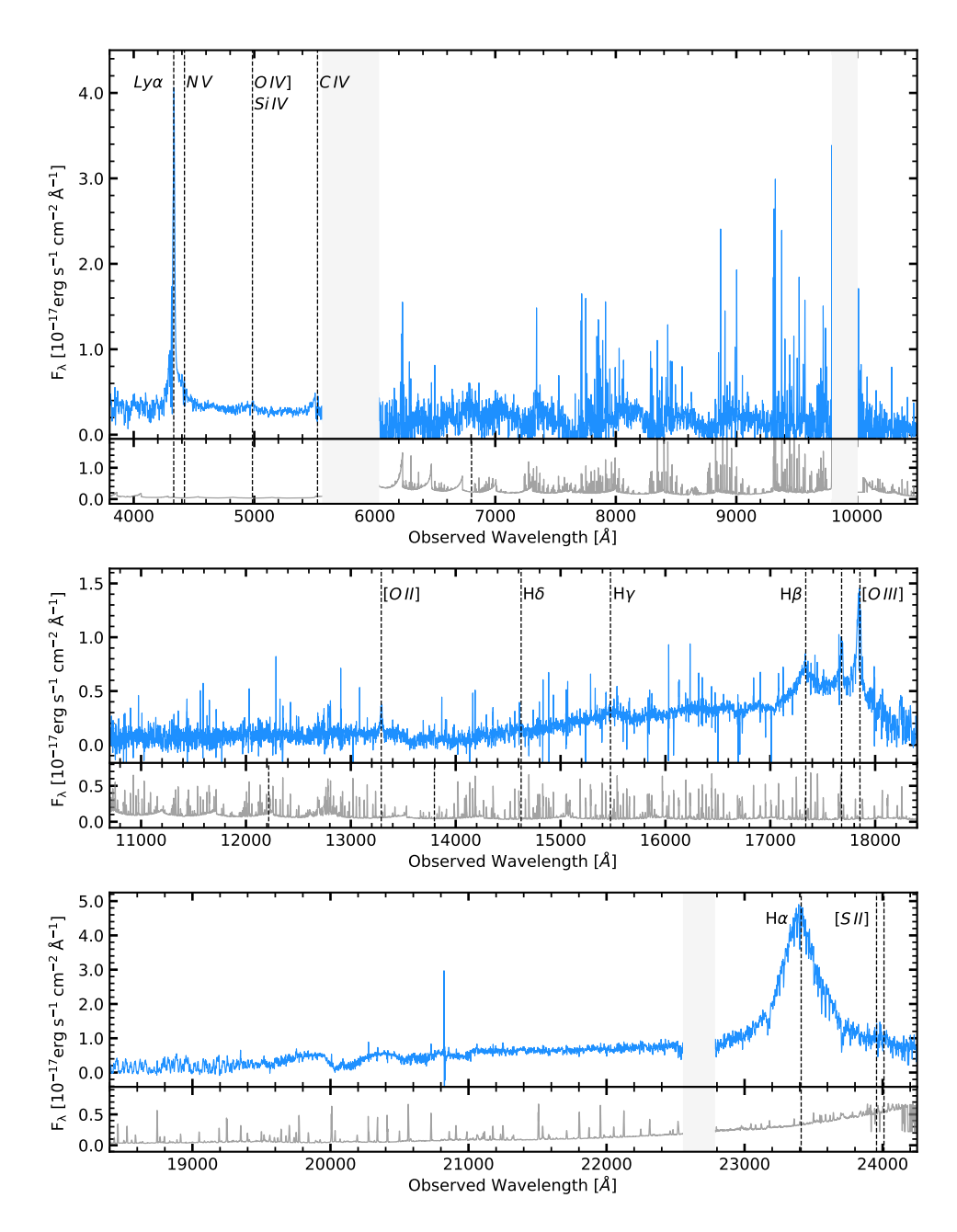


FIGURE 4.1: The full flux calibrated 1D spectrum of ULASJ2315+0143 is presented in the top panels of each exert (blue). In addition, the corresponding noise spectrum is presented in the lower panels (grey). Noise spikes marking the transition between arms at $\sim 5800 \mbox{\normalfont\AA}$ and $\sim 10,000 \mbox{\normalfont\^{A}}$ have been masked out, as too has a region of high noise redward of the H\$\alpha\$ emission. Prominent emission lines are marked by dashed vertical black lines and labelled accordingly.

4.3 Results

4.3.1 Rest-frame UV Image Decomposition

Section 4.3.1 details analysis conducted in collaboration with Dr. Shenli Tang.

We begin by conducting image decomposition analysis to better understand the source of the rest-frame UV emission in ULASJ2315+0143. We consider the morphology of this emission as traced by the imaging data from HSC in the *g*-band. We follow the work of Silverman *et al.* (2020) and Tang *et al.* (2021) to perform a 2D image decomposition analysis on the HSC *g*-band image of ULASJ2315+0143, which covers 4000-5500Å in the observed frame (Kawanomoto *et al.*, 2018). We apply the tool GALIGHT (Galaxy shapes of Light Ding *et al.*, 2022), which was developed based on the image modelling capabilities of LENSTRONOMY (Birrer *et al.*, 2021). The tool accepts a preset of number of point sources to be used in fitting. We tested three cases: (i) no point source (i.e. no AGN contribution to the rest-frame UV), (ii) one point source (i.e. a single quasar contribution to the rest-frame UV). As a result, the algorithm failed to find a secondary point source in the third case, and favoured at most one point source in the region.

The algorithm then finds as many extended sources as necessary in the field, and fits them with Sérsic profiles simultaneously with the point sources. We show the results in Fig. 4.2, with the first row showing the case of no point source and the second row showing the model for one point source. For the model with one point source, we also show the image after subtracting the point source model from the data (second row, second column). The third column shows the normalised residual of the fitting. The final column shows the 1D annulus light profiles from the centre of the source to the outer regions. The reconstructed models are shown by the blue curves, in comparison with the data, shown by the open circles. The bottom sub-panels show the fractional residuals in 1D.

We find that the light profile of this system can either be explained by one point-spread function (PSF) and four Sérsic profiles or just four Sérsic profiles. We also compared the reduced χ^2 of the two fits, which are 1.09 for the model without a point source, and 1.04 for the model with a point source. We therefore conclude that the rest-frame UV morphology of this source can be equally well reconstructed with and without a PSF contribution to the *g*-band. We are therefore motivated to explore spectral energy distribution (SED) models that exploit both star-forming host galaxy emission or blue quasar emission.

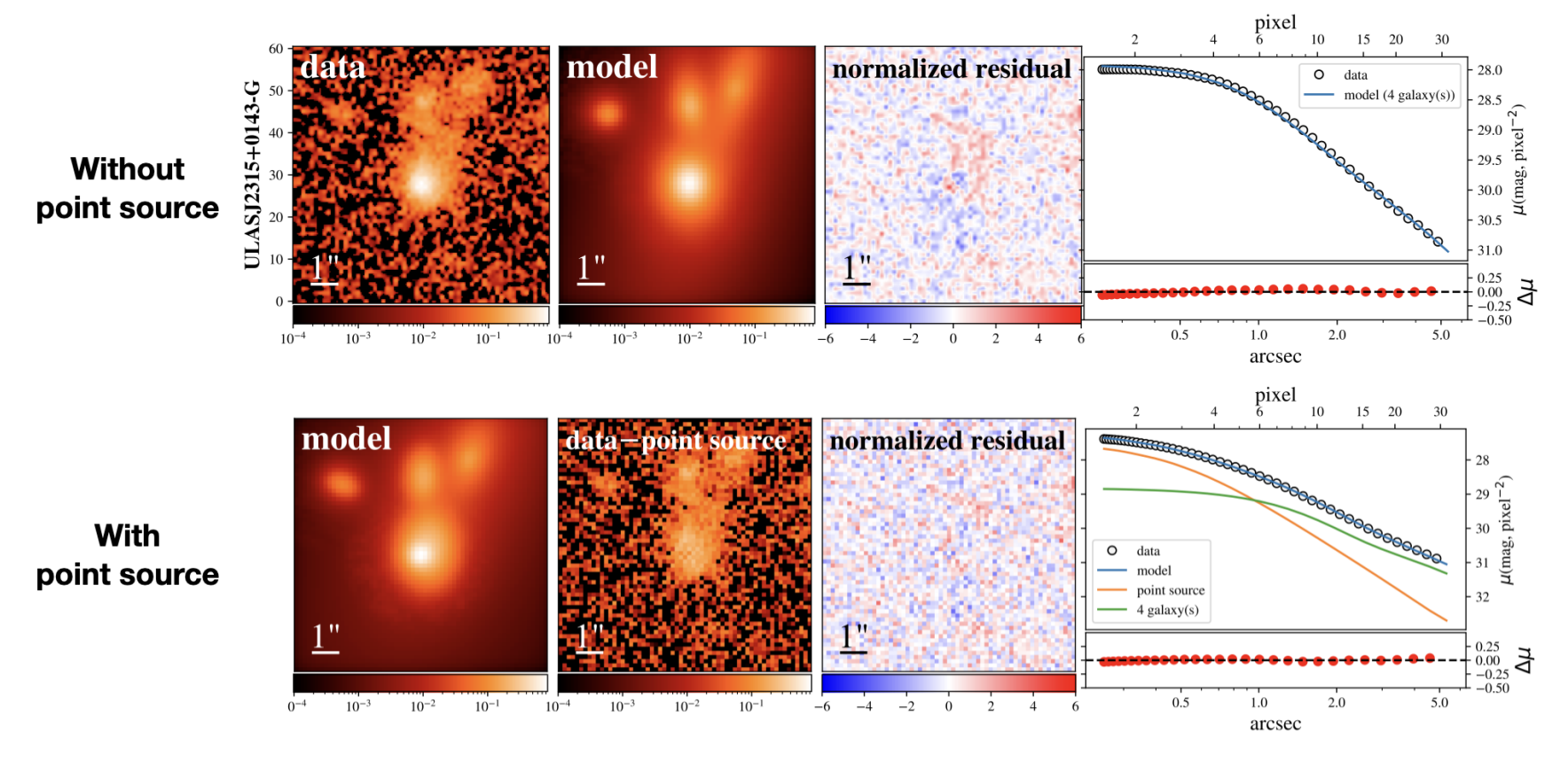


FIGURE 4.2: GALIGHT fitting results on the HSC *g* band image of ULASJ2315+0143. The first row shows the case when use a model incorporating only the Sérsic profiles. The second row shows the case when we include one point source in the model. The reconstructed images are shown by the second and first panel of the rows, respectively. In the second panel of second row, we also show the image after subtracting the point source model from the data. The third column shows the 2D normalised residual map of the fitting. The final column shows the 1D annulus light profiles for the data and the reconstructed model, with the fractional residual shown in the bottom sub-panel.

4.3.2 Spectral energy distribution

In this section we explore the rest-frame UV to optical SED of ULASJ2315+0143. As noted from Fig. 4.1, the spectral shape is inconsistent with a single reddened quasar SED with excess blue flux detected in the UVB arm relative to this SED. Motivated by Fig. 4.2, we explore two distinct possibilities to explain the excess UVB flux - (i) a blue quasar component either originating from leaked/scattered light or a secondary AGN and (ii) a star-forming host galaxy. We model the quasar components using the QSOGEN³ tool, a Python package that implements an empirically-motivated parametric model to simulate quasar colours, magnitudes and SEDs (Temple *et al.*, 2021b). The host galaxy component is modelled using the BAGPIPES⁴ package. Model fits were conducted using a Bayesian Markov-Chain Monte-Carlo (MCMC) method. We again utilise EMCEE, a Python package⁵ that explores the likelihood space using the affine-invariant ensemble sampler proposed by Goodman & Weare (2010).

4.3.2.1 Reddened quasar + blue quasar light

The first model explored is the combination of a reddened quasar SED with some blue AGN component representing a fraction of the total quasar luminosity leaked/scattered along our line of sight or a less luminous secondary AGN. The free parameters are the luminosity of the primary quasar, $\log_{10}{\{\lambda L_{\lambda}(3000 \text{ Å})[erg\ s^{-1}]\}}$, the dust reddening of the primary quasar, $E(B-V)^{QSO}$ and the fraction of the total intrinsic SED of the primary quasar emitted in the rest-frame UV, f_{UV} . QSOGEN also allows flexibility in the emission line contributions to the quasar SED via the emline_type parameter, which essentially controls the equivalent widths of the key quasar emission lines (Temple et al., 2021b). Hence, we also set the emline_type as a free parameter in the fit. The model includes no contribution from the quasar host galaxy to the SED. The quasar extinction law assumed by QSOGEN is discussed in Section 2.6 of Temple et al. (2021b) and is similar to those derived by Czerny et al. (2004) and Gallerani et al. (2010). We permit the EMCEE package to explore an N-dimensional Gaussian likelihood function, where N represents the number of free parameters in the fit (N=4), and apply uniform priors. Regions significantly affected by telluric absorption are excluded from the SED fit. The best-fit SED is presented in Fig. 4.3 overlaid on the X-Shooter spectrum.

³https://github.com/MJTemple/qsogen

⁴https://github.com/ACCarnall/bagpipes

⁵https://github.com/dfm/emcee

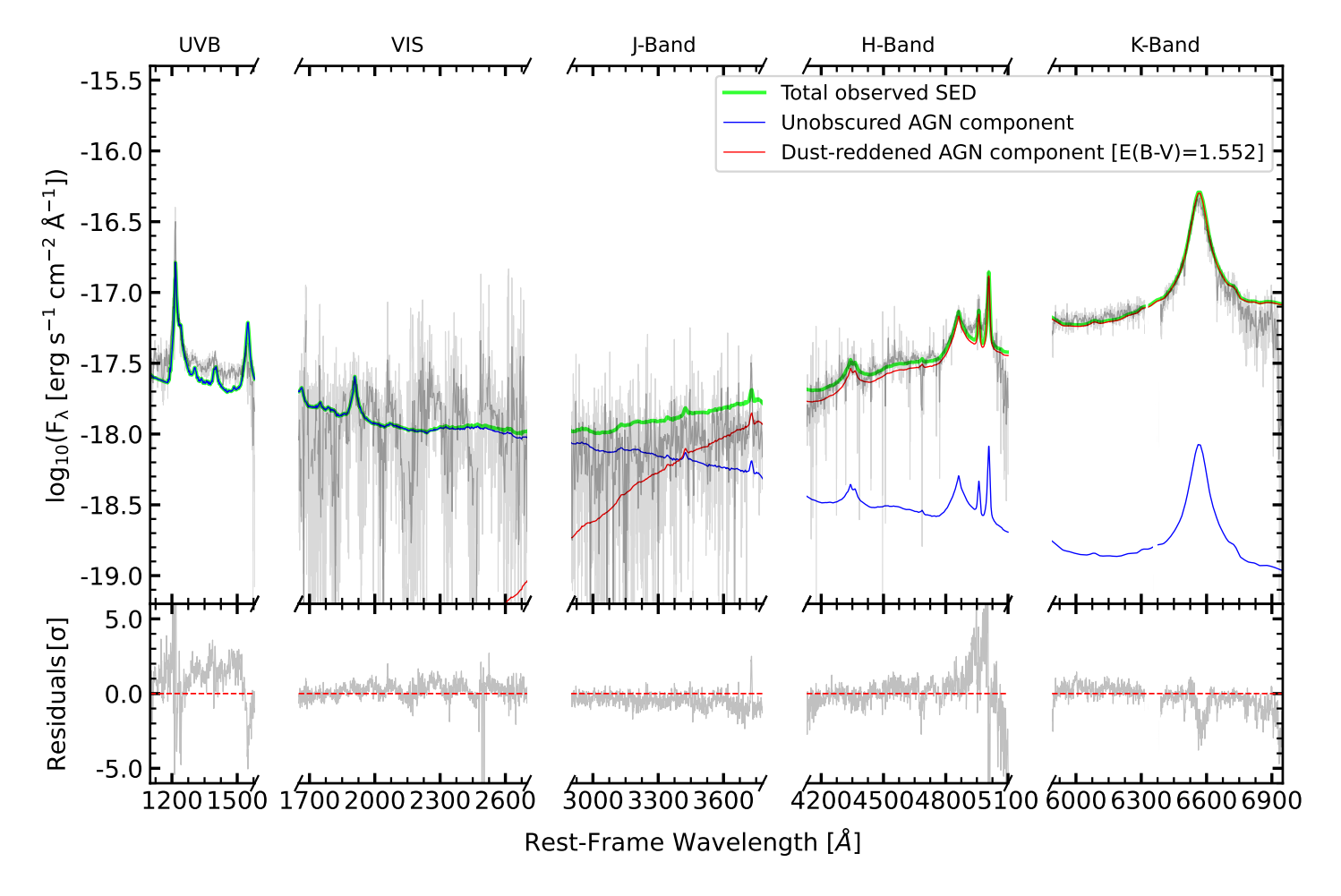


FIGURE 4.3: We present the spectrum of ULASJ2315+0143 in light grey with the 20-pixel rebinned spectrum overlaid in dark grey. Our best-fit SED model is plotted in green. The unobscured AGN component is presented in blue, while the dust-reddened AGN component is presented in red. Regions of high telluric absorption have been masked to aid readership. The bottom panel illustrates the model residuals.

Parameter	Best-Fitting Value	
emline_type	1.71 ± 0.01	
$E(B-V)^{QSO}$ [mag]	1.552 ± 0.002	
$\log_{10}\{\lambda L_{\lambda}(3000\text{Å})[erg\ s^{-1}]\}$	47.907 ± 0.003	
fray	$0.0450 \pm 0.0003\%$	

TABLE 4.2: Best-fit QSOGEN parameters for the SED fit shown in Fig. 4.3. Uncertainties represent the MCMC uncertainties.

The model is able to successfully reproduce the spectrum redward of \sim 4200Å as well as the the broad shape of the SED blueward of 1600Å. However in the interval [2900,3800]Å the continuum is overestimated. The best-fit parameters of this model are presented in Table 4.2 and Fig. 4.4, the quoted uncertainties represent the Monte-Carlo uncertainties on the free parameters and hence do not account for the uncertainties associated with the flux calibration. The reddening of the quasar is estimated to be $E(B-V)^{QSO}=1.552\pm0.002$, which is consistent with the results from SED-fitting to the broadband photometry conducted by Wethers *et al.* (2018). The dust-corrected optical luminosity is estimated to be $\log_{10}\{\lambda L_{\lambda}(3000\text{Å})[erg\ s^{-1}]\}=47.907\pm0.003$. Only 0.0450 ± 0.0003 per cent of this intrinsic quasar luminosity is required to be scattered or leaked into our line-of sight to reproduce the UVB flux. This is a much smaller fraction than is reported in other

obscured AGN populations at similar redshifts e.g. (~1-3 per cent in HotDOGs; Assef

et al., 2020). We will discuss these results further in Section 4.4.1.

The marginalised distributions presented in Fig. 4.4 show that each parameter is well converged, however, there are several model degeneracies. We observe a strong anti-correlation between f_{UV} and both $\log_{10}\{\lambda L_{\lambda}(3000\text{\AA})\}$ and $E(B-V)^{QSO}$ which in turn are positively correlated with each other. This behaviour is expected as should the quasar be more luminous, a lower scattering fraction is required to reproduce the rest-frame UV emission. Equally, should the quasar suffer heavier dust attenuation, we require a more luminous quasar to reproduce the rest-frame optical and hence the scattering fraction must again be lower to compensate for the increase in luminosity. The *emline_type* parameter is independent of the other three model parameters since the Temple *et al.* (2021b) SED model allows for line strength variations independent of the continuum parameters.

The primary weakness of this SED model is that it is unable to reproduce the narrow [O II] emission as well as over-predicting the continuum flux in the interval [2900,3800]Å. Strong [O II] emission in the absence of [Ne III] and [Ne V] could be attributed to ongoing star formation (Maddox, 2018). Despite the need for an AGN component to explain the broad UV emission lines, it is unclear to what extent the AGN is contributing to the continuum.

4.3. Results 85

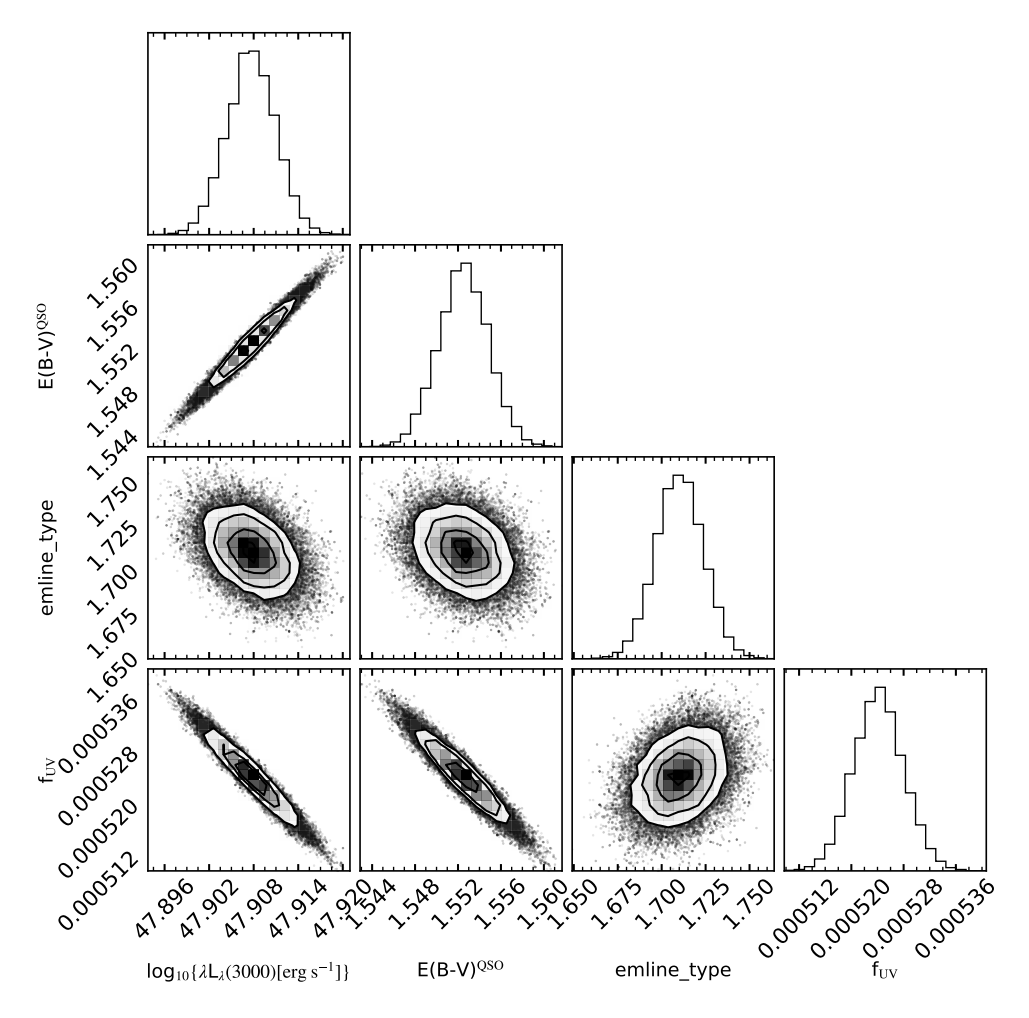


FIGURE 4.4: The reddened quasar + blue quasar light SED model (see Section 4.3.2) corner plots. In order left-to-right/top-to-bottom the marginalised distributions represent $\log_{10}\{\lambda L_{\lambda}(3000\text{\AA})\}$, $E(B-V)^{QSO}$, emline_type and f_{UV} . The corner plot illustrates that the model is well-converged and highlights the degeneracies between several model parameters.

4.3.2.2 Reddened quasar + star-forming host galaxy

The second model explored is then the combination of a star-forming host galaxy and dust reddened quasar SED. We model the host galaxy spectrum using BAGPIPES. We assume a burst-like star formation history (SFH), consistent with the observation of a gas-rich major merger in the ULASJ2315+0143 system (Banerji *et al.*, 2021). Our goal is to find whether a reasonable star-forming galaxy SED model can reproduce the observed UV-continuum shape. Given the dominance of the quasar emission in the rest-frame optical, we do not necessarily expect to obtain robust constraints on the host galaxy properties.

We set the duration of the burst, the stellar mass of the galaxy, $log(M_*/M_{\odot})$, the galaxy dust extinction A_V^{Gal} , the metallicity, $log_{10}(Z/Z_{\odot})$ and ionisation parameter, $log_{10}(U)$ as free parameters in the MCMC simulation. We set flat priors on the

metallicity and ionisation parameter in the range $-2 < log_{10}(Z/Z_{\odot}) < 0.3$ and $-3.5 < log_{10}(U) < -1$. We assume the Calzetti *et al.* (2000) extinction law. Finally, we set Gaussian priors on the optical luminosity of the quasar, quasar emission line type and quasar dust extinction, defining the position and width of the priors by the best-fit values and uncertainties of these parameters from Table 4.2.

The results are presented in Fig. 4.5. We are able to better reproduce the narrow [O II] emission and broad continuum shape in the interval [2900,3800]Å with the inclusion of a star-forming galaxy to the SED model. While the star-forming galaxy component is unable to reproduce the broad emission lines observed blueward of 1600Å, the broad continuum shape at these bluer wavelengths is also well fit by the star-forming galaxy. The best-fit parameters for this SED model are presented in Table 4.3, again the uncertainties presented represent the Monte-Carlo errors only, and do not account for uncertainties in the flux calibration.

Firstly, we note that the quasar dust attenuation and continuum luminosity for this model are consistent with the values predicted by the previous SED model, confirming that the continuum at redder wavelengths is indeed quasar dominated. We do not place particular emphasis on the physical values of the galaxy parameters in the fit given the degeneracies between these parameters. The lack of data straddling the 4000Å break, which falls within the gap between the J and H-bands, prevents us from placing strong constraints on the stellar mass of the host galaxy and the value of the stellar mass from the SED fit should therefore not be interpreted as representing the total stellar mass of the quasar host. The best-fit ionisation parameter of $-log_{10}(U) = 1.001 \pm 0.007$ is high for a star-forming galaxy (Costa *et al.*, 2018), but can almost certainly be explained by some AGN contamination to the emission lines, many of which have broad components. Nevertheless, we can conclude that a star-forming galaxy SED can reproduce the UV continuum shape and narrow emission line features seen in the X-Shooter spectrum.

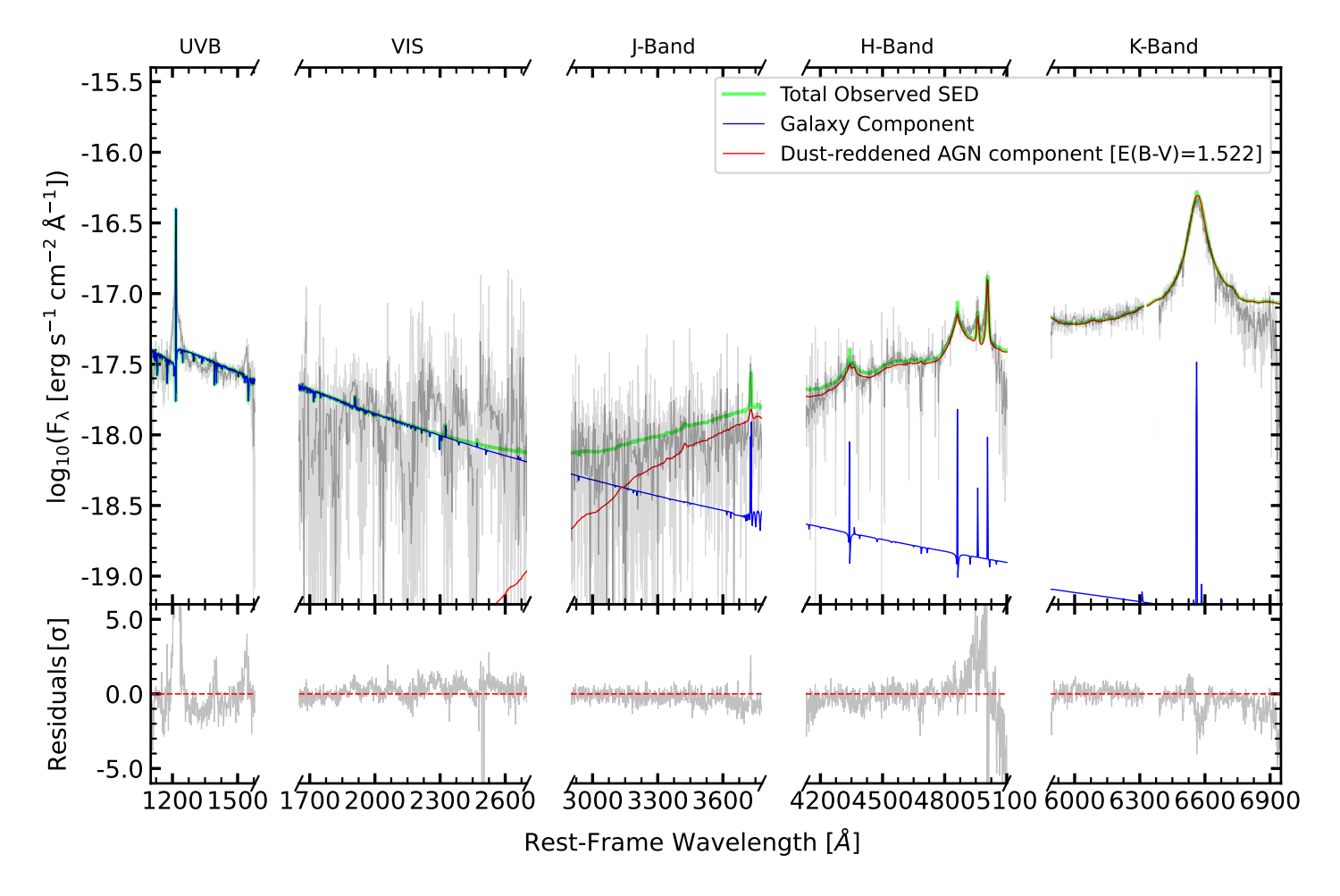


FIGURE 4.5: Same as Fig. 4.3, but instead the rest-frame UV is modelled by a star-forming galaxy, generated using BAGPIPES.

Parameter	Best-Fitting Value	
emline_type	1.24 ± 0.02	
$E(B-V)^{\overline{QSO}}$ [mag]	1.522 ± 0.003	
$\log_{10}\{\lambda L_{\lambda}(3000\mathring{A})[erg\ s^{-1}]\}$	47.901 ± 0.004	
A _V ^{Gal} [mag]	0.41 ± 0.03	
$\log_{10}\left(\mathrm{M_{*}}\ /\ \mathrm{M_{\odot}}\right)$	9.47 ± 0.02	
t _{Burst} [Myrs]	10.4 ± 0.7	
$log_{10}(U)$	$> -1.001 \pm 0.007$	
$log_{10}(Z/Z_{\odot})$	1.70 ± 0.04	

TABLE 4.3: QSOGEN and BAGPIPES user-level parameters for the SED fit shown in Fig. 4.5. Uncertainties represent the MCMC uncertainties.

If we assume that the entire rest-frame UV continuum originates from young stellar populations, we can calculate a maximum SFR for ULASJ2315+0143 using Eqn. 4.2;

$$SFR_{FUV}(M_{\odot} yr^{-1}) = log_{10}(\lambda L_{\lambda}(1550 \, \mathring{A})) + log_{10}(C_{FUV})$$
 (4.2)

where the continuum flux at 1550Å, $\lambda L_{\lambda}(1550 \text{ Å}) = 10^{44.8} erg \, s^{-1}$ and $log_{10}(C_{FUV}) = 43.35$ (Murphy *et al.*, 2011; Hao *et al.*, 2011; Kennicutt & Evans, 2012). Eqn. 4.2 yields $SFR_{FUV} = 88 \, M_{\odot} \, yr^{-1}$, consistent with the SFR estimated for this object using broad-band photometry (130 \pm 95 $M_{\odot} \, yr^{-1}$; Wethers *et al.*, 2018).

4.3.2.3 Reddened quasar + blue quasar light + star-forming host galaxy

Figures 4.3 & 4.5 show that both an AGN SED and a star-forming galaxy SED can reproduce the broad continuum shape of the UVB spectrum. With both strong narrow [O II] in the *J*-band and broad C IV and N V in the UVB arm a model that combines a star-forming host galaxy with a blue quasar component to reproduce the flux seems well motivated. This is also justified by the image decomposition in Fig. 4.2, which suggests that both point-like and extended emission contribute to the rest-frame UV flux of this source.

However, the parameters dictating the nebular emission line strength, such as metallicity, ionisation parameter and age, are degenerate with the stellar mass. A less massive star-forming galaxy with strong nebular emission makes a similar contribution to the total SED as a more massive galaxy with weaker nebular emission. Furthermore, the stellar mass of the galaxy is degenerate with the fraction of the primary quasar contribution to the UV flux, f_{UV} . Consequently, with all three components of the SED, the fit failed to converge tending to the limits set by the priors on the stellar mass, metallicity and ionisation parameter. We therefore did not explore a three component SED model further but conclude that the observed spectrum and

4.3. Results 89

UV image analysis suggests contributions from both a star-forming host galaxy and a blue AGN component in the UV.

4.3.3 Emission and absorption line properties

We now turn our attention to analysing the spectral line properties. We utilise the PyQSOFit package⁶, a python code developed by Guo *et al.* (2018) for all line fits. In all cases uncertainties on line properties are derived by sampling 500 spectra perturbed by Gaussian noise consistent with the noise array and looking at the mean properties and scatter on these properties from the simulated spectra.

4.3.3.1 Systemic redshift and star formation rate from [O II]

We begin with an analysis of the NIR arm, which traces the rest-frame optical emission in this object. We fit the *J*, *H* and *K* band spectra separately so that the continuum fitting is not affected by telluric absorption.

The *J*-band contains the narrow [O II] line. The [O II] doublet is spectrally resolved and provides a good indicator of the systemic redshift. The previous best systemic redshift estimate of ULASJ2315+0143 was calculated using the CO(3–2) emission line from ALMA data, yielding $z_{sys}=2.566$ (Banerji *et al.*, 2021). We fit the [O II] emission doublet without the PyQSOFit iron template, since the wavelength coverage is too restricted to constrain the fit. A set of broad and a set of narrow components, whose widths and velocity offsets are tied, are used to represent the quasar and galaxy emission. We present the results in Fig. 4.6. We estimate a redshift, $z_{sys}=2.5656\pm0.0005$ from [O II] which is entirely consistent with the value derived from the CO(3-2) line and is adopted as the systemic redshift for the remainder of the paper.

We can also estimate a value for the instantaneous, unobscured SFR of any host galaxy component using [O II] emission line luminosity by assuming that the line flux does not have any contributions from the AGN. We note however that even under this assumption, the [O II] line flux can be significantly affected by both dust extinction and metallicity. Since it is unclear to what degree the line is affected by dust extinction relative to the quasar continuum, we estimate lower limits on the [O II] line luminosity and SFR([O II]), assuming E(B-V)=0 towards the star-forming regions in the host galaxy. We calculate the SFR([O II]) with Eqn. 4.3 (Kennicutt, 1998);

$$SFR_{\rm [O\,II]}(M_{\odot}\,yr^{-1}) = (1.4 \pm 0.4) \times 10^{-41} L({\rm [O\,II]})$$
 (4.3)

 $^{^6 {\}tt https://github.com/legolason/PyQSOFit}$

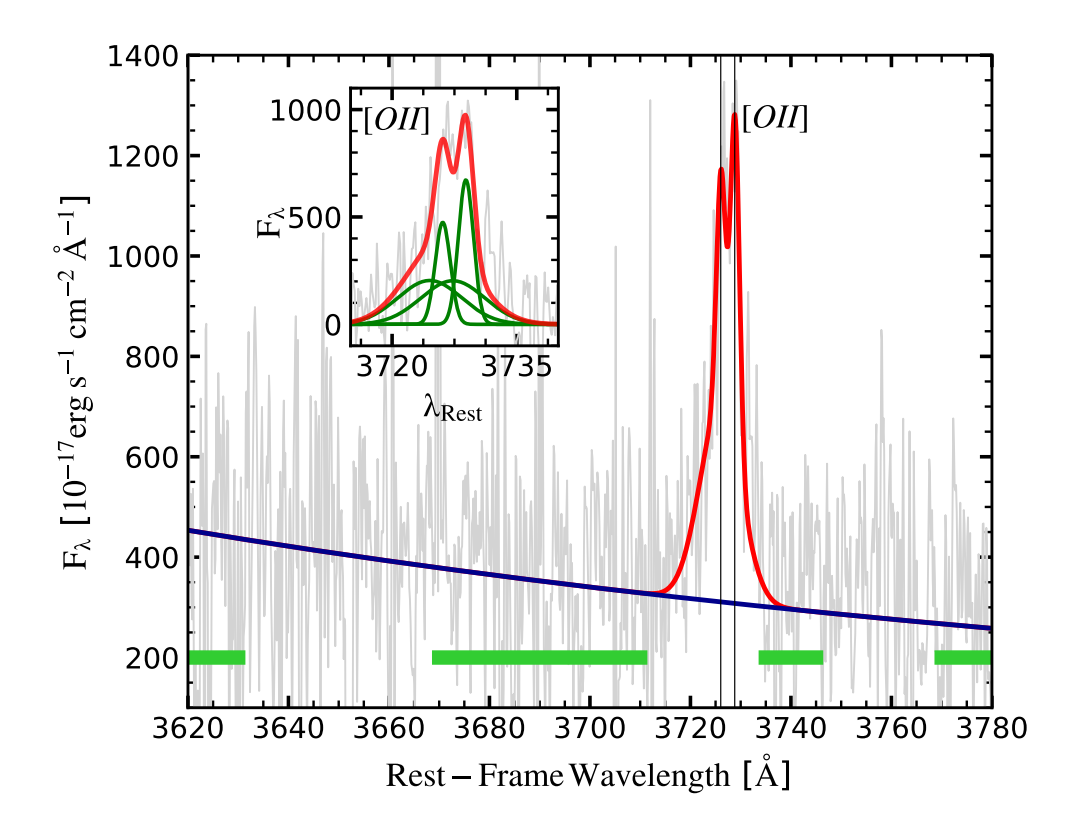


FIGURE 4.6: *J*-Band spectrum for ULASJ2315+0143 with a dust correction, $E(B-V)^{QSO}=1.55$, applied in grey and showing the [O II] doublet. The continuum is presented in navy blue, and the windows over which the continuum was fitted are denoted by the thick, lime-green lines. The final fit of the spectrum is presented in red. The smaller panel shows the continuum subtracted total fit in red. The broad components contributing to the total fit are presented in blue and the narrow components are presented in green.

where the [O II] line luminosity L([O II]) = $10^{42.34\pm0.10}$ erg s⁻¹ for ULASJ2315+0143 . Eqn. 4.3 then yields a SFR_[O II] = 31.1 ± 9.3 $M_{\odot}yr^{-1}$.

4.3.3.2 Black-hole mass, Eddington ratio and narrow-line region outflows

From Section 4.3.2, it is clear that redward of 4200Å the spectrum is dominated by the dust-reddened Type 1 QSO component. For this reason, we apply a dust correction, using the $E(B-V)^{QSO}=1.55$ estimate from Table 4.2 to both the H and K bands before fitting the spectral lines. We model the $H\gamma$ emission with a single broad component. The $H\beta$ emission was modelled by two broad components and an additional narrow component. Both [O III] lines were modelled by a single broad component paired with an additional narrow line contribution whose widths and velocity offsets were tied. In the K-Band, we model $H\alpha$ with two broad components and a single narrow component. Additionally, we model the [S II] $\lambda\lambda6716,6730$ emission doublet with a further two narrow components, whose widths and velocity

4.3. Results 91

offsets are tied. Due to the extreme H α emission strength, we are unable to robustly model the narrow [N II] emission. The results are presented in Fig. 4.7 and Fig. 4.8.

Using these fits, we estimate the equivalent width (EW), full-width half-maximum (FWHM), emission line blueshifts and signal-to-noise ratio for each emission line. Again, we define emission line blueshifts using Eqn. 3.1 and the use of line centroids to define blueshifts reflects the well-known line asymmetries of some emission features such as C IV (Richards *et al.*, 2011; Rankine *et al.*, 2020; Temple *et al.*, 2023; Stepney *et al.*, 2023).

Furthermore, for the [O III] emission, we also calculate the W80=V90-V10, since the [O III] emission line width is often used as an indicator of narrow-line region outflows (e.g. Shen, 2016; Perrotta *et al.*, 2019; Coatman *et al.*, 2019; Temple *et al.*, 2019; Villar Martín *et al.*, 2020). V10 and V90 are calculated using Eqn. 3.1, evaluated at the 10th and 90th percentile of the line flux, respectively. The S/N of the emission lines are estimated by calculating the ratio between the maximum continuum-subtracted flux and the mean noise across the emission line feature. A summary of the quasar emission line properties can be found in Table 4.4.

We observe broad blue wings associated with the [O III] emission in Fig. 4.7, which is reflected in the large line width, W80 = $1830\pm350~{\rm km\,s^{-1}}$. The estimated [O III] line luminosity, L([O III]) = $10^{43.71\pm0.04}~erg~s^{-1}$. Our estimate of L([O III]) is sensitive to dust extinction, hence this value serves as a lower limit assuming E(B-V)=0 since we do not know to what extent the narrow-line region is affected by the attenuation suffered by the quasar continuum. The presence of significant line blueshifts in the [O III] emission is consistent with the high UV/optical continuum luminosity estimated by the SED fitting in Section 4.3.2 and the large L([O III]). The [O II] emission centroid is located at the systemic redshift by definition.

The Balmer lines are very broad as seen in Table 4.4. We calculate the SMBH mass, MBH, of ULASJ2315+0143 from the measured width of the H β emission using the following equation (Vestergaard & Peterson, 2006);

$$log(H\beta, MBH[M_{\odot}]) = log \left\{ \left[\frac{FWHM(H\beta)}{1000 \,\mathrm{km \, s^{-1}}} \right]^{2} \left[\frac{\lambda L_{\lambda}(5100 \,\mathring{A})}{10^{44} \,erg \,s^{-1}} \right]^{0.50} \right\}$$
 (4.4)
$$+ (6.91 \pm 0.02)$$

where $\lambda L_{\lambda}(5100 \text{ Å}) = 10^{47.51} \, erg \, s^{-1}$ is the continuum luminosity evaluated at 5100Å, for ULASJ2315+0143 , using the best-fit continuum from PyQSOFit in the *H*-Band.

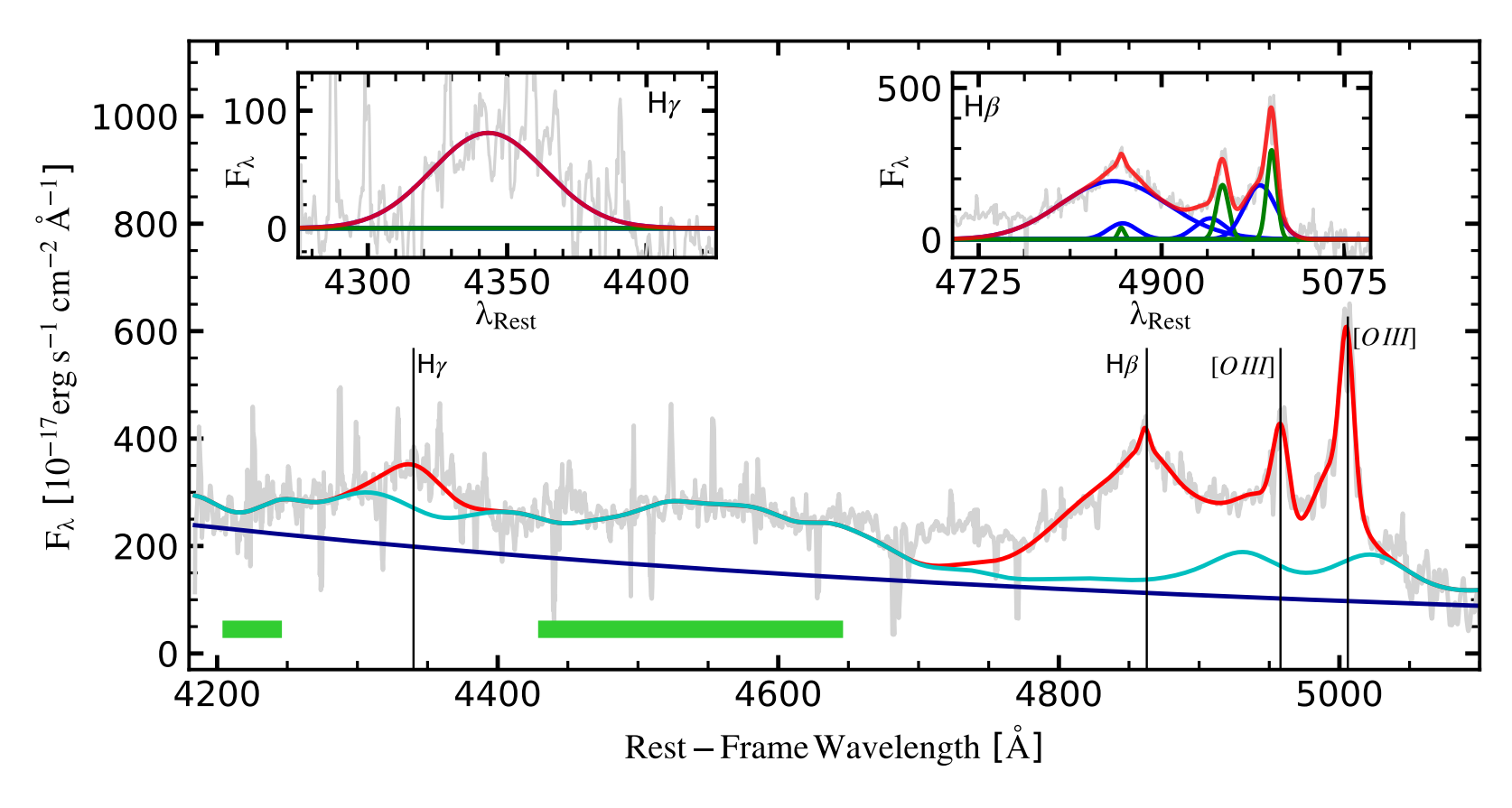


FIGURE 4.7: We present the H-Band spectrum for ULASJ2315+0143 with a dust correction, $E(B-V)^{QSO}=1.55$, applied in grey. The continuum is presented in navy blue, and the windows over which the continuum was fitted are denoted by the thick, lime-green lines. In addition, the combination of the continuum and iron template are presented in teal. The final fit of the spectrum is presented in red. Noteworthy emission lines are marked by thin black lines and labelled appropriately. The smaller panels are labelled by the line/complex they represent. The continuum subtracted total fit is presented in red, the broad components contributing to the total fit are presented in blue and finally, the narrow components are presented in green.

4.3. Results 93

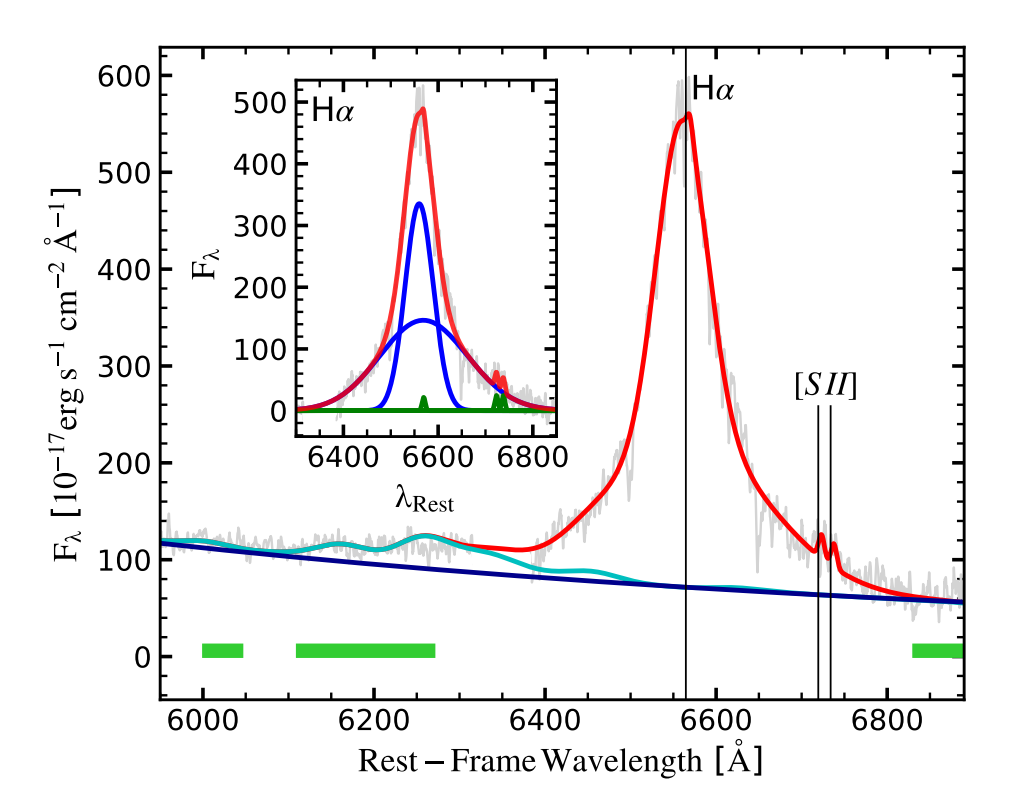


FIGURE 4.8: Same as Fig. 4.7, but instead we present the K-Band spectrum.

Eqn. 4.4 yields $log_{10}(H\beta, M\text{BH}[M_\odot]) = 10.26 \pm 0.05$, consistent with the analysis of a much shorter exposure SINFONI spectrum of this target in Banerji et~al.~(2015). Using the FWHM correction between H β and H α detailed in Greene & Ho (2005), we can also estimate MBH from the H α emission, yielding $log_{10}(H\alpha, M\text{BH}[M_\odot]) = 10.17 \pm 0.09$. The uncertainties in $\lambda L_{\lambda}(5100~\text{Å})$ were calculated by generating 500 simulated spectra perturbed with Gaussian noise consistent with the noise spectrum and implementing PyQSOFit after each iteration. Uncertainty estimates in MBH were then calculated by propagating the uncertainty in the continuum luminosity through Eqn. 4.4, drawing the normalisation constant from a Gaussian distribution with $\mu = 6.91~\text{\&}~\sigma = 0.02$. This does, however, neglect the large (\sim 0.5 dex) systematic uncertainties reported in single-epoch MBH estimates by Vestergaard & Peterson (2006). Previous estimates of the dynamical mass of this system based on CO(3-2) observations suggest $log_{10}(M_{dyn}/M_\odot) \simeq 11$ (Banerji et~al., 2021). The SMBH in ULASJ2315+0143 is therefore over-massive with respect to the host galaxy but broadly consistent with the scaling relation for high-redshift luminous quasars (e.g. Pensabene et~al., 2020).

TABLE 4.4: Quasar emission line properties inferred from the ULASJ2315+0143 X-Shooter spectrum. Since the [O II] emission was used to determine z_{sys} , its V50 velocity is zero by definition. Here, the results pertaining to the [O III] emission refer to the $\lambda 5008 \text{Å}$ line.

Species	S/N	EW [Å]	$FWHM [km s^{-1}]$	$V50 [km s^{-1}]$
Lyα	254	97±2	1070±10	-350±20
NV	11.9	16±1	4227 ± 3	-930±210
O IV/Si IV	4.3	7.0 ± 0.3	5773 ± 6	-940±160
CIV	16.1	24±1	3900 ± 390	-1080±110
OII	12.8	8±2	330 ± 120	0
$H\gamma$	2.5	21±1	3340 ± 190	+60±20
Нβ	23.9	230±30	6030 ± 580	-120±50
OIII	37.0	68±12	940 ± 80	-380±90
Нα	42.8	820±10	$4040{\pm}70$	-320±30

Using the relation between $L_{\lambda}(5100 \text{ Å})$ and L_{Bol} from Netzer (2019) we define a bolometric correction $BC_{5100} = 4.46$, yielding $L_{Bol} = 10^{48.16} \, erg \, s^{-1}$ for ULASJ2315+0143. Using this bolometric luminosity and our estimate of the black-hole mass yields an Eddington-scaled accretion rate of $log_{10}(\lambda_{Edd}) = -0.19$. Given the intrinsic X-ray luminosity $L_{X,int}=10^{45.6}\,erg~s^{-1}$ for ULASJ2315+0143 (Lansbury et al., 2020), the corresponding X-ray bolometric correction $log_{10}(k_{Bol}, L_X) = 2.56$. While this is extreme, X-ray bolometric corrections as large as $k_{Bol,X} = 100 - 1000$ have already been observed in the WISE/SDSS selected hyper-luminous (WISSH) quasar sample with bolometric luminosities $L_{Bol} > 2 \times 10^{47} \, erg \, s^{-1}$. Indeed, the inferred X-ray bolometric correction is consistent with the trends in bolometric correction with both black-hole mass and Eddington-scaled accretion rate inferred in other hyper-luminous infrared-selected quasar populations (Martocchia et al., 2017). Similarly, the mid-infrared luminosity inferred from Wide-field Infrared Survey Explorer (WISE) photometry, $log_{10}(L_{6\mu m})=47.5$, suggests a mid-infrared bolometric correction $log_{10}(k_{Bol}, L_{6um}) = -0.66$. This is consistent with the $log_{10}(k_{Bol}, L_{7.8um}) = -0.35 \pm 0.4$ reported amongst blue AGN (Weedman et al., 2012).

4.3.3.3 UV Emission and Absorption Line Features

In Section 4.3.2 we concluded that the broad emission lines seen in the UVB can be explained by a scattered or leaked quasar component. Hence we do not apply any dust correction to the UVB spectrum before fitting the lines using PyQSOFit. We model three main broad-line complexes in the UVB. We parametrise the Ly α /N V complex with four Gaussians, one broad component attributed to the N v contribution and the remainder attributed to the Ly α contribution. The Si IV/O IV] complex is modelled by two broad components and so too is the C IV emission. To enable a more robust reconstruction of the emission line profile, narrow absorption features must

4.3. Results 95

first be masked. We adopt an iterative approach for this. First we fit the raw spectrum with PyQSOFit, the result of which serves as a pseudo-continuum for subsequent fits. Pixels whose flux $> 2\sigma$ below the pseudo-continuum are replaced by the corresponding flux element in the pseudo-continuum itself. The process is then repeated until successive models converge (in this case, five iterations were sufficient). The results are presented in Fig. 4.9 and the emission line properties are summarised in Table 4.4.

In Fig. 4.9 the C IV emission line appears broad, blueshifted and of modest EW. These C IV properties are typical of those found in luminous, blue, Type 1 QSOs and have been associated with broad line region (BLR) winds along certain sight-lines (Richards *et al.*, 2011; Rankine *et al.*, 2020; Temple *et al.*, 2023; Stepney *et al.*, 2023). The N V emission is also blueshifted. As N V has a similar ionising potential to C IV, the two species are likely emitting from similar regions in the BLR, hence, the broadly consistent line properties are to be expected. Conversely, the Ly α EW is uncharacteristically large in comparison to N V. The velocity off-set of the narrow component of the Ly α emission (green Gaussian in top left panel of Fig. 4.9) is $-16\pm170~km~s^{-1}$, consistent with the uncertainties on the systemic redshift. We measure a line ratio N V/Ly α \sim 0.16 for ULASJ2315+0143 , significantly less than the N V/Ly α \sim 0.31 observed in blue Type 1 QSOs (Shen, 2016). We propose that the line profile can be explained either by a contribution from a star-forming galaxy (as discussed in Section 4.3.2) or some scattering of the quasar light. For a full discussion see Section 4.4.1.

We searched for absorption features associated with a number of high ionisation species in the UV spectrum as follows. First the spectrum is renormalised by a pseudo -continuum defined by the best PyQSOFit broad emission line model (Fig. 4.9, red). We then employ a cross-correlation technique similar to that described in Hewett & Wild (2010); Rankine et al. (2020); Stepney et al. (2023). Our default model is defined as $F/F_{cont} = 1$. We then define a grid of Gaussian absorption line models with various line depths and widths (the narrowest model explored has width $\sigma \sim 30 \, km \, s^{-1}$ equal to the resolution of X-Shooter in the UVB arm). For doublets, the line widths and line off-sets are tied and we additionally explore the following line ratios; 1:3, 1:2, 2:3, 1:1. The best model parameters and corresponding cross-correlation value are recorded at each line off-set. The absorption line model whose combination of off-set, depth, width and line ratio yields the maximum cross-correlation value is added to the default model and the process is then repeated. If the best absorption model does not represent a $> 4\sigma$ improvement in cross-correlation value over the default model or the new absorption feature does not exceed a signal-to-noise of three (S/N > 3), the new absorption line model is rejected and the search is complete.

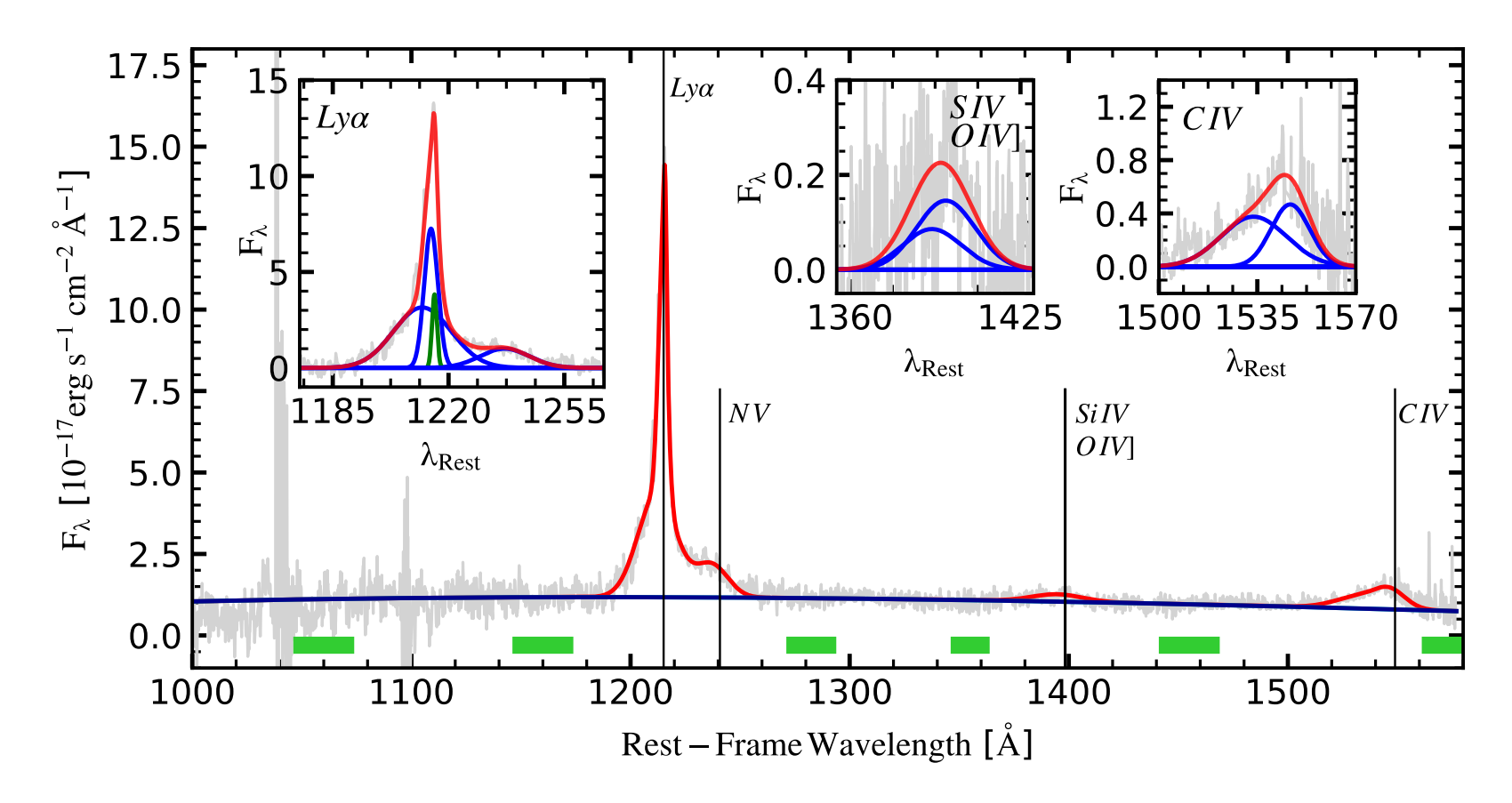


FIGURE 4.9: Same as Fig. 4.7, but instead we fit the UVB spectrum without a dust correction applied.

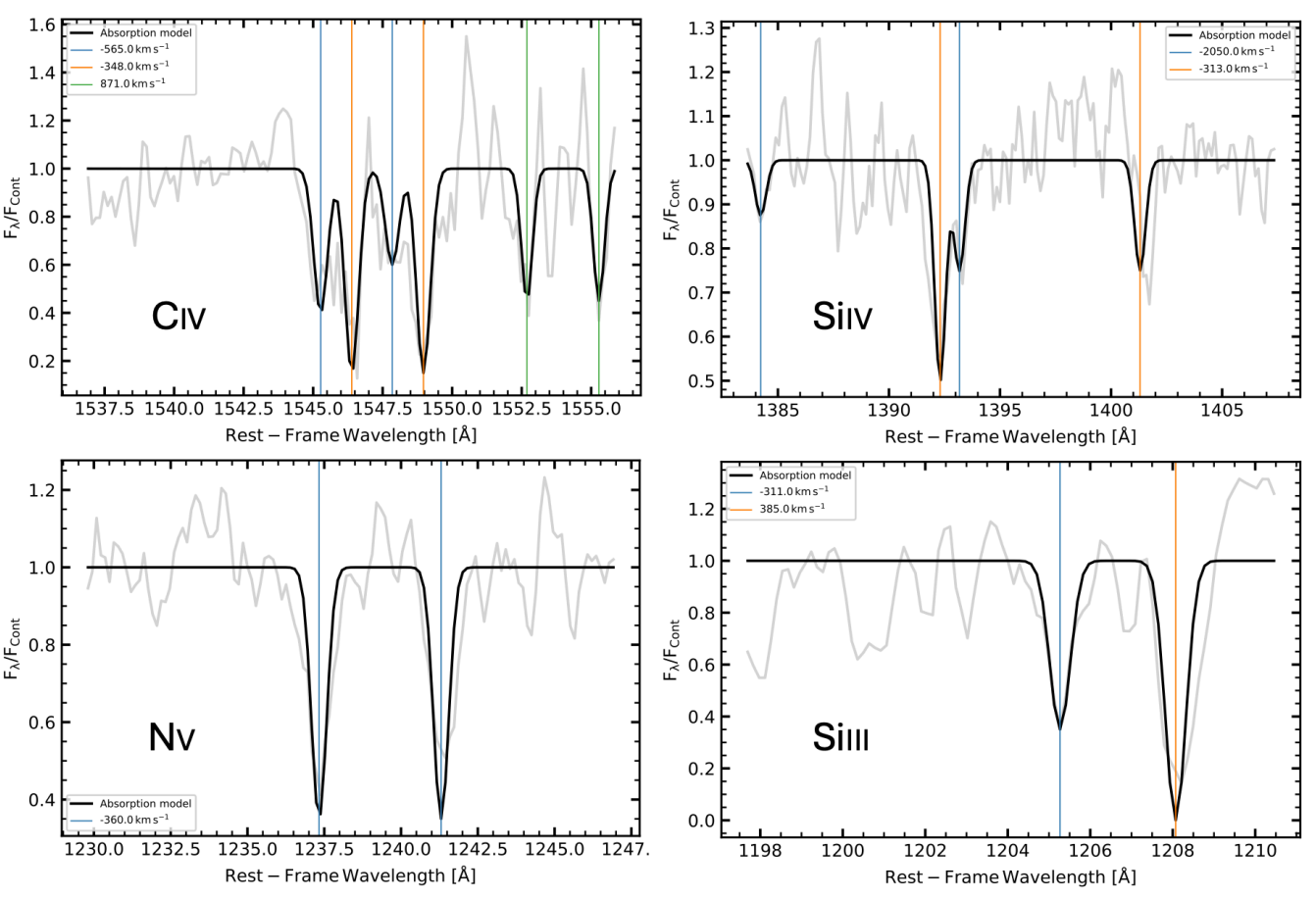


FIGURE 4.10: The UVB narrow absorption line features detected in the X-Shooter spectrum. The flux density normalised by the PyQSOFit pseudocontinuum is presented in grey. The absorption model reconstructions are presented in black. The species are labelled in each panel. We mark the various velocity components with vertical lines in each panel.

TABLE 4.5: Summary of different velocity components of narrow associated absorption line systems (AALs) shown in Fig. 4.10. Velocity offsets are relative to the [O II] systemic redshift. We group velocity components whose off-sets are consistent within the uncertainty on z_{sys} .

Species	Component	Offset [km s ⁻¹]
C IV $\lambda\lambda 1548.19, 1550.77$	2	-565
	3	-348
	5	871
Si IV $\lambda\lambda$ 1393.76, 1402.77	1	-2050
	3	-313
Νν λλ1238.82, 1242.80	3	-360
Si III λ1206.52	3	-311
	4^a	385

^a Potentially blueshifted H_I absorption, $V_{off-set} = -1870 \,\mathrm{km \, s}^{-1}$

The results are summarised in Table 4.5 and Fig. 4.10. Five distinct velocity components are detected, with component 3 at $v \simeq -340 km \, s^{-1}$ detected in all species, suggestive of outflowing gas at a range of ionisation parameters. The absorption in C IV at this velocity is saturated, suggesting a high covering fraction of C IV gas. In other species, such as N V and Si IV, the covering fraction of the gas is much lower. We also see additional absorption components in C IV at velocities of \simeq -565 $km \, s^{-1}$ and \simeq +871 $km \, s^{-1}$ that are not present in N V or Si III λ 1206.52 and Si IV, and have a lower covering fraction relative to the -340 $km \, s^{-1}$ component. Furthermore, we observe a very high velocity component in the Si IV absorption, with a velocity \simeq -2050 $km \, s^{-1}$. We also note that the redshifted Si III λ 1206.52 component at +385 $km \, s^{-1}$ could conceivably also represent blueshifted Ly α absorption.

4.4 Discussion

4.4.1 Source of the UV emission

In Section 4.3.2, we concluded that a simple dust-attenuated Type 1 QSO SED model is unable to reproduce the emission blueward of $\sim 4000 \text{\AA}$ in ULASJ2315+0143 and that emission from a secondary blue AGN component and/or a star-forming host galaxy likely contributes in this region. We now further explore the origin of the excess UV emission.

4.4. Discussion 99

4.4.1.1 A dual AGN system?

Could the blue AGN component seen in the X-Shooter spectrum of ULASJ2315+0143 be consistent with the presence of a second AGN in the system, which is more than 1000 times fainter in the UV than the primary dusty quasar? ULASJ2315+0143 is hosted in a major merger based on the ALMA observations reported in Banerji *et al.* (2021). The two galaxies in the merger are both detected in CO(3-2) and are separated by \sim 15 kpc in projection. During galaxy mergers, when both of the SMBHs are activated, a dual quasar could be formed (Begelman *et al.*, 1980). Observations over the past decades have reported hundreds of dual quasars with redshifts from local to z=5.66 (Yue *et al.*, 2021), and separations from Mpc scale down to 230 pc (Koss *et al.* (2023). Therefore a secondary quasar could be a plausible source of the UV emission.

If a secondary AGN is present however, it is likely not associated with the companion merging galaxy detected in CO with ALMA. The merging companion galaxy has gas excitation conditions that are more typical of star-forming galaxies rather than AGN as well as narrower molecular emission lines compared to the quasar host (Banerji et al., 2018), all of which seems to suggest no actively accreting black hole in this galaxy. Moreover, the image decomposition presented in Fig. 4.2 suggests the presence of at most a single point-source contributing to the UV emission, located at the centroid of the primary quasar host rather than the merging companion. If this is a dual AGN system, then the separation between the secondary AGN and the quasar host galaxy must therefore be less than the typical seeing of the HSC images (0.6 arcsec, or 4.8 kpc at z=2.566). The observational constraints of dual fractions at this separation are still poor, due to the limited resolution (e.g., Silverman et al., 2020). On the other hand, Steinborn et al. (2016) studied the statistics and properties of closely-separated (<10 kpc) dual AGN at z=2 in the Magneticum simulation. This cosmological simulation encloses a volume of 182 Mpc³ and produces 35 BH pairs, among which nine are dual AGN. Thus the spatial density of dual AGN is $\sim 0.05 \,\mathrm{Mpc^{-3}}$. They also report that the dual fraction (the ratio of the number of dual AGN and the total number of AGN) is $1.2 \pm 0.3\%$ in the simulation (also see Volonteri et al., 2016; Rosas-Guevara et al., 2019, this fraction varies roughly between 0.1-5%). Therefore, the dual AGN scenario, although cannot be fully ruled out, is statistically unlikely.

4.4.1.2 Leaked or scattered light from the primary quasar?

Since the AGN emission is unlikely to originate from a secondary source, the broad UV emission most likely originates from the primary quasar. Here we will discuss two potential scenarios - (i) leaked AGN emission, escaping through "windows" in a patchy dust morphology and (ii) scattered AGN emission.

et al., 2021a).

In Section 4.3.2, we show that when modelling the rest-frame UV portion of the SED with an unattenuated AGN component, just 0.05 per cent of the intrinsic quasar emission is required to reproduce the continuum. Since the UV continuum is consistent with the shape of a blue AGN, we require a consistent covering factor across all wavelengths to preserve the shape of the the accretion disk's multi-temperature black body in a "leaked" light scenario. For such a small fraction of the intrinsic radiation to be observed, we would require the obscuring medium to populate the extremely local regions of the AGN. The required dust morphology is then extremely contrived and hence we conclude that leaked AGN emission through a patchy obscuring medium is an unlikely cause of the UV-excess (Assef *et al.*, 2015).

An alternative scenario is that AGN emission is scattered towards the line-of-sight by the obscuring medium. This is the favoured explanation in HotDOGs, where broad-band UV photometry confirms that the emission is linearly polarised, having been scattered from ionised gas (Assef *et al.*, 2015, 2020, 2022). However, unlike HotDOGs and ERQs, ULASJ2315+0143 shows evidence of high-ionisation line blueshifts in the rest-frame UV emission (See Fig. 4.9 and Table 4.4). While this does not completely rule out the scattered light scenario, it does limit the number of feasible dust geometries.

Should the obscuring medium be distant enough such that the incident AGN emission features only the sight lines with blue-shifted high-ionisation lines, the scattered spectrum could also exhibit blueshifts. A candidate for the obscuring medium is then some kind of dusty toroidal structure outside the BLR. In Fig. 4.11 we show the infrared photometry of ULASJ2315+0143 from UKIDSS and *WISE* compared to the best-fit SED from Section 4.3.2. The infrared emission in the SED model represents the average infrared SED for an SDSS quasar at $z\sim 2$ (Temple *et al.*, 2021a) with a hot dust temperature of $T_{bb}=1243 {\rm K}$ and a hot dust normalisation - defined as the ratio between the hot dust and accretion disk luminosities at 2 μ m - $L_{2\mu m,Dust}/L_{2\mu m,QSO}=2.5$. We can immediately see that this SED model is inconsistent with the photometry of ULASJ2315+0143 when extrapolated to mid-infrared wavelengths. A value of $L_{2\mu m,Dust}/L_{2\mu m,QSO}=0.5$ however is better able to match the observed photometry. The flux density observed in the W4-Band (not shown in Fig. 4.11) is $10^{-17.1\pm0.1}erg\,s^{-1}\,cm^{-2}\,\mathring{A}^{-1}$. The mid-infrared SED therefore remains flat to a

The absence of hot dust emission on typical torus scales could suggest that the obscuring medium responsible for the significant ($E(B-V)^{QSO}=1.552$ mag) extinction towards the quasar continuum is likely on ISM, rather than nuclear scales. Alternatively, self-absorbed cold torus models have been invoked to explain flatter

rest-frame wavelength $\sim 6\mu m$ (corresponding to a dust temperature of $\sim 450K$). We therefore conclude that the ratio between the hot dust and accretion disk luminosities in ULASJ2315+0143 is significantly lower than observed in blue quasars (see Temple

4.4. Discussion 101

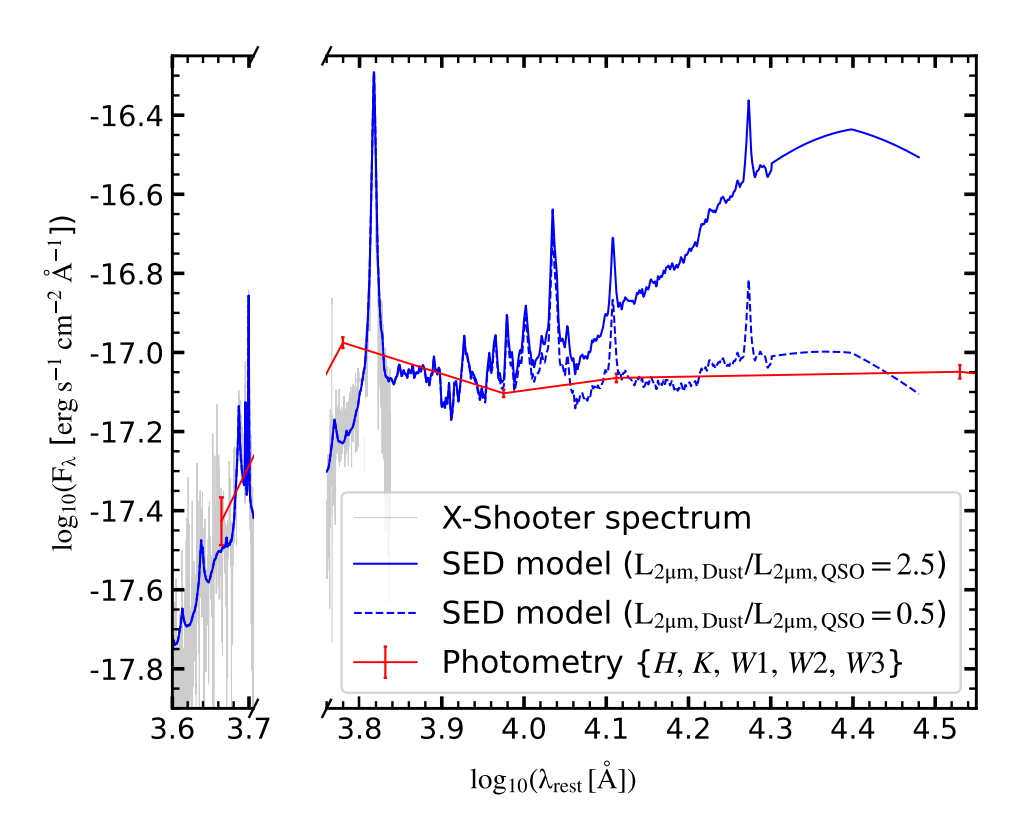


FIGURE 4.11: The X-Shooter spectrum of ULASJ2315+0143 is presented in grey, with the broad-band photometry from UKIDSS and *WISE* overlaid in red. The best-fit UV/optical SED, see Section 4.3.2, is extrapolated to mid-infrared wavelengths (blue, solid), assuming $L_{2\mu m,Dust}/L_{2\mu m,QSO}=2.5$. The photometry is inconsistent with the SED model redward of the W1 filter. The same SED model assuming $L_{2\mu m,Dust}/L_{2\mu m,QSO}=0.5$ (blue, dashed) is more consistent with the photometry. Both SED models assume a hot dust temperature of 1243K. This suggests that the ULASJ2315+0143 system contains less hot dust than the typical blue SDSS quasar, where $L_{2\mu m,Dust}/L_{2\mu m,OSO}\gtrsim 1.0$ (Temple *et al.*, 2021a).

mid-infrared SEDs (e.g. Hönig, 2019). However we might expect a more symmetrical line profile in C IV, with weaker blueshifts should the scattering medium lie primarily on nuclear scales close to the quasar BLR. Hence, we favour the depleted torus scenario, proposing a plausible geometry for ULASJ2315+0143 in Fig. 4.12. A more complete analysis of the mid infra-red SEDs of the HRQ population is deferred to Chapter 5. In Fig. 4.12, the excess UV emission seen in the spectrum is traced by dashed black arrows. We show multiple sight-lines originating from the accretion disk scattered by interstellar dust towards the observer.

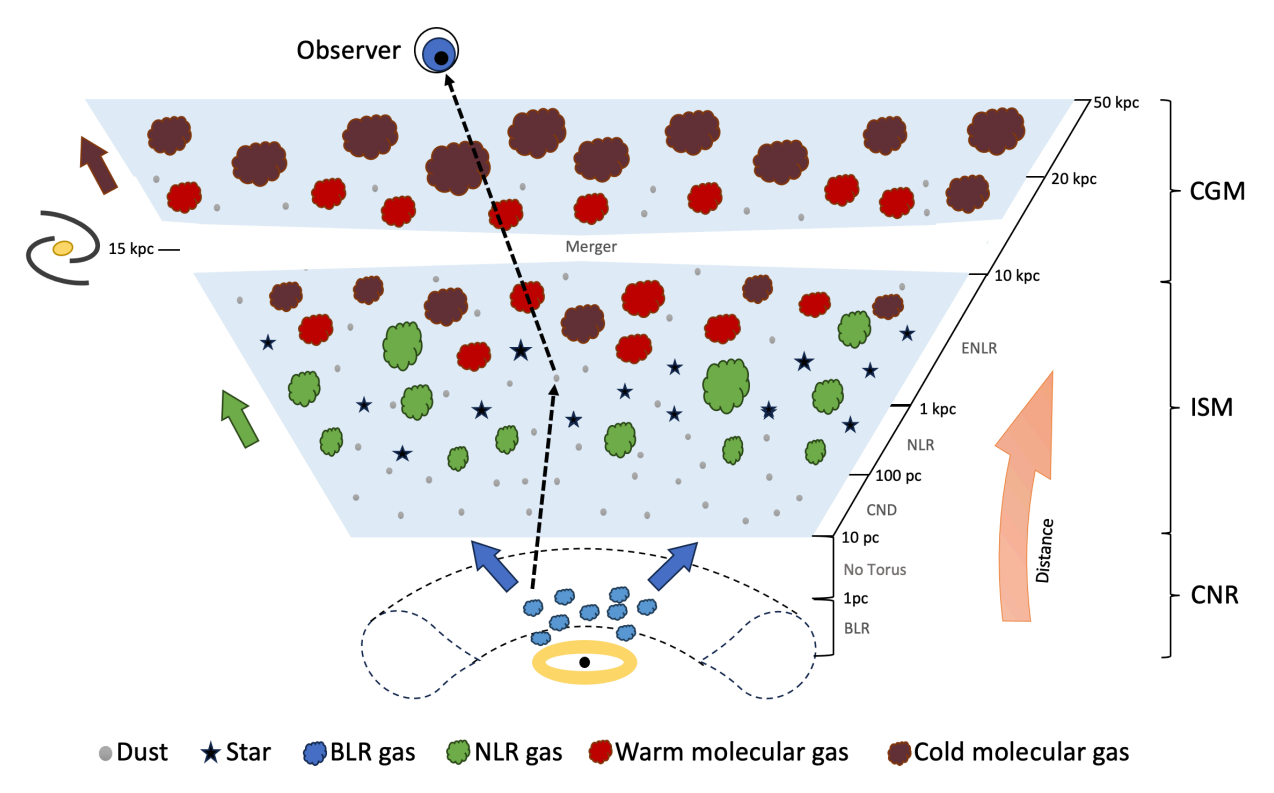


FIGURE 4.12: An illustration of our proposed geometry that best describes ULASJ2315 +043 focusing on the different scales associated with different features in the X-Shooter spectrum and the multi-wavelength observations of this source. On sub-pc scales we illustrate the BLR gas with blue clouds. Since the mid-infrared SED is devoid of hot dust (Fig. 4.11), we illustrate the missing/depleted torus with dotted black lines stretching to \sim 10 pc. ALMA observations suggest that the ISM dust is on scales of \sim 15-20 kpc based on the size of the millimetre continuum emission. NLR gas and star-forming regions are represented with green clouds and black stars respectively. The warm molecular gas is depicted with red clouds and the cold molecular gas is depicted with maroon clouds. A cartoon sight line, scattered from ISM dust and then subsequently absorbed by the warm and cold gas reservoirs, potentially giving rise to the AAL features in the UV spectrum, is illustrated by the dashed black arrow. The merging companion galaxy resides at 15 kpc and is illustrated to the left of the sketch. Blue, green and maroon arrows represent BLR, NLR and cold molecular gas flows respectively all of which exhibit significant velocity offsets relative to the systemic redshift.

4.4. Discussion 103

4.4.1.3 Associated Absorption Line Systems in ULASJ2315+0143

In Fig. 4.10 we can see numerous narrow absorption features in the rest-frame UV spectrum with linewidths of a few hundred $km s^{-1}$ and that lie within 3000 $km s^{-1}$ of the quasar systemic redshift. These properties are consistent with the associated absorption line (AAL) systems that have been detected in the spectra of numerous luminous quasars (e.g. Vanden Berk et al. 2008; Hamann et al. 2011; Shen & Ménard 2012; Chen et al. 2018). AALs can have a wide range of origins tracing gas in quasar inflows and outflows, in the halos of the quasar host galaxy or indeed gas reservoirs on circumgalactic scales (Foltz et al., 1986; Tripp et al., 1998). Statistical studies suggest that most AALs are intrinsic to the quasars, and hence can serve as important probes of the quasar environment (Nestor et al., 2008; Wild et al., 2008). As such, the detection of significant absorption in this gas-rich merger is perhaps not surprising. Dust-reddened quasars in the Sloan Digital Sky Survey (SDSS) have been associated with a higher incidence of AALs (Richards et al., 2003; Vanden Berk et al., 2008) and 2MASS red quasars with a higher incidence of Broad Absorption Line (BAL) features (e.g. Urrutia et al. 2009). However, to our knowledge, our study represents the first detection of multiple AAL systems in a quasar with such extreme dust reddening of E(B-V) > 1.5.

The most prevalent absorption feature detected in multiple species is at a velocity of \sim -340 $km\,s^{-1}$ relative to systemic. The higher ionisation gas at -340 $km\,s^{-1}$ could conceivably be associated with the merging companion, which is located 15 kpc away in projected distance from the quasar and blueshifted in CO(3-2) emission by 170 $km\,s^{-1}$ relative to the quasar (Banerji *et al.*, 2021). However, the high ionisation gas is most likely located closer to the ionising source, effectively shielding the lower ionisation gas, which is likely spatially co-incident with the warm molecular gas traced by CO(3-2). We also detect redshifted AALs at a velocities of \simeq 385 $km\,s^{-1}$ and \simeq 870 $km\,s^{-1}$. These components may be associated with the CO(1-0) cold gas reservoir in this quasar, which is off-set in velocity by \simeq 500 $km\,s^{-1}$ (Banerji *et al.*, 2018). The cold gas reservoir is also very spatially extended on projected scales of \sim 50 kpc. The geometry of the system showing the different spatial scales for the gas potentially producing the AAL features is shown in Fig. 4.12.

4.4.1.4 Star-forming host

As discussed in Section 4.3.2, HSC imaging is suggestive of a host galaxy contribution to the rest-frame UV flux. This is also consistent with the strong nebular emission observed in Ly α and [O II] as well as the presence of multiple narrow absorption line systems in Fig. 4.10 which could conceivably be associated with the gas in the quasar host galaxy. The $SFR_{FUV} \sim 3 \times SFR_{[O\,II]}$. The unobscured SFR, predicted by the

far-infrared and submillimeter continuum emission, for this source is $SFR_{FIR} = 680 \pm 100\,M_{\odot}\,yr^{-1}$ (Banerji *et al.*, 2018). Main sequence galaxies at similar redshifts and A_V^{Gal} , report similar SFR_{FIR} to ULASJ2315+0143, with their average $SFR_{H\alpha,obs} = 20\,M_{\odot}\,yr^{-1}$ consistent with our own estimate of the SFR from [O II] (Puglisi *et al.*, 2017). Given SFR_{FUV} , $SFR_{[O\,II]}$ and $SFR_{H\alpha,obs}$ estimates make similar assumptions regarding the dust extinction, it would be reasonable to conclude that the [O II] estimate is less than than the FUV estimate for ULASJ2315+0143 because the rest-frame UV continuum emission in this source does not originate purely from a star-forming host galaxy but rather has some contribution from scattered AGN light as discussed above.

4.4.2 Multi-phase winds in ULASJ2315+0143

In this section, we discuss the line properties of ULASJ2315+0143 in the context of AGN-driven winds as well as drawing comparisons to observations from other QSO populations.

There exists a relationship between BLR outflows, as probed by the C IV blueshift, and both MBH and Eddington-scaled accretion rate in blue quasars. This relationship is evident in both simulations (e.g. Giustini & Proga, 2019) and observations of blue Type 1 SDSS quasars up to $z_{sys} \sim 4$ (e.g. Temple *et al.*, 2023; Stepney *et al.*, 2023). The dependence of C IV blueshift on the MBH- λ_{Edd} plane tells us how BLR outflows are linked to the accretion physics of QSOs. For significant (> $1000 \, km \, s^{-1}$) C IV blueshifts, quasars require $\lambda_{Edd} > 0.2$ and MBH > $10^9 M_{\odot}$. Our observations of ULASJ2315+0143 are consistent with this picture, with a relatively strong C IV blueshift, V50 = $1075 \, km \, s^{-1}$, owing to the large SMBH mass, MBH = $10^{10.26} \, M_{\odot}$, and Eddington-scaled accretion rate, $log_{10}(\lambda_{Edd}) = -0.19$. Fundamentally, this suggests that the dependence of BLR outflow velocities on black hole mass and accretion rate is broadly similar in blue and heavily reddened quasars.

Moving to kpc-scales, we can probe NLR winds with the [O III] emission line W80 (e.g. Perrotta *et al.*, 2019; Coatman *et al.*, 2019; Temple *et al.*, 2019; Villar Martín *et al.*, 2020). In Fig. 4.13, we compare the BLR and NLR wind velocities of ULASJ2315+0143 to a sample of blue QSOs Temple *et al.* (2024) and show that ULASJ2315+0143 appears consistent with the trend observed in optically selected quasars. While ULASJ2315+0143 shows evidence of significant NLR winds, as probed by [O III] W80, the object is not extreme. This picture is consistent with the BLR winds as probed by C IV blueshift. Since the winds in both the broad and narrow line regions are similarly moderate, a common mechanism could be responsible for the gas velocities at these different scales.

4.4. Discussion 105

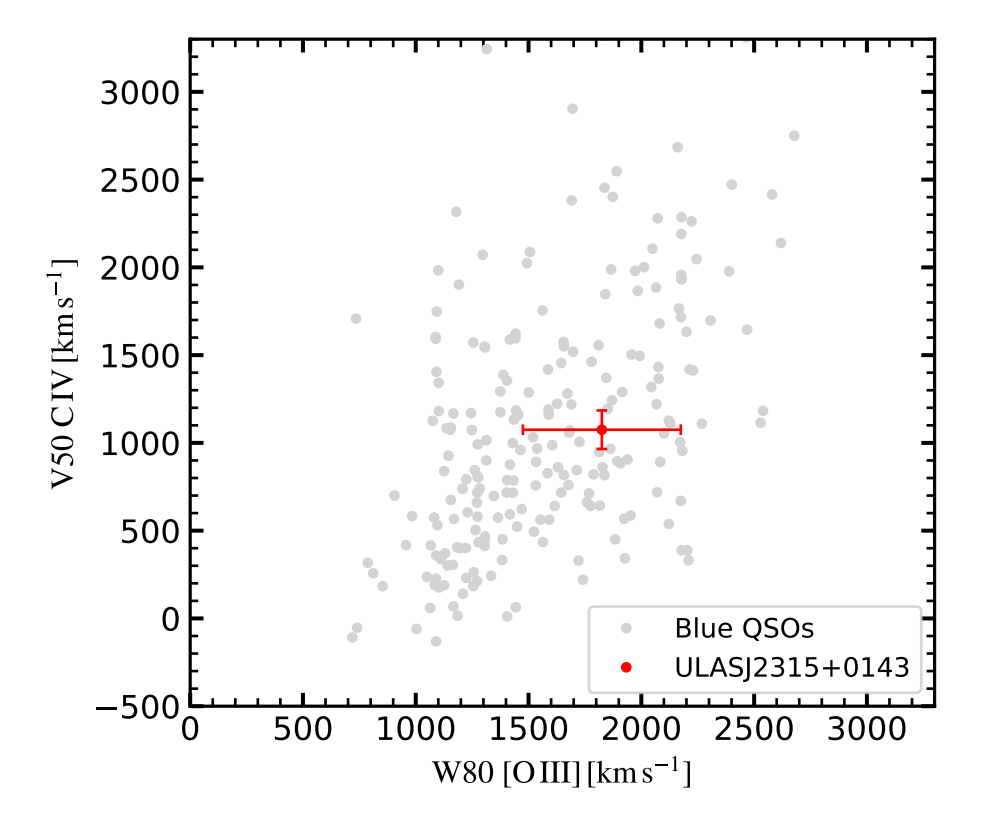


FIGURE 4.13: The C IV emission line centroid [O III] W80 relation for a sample of blue SDSS quasars Temple *et al.* (2024) are presented in grey. ULASJ2315+0143, presented in red, shows evidence of significant (though not extreme) BLR and NLR winds, consistent with the trend observed in blue SDSS quasars.

In addition, we can harness the [O III] emission to investigate the energetics of the outflowing ionised gas. By assuming a symmetric biconical geometry and that the emitting clouds have the same density, Cano-Díaz *et al.* (2012) derive the following expression for the mass-loss rate of the NLR outflow;

$$\dot{M}_{out}^{ion} = 164 \, \frac{L_{44}([\text{O\,III}]) \, v_3}{\langle n_{e3} \rangle \, 10^{[\text{O/H}]} \, R_{kpc}} \, M_{\odot} \, \text{yr}^{-1}$$
(4.5)

where $L_{44}([O\,III])$ is the broad $[O\,III]$ line luminosity in units $10^{44}\,erg\,s^{-1}$, v_3 is the outflow velocity in units of $1000\,km\,s^{-1}$, $\langle n_{e3}\rangle$ is the NLR outflow electron density in units of $1000\,cm^{-3}$, $10^{[O/H]}$ is the oxygen abundance in solar units and R_{kpc} is the radius of the outflowing region in units of kpc. Given the uncertainty in the amount of dust attenuation affecting the NLR, we use the measured $[O\,III]$ luminosity from the spectrum before any dust correction is applied. The kinetic power associated with the outflow is then given by Eqn. 4.6;

$$\dot{\epsilon}_{k}^{ion} = 5.17 \times 10^{43} \frac{C L_{44}([\text{O III}]) v_{3}^{3}}{\langle n_{e3} \rangle 10^{[\text{O/H}]} R_{kpc}} erg \, s^{-1}$$
(4.6)

where $C = \langle n_{e3} \rangle^2 / \langle n_{e3}^2 \rangle \approx 1$. As in Perrotta *et al.* (2019), we assume that since the [O III] emission is not core dominated in ULASJ2315+0143 , $v_{98} = 2521 \, km \, s^{-1}$ serves as a good indicator for the outflow velocity and adopt solar metallicities. Using the line ratios between the narrow and broad components of [O III] (Fig. 4.7), we attribute ~ 75 per cent of the total line luminosity to the broad outflow component. Bischetti *et al.* (2017) find that amongst the WISSH broad-line quasar sample $\langle n_{e3} \rangle \sim 200 cm^{-3}$ and the [O III] emission regions are extended to 1-7 kpc. Since we have no spatially resolved data for the [O III] emission in ULASJ2315+0143 at present, we adopt the 4 kpc threshold for strong [O III] winds reported in another HRQ from our sample in Banerji *et al.* (2012) - ULASJ1002+0137 - which was observed by Veilleux *et al.* (2023). Applying these assumptions to Eqn. 4.5 and Eqn. 4.6 yields $\dot{M}_{ion}^{out} = 199 \, M_{\odot} \, yr^{-1}$ and $\dot{e}_k^{ion} = 10^{44.61} erg \, s^{-1} \sim 0.001 \, L_{Bol}$.

The kinetic power of the ionised gas outflows in ULASJ2315+0143 is consistent with the blue quasars presented in Shen et al. (2011), given its bolometric luminosity, however, they seems relatively weak when compared to the ERQs presented in Perrotta et al. (2019). It is important though to be mindful of the different assumptions made in the kinetic power estimates of the two samples. Firstly in ERQs the entire [O III] line luminosity is attributed to the outflow whereas we attribute \sim 75 per cent of the total line luminosity to the broad outflow component based on our line fits. Secondly, Perrotta et al. (2019) adopt $R_{kpc} = 1$ since two of their ERQ's [O III] emission regions are spatially unresolved down to a resolution of \sim 1.2kpcs by the W.M. Keck Observatory OSIRIS integral field spectrograph (IFS) significantly smaller than our assumption of 4 kpc. Both of these assumptions are likely to overestimate the kinetic power of the outflows by a factor of several relative to our assumptions. In addition, if we assume the colour $[i - W3_{Vega}]$ is a good indicator of the dust extinction in these systems ([$i-W3_{Vega}$] \sim 7.78 for ULASJ2315+0143), ULASJ2315+0143 suffers more extinction than the average ERQ. Hence the [O III] line luminosity may be more attenuated in ULASJ2315+0143, resulting in an underestimate of the kinetic power when compared to the ERQ sample. Neither estimate corrects the observed [O III] luminosity for dust extinction. Given these assumptions, the ionised outflows observed in ULASJ2315+0143 are likely similar to those observed in ERQs in terms of mass-loss rate and kinetic power.

4.5. Conclusions

4.5 Conclusions

We have presented a high-resolution rest-frame UV to optical X-Shooter spectrum of a hyper-luminous heavily reddened quasar at z=2.566 - ULASJ2315+0143 . We spectroscopically confirm the presence of excess UV emission relative to a dust-reddened quasar SED, which was initially noted in broadband photometric observations of this source. We fit the spectrum with several composite SED models to simultaneously explain the dust-attenuated rest-frame optical and excess rest-frame UV emission and also conduct a comprehensive analysis of the numerous emission and absorption line features detected in the spectrum. Our main findings are as follows:

- We confirm that the blue photometric colours of this source (Wethers *et al.*, 2018) can not be explained by a simple dust-attenuated quasar model. If a secondary AGN component is responsible for the excess UV emission as seems likely based on the detection of broad emission lines in the UV, the luminosity of this blue AGN component is just 0.05 per cent of the total luminosity inferred from the dust-attenuated quasar component which has $\log_{10}\{\lambda L_{\lambda}(3000\text{\AA})[erg\ s^{-1}]\}=47.9$ and a dust extinction of $E(B-V)^{QSO}=1.55$ mag. Based on analysis of the rest-frame UV imaging for this source, we rule out the presence of a dual AGN system. We conclude that we would require an extremely contrived dust geometry for just 0.05 per cent of the intrinsic AGN emission to "leak" through the obscuring medium and we therefore suggest that scattered AGN light scattering off dust in the interstellar medium of the host galaxy can explain the broad emission lines seen in the rest-frame UV and potentially the UV continuum emission.
- We detect narrow [O II] emission without any significant emission from either [Ne III] or [Ne V] and we therefore suggest that at least some of this [O II] emission is likely coming from the star-forming host galaxy of the dusty quasar. We also detect narrow $Ly\alpha$ emission at the systemic redshift of the quasar with an equivalent width and $Ly\alpha$ to NV ratio that is much higher than typically observed in blue quasars. Once again, some contribution from a star-forming host galaxy could be responsible for the narrow $Ly\alpha$ emission. Finally a composite dusty quasar + star-forming host galaxy fit to the X-Shooter spectrum provides a good match to the rest-frame UV and optical continuum shape though of course it cannot reproduce the broad emission lines in the UV. We conclude that the narrow low-ionisation nebular emission lines seen in the spectrum and potentially some of the UV continuum could also be coming from the quasar host galaxy. This is corroborated by analysis of the rest-frame UV image of this source from HyperSuprimeCam which shows evidence for spatially extended emission.

- We analyse the mid infra-red SED of ULASJ2315+0143 in an attempt to constrain the location of any dust that is responsible for attenuating the quasar emission and also potentially scattering some of the rest-frame UV emission to our line-of-sight. We find that ULASJ2315+0143 has an extremely flat and atypical mid infrared SED with a ratio between the hot dust and accretion disk component at 2μm that is at least a factor of 5 lower than the average blue SDSS quasar at the same redshift. This suggests significant depletion of any hot (> 1000K) dust component on toroidal scales. Hence, we propose that the bulk of the obscuring medium is on ISM, rather than nuclear, scales. An extended scattering medium is consistent with the blueshifts observed in the rest-frame UV high-ionisation lines -e.g. C IV and N V, since a dense circumnuclear cocoon would likely result in the symmetrical line profiles such as those observed in ERQs.
- We detect numerous associated absorption line (AAL) systems in the rest-frame UV across a range of species and velocity components including blueshifted absorption features in C IV, N V, Si IV and Si III as well as potentially redshifted features in Si III and C IV.
- Using the Balmer lines and the optical continuum luminosity ($L_{\lambda}(5100 \, \text{Å})$), we estimate the black-hole mass $log_{10}(H\beta, MBH[M_{\odot}]) = 10.26 \pm 0.05$, bolometric luminosity $L_{Bol} = 10^{48.16} \, erg \, s^{-1}$ and Eddington-scaled accretion rate $log_{10}(\lambda_{Edd}) = -0.19$. Our optical-derived bolometric luminosity implies an X-ray bolometric correction $log_{10}(k_{Bol}, L_X) = 2.56$. The bolometric correction implied from the mid-infrared luminosity $log_{10}(k_{Bol}, L_{6\mu m}) = -0.66$.
- We find evidence for significant outflows affecting both the BLR and NLR gas. The C IV blueshift is $1080\pm110~km~s^{-1}$ and the [O III] W80 is $1830\pm350~km~s^{-1}$. However, in the context of outflows seen in other luminous quasar populations, these values are not extreme and could be explained by the significant black hole mass of ULASJ2315+0143 . Using the [O III] velocity we estimate the mass outflow rate for the ionised gas $\dot{M}_{ion}^{out}=199~M_{\odot}~yr^{-1}$, with a corresponding kinetic power $\dot{\varepsilon}_k^{ion}=10^{44.61}erg~s^{-1}\sim0.001~L_{Bol}$. This is consistent with SDSS blue quasars at comparable luminosity.

Chapter 5

The spectral energy distributions of heavily reddened quasars

"The road of [UV]excess leads to the palace of wisdom"

William Blake

5.1 Introduction

As discussed in Chapters 1 & 4, the last 10 years have seen a proliferation in the discovery of numerous classes of dust-obscured AGN - e.g. heavily-reddened quasars (HRQs; Banerji *et al.*, 2012, 2015; Stepney *et al.*, 2024), Extremely Red Quasars (ERQs; Hamann *et al.*, 2017) and Hot Dust Obscured Galaxies (Hot DOGs; Eisenhardt *et al.*, 2012; Assef *et al.*, 2015). More recently, at $z_{sys} \gtrsim 5$, JWST observations have also uncovered a new population of "Little Red Dots" (LRDs; Onoue *et al.*, 2023; Kocevski *et al.*, 2023; Williams *et al.*, 2024; Greene *et al.*, 2024; Gillette *et al.*, 2024). While the true nature of some sub-samples of LRDs is still hotly debated (e.g. Matthee *et al.*, 2024), 60 per cent of the objects from the UNCOVER field show definitive evidence of broad (FWHM > 2000 $km \, s^{-1}$) H α emission and are therefore classified as dust-reddened AGN (Greene *et al.*, 2024).

The primary aim of this chapter is to understand the full ultraviolet to near-infrared SED properties of the HRQ population, placing them in the context of the other classes of red AGN - which may each represent a different stage in black hole/galaxy growth (Hopkins *et al.*, 2008). A key finding from Chapter 4 is the identification of a significant excess in the rest-UV continuum emission of ULASJ2315+0143 , despite the significant level of extinction suffered at rest-optical wavelengths. The SEDs of an additional 13 luminous ($L_{Bol} > 10^{46} \ {\rm erg \ s^{-1}}$) HRQs also show evidence of similarly blue photometric colours in the rest-UV (Wethers *et al.*, 2018), however, the rest-UV photometry has since been superseded by significantly deeper and higher resolution data since the study was conducted and it is unclear whether such a continuum is ubiquitous amongst the whole HRQ population.

Looking to other red populations, a UV excess has been detected in a number of Hot DOGs - although the relative strength of the UV continuum is higher than that detected in ULASJ2315+0143 (Assef *et al.*, 2020). Interestingly, polarisation studies of Hot DOGs confirm that scattered AGN emission is at least partially responsible for their blue rest-UV continua (Assef *et al.*, 2022), consistent with our Chapter 4 finding that ULASJ2315+0143 hosts broad emission lines in the rest-UV. Similarly, many LRDs are known to host blue rest-frame UV photometric colours (e.g. Onoue *et al.*, 2023; Kocevski *et al.*, 2023; Greene *et al.*, 2024; Kocevski *et al.*, 2024). SED models suggest that the rest-UV continuum of LRDs is consistent with both host galaxy star formation (e.g, Pérez-González *et al.*, 2024) as well as scattered light from the dust-obscured AGN (e.g. Williams *et al.*, 2024) - similar to the models we explored for ULASJ2315+0143 in Chapter 4. Furthermore, the inferred rest-frame UV luminosities of LRDs are significantly fainter than that of UV-selected AGN at similar epochs ($-20 < M_{UV} < -16$), consistent with a less-than-one per cent scattering of the accretion disk emission (Greene *et al.*, 2024) and our work on ULASJ2315+0143.

5.1. Introduction 111

In addition to the rest-UV continuum, in Chapter 4 we find that the SED of ULASJ2315 +0143 hosts peculiar near-infrared properties. The discovery of weak sublimation temperature dust emission in ULASJ2315+0143 when compared to luminous blue quasars from SDSS (e.g. Temple et al., 2021b) could be interpreted as evidence for a "blow-out" phase (Stepney et al., 2024). In the "blow-out" phase framework, the earliest phase most likely features a reservoir of dense gas and dust surrounding the central engine. Assuming that the different dusty quasar populations correspond to distinct evolutionary phases, this cocoon-like structure is consistent with the extreme column densities (N_H $\sim 10^{23-24}$ cm⁻²) observed in both Hot DOGs (Assef *et al.*, 2015) and ERQs (Goulding et al., 2018). In Chapter 4, we argue that the transition phase from heavily obscured systems (e.g. ERQs and Hot DOGs) to the UV-luminous quasars observed in SDSS corresponds to HRQs. Observations of HRQs confirm more modest column densities $N_H \sim 10^{22} \, \text{cm}^{-2}$ and strong outflows in the ionised gas - (e.g. Lansbury et al., 2020; Stepney et al., 2024) - suggesting that strong radiative feedback processes have begun clearing gas and dust from the central engine in a "blow-out" phase.

While the Hot DOG selection biases the sample towards dust-rich objects (Eisenhardt et al., 2012; Assef et al., 2015), the mid-infrared photometry of a sub-sample of LRDs show evidence of remarkably similar mid-infrared emission to ULASJ2315+0143 (Williams et al., 2024; Akins et al., 2024) - suggesting that heavily extincted AGN may still host sublimation-temperature dust-poor environments. Interestingly, only 2/341 LRDs are detected in the X-ray, however, both X-ray detected LRDs show evidence of high column densities, $log_{10}(N_H | cm^{-2}|) \sim 23$, consistent with ERQs and Hot DOGs (Goulding et al., 2018; Assef et al., 2015). One interpretation for the absence of X-ray detections across the rest of the LRD sample is that they generally host denser gas columns of neutral hydrogen with higher covering fractions than typically observed in HRQs (e.g. $log_{10}(N_H) \sim 22$; Lansbury et al., 2020), which can extend to ISM scales (Kocevski et al., 2024). Alternatively, Greene et al. (2024) propose that prolonged episodes of super-Eddington accretion could explain why LRDs are X-ray weak when compared to their optical luminosities. However, without large-scale spectroscopic confirmation it is still possible that some LRDs are starburst galaxies and the observed absence of hot (> 1000K) dust emission is due to their mid-infrared SEDs tracing stellar populations whose spectra peak at $\sim 0.5 - 3\mu m$ in the rest frame (Sawicki, 2002).

Given the diversity of red AGN populations, their ubiquity, and their potentially crucial role in galaxy/black hole co-evolution, it is necessary to extend the study of HRQs to larger samples so that the links between the various red AGN populations can be studied more robustly. For this reason, we will explore the SED properties of 60 HRQs in the rest-frame ultra-violet to near-infrared. Studying the SED properties of the broader HRQ population will help develop the understanding of obscured

accretion and enable a more robust comparison between the HRQ phase and other cosmic noon quasar populations such as luminous blue quasars, ERQs and Hot DOGs. Furthermore, by comparing HRQs with the newly emerging LRD population, it will be possible to infer the similarities and differences between obscured accretion in objects of different black-hole mass and redshift.

The structure of this chapter is as follows: Section 5.2 details the selection and preparation of the photometric data. In Section 5.3 we detail the spectral energy distribution modelling of 60 HRQs before discussing our results in Section 5.4. Then, in Section 5.5, we discuss the full ultra-violet to near-infrared SED properties of HRQs in the context of *JWST*'s LRD population, as well as Hot DOGs, ERQs and blue quasars - before presenting our conclusions in Section 5.6.

5.2 Data

5.2.1 Photometric data and sample selection

In this work we study the heavily reddened quasars (HRQs) selected in Banerji *et al.* (2012), Banerji *et al.* (2013), Banerji *et al.* (2015) and Temple *et al.* (2019). The selection of the HRQ sample is discussed in detail in Banerji *et al.* (2012) and Banerji *et al.* (2015), however, we briefly summarise it here. We utilise photometry from the United Kingdom Infrared Deep Sky Survey (UKIDSS), the Visible and Infrared Survey Telescope for Astronomy (VISTA) and the Wide-field Infrared Sky Explorer (*WISE*) for the selection. The rest-optical emission is likely quasar dominated (e.g. Wethers *et al.*, 2018), hence point-like magnitudes are extracted in the infrared. The sources are selected via their near and mid-infrared colours, with additional *i*-band constraints (where available at the time of selection) to ensure red continua at rest-UV/optical wavelengths. Consequently, the selection criteria are as follows;

- $K_{AB} < 18.9 \mid K_{AB} < 20.3^1$
- $(J K)_{AB} > 1.6$
- (W1 W2) > 0.85
- $i_{AB} > 20.5$
- $(i K)_{AB} > 2.5$

 $^{^{1}}$ For the shallower surveys - e.g. the VISTA Hemisphere Survey (VHS; McMahon *et al.*, 2013) and the UKIDSS Large Area Survey (UKIDSS-LAS; Lawrence *et al.*, 2007) - $K_{\rm AB} < 18.9$ mag was used. For the deeper VISTA Kilo-degree Infrared Galaxy survey (VIKING; Edge *et al.*, 2013), $K_{\rm AB} < 20.3$ mag was used.

5.2. Data 113

To extend our photometric coverage to bluer wavelengths, we adopt a 1" search radius to cross-match the HRQ sample with the following optical surveys; the Panoramic Survey Telescope and Rapid Response System (Pan-STARRS - DR1; Chambers *et al.*, 2016), the Sloan Digital Sky Survey (SDSS - DR16; Ahumada *et al.*, 2020), the Dark Energy Survey (DES - DR2; Abbott *et al.*, 2021), HyperSuprime Camera Subaru Strategic Program (HSCSSP - DR3; Aihara *et al.*, 2022) and the Kilo-Degree Survey (KiDS - DR5; Wright *et al.*, 2024). Combining these surveys enables the study of the ugriz - YJHK - W1W2 photometry, where available, with an approximate rest-frame wavelength coverage $1000\text{Å}-3\mu m$ at $z_{\rm sys} \sim 2$. Given the tendency of HRQs to be extended in the rest-UV (Wethers *et al.*, 2018), we make use of extended magnitudes in the optical surveys - e.g. CModel magnitudes for HSC and MAG_AUTO for DECam, Pan-STARRS and SDSS. The result is a sample of 60 HRQs with redshifts $0.7 \lesssim z_{\rm sys} \lesssim 2.6$ (calculated from rest-optical spectra; Banerji *et al.*, 2012, 2015; Temple *et al.*, 2019), 49 of which have redshifts $z_{\rm sys} > 1.5$.

Several of the HRQs have photometric coverage in the same band from multiple surveys, therefore, we calculate weighted means across the bands to combine the photometry and boost the signal-to-noise, where possible. The weights are defined by the inverse variance of each observation. The name and weight of each filter contributing to a given photometric band is then recorded so that the photometry can be self-consistently modelled while fitting the spectral energy distributions (SEDs - see Section 5.3 for details). The uncertainties in a given band are calculated using the standard error on the weighted mean.

There are a total of seven sources for which we have rest-UV/optical data from Pan-STARRS, SDSS, DECam **and** HSC. We find that the average percentage difference between the surveys and the weighted mean calculated for each band is ~ 10 per cent. This difference is consistent with the known variability observed in quasar continua at rest-UV/optical wavelengths (e.g. Hook *et al.*, 1994). Hence, to account for this variability, we impose a 10% floor on the photometric uncertainties in bands for which there is only photometric data available from a single survey. Finally, we discard any photometric bands whose signal-to-noise, S/N < 3. The final catalogue is presented in Appendix A.

5.2.2 Spectroscopic data

In addition to the broad-band photometry, we have also obtained rest-frame UV spectroscopic data for the HRQ with the brightest g-band flux - ULASJ2200+0056. The spectra were obtained via the Robert Stobie Spectrograph (RSS; Burgh et~al., 2003; Kobulnicky et~al., 2003; Rangwala et~al., 2008) mounted to the Southern African Large Telescope (SALT; Buckley et~al., 2006). The observations were designed to obtain moderate signal-to-noise (S/N \sim 5) rest-UV spectra of the HRQs. The pg0900 grism,

with an observed wavelength coverage of 4486 to 6533Å, was chosen for the observations. All camera angles were considered to ensure that the C IV, He II and [C III] emission lines do not overlap with the gaps between the CCD chips. Given the faint nature of the rest-UV emission ($r_{AB} \simeq 21.48$), the exposure time for ULASJ2200+0056 was 2478 seconds.

The spectra were reduced using the PyRAF package - an STScI-developed command language for running IRAF tasks in Python (Science Software Branch at STScI, 2012). The individual spectra were then extracted using standard IRAF procedures for wavelength calibration, background subtraction and extraction of the 1D spectra. The wavelength calibration was performed using Xenon (Xe) lamp exposures taken immediately after the science spectra.

5.3 Methods

In this section, we discuss the spectral energy distributions (SEDs) of the HRQ sample discussed in Section 5.2. As in Chapter 4, we model the quasar emission using the QSOGEN² tool, a Python package that implements an empirically-motivated parametric model to simulate quasar colours, magnitudes and SEDs (Temple *et al.*, 2021b). We again make use of EMCEE, a Python package³ that explores the likelihood space using the affine-invariant ensemble sampler - proposed by Goodman & Weare (2010). Given that QSOGEN adopts a single blackbody with an effective temperature $T_{\rm eff}=1280\,\rm K$ and peak wavelength $\lambda_{peak}=2\mu m$ to describe the sublimation temperature dust emission, we limit our SED fits to $1000\rm \AA < ^{\sim} < 3^{-}m$ in the rest frame. This prevents the overextension of the SED model into redder wavelengths, where it is not designed to reproduce dust emission at colder temperatures, and is consistent with the method adopted in Temple *et al.* (2021a) for blue SDSS quasars - with redshifts, $1.5 < z_{\rm sys} < 2.65$ and an average 3000Å continuum luminosity $\log_{10}\{\lambda \rm L_{\lambda}(3000\mbox{Å}) \ [erg s^{-1}]\} = 45.6.$

5.3.1 Dust-reddened quasar model fit

In Chapter 4, we discovered that the HRQ - ULASJ2315+0143 - hosts an excess in the rest-UV emission given the extinction inferred at rest-optical wavelengths. However, it remains unclear whether excess UV emission is ubiquitous in the HRQ population. Consequently, we initially chose a dust-reddened quasar SED model with just three free parameters to fit the entire sample. The free parameters are as follows - (i) the 3000Å continuum luminosity of the quasar, $\log_{10}\{\lambda L_{\lambda}(3000\text{\AA})[\text{erg s}^{-1}]\}$ - (ii) the dust

²https://github.com/MJTemple/qsogen

³https://github.com/dfm/emcee

5.3. Methods 115

extinction, E(B-V)^{QSO} and (iii) the ratio in luminosity between the sublimation temperature dust and the tail of the UV/optical continuum slope at $2\mu m$, $L_{Dust}/L_{Disk}|_{2\mu m}$, which can be used as a proxy for the amplitude of the sublimation temperature dust emission (e.g. Figure 1; Temple *et al.*, 2021a). Hence, we permit the EMCEE package to explore an N-dimensional Gaussian likelihood function, where N represents the number of free parameters in the fit (N=3), and apply uniform priors.

As in Stepney *et al.* (2024), we assume the quasar extinction law discussed in Section 2.6 of Temple *et al.* (2021b), which is similar to those derived by Czerny *et al.* (2004) and Gallerani *et al.* (2010). In addition, QSOGEN features the *emline_type* parameter, which controls the equivalent widths of the key quasar emission lines - such as H α and C IV - giving the code the flexibility to vary the emission line contributions to the SED (Temple *et al.*, 2021b). The code is constructed such that the *emline_type* parameter scales linearly with the observed EWs; therefore, we use the H α EWs reported in (Banerji *et al.*, 2012, 2015; Temple *et al.*, 2019; Stepney *et al.*, 2024) to fix the *emline_type* parameter in our fitting. To estimate the *emline_type*, we use the measured H α EW as well as the H α EW and *emline_type* of ULASJ2315+0143 from Chapter 4 to conduct a linear interpolation. We use the default value - *emline_type* = 0 - for those objects for which we do not have H α measurements, as there is no evidence to suggest that the line EWs of HRQs differ from the blue SDSS quasars on which QSOGEN was developed (Temple *et al.*, 2019). We list the *emline_type* of each HRQ in Table 5.1.

QSOGEN also has the ability to model the effect of the host galaxy on a quasar's SED. The default host galaxy model used in QSOGEN is the S0 template from the SWIRE library (Polletta *et al.*, 2007; Rangwala *et al.*, 2008). The S0 template was chosen as it best replicates the median near-infrared photometry of the blue SDSS quasars (section 2.5; Temple *et al.*, 2021b). For the purpose of our preliminary SED fits, we set the host galaxy fraction, fragal = 0, however, we do explore the effects of introducing a non-zero host galaxy contribution on our final SED fits in Section 5.3.2.1.

Given that, for many of the HRQs, the photometric data comprise the weighted means of multiple surveys with different filter transmission curves, we adopt the following recipe to ensure that the model photometry is consistent with how the corresponding photometric data were constructed. First, we download the appropriate filter transmission curves from the SVO Filter Profile Service (Rodrigo *et al.*, 2012; Rodrigo & Solano, 2020). We then calculate the model photometry for each filter and combine like photometric bands using the same weights as adopted when constructing the initial data.

TABLE 5.1: The H α EWs taken from Banerji *et al.* (2012, 2015); Temple *et al.* (2019); Stepney *et al.* (2024) and their corresponding *emline_type* for the entire HRQ sample. Where H α EWs are unavailable, we assume *emline_type* = 0.

Object	Hα EW	emline_type			
ULASJ0016-0038	883	2.2			
ULASJ0041-0021	281	-3.2			
ULASJ0123+1525	1379	4.0			
ULASJ0141+0101	490	-1.3			
ULASJ0144+0036	377	-2.3			
ULASJ0144-0114	286	-3.2			
ULASJ0221-0019	656	0.1			
ULASJ1002+0137	_	0.0			
ULASJ1234+0907	432	-1.8			
ULASJ1415+0836	_	0.0			
ULASJ1539+0557	_	0.0			
ULASJ2200+0056	461	-1.5			
ULASJ2224-0015	624	-0.1			
ULASJ2312+0454	_	0.0			
ULASJ2315+0143	820	1.4			
VHSJ1117-1528	342	-2.6			
VHSJ1122-1919	513	-1.1			
VHSJ1301-1624	364	-2.4			
VHSJ1350-0503	_	0.0			
VHSJ1409-0830	_	0.0			
VHSJ1556-0835	733	0.7			
VHSJ2024-5623	1148	3.9			
VHSJ2028-4631	647	0.1			
VHSJ2028-5740	905	2.3			
VHSJ2048-4644	796	1.3			
VHSJ2100-5820	672	0.2			
VHSJ2101-5943	1193	4.0			
VHSJ2109-0026	1070	3.1			
VHSJ2115-5913	529	-1.0			
VHSJ2130-4930	448	-1.7			
VHSJ2141-4816	767	0.9			
VHSJ2143-0643	845	1.9			
VHSJ2144-0523	768	0.9			
VHSJ2212-4624	1539	4.0			
VHSJ2220-5618	450	-1.7			
VHSJ2227-5203	695	0.4			
Continued on next page					

5.3. Methods 117

Table 5.1 – continued from previous page

Object	Hα EW	emline_type
VHSJ2256-4800	650	0.1
VHSJ2257-4700	1320	4.0
VHSJ2306-5447	1686	4.0
VHSJ2332-5240	960	2.7
VHSJ2355-0011	1155	3.3
VIKJ2205-3132	485	-1.3
VIKJ2214-3100	_	0.0
VIKJ2228-3205	560	-0.7
VIKJ2230-2956	_	0.0
VIKJ2232-2844	762	0.8
VIKJ2238-2836	_	0.0
VIKJ2241-3006	_	0.0
VIKJ2243-3504	445	-1.7
VIKJ2245-3516	_	0.0
VIKJ2251-3433	_	0.0
VIKJ2256-3114	394	-2.2
VIKJ2258-3219	_	0.0
VIKJ2306-3050	_	0.0
VIKJ2309-3433	647	0.0
VIKJ2313-2904	_	0.0
VIKJ2314-3459	414	-2.0
VIKJ2323-3222	475	-1.4
VIKJ2350-3019	337	-2.7
VIKJ2357-3024	_	0.0

We calculate an average reduced chi-squared statistic, $\langle \overline{\chi_{\nu}^2} \rangle = 15.3$, for the single-component SED model, however, this reduces to $\langle \overline{\chi_{\nu}^2} \rangle = 2.2$ when we consider only the 10/60 HRQs whose wavelength coverage does not extend blue-ward of 4000Å. This both suggests that the average HRQ SED is inconsistent with a typical dust-attenuated quasar SED and that the primary driver of the poor SED fits is the rest-frame UV photometry. Given that a single-component SED model is seemingly insufficient to fit the photometric data for most HRQs, we explore a multi-component SED model as an alternative in Section 5.3.2.

5.3.2 Dust-reddened quasar + scattered light model fit

In Chapter 4, we find that the UV continuum of ULASJ2315+0143 is consistent with both scattered AGN emission **and** star formation in the merging host. Consequently, these two models are degenerate and yield an equally good fit to the continuum. Therefore, we need only adopt one multi-component SED model to fit the rest-UV photometry of HRQs. Since broad rest-frame UV emission lines are also detected in ULASJ2315 +0143, we employ a two-component SED model composed of a dust-attenuated quasar and scattered AGN emission for the 50/60 HRQs whose wavelength coverage extends blue-ward of 4000Å in the rest frame.

Our updated SED model now has an additional free parameter - i.e. the fraction of the total intrinsic quasar SED scattered at rest-UV wavelengths, F_{UV} . Therefore, only those objects whose wavelength coverage extends across ≥ 5 photometric bands are re-fit with the updated model - accounting for all 50/60 HRQs with coverage blue-ward of 4000\AA . We impose the following criteria for the UV excess to be considered statistically significant - (i) the scattered component must contribute at least 50 per cent of the flux to the blue-most photometric band - (ii) the $\overline{\chi}^2_\nu$ of the two-component model must represent > 2 multiplicative factor improvement over the single-component model and (iii) the best-fit SED model **without** the additional scattered component must satisfy $\overline{\chi}^2_\nu \geq 5$. Objects that meet just two of these criteria are considered *inconclusive* results. Objects that fail to meet at least two of these criteria are not considered to host a statistically significant UV excess, and the scattered component is therefore *rejected*. Should all three criteria be met, the UV excess is considered *confirmed*. An example of each case is presented in Fig. 5.1.

5.3. Methods 119

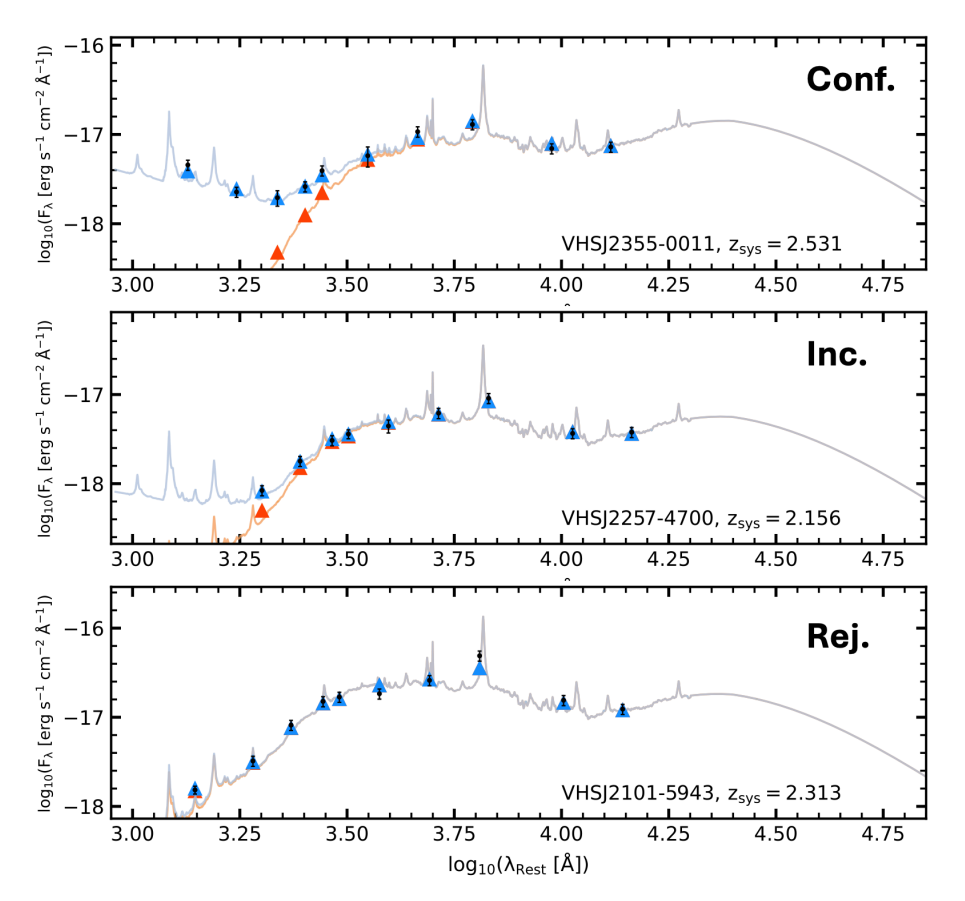


FIGURE 5.1: Example SED fits for HRQs where a UV excess is "confirmed" (top), "inconclusive" (middle) or "rejected" (bottom). The photometric data and associated uncertainties are presented in black. The best-fit SED model and photometry are presented by the blue line and triangles. The dust attenuated quasar component and photometry are presented by the orange line and triangles. In the "confirmed" case, there is clear evidence of a UV excess. In the "inconclusive" case, there is tentative evidence of a UV excess, but the wavelength coverage does not extend blue enough to constrain the model. In the "rejected" case, there is no evidence to support that the two-component model yields a better fit than a single-component reddened quasar SED.

5.3.2.1 Exceptions and special cases

The quality of the SED fits is again determined by the reduced chi-squared statistic, $\overline{\chi_{\nu}^2}$. We initially calculate an average reduced chi-squared for the entire HRQ sample, $\langle \overline{\chi_{\nu}^2} \rangle = 2.6$ for our multi-component model. This increases to $\langle \overline{\chi_{\nu}^2} \rangle = 7.6$ when only objects whose systemic redshifts satisfy $z_{\rm sys} < 1.5$ are considered. The poorer model fitting to the lower redshift objects is most likely driven by contributions from old stellar populations in the quasar host galaxy. The average optical luminosity of the $z_{\rm sys} < 1.5$ sample is $\log_{10}\{\lambda L_{\lambda}(3000 \text{\AA}) \text{ [erg s}^{-1}]\} = 45.7$ compared to $\log_{10}\{\lambda L_{\lambda}(3000 \text{Å}) \text{ [erg s}^{-1}]\} = 47.1$ at $z_{\rm sys} > 1.5$. Consequently, the stellar continuum in the lower-redshift objects may contribute more significantly to the SED at near-infrared wavelengths.

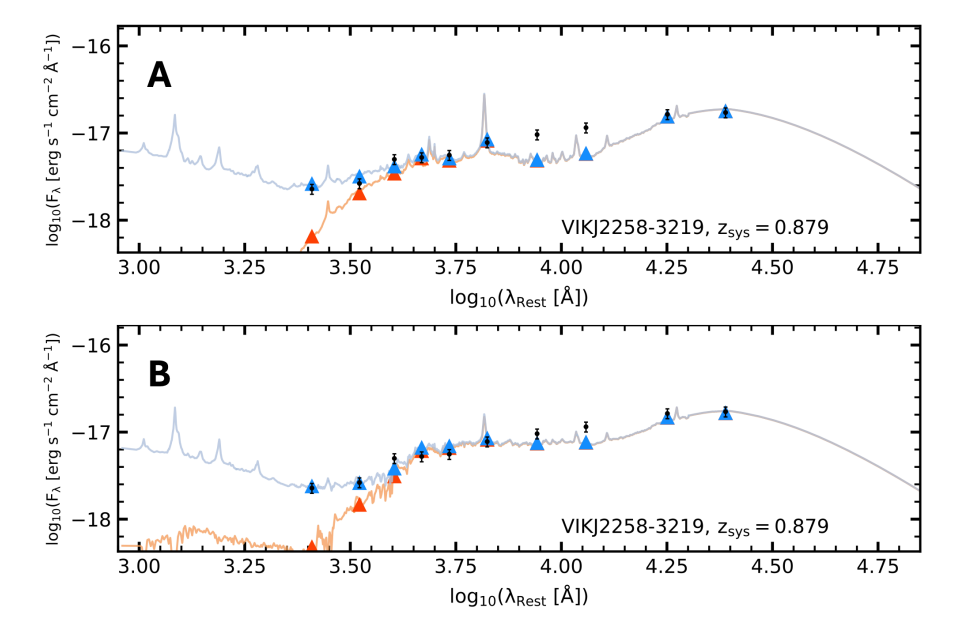


FIGURE 5.2: The "best-fit" SED for the HRQ VIKJ2258-03219 with no galaxy contribution (Panel A) and with fragal=0.05 (Panel B). The photometric data and associated uncertainties are presented in black. The best-fit SED model and photometry are presented by the blue line and triangles. The dust attenuated quasar component and photometry are presented by the orange line and triangles. At near-infrared wavelengths the model is unable to reproduce the photometry in Panel A, suggestive of old stellar populations having a significant contribution to the SED in this region. Hence, the inclusion of a galaxy component in Panel B improves the fit.

As discussed in Section 5.3.1, QSOGEN has the flexibility to model the host galaxy contribution to the SED via the inclusion of the SWIRE S0 template. The S0 template was chosen as it best replicates the median near-infrared photometry of the blue SDSS quasars on which QSOGEN was designed (section 2.5; Temple et al., 2021b), and therefore we do not expect the template to fully reproduce the UV excess in the z_{sys} < 1.5 HRQ sample. To determine the optimal galaxy fraction, we model the SEDs of the low-redshift sample setting the host galaxy fraction, fragal = 0.01, 0.03, 0.05, 0.07, 0.09. We then determine the average reduced chi-squared statistic after each run and find that the optimum galaxy fraction is fragal = 0.05, yielding an average reduced chi-squared of $\langle \overline{\chi_{\nu}^2} \rangle = 3.2$. An example SED is presented in Fig. 5.2, illustrating how the inclusion of the host galaxy component can significantly improve the SED model at infrared wavelengths. With the addition of the host galaxy component, the average reduced chi-squared for the $z_{sys} > 1.5$ sample is $\langle \chi_{\nu}^2 \rangle = 2.4$, decreasing to $\langle \chi_{\nu}^2 \rangle = 1.9$ when the S0 template is omitted - for this reason we only include a host galaxy component in the SED fits for those HRQs whose redshifts satisfy the condition; $z_{\rm sys} < 1.5$.

5.3. Methods 121

Finally, should a single photometric band dominate the $\overline{\chi^2_{\nu}}$ - i.e. a single band constitutes > 50 per cent of the model uncertainty - the photometry is culled and the fit is rerun. The following objects have one photometric band removed from the fits due to anomalous photometry⁴;

- ULASJ0123+1525: *i*-band (Erroneous Photometry)
- ULASJ0141+0101: *J*-band (Erroneous Photometry)
- ULASJ2312+0454: *J*-band (Erroneous Photometry)

- VHSJ2028-4631: *J*-band (Erroneous Photometry)
- VIKJ2251-3433: *J*-band (Erroneous Photometry)
- VIKJ2205-3123: r-band ([C III] emission)

The final best-fit parameters are presented in Table 5.2, the quoted uncertainties represent only the Monte-Carlo uncertainties on the free parameters, and hence do not account for the uncertainties associated with flux extraction and calibration. The 10 HRQs for which it was not possible to conduct a multi-component SED fit to model the UV Excess are classified as "N/A". In addition, we present **all** SED fits in Appendix B.

 $^{^4}$ These amendments are reflected in the final catalogue presented in Appendix A

TABLE 5.2: The best-fit parameters for the 60 HRQs for which we conducted an SED fit with QSOGEN. Objects for which it was not possible to model the UV Excess are classified as "N/A". Objects for which a UV excess was confirmed, rejected or yielded inconclusive results are denoted as "Conf.", "Rej." or "Inc." respectively. HRQs whose redshift $z_{sys} < 1.5$ are modelled with fragal = 0.05, otherwise fragal = 0.00 Uncertainties represent the MCMC uncertainties only, and are therefore likely to be underestimated.

Object	\mathbf{z}_{sys}	$\log_{10}\{\lambda L_{\lambda}(3000\mathring{A})[\text{erg s}^{-1}]\}$	E(B-V) ^{QSO} [mag]	F _{UV} [%]	$L_{Dust}/L_{Disk} _{2\mu m}$	$\overline{\chi}^2_{ u}$	UV Excess
ULASJ0016-0038	2.194	46.63 ± 0.05	0.51 ± 0.03	_	2.40 ± 0.36	2.7	Rej.
ULASJ0041-0021	2.517	$47.27 {\pm} 0.04$	0.87 ± 0.02	0.05 ± 0.01	$0.35 {\pm} 0.22$	3.3	Conf.
ULASJ0123+1525	2.629	$48.12 {\pm} 0.09$	1.74 ± 0.09	0.05 ± 0.01	2.06 ± 0.37	5.9	Conf.
ULASJ0141+0101	2.562	46.61 ± 0.05	$0.48 {\pm} 0.03$	0.86 ± 0.04	1.94 ± 0.39	4.4	Conf.
ULASJ0144-0114	2.505	47.31 ± 0.10	$0.84{\pm}0.04$	0.11 ± 0.01	1.96 ± 0.29	1.3	Conf.
ULASJ0144+0036	2.283	47.14 ± 0.10	$0.84{\pm}0.04$	0.02 ± 0.01	$0.44{\pm}0.29$	1.6	Conf.
ULASJ0221-0019	2.247	46.91 ± 0.04	0.74 ± 0.02	0.10 ± 0.02	2.43 ± 0.27	1.1	Conf.
ULASJ1002+0137	1.595	46.59 ± 0.06	1.13 ± 0.07	0.06 ± 0.01	0.50 ± 0.26	1.8	Conf.
ULASJ1234+0907	2.503	48.13 ± 0.07	1.69 ± 0.08	_	1.05 ± 0.34	7.8	N/A
ULASJ1415+0836	1.120	45.95 ± 0.16	1.43 ± 0.09	_	$8.94 {\pm} 0.16$	24.2	N/A
ULASJ1539+0557	2.658	48.03 ± 0.07	1.26 ± 0.06	_	1.26 ± 0.37	0.4	N/A
ULASJ2200+0056	2.541	$47.44 {\pm} 0.05$	0.63 ± 0.02	0.28 ± 0.02	1.23 ± 0.36	0.5	Conf.
ULASJ2224-0015	2.223	46.97 ± 0.05	0.71 ± 0.03	0.13 ± 0.02	$1.86 {\pm} 0.34$	0.6	Conf.
ULASJ2312+0454	0.700	45.17 ± 0.16	$1.14{\pm}0.04$	1.49 ± 0.04	7.85 ± 0.18	3.5	Conf.
Continued on next page							

Continued on next page

Table 5.2 – continued from previous page

Object	\mathbf{z}_{sys}	$\log_{10}\{\lambda L_{\lambda}(3000\mathring{A})[\text{erg s}^{-1}]\}$	E(B-V) ^{QSO} [mag]	F _{UV} [%]	$L_{Dust}/L_{Disk} _{2\mu m}$	$\overline{\chi}^2_{ u}$	UV Excess
ULASJ2315+0143	2.566	47.69 ± 0.08	$1.40 {\pm} 0.08$	0.10 ± 0.02	1.68 ± 0.35	1.2	Conf.
VHSJ1117-1528	2.428	47.18 ± 0.07	0.97 ± 0.07	_	1.18 ± 0.35	1.2	N/A
VHSJ1122-1919	2.464	47.36 ± 0.06	0.87 ± 0.06	_	0.68 ± 0.32	4.2	N/A
VHSJ1301-1624	2.138	47.45 ± 0.07	$1.14{\pm}0.07$	_	1.07±0.27	1.2	N/A
VHSJ1350-0503	2.176	47.18 ± 0.05	0.77 ± 0.03	0.26 ± 0.01	1.04 ± 0.35	0.8	Conf.
VHSJ1409-0830	2.300	47.13 ± 0.07	$0.94{\pm}0.08$	_	2.10±0.34	1.6	N/A
VHSJ1556-0835	2.188	46.93 ± 0.07	0.78 ± 0.06	0.55 ± 0.04	0.75 ± 0.29	0.9	Conf.
VHSJ2024-5623	2.282	46.72 ± 0.09	0.91 ± 0.12	_	0.76 ± 0.30	0.4	N/A
VHSJ2028-4631	2.464	46.59 ± 0.05	0.49 ± 0.03	1.51±0.06	2.42±0.29	0.6	Conf.
VHSJ2028-5740	2.121	47.66 ± 0.06	1.19 ± 0.04	0.03 ± 0.01	1.60 ± 0.33	3.1	Conf.
VHSJ2048-4644	2.182	46.79 ± 0.05	0.09 ± 0.01	0.86 ± 0.06	2.87±0.29	1.3	Conf.
VHSJ2100-5820	2.360	47.08 ± 0.06	0.90 ± 0.03	0.03 ± 0.01	1.58 ± 0.31	1.9	Conf.
VHSJ2101-5943	2.313	47.27 ± 0.09	0.63 ± 0.03	_	2.41±0.33	1.9	Rej.
VHSJ2109-0026	2.344	46.66 ± 0.04	$0.64 {\pm} 0.03$	0.29 ± 0.02	1.73 ± 0.34	2.9	Conf.
VHSJ2115-5913	2.115	47.49 ± 0.05	1.07 ± 0.04	0.12 ± 0.01	1.62±0.32	1.6	Conf.
VHSJ2130-4930	2.448	47.21 ± 0.06	0.92 ± 0.04	0.13 ± 0.02	1.43 ± 0.37	2.2	Conf.
Continued on next need							

Continued on next page

Table 5.2 – continued from previous page

Object	\mathbf{z}_{sys}	$\log_{10}\{\lambda L_{\lambda}(3000\mathring{A})[\text{erg s}^{-1}]\}$	E(B-V) ^{QSO} [mag]	F _{UV} [%]	$L_{Dust}/L_{Disk} _{2\mu m}$	$\overline{\chi}^2_{\nu}$	UV Excess
VHSJ2141-4816	2.655	47.38±0.05	0.87 ± 0.03	$0.14{\pm}0.01$	1.14±0.38	0.6	Conf.
VHSJ2143-0643	2.383	46.93 ± 0.08	$0.81 {\pm} 0.09$	0.75 ± 0.04	1.99 ± 0.28	0.4	Inc.
VHSJ2144-0523	2.152	46.81 ± 0.07	$0.82 {\pm} 0.08$	_	2.26 ± 0.35	1.7	N/A
VHSJ2212-4624	2.141	46.87 ± 0.06	0.97 ± 0.07	_	2.52 ± 0.37	3.4	N/A
VHSJ2220-5618	2.220	47.74 ± 0.04	0.92 ± 0.02	0.04 ± 0.01	$2.24{\pm}0.37$	1.4	Conf.
VHSJ2227-5203	2.656	47.15 ± 0.08	0.76 ± 0.04	0.13 ± 0.02	2.14 ± 0.36	7.9	Conf.
VHSJ2256-4800	2.250	47.23 ± 0.05	$0.85 {\pm} 0.03$	0.19 ± 0.02	2.63 ± 0.35	3.1	Conf.
VHSJ2257-4700	2.156	46.69 ± 0.05	0.74 ± 0.03	0.13 ± 0.03	2.48 ± 0.36	0.3	Inc.
VHSJ2306-5447	2.372	46.93 ± 0.05	0.78 ± 0.03	0.11 ± 0.01	1.32 ± 0.34	1.1	Conf.
VHSJ2332-5240	2.450	$46.64{\pm}0.04$	0.73 ± 0.04	0.53 ± 0.01	1.78 ± 0.35	3.7	Conf.
VHSJ2355-0011	2.531	47.29 ± 0.05	$0.90 {\pm} 0.04$	0.24 ± 0.02	$2.68 {\pm} 0.34$	0.8	Conf.
VIKJ2205-3132	2.307	46.57 ± 0.05	0.71 ± 0.03	0.15 ± 0.02	0.70 ± 0.30	4.0	Conf.
VIKJ2214-3100	1.069	45.72 ± 0.04	$1.47{\pm}0.12$	0.25 ± 0.03	7.37 ± 0.34	14.5	Inc.
VIKJ2228-3205	2.364	46.13 ± 0.06	$0.66 {\pm} 0.04$	0.39 ± 0.03	2.14 ± 0.37	0.6	Conf.
VIKJ2230-2956	1.319	46.08 ± 0.03	1.63 ± 0.13	0.36 ± 0.03	6.06 ± 0.36	6.6	Conf.
VIKJ2232-2844	2.292	46.92 ± 0.03	0.89 ± 0.06	_	1.76 ± 0.26	0.9	Rej.

Continued on next page

Table 5.2 – continued from previous page

Object	\mathbf{z}_{sys}	$\log_{10}\{\lambda L_{\lambda}(3000\mathring{A})[\text{erg s}^{-1}]\}$	E(B-V) ^{QSO} [mag]	F _{UV} [%]	$L_{Dust}/L_{Disk} _{2\mu m}$	$\overline{\chi}^2_{\nu}$	UV Excess
VIKJ2238-2836	1.231	46.18 ± 0.03	$1.46 {\pm} 0.08$	0.49 ± 0.03	5.11 ± 0.32	3.6	Inc.
VIKJ2241-3006	0.720	45.33 ± 0.06	1.47 ± 0.23	0.38 ± 0.04	7.30 ± 0.33	4.8	Conf.
VIKJ2243-3504	2.085	47.32 ± 0.05	1.19 ± 0.05	0.24 ± 0.03	1.72 ± 0.31	1.1	Conf.
VIKJ2245-3516	1.335	46.02 ± 0.03	1.38 ± 0.09	_	12.72 ± 0.41	9.3	Rej.
VIKJ2251-3433	1.693	46.38 ± 0.05	1.07 ± 0.17	0.27 ± 0.03	2.77 ± 0.36	2.0	Conf.
VIKJ2256-3114	2.329	46.85 ± 0.04	$0.88 {\pm} 0.04$	0.45 ± 0.03	1.91 ± 0.36	0.7	Conf.
VIKJ2258-3219	0.879	45.78 ± 0.04	$1.46 {\pm} 0.15$	0.39 ± 0.04	5.82 ± 0.32	3.6	Conf.
VIKJ2306-3050	1.060	45.51 ± 0.05	$1.44{\pm}0.16$	0.25 ± 0.04	3.40 ± 0.32	3.6	Inc.
VIKJ2309-3433	2.159	46.12 ± 0.04	$0.67 {\pm} 0.04$	0.88 ± 0.04	3.60 ± 0.35	1.7	Conf.
VIKJ2313-2904	1.851	46.38 ± 0.04	0.99 ± 0.08	0.62 ± 0.04	3.29 ± 0.35	3.7	Conf.
VIKJ2314-3459	2.325	46.66 ± 0.04	0.75 ± 0.03	0.50 ± 0.03	2.28 ± 0.34	1.8	Conf.
VIKJ2323-3222	2.191	47.02 ± 0.06	$0.97{\pm}0.04$	0.07 ± 0.01	$0.86 {\pm} 0.31$	2.3	Conf.
VIKJ2350-3019	2.324	46.61 ± 0.05	0.75 ± 0.03	0.16 ± 0.02	1.25 ± 0.36	1.0	Conf.
VIKJ2357-3024	1.129	45.77 ± 0.05	1.38 ± 0.15	0.24±0.03	$4.47{\pm}0.37$	4.5	Conf.

5.4 Results

5.4.1 Ubiquitous excess UV emission in HRQs

Our analysis suggests that excess UV emission is ubiquitous amongst HRQs. We find a statistically significant UV excess in 41/50 of the HRQs for which photometric data blue-ward of 4000Å was available, representing 82 per cent of the sample. Objects without a statistically significant UV excess represent just 4/50 of the sample, or equivalently 8 per cent. The remaining 5/50, or equivalently 10 per cent, of the HRQs are considered inconclusive by our analysis. However, the average scattering fraction of the HRQ sample is low - i.e. $\langle F_{\rm UV} \rangle_{HRQs} = 0.26\%$ - when compared to other red AGN populations (e.g. \sim 3% in LRDs; Greene *et al.*, 2024). Since the HRQ selection was derived prior to the discovery of blue photometric colours in their rest-UV continua (i.e. Wethers *et al.*, 2018) and also the discovery of *JWST*'s LRDs, the *i*-band magnitude and $(i-K)_{\rm AB}$ colour selections may inadvertently show preference to HRQs for which the scattering fraction, $F_{\rm UV}$, is low.

Fig. 5.3 shows that the *i*-band magnitude selection is unlikely to be the primary driver of the low scattering fractions observed in HRQs. The *i*-band selection threshold (20.5 mag) is $\sim 3.2\sigma$ from the sample mean, $\langle i_{\rm AB} \rangle = 22.69 \pm 0.69$, and there is no correlation between $i_{\rm AB}$ and $F_{\rm UV}$, hence, the *i*-band selection is not *directly* linked to the low scattering fractions. However, the $(i-K)_{\rm AB}$ colour selection threshold (2.5 mag) is only $\sim 2.0\sigma$ from the sample mean, $\langle (i-K)_{\rm AB} \rangle = 3.98 \pm 0.75$. We also observe a strong anti-correlation between the scattering fraction, $F_{\rm UV}$, and the $(i-K)_{\rm AB}$ colour-with a Pearson Correlation Co-efficient $R_{PCC} = -0.86$ and p-value = 3×10^{-12} . This suggests that should HRQs with scattering fractions $F_{\rm UV} \gtrsim 1\%$ exist, they would breach the $(i-K)_{\rm AB}$ colour selection and therefore would not appear in our sample.

5.4.1.1 Rest-Ultraviolet line properties of ULASJ2200+0056

A primary aim of this work is to determine the nature of the UV-excess in the HRQ sample. Broad emission lines at rest-UV wavelengths have already been detected in the VLT-XShooter spectrum of the HRQ - ULASJ2315+0143 - which has been interpreted as scattered quasar emission (Stepney *et al.*, 2024, see Chapter 4). To determine whether scattered quasar emission is the primary source of the UV excess in another HRQ, we turn our attention to analysing the rest-UV spectral line properties of ULASJ2200+0056.

We detect both C IV $\lambda\lambda$ 1548, 1551 and He II λ 1640 emission in the SALT spectrum of ULASJ2200+0056 - Fig. 5.4. To determine the C IV line properties, we first define a power-law continuum, $f(\lambda) \propto \lambda^{-\alpha}$ following the same recipe as described in Chapter

5.4. Results 127

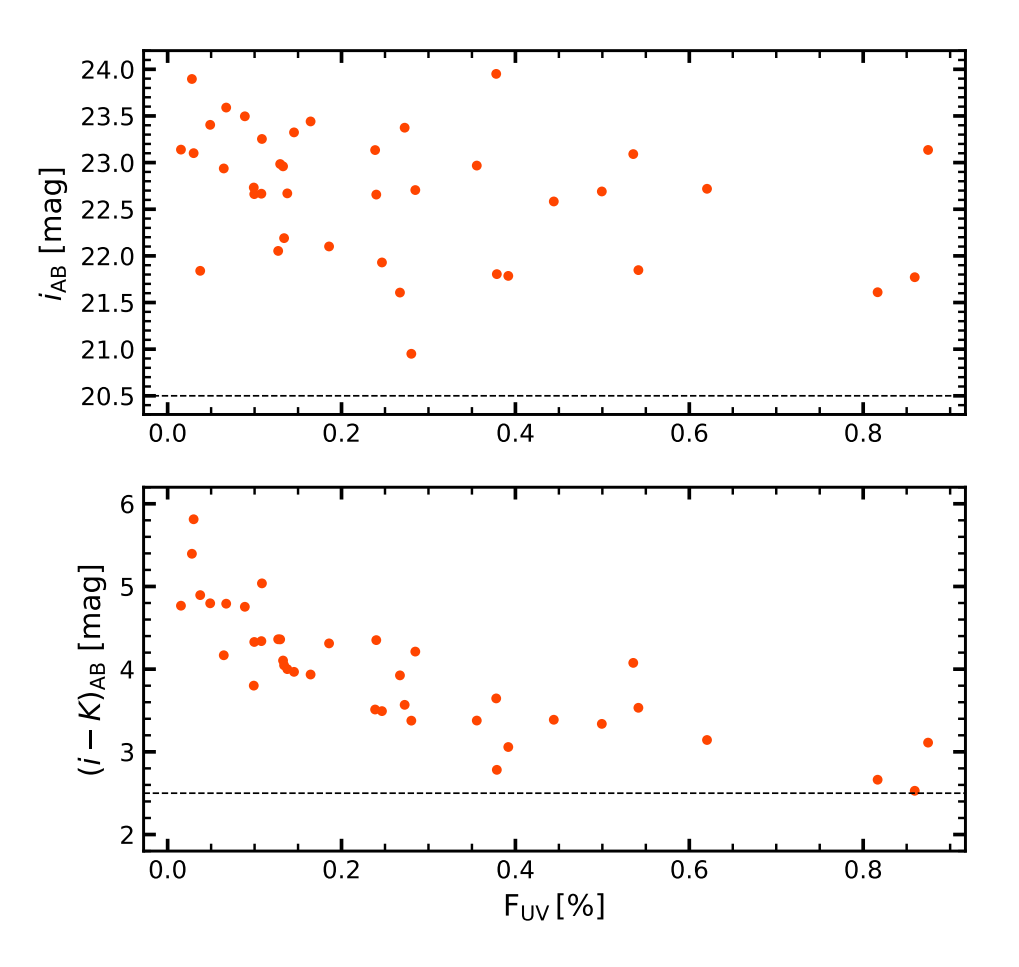


FIGURE 5.3: The scattering fraction, $F_{\rm UV}$, vs the i-band magnitude (top) and the $(i-K)_{\rm AB}$ colour (bottom), calculated from the best-fit SED models for the 39 HRQs that exhibit a statistically significant UV excess. The HRQ selections are represented by dashed black lines in their respective panels. The i-band magnitude does not appear correlated with $F_{\rm UV}$, however, there is a strong anti-correlation between $F_{\rm UV}$ and the $(i-K)_{\rm AB}$ colour. It is likely that this colour selection prevents HRQs with higher scattering fractions from being selected.

3 - i.e., we implement a non-parametric approach in which the median values of F_{λ} in the two wavelength regions 1445–1465Å and 1700–1705Å are used to anchor the power-law approximation (see; Coatman *et al.*, 2016, 2017, for details). We use the same recipe for He II, but adjust the blue wavelength region to 1600–1610Å.

We fit the C IV emission with a composite Gaussian model containing two components - the first to reconstruct the core emission and the second to reconstruct any blue wings. The detection of blue asymmetries in the C IV profile is interpreted as evidence for broad-line region outflows (e.g. Richards *et al.*, 2011; Baskin *et al.*, 2015; Rankine *et al.*, 2020; Temple *et al.*, 2024; Stepney *et al.*, 2024). We fit the He II with a single Gaussian component as low-ionisation lines are not expected to trace outflows. To enable the most robust reconstructions of the emission line profiles, narrow absorption features must first be masked. We adopt an iterative approach for this - similar to Stepney *et al.* (2024). First, we fit the SALT spectra with our emission line model

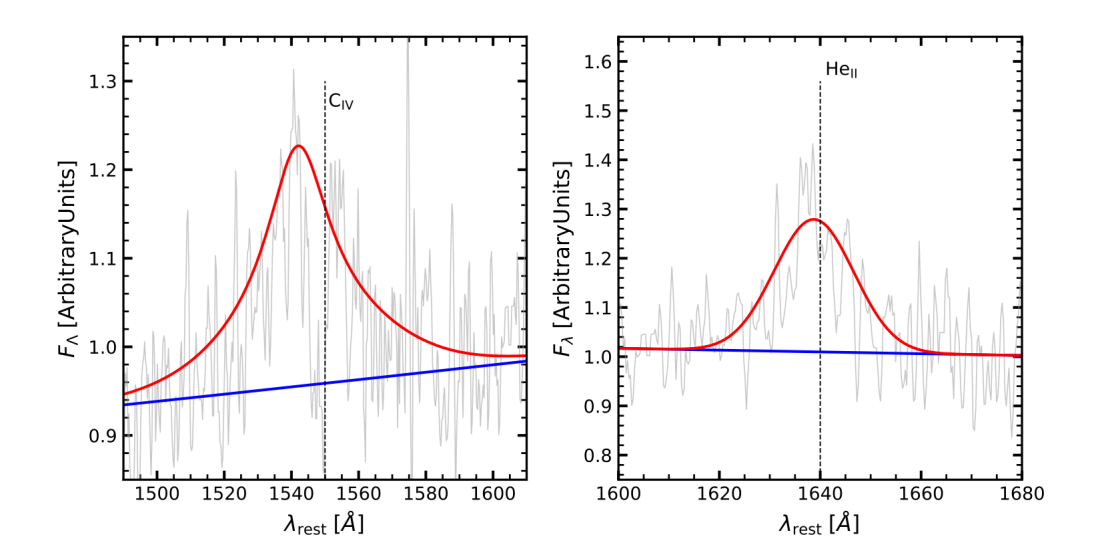


FIGURE 5.4: The SALT spectra of ULASJ2200+0056 in the C IV and He II emission regions are presented in grey. The continua are presented in blue and the final line reconstructions are presented in red. Both emission lines exhibit a FWHM >> 1000 km s⁻¹ and are hence considered broad.

TABLE 5.3: The rest-UV emission line properties of the HRQ, ULASJ2200+0056.

Species	EW [Å]	$V50 [{\rm km s^{-1}}]$	$FWHM [km s^{-1}]$
CIV	9.4 ± 0.8	966±352	6860±1250
He II	5.2 ± 0.6	310±180	3510±620

without masking, the result of which serves as a pseudo-continuum for subsequent fits. Pixels whose flux falls $> 2\sigma$ below the pseudo-continuum are then replaced by the corresponding flux element in the pseudo-continuum itself. The fitting procedure is then repeated. We find that three iterations are sufficient to robustly mask the narrow absorption. The line reconstructions are presented in Fig. 5.4.

The EW measurements are made via numerical integration. Due to the well-known asymmetry of the C IV emission line (Richards *et al.*, 2011), we again define line blueshifts with Eqn. 3.1 - i.e. the difference in velocity between the line centroid (V50) and the rest-frame wavelength. For both emission lines, uncertainties are derived by sampling 500 spectra perturbed by Gaussian noise consistent with the noise array. We then use the distribution means and standard deviations to determine our final results - presented in Table. 5.3. The detection of broad (FWHM \geq 1000 km s⁻¹) C IV and He II emission confirms the presence of quasar emission at blue wavelengths in ULASJ2200+0056.

5.4. Results 129

5.4.2 Sublimation temperature dust properties

With WISE photometry available for all sources in the HRQ sample, it is possible to constrain their sublimation temperature dust properties. The dust sublimation temperature assumed by QSOGEN ($T_{\rm eff}=1280\,{\rm K}$), is consistent with the sublimation temperature of silicate dust (Rosa et al., 2013; Temple et al., 2021a) and determines the maximum permitted dust temperature before the dust grains are destroyed by the quasar radiation field. Hence, the relative amplitude of the sublimation temperature dust emission with respect to the tail of the accretion disk blackbody (i.e. $L_{Dust}/L_{Disk}|_{2\mu m}$) is a good measure of the amount of dust present on 10s-of-pc scales (Temple et al., 2021a).

In Chapter 4 we conclude that ULASJ2315+0143 has atypical sublimation- temperature dust properties, featuring much weaker $2\mu m$ dust emission than blue quasars of equivalent black-hole mass, luminosity and redshift. We calculate the mean sublimation temperature dust amplitude of the 60 HRQs for which an SED fit was conducted, yielding $\langle L_{Dust}/L_{Disk}|_{2\mu m}\rangle=1.7\pm0.8$ - consistent with ULASJ2315+0143 . To understand whether this result is biased by the infrared selection of the HRQ sample, we use QSOGEN to generate a family of models with various sublimation temperature dust amplitudes and trace how the $(J-K)_{AB}$ and (W1-W2) colour evolves with redshift. The results are presented in Fig. 5.5 and Fig. 5.6.

Figure 5.5 illustrates how the $(J-K)_{AB}$ colour is insensitive to the sublimation temperature dust at redshifts $z_{\rm sys} \geq 1.5$. Hence, when comparing sublimation temperature dust amplitudes across populations, we decide to consider only HRQs whose redshifts satisfy the condition: $z_{\rm sys} \geq 1.5$. This is because the hot dust amplitude in the lower redshift subsample is largely shaped by near-infrared selection effects - i.e. only the highest sublimation temperature dust amplitudes produce the required $(J-K)_{\rm AB}$ colour at low redshifts. The fact that we only observe objects whose sublimation temperature dust amplitudes are much larger than the sample mean at $z_{\rm sys} \sim 1$ is also consistent with Fig. 5.5. Conversely, Fig. 5.6 illustrates the strong dependence of the (W1-W2) colour on the sublimation temperature dust amplitudes, biasing the sample to higher dust amplitudes at redshift, $z_{\rm sys} \geq 2.0$. We note that increasing the E(B-V)^{QSO} enables HRQs with lower sublimation temperature dust amplitudes to meet the (W1-W2) colour selection.

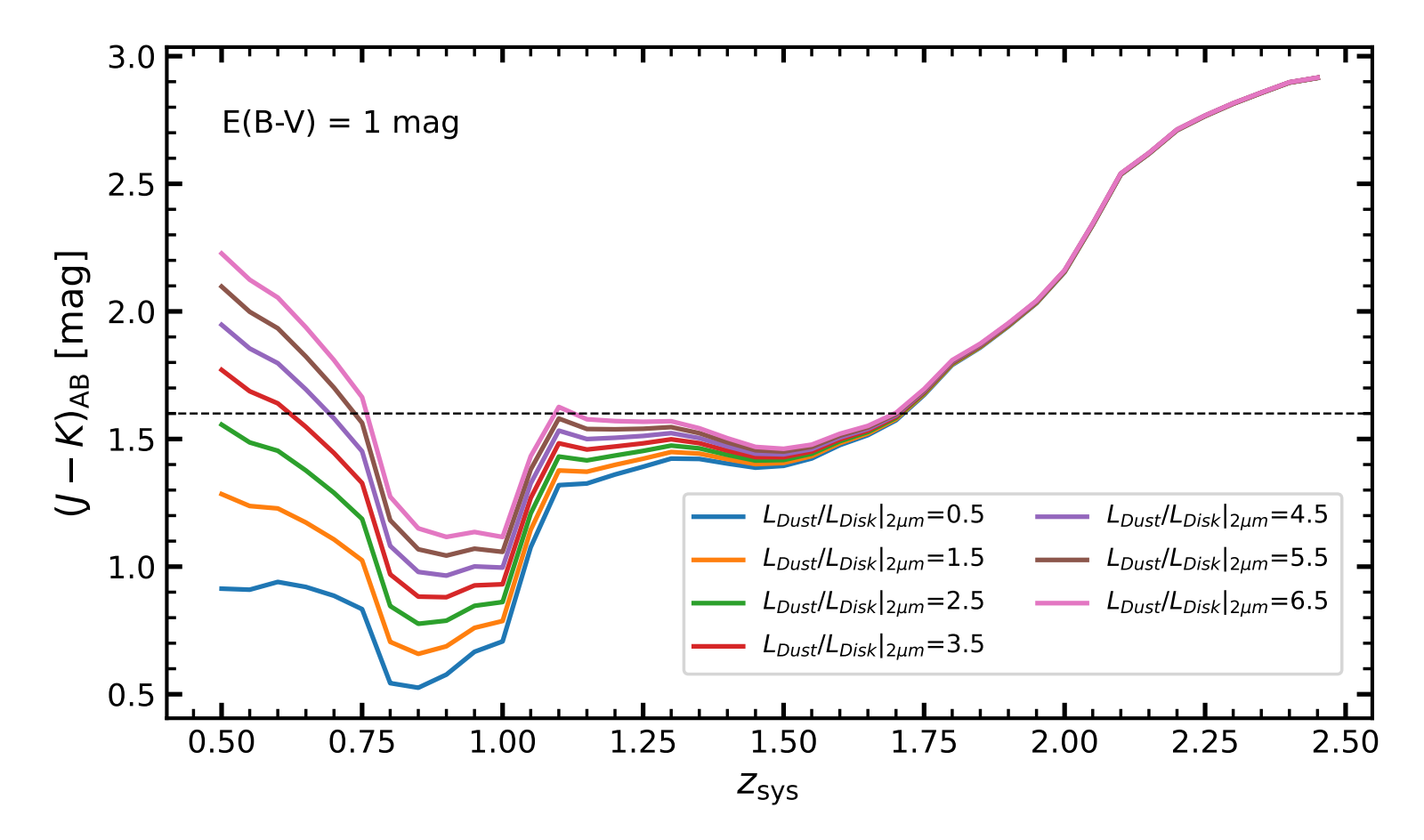


FIGURE 5.5: We present the $(J-K)_{AB}$ colours of various QSOGEN SED models as a function of the systemic redshift. Our $(J-K)_{AB}=1.6$ mag colour selection is illustrated by the black dashed line. We opt for an extinction $E(B-V)^{QSO}=1$ mag and a 3000Å continuum luminosity $\log_{10}\{\lambda L_{\lambda}(3000\text{Å})\}=47$ erg s⁻¹ - consistent with the mean extinction observed in the 60 HRQs for which an SED model was conducted. At $z_{\rm sys}\geq 1.5$, the $(J-K)_{\rm AB}$ colour is insensitive to the sublimation temperature dust amplitude. Below this redshift, the distribution is shaped by selection effects.

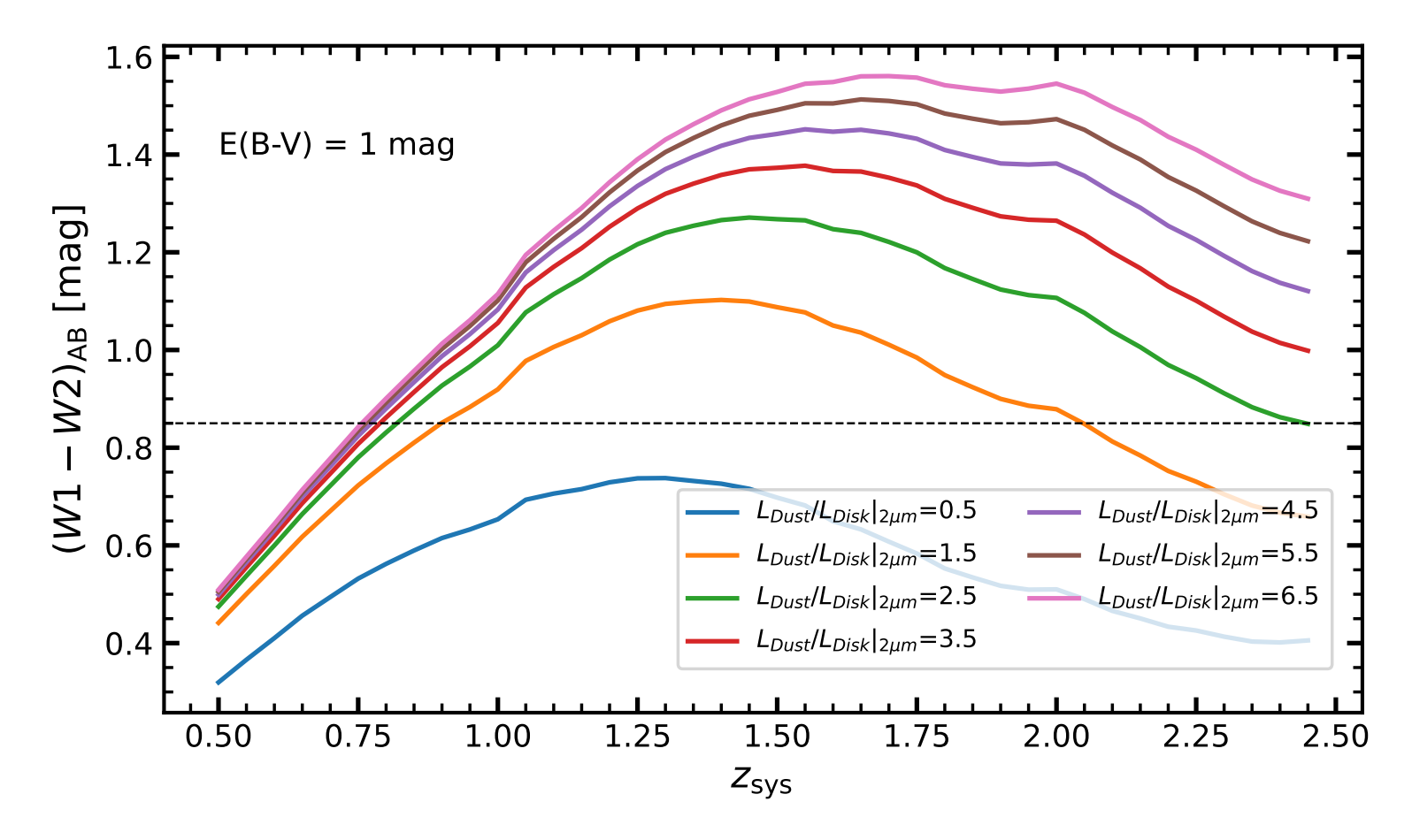


FIGURE 5.6: We present the (W1-W2) colours of various QSOGEN SED models as a function of the systemic redshift. Our (W1-W2)=0.85 mag colour selection is illustrated by the black dashed line. We opt for an extinction $E(B-V)^{QSO}=1$ mag and a 3000Å continuum luminosity $\log_{10}\{\lambda L_{\lambda}(3000\text{Å})\}=47$ erg s⁻¹ - consistent with the mean extinction and luminosity observed in the 60 HRQs for which an SED model was conducted. The (W1-W2) colour selection appears to bias our sample towards HRQs with higher sublimation temperature dust amplitudes.

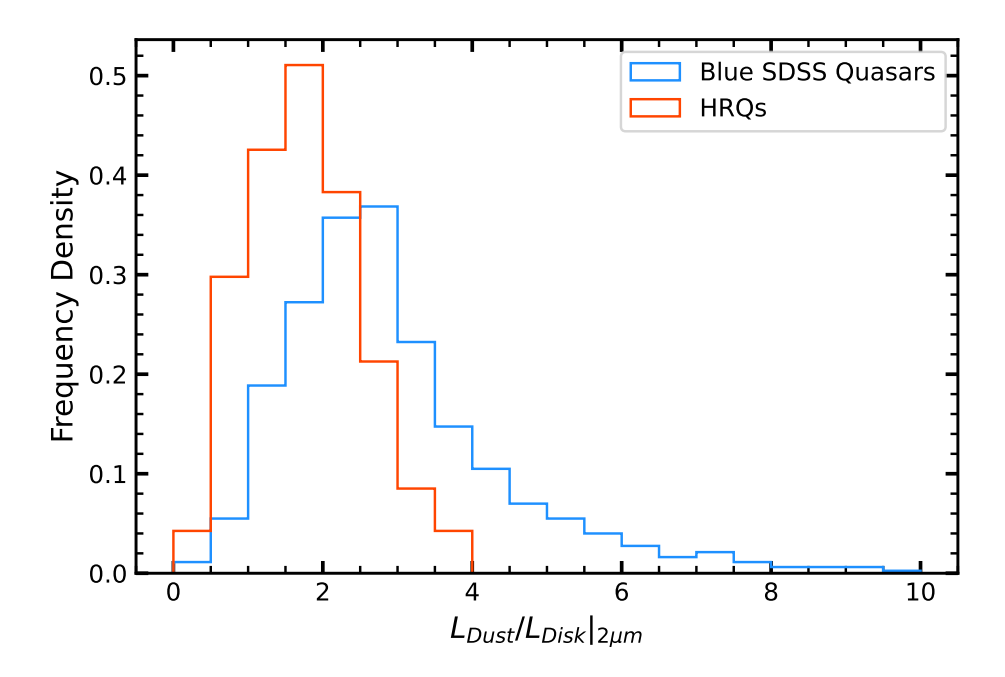


FIGURE 5.7: Histograms illustrating the ratio in luminosity between the sublimation temperature dust blackbody and the tail of the UV continuum slope at $2\mu m$. The $z_{\rm sys} \geq 1.5$ HRQ sample is presented in orange and the blue SDSS quasars studied in Temple et al. (2021a) are presented in blue. The HRQ histogram is systematically biased toward lower sublimation temperature dust amplitudes, implying that there is less dust in the inner regions of HRQs with respect to blue quasars at equivalent black-hole mass, luminosity and redshift.

The histograms in Fig. 5.7 illustrate the distribution of sublimation temperature dust amplitudes for the $z_{\rm sys} \geq 1.5$ HRQ sample in addition to the blue SDSS quasars studied by Temple *et al.* (2021a). While this does not account for the mid-infrared selection effects, it does ensure that our near-infrared selection has a minimum impact on the results. A "two-sided" Kolmogorov-Smirnov (KS) test yields a *p*-value = 2×10^{-5} , suggesting that the two distributions are statistically distinct. While HRQs do host a range of sublimation temperature dust amplitudes, they appear to be systematically biased towards lower amplitudes than those generally observed in the blue SDSS quasar sample. Since the (W1-W2) colour selection biases the HRQ sample to $L_{Dust}/L_{Disk}|_{2\mu m}>2.5$ at $z_{\rm sys}>2$ when we assume the average dust extinction of an HRQ (E(B-V)=1 mag), we would expect that there exists many more HRQs with low sublimation-temperature dust amplitudes that have escaped our selection, serving only to amplify the difference between the distributions. This result implies that HRQs host significantly less torus-scale dust than their blue counterparts.

5.5. Discussion 133

5.5 Discussion

In this section, we discuss our results in the context of other AGN populations. First we compare the origin of the blue photometric colours observed in HRQs to that of "little red dots" (LRDs). Then we discuss the sublimation temperature dust properties of the HRQ population and draw comparisons to other red AGN populations as well as dust-poor blue quasars and the Temple *et al.* (2021b) blue SDSS quasar sample. We end with a discussion on the potential links between the rest-UV and infrared properties of HRQs and suggest amendments to the selection so that a more complete sample of extincted quasars can be identified at comic noon.

5.5.1 The source of the UV excess in red AGN

A defining characteristic of *JWST*'s LRDs is their red rest-optical continua in addition to their blue rest-UV photometric colours - e.g. Onoue *et al.* (2023); Kocevski *et al.* (2023); Greene *et al.* (2024); Kocevski *et al.* (2024). In Section 5.4.1 we conclude that excess emission at rest-UV wavelengths is common in the HRQ sample. Given the qualitative similarities between the UV/optical SEDs observed in HRQs and LRDs, HRQs could trace hyper-luminous analogues of the LRD population at cosmic noon (Stepney *et al.*, 2024). We now further explore the source of the UV excess in HRQs and test whether HRQs and LRDs are tracing similar physics in their respective red AGN phases.

5.5.1.1 Photometric selection: LRDs vs HRQs

Using the LRD selection criteria described in Kocevski *et al.* (2024), we first determine which of our HRQs could be formally classified as an LRD. The selection criteria is defined in the rest-frame and describes the continuum blue-ward and red-ward of the 3645Å break, hence, we only conduct this analysis on the 50 HRQs for which we have rest-UV coverage. To determine the UV and optical continuum slopes, $\beta_{\rm uv}$ and $\beta_{\rm opt}$, the continuum is split at 3645Å. Both sides are then fit via a least-squares minimisation of Eqn. 5.1;

$$m_i = -2.5 \,\beta \log_{10}(\lambda_i) + c \tag{5.1}$$

where m_i is the AB magnitude of the i^{th} filter, β is the continuum slope, λ_i is the effective wavelength of the i^{th} filter in μm and c is a normalisation constant. An object is formally considered an LRD if it's continua meet the following criteria (Kocevski *et al.*, 2024);

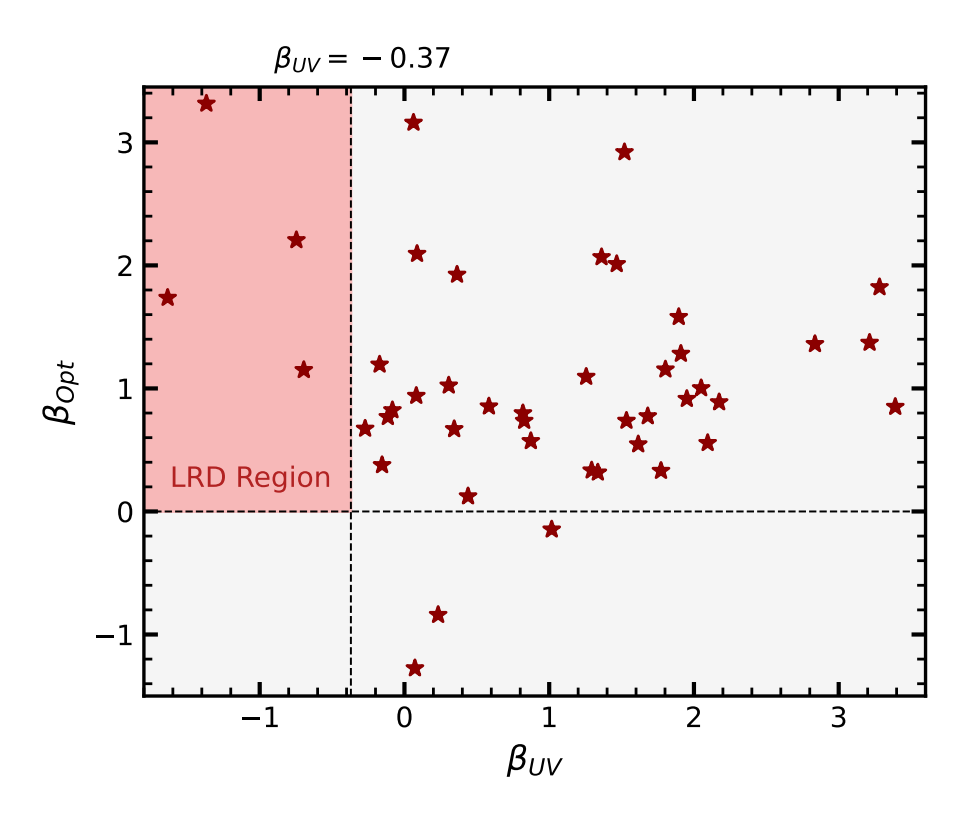


FIGURE 5.8: The optical continuum slope, $\beta_{\rm opt}$, vs the UV continuum slope, $\beta_{\rm uv}$, is presented for the 50 HRQs analysed in *this* work. The red shaded region represents the LRD parameter space and the dashed lines along the boundary mark the LRD selection criteria, $\beta_{\rm opt}>0$ and $-2.8<\beta_{\rm uv}<-0.37$. While 47/50 HRQs host sufficiently red rest-optical continua, only 4/50 host sufficiently blue rest-UV continua and would therefore be considered LRDs by this formalism.

1.
$$\beta_{\text{opt}} > 0$$

2.
$$-2.8 < \beta_{uv} < -0.37$$

By applying these criteria to the HRQ sample we find just 4/50 objects formally satisfy the constraints. In Fig. 5.8, we present the UV and optical continuum slopes of the HRQ sample, with the LRD selection criteria highlighted. From Fig. 5.8 it is clear that despite most sources (47/50) hosting sufficiently red optical continua, HRQs are insufficiently blue at rest-UV wavelengths to be considered an LRD in this formalism. To understand this result, we construct a noise-weighted pan-chromatic composite SED of the full HRQ sample and compare it to a composite SED of the LRD population - produced using COSMOS photometry (Akins *et al.*, 2024).

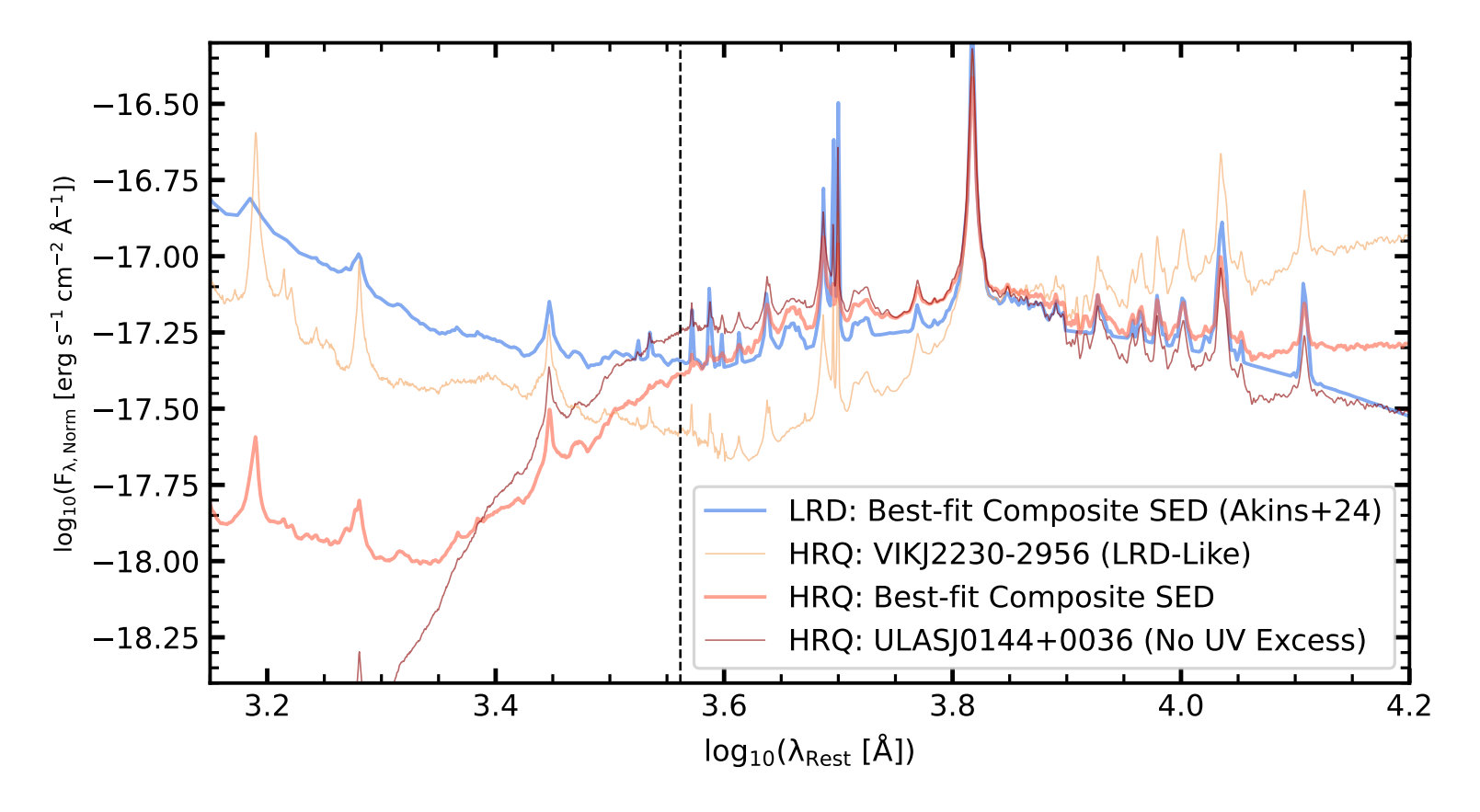


FIGURE 5.9: We present a composite SED model for LRDs (Akins *et al.*, 2024), in blue. The best-fit SED model for the "LRD-Like" HRQ - VIKJ2230-2956 - is presented in beige. The noise-weighted composite SED model for HRQs is presented in coral. The best-fit SED model for an HRQ with no statistically significant UV excess - ULASJ0144+0036 - is presented in maroon. The SEDs were normalised in the *K*-band at the average HRQ redshift, $z_{sys} = 2.12$. The Balmer Break is denoted by the dashed black line. At rest-optical wavelengths, LRDs and HRQs have similar SED shapes, however, the SEDs diverge blueward of H β , with LRDs exhibiting bluer continua than HRQs.

Both populations appear to host generally consistent continua at the rest-optical wavelengths, however, there is an unambiguous difference in the continua at rest-UV wavelengths. LRDs appear to host much bluer continua than the average HRQ, as expected from Fig. 5.8. Given that $(i-K)_{AB,Akins} \simeq 2.8$, the LRD composite SED represents the ceiling of the HRQ selection criteria discussed in Section 5.2, hence LRD-like HRQs with comparatively more luminous UV continua are most likely removed from our sample by our $(i-K)_{AB}$ colour selection. Nevertheless, the parameter space inhabited by HRQs in Fig. 5.8 is sparsely populated by LRDs in the UNCOVER field (Figure 3; Kocevski *et al.*, 2024), meaning there is a possibility that the source of the UV excess is fundamentally different in the two populations.

5.5.1.2 Exploring a different dust extinction law

The origin of the UV excess in LRDs is still hotly debated. While multi-component SED models comprised of host galaxy emission and an obscured AGN have been proposed (e.g. Greene *et al.*, 2024), there is an emerging consensus that the "V-shaped" UV/optical continuum is an intrinsic feature of the SED in LRDs. One such explanation invokes atypical dust properties, where an obscuring medium with a deficit of smaller-scale dust grains is unable to efficiently scatter emission at bluer wavelengths. A scattering medium with such properties can be found in the Orion nebula (Baldwin *et al.*, 1991), and it is reported that the Orion dust extinction law can well-reproduce the stacked photometric data of LRDs from the COSMOS field (Akins *et al.*, 2024) and JADES survey (Pérez-González *et al.*, 2024) without the need for an additional scattered/stellar emission component (Li *et al.*, 2025).

Since QSOGEN has the flexibility to run a custom dust extinction law (Temple *et al.*, 2021b), we refit the HRQ sample with a single-component SED model and adopt the Orion dust extinction law used by Li *et al.* (2025). In Fig. 5.10 we present the best-fit SED models for VIKJ2115-5913 (an HRQ that satisfies the LRD selection criteria with $\beta_{uv} = -0.7$ and $\beta_{opt} = 1.2$) and ULASJ0144-0114 (a more typical HRQ with $\beta_{uv} = 1.8$ and $\beta_{opt} = 0.3$). The Orion dust extinction law is much flatter than the Small Magellanic Cloud (SMC) dust extinction law (Figure 1; Li *et al.*, 2025), on which the default QSOGEN description of the dust is based. Hence, the Orion dust extinction law can broadly reproduce the shape of the continuum at rest-UV wavelengths without the need for a secondary scattered component. However, because the Orion dust law is so flat, it is unable to reproduce the rest-optical photometry.

5.5. Discussion 137

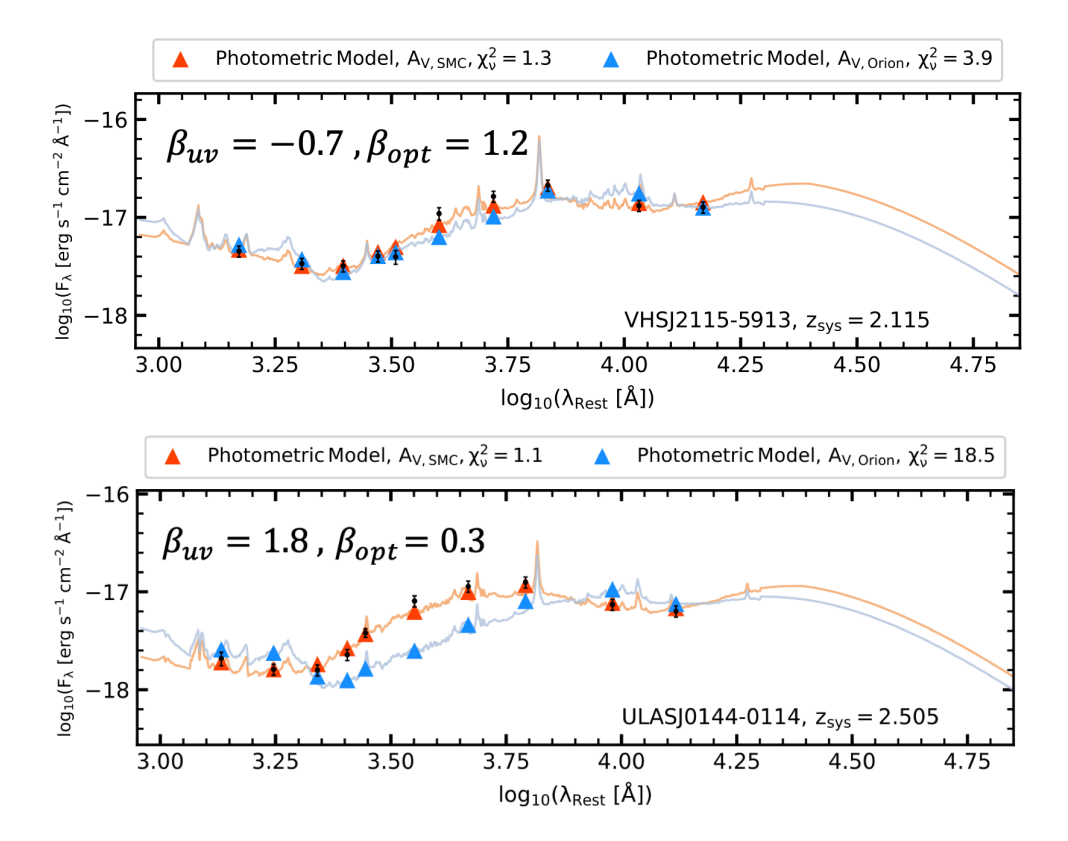


FIGURE 5.10: SED fits for the HRQs; VIKJ2115-5913 (top) and ULASJ0144-0114 (bottom). The photometric data and associated uncertainties are presented in black. The best-fit SED models using the Orion dust law are presented by the blue lines and triangles. The best-fit SED models using the SMC-like dust law used in QSOGEN are presented by the orange lines and triangles. In both cases, a multi-component model with an SMC-like dust extinction law is favoured (see the $\overline{\chi}^2_{\nu}$ statistics), despite VIKJ2243-3504 satisfying the LRD selection criteria. The Orion dust extinction law is flatter than the dust law used in QSOGEN. While this can produce favourable fits at rest-UV wavelengths, it is too flat to reproduce the rest-optical emission.

In Fig. 5.10, we see that the Orion dust extinction law produces better fits to HRQs that satisfy the LRD selection criteria than those that do not. Nevertheless, their respective multi-component SED models produce more successful fits to the photometry based on their $\overline{\chi}^2_{\nu}$ statistics. We find that not a single HRQ favours the Orion dust extinction law over the initial multi-component model discussed in Section 5.3. While it is possible that the scattering media of HRQs each host their own unique distribution of grain sizes and - by extension - their own atypical dust extinction laws, this interpretation of the UV excess is contrived, requiring a physically motivated description of multiple different dust geometries and properties. Consequently, we conclude that Orion-like dust properties are unlikely to be the primary cause of the UV excess in HRQs.

5.5.1.3 Balmer Absorption

The population densities of LRDs peak at much higher redshifts than HRQs (Kocevski et al., 2024), implying that the LRD population are a younger class of AGN.

Consequently, the fundamental differences in the SEDs of HRQs and LRDs could be interpreted as evidence that the two populations trace distinct red AGN phases - the older, more massive HRQs may be tracing a post-merger evolutionary phase whereas the younger, less massive LRDs likely trace a period of much earlier galaxy growth. This interpretation is supported by newly emerging evidence suggesting that the dense neutral gas, in which the accretion disk of LRDs is embedded, hosts very low metallicities (e.g. de Graaff et al., 2025; Naidu et al., 2025). Therefore, an alternative description of the UV excess observed in LRDs invokes strong Balmer Absorption - whereby the AGN accretion disk is embedded in dense neutral gas clumps, effectively absorbing the continuum emission blue-ward of the Balmer Break (e.g. Inayoshi & Maiolino, 2025; de Graaff et al., 2025; Naidu et al., 2025).

Balmer Absorption as a means to describe the UV excess in LRDs is particularly attractive since it can explain the sharp inflection points commonly observed in their SEDs $\lambda_{\rm rest} = 3645$ Å (e.g. Kocevski *et al.*, 2023; Kocevski *et al.*, 2024; Greene *et al.*, 2024; Li *et al.*, 2025). Furthermore, a non-stellar origin of the LRD continuum would explain their larger-than-expected stellar masses (Inayoshi & Maiolino, 2025). de Graaff *et al.* (2025) find evidence of extremely strong Balmer Absorption as well as broad H α and He I emission in a bright LRD at $z_{\rm sys} = 3.5$ in the absence of any significant metal lines. Hence, the continuum is unlikely to originate from stellar populations. Instead, the system has been dubbed a "Black Hole Star", characterised by a central ionising source embedded in dense, metal-poor absorbing gas with no need for a multi-component SED model such as the one described in Section 5.3 to explain the blue photometric colours in the rest-UV. Further evidence of the "Black Hole Star" model has been reported by Naidu *et al.* (2025), who also observe an exceptional Balmer Break in the LRD - MoM-BH* - which also cannot be explained by stellar populations.

In Fig. 5.8, we see that the HRQ photometry blue-ward of the Balmer Break traces redder continua than what is observed in LRDs. This implies that either the UV continua observed in the HRQ sample is redder than that of LRDs or that the inflection point of the rest-UV/optical SED in HRQs is not at $\lambda_{\rm rest}=3645$ Å. To calculate the inflection points of the HRQ sample, we determine the rest-frame wavelength at which their "best-fit" SEDs reach a minimum - in the wavelength range 1000-10000Å. In Fig. 5.11, we see that the rest-UV/optical inflection points of the 41 HRQ SEDs in which a statistically significant UV excess was observed are much bluer than the Balmer Break. In addition, unlike LRDs, the rest-UV/optical inflection points of the HRQ sample are **not** consistent with a single wavelength. We find that the average UV/optical inflection point $\langle \lambda_{\rm rest} \rangle = 2156 \pm 493$ Å in HRQs. Given that the

5.5. Discussion 139

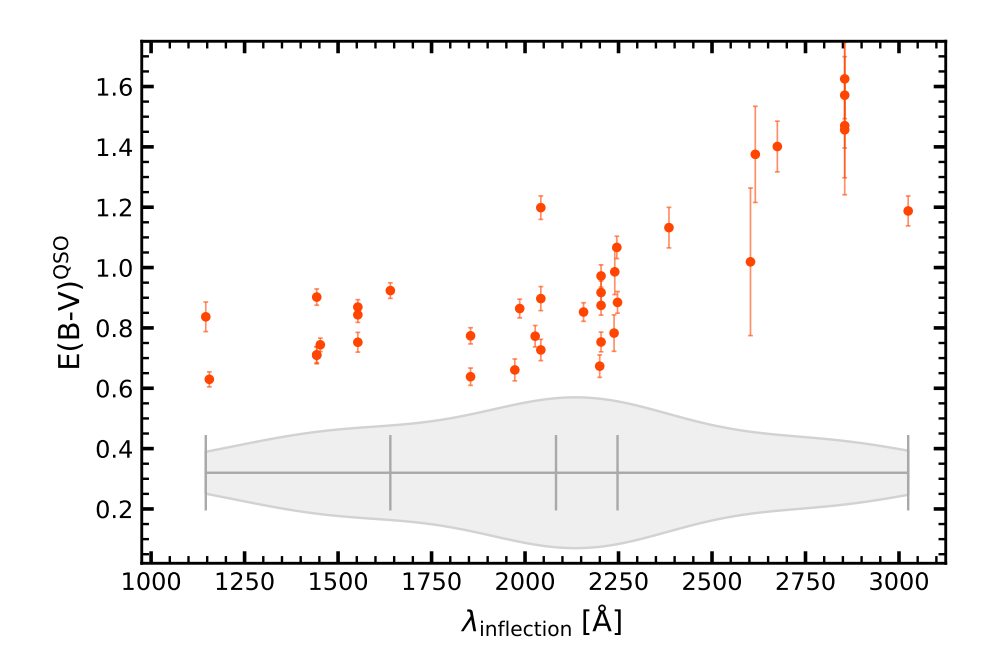


FIGURE 5.11: The UV/optical inflection point wavelength as a function of E(B-V)^{QSO} for the HRQ sample. The violin plot represents the rest-UV/optical inflection point wavelengths for the HRQ sample. The 1^{st} , 2^{nd} and 3^{rd} quartiles are represented by the box plot. The HRQ inflection points are inconsistent with the Balmer Break, $\lambda_{\rm rest} = 3645 \text{Å}$, and the dispersion in the distribution is large. Hence, a two-component model for HRQ SEDs is preferred over the Balmer Absorption models proposed for LRDs. The positive correlation illustrates the flexibility of multi-component SED models, showing that the SED inflection point can migrate red-wards should the quasar continuum suffer a higher degree of dust extinction.

Balmer Break is $\sim 3.0\sigma$ red-ward of the distribution mean, it is extremely unlikely that Balmer Absorption is the primary source of the UV excess in HRQs.

The large dispersion in the distribution of UV/optical inflection points in the HRQ sample favours a multi-component model - like that proposed in Section 5.3 - as the best description of their SEDs. Multi-component SED models have the flexibility to reproduce a variety of UV/optical inflection points because, in this framework, the inflection point of a given SED depends on the relative contributions of the scattered and dust attenuated components. In Fig. 5.11, we observe a correlation between the inflection point wavelength and best-fit E(B-V)^{QSO} amongst HRQs - with a Pearson Correlation Co-efficient $R_{PCC} = 0.76$ and a p-value = 4×10^{-8} . Conversely, in single-component models where some intrinsic quality like Balmer Absorption is the primary cause of the UV excess, the inflection point is determined by the Balmer Limit, inconsistent with the dust-extinction dependent inflection points observed in HRQs.

The similarities between the SEDs of HRQs and LRDs are striking, however, there are still clear differences between their physical properties and SED shapes. For example, low metallicities are not observed in HRQs, where strong Fe II emission has been observed at rest-optical wavelengths (e.g. Temple et al., 2019; Stepney et al., 2024). These higher metallicities reflect the age of HRQs and highlight a key physical difference between the HRQ and LRD populations. Furthermore, the two populations probe completely different regions of the quasar luminosity function and the MBH- λ_{Edd} plane as LRDs are significantly less luminous than HRQs, hosting black-hole masses $\sim 10^{6-8} M_{\odot} yr^{-1}$ and $\lambda_{Edd} \sim 1$ (Kocevski *et al.*, 2024). Nevertheless, many of the qualitative differences in their SED shapes can be attributed to selection effects. The average HRQ appears to host a weaker UV excess than the average LRD, however, the difference is most likely due to the $(i - K)_{AB}$ colour selection applied to the HRQ sample. While the region occupied by HRQs in Fig. 5.8 is sparsely populated by LRD candidates (Kocevski et al., 2024), relaxing the HRQ selection criteria could allow for the discovery of many more LRD analogues - or "Big Red Dots" - at cosmic noon.

5.5.2 Dust poor AGN at cosmic noon and beyond

In Section 5.4.2 we find that HRQs generally exhibit lower sublimation-temperature dust amplitudes than blue SDSS quasars (Temple *et al.*, 2021a), suggesting that the HRQ population is dust-poor on torus scales. Given the significant level of extinction suffered by HRQs when compared to blue SDSS quasars, the obscuring medium of HRQs must be extended to kpc-scales - supported by the extreme far-infrared luminosities observed in HRQs (e.g. Banerji *et al.*, 2014, 2018). Since the mid-infrared colour selection, (W1 - W2) > 0.85, biases the HRQ sample to **higher** sublimation-temperature dust amplitudes at $z_{\rm sys} > 2$, we expect that there may exist many dust-poor red AGN with an extended scattering medium at cosmic noon which have escaped our initial selection.

The low sublimation-temperature dust amplitudes observed in HRQs could be interpreted as evidence for the "blow-out" phase framework - where strong radiative feedback processes have blown the traditional torus out to interstellar medium scales. Should a "blow-out" phase be driving the low sublimation-temperature dust amplitudes in HRQs, we might expect to observe similarly weak sublimation-temperature dust emission in other obscured AGN populations. For example, LRDs also appear to host flat mid-infrared SEDs (Wright *et al.*, 2024; Akins *et al.*, 2024), implying that they also host low sublimation-temperature dust amplitudes (E.g. Fig ??). However, LRDs are weak far-infrared emitters and host very low metallicities (Akins *et al.*, 2024; de Graaff *et al.*, 2025), meaning that their obscuring medium may be devoid of dust entirely - instead primarily composed of the

5.5. Discussion 141

metal-poor gas that shrouds their central engines (Naidu *et al.*, 2025). In addition, while Hot DOGs host extremely red continua, with dust extinctions E(B-V)=2-20 mag (Assef *et al.*, 2015), their selection is biased towards mid-infrared bright and therefore dust-rich sources by design (e.g. (W2-W3)>5.3 mag and W3<10.6 mag; Assef *et al.*, 2015). Hence, sublimation-temperature dust-poor objects are unlikely to be selected as hot DOGs.

The fact that heavily extincted quasar populations - such as HRQs - can be sublimation-temperature dust poor is counter-intuitive. Indeed, until now, most studies conducted on sublimation-temperature dust-poor quasars were limited to luminous blue samples from cosmic noon to the very early Universe - e.g. $z_{\rm sys} > 6$. For example, Jiang $et\ al.\ (2010)$; Jun & Im (2013) assumed that sublimation-temperature dust-poor quasars probe a critical period in early galaxy assembly and invoked the following selection;

$$F_{2,3} = \log_{10}\{\lambda F_{\lambda}|_{2.3\,\mu m}/\lambda F_{\lambda}|_{0.51\,\mu m}\} < -0.5 \tag{5.2}$$

By de-reddening the SEDs of the 47 HRQs whose redshifts $z_{\rm sys} \geq 1.5$ and $\overline{\chi_{\nu}^2} < 5.0$, it becomes possible to test how many HRQs would be considered sublimation-temperature dust poor by the Jun & Im (2013) formalism, and for which values of $L_{\rm Dust}/L_{\rm Disk}|_{2^{\rm -m}}$ the Jun & Im (2013) condition is satisfied. In Fig. 5.12, we show that 7/47 or equivalently 15 per cent of the HRQ sample meet the selection described by Eqn. 5.2. The mean of the distribution in $F_{2,3}$ is $\langle F_{2,3} \rangle|_{HRQ} = -0.28 \pm 0.19$ for the HRQ population, placing the Jun & Im (2013) condition for dust poorness just 1σ from the sample mean.

As we would expect, the sublimation-temperature dust amplitude increases with $F_{2,3}$ or the ratio between the the $2.3\mu m$ and 510 nm continuum flux. From Fig. 5.12, we also see that HRQs with sublimation-temperature dust amplitudes, $L_{Dust}/L_{Disk}|_{2\mu m}\lesssim 1.0$, satisfy the Jun & Im (2013) condition. Given that the HRQ (W1 - W2) colour selection biases our sample to higher sublimation-temperature dust amplitudes (e.g. $L_{Dust}/L_{Disk}|_{2\mu m}>2.5$ at $z_{\rm sys}>2$), it is likely that there exists many more heavily reddened dust-poor quasars at cosmic noon that have escaped our current selection.

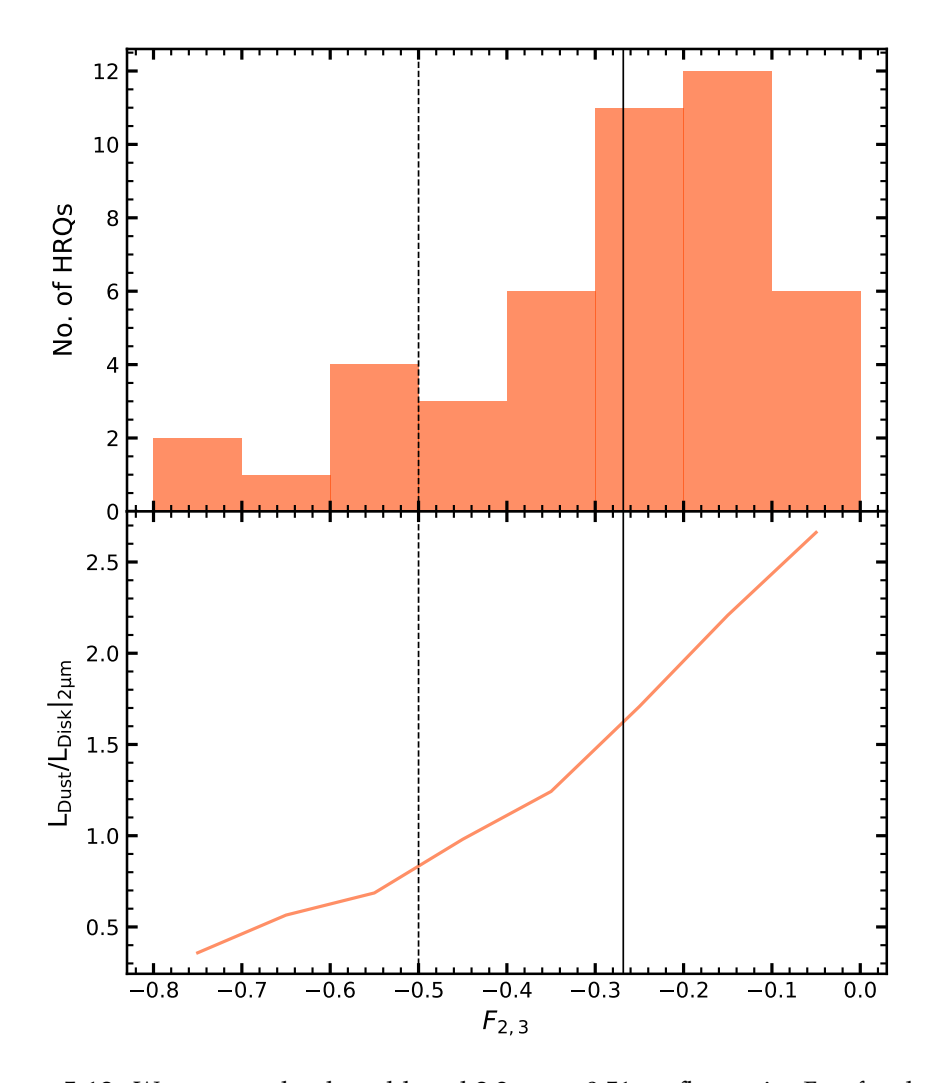


FIGURE 5.12: We present the de-reddened $2.3\mu m$ to $0.51\mu m$ flux ratio, $F_{2,3}$, for the 47 HRQs whose redshifts $z_{\rm sys} \geq 1.5$ and $\overline{\chi_{\nu}^2} < 5.0$ (top). The Jun & Im (2013) condition for dust-poor quasars is marked by the dashed black line. The mean of the HRQ sample ($\langle F_{2,3} \rangle|_{HRQ} = -0.27$) is marked by the solid black line. The mean sublimation-temperature dust amplitude, $L_{Dust}/L_{Disk}|_{2\mu m}$, per bin is plotted in the bottom panel and is shown to increase with $F_{2,3}$.

5.5. Discussion 143

5.5.3 Linking the UV and infrared SED properties of HRQs

Should the primary source of the UV excess in HRQs be scattered emission from the obscured quasar, we may expect to find links between the UV continuum luminosity and the quasar dust properties as probed by the near-infrared emission. Fig. 5.13 illustrates that the scattering fraction, F_{UV} , is weakly anti-correlated with the extinction suffered by the quasar continuum, E(B-V) - with a Pearson Correlation Co-efficient $R_{PCC} = -0.35$ and a *p*-value = 0.02. Hence, the UV continuum luminosities of HRQs are generally fainter in the more heavily extincted sources. Given that the scattering fraction F_{UV} and the dust extinction, E(B-V), are independent parameters in the multi-component SED model explored in Section 5.3.2, the anti-correlation between the UV continuum luminosity and the dust extinction amongst HRQs can be interpreted as evidence for the scattered light hypothesis. Should the UV excess be independent of the level of dust extinction, it would imply that the UV continuum does not originate from the quasar, however, since only moderately extincted HRQs have high UV continuum luminosities, the UV excess is most likely scattered from the same obscuring medium that attenuates the rest-optical emission.

As discussed in Section 5.4.2, we can use the sublimation temperature dust amplitude of a quasar to measure the amount of dust present on 10s-of-pc scales (Temple *et al.*, 2021a). In Fig. 5.14, we see evidence of a weak positive correlation between the UV continuum luminosity of HRQs and their sublimation temperature dust amplitudes - with a Pearson Correlation Co-efficient $R_{PCC} = 0.31$ and a p-value = 0.05. This implies that the UV continuum luminosity is brightest when the obscuring medium is predominantly distributed on torus scales - consistent with both the Hot DOG population, which host larger scattering fractions than HRQs and are most likely enshrouded in a dense cocoon-like obscuring medium (Assef *et al.*, 2020), and blue SDSS quasars which are known to host larger sublimation temperature dust amplitudes than HRQs.

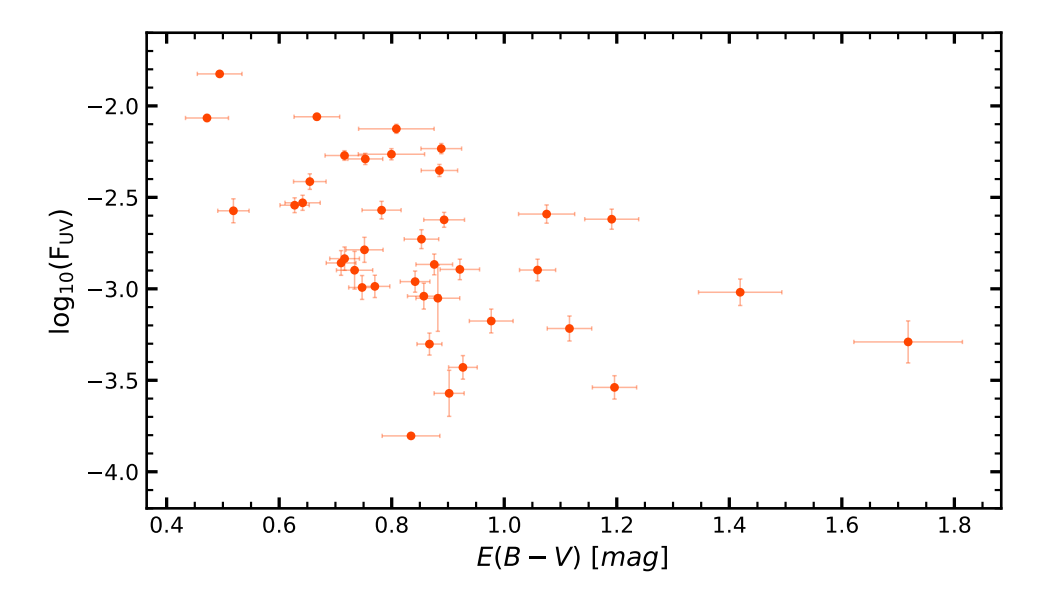


FIGURE 5.13: The rest-frame ultraviolet scattering fraction, F_{UV} , of an HRQ as a function of their dust extinctions, E(B-V). We see evidence of a negative correlation, suggesting that the more heavily extincted HRQs have weaker UV continuum luminosities or larger scattering fractions.

To more robustly test the trend observed in Fig. 5.14, we require a larger sample of dust-obscured quasars with a broader dynamic range in F_{UV} as well as a more complete distribution in sublimation temperature dust amplitudes. By extrapolating the relationship in Fig. 5.3, we estimate that by amending the $(i-K)_{AB}$ colour selection criteria to $(i-K)_{AB}>0$ mag, HRQs with scattering fractions $F_{UV}\sim 2\%$ would no longer escape the selection and facilitate a less biased analysis. Furthermore, by relaxing the mid-infrared colour selection to (W1-W2)>0.4 mag, we estimate that the sublimation temperature dust amplitude distribution of the HRQ sample will be complete at $z_{\rm sys}\geq 2$. However, relaxing the mid-infrared colour constraint is likely to pose challenges given that the typical colour of contaminants such as foreground stars and local galaxies are $(W1-W2)_{star}\simeq 0-0.6$ mag and $(W1-W2)_{gal}\simeq 0-0.8$ mag, respectively (Wright *et al.*, 2010).

5.6. Conclusions 145

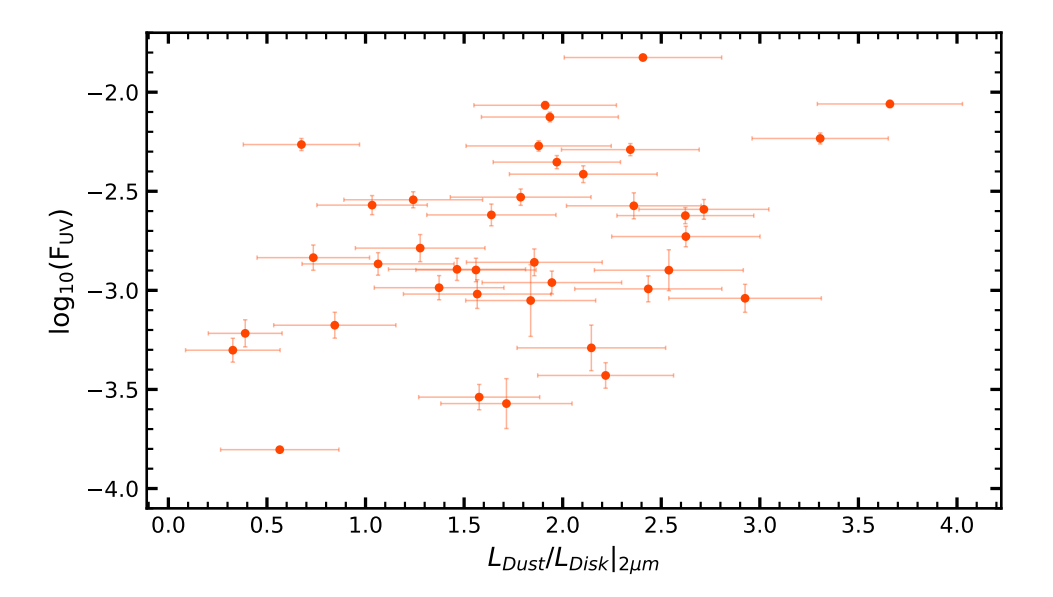


FIGURE 5.14: The rest-frame ultraviolet scattering fraction, F_{UV} , of an HRQ as a function of their sublimation temperature dust amplitudes, $L_{Dust}/L_{Disk}|_{2\mu m}$. We see evidence of a positive correlation, suggesting that the HRQs whose obscuring medium is distributed close to their sublimation temperature radii host stronger UV continuum luminosities or larger scattering fractions.

5.6 Conclusions

We have presented the spectral energy distribution properties of a sample of 60 heavily reddened quasars at $0.7 \lesssim z_{\rm sys} \lesssim 2.6$. Where possible, we study the full rest-frame ultraviolet to near-infrared SEDs of the quasars using the ugriz-YJHK-W1W2 filters, which corresponds to a wavelength coverage of $1000\text{\AA}-2\mu m$ at $z_{\rm sys}\sim 2$. We primarily explore a multi-component SED model to fit the photometric data, featuring a dust-attenuated quasar component and an additional blue component which represents scattered quasar emission. The objects for which we do not have optical photometric data are fit with only a dust-attenuated quasar SED, to ensure their respective fits fully converge. We also detail the reduction and analysis of the rest-UV SALT spectrum of the HRQ - ULASJ2200+0056. Our main findings are as follows;

• We confirm that blue photometric colours at rest-UV wavelengths are ubiquitous in the HRQ sample, with a UV excess consistent with scattered quasar emission detected in 41/50 of the HRQs on which a multi-component SED model was conducted. Conversely just 4/50 HRQs do not feature a statistically significant UV excess and the remaining 5/50 yielded inconclusive results. We calculate an average scattered component - $\langle F_{\rm UV} \rangle_{HRQs} = 0.26\%$. While comparatively lower than other red AGN populations (e.g. Greene *et al.*, 2024), this is most likely a product of selection effects. We find a strong anti-correlation between the observed scattering fraction and the $(i-K)_{\rm AB}$ colour in HRQs. When

- extrapolated to our selection limit $(i K)_{AB} > 1.6$ HRQs whose $F_{UV} \gtrsim 1\%$ are removed from the sample.
- Through the analysis of a rest-UV SALT spectrum of the HRQ ULASJ2200+0056

 we find evidence of broad emission lines, suggesting that scattered emission from the obscured quasar is making a significant contribution to the UV continuum. This result is consistent with our findings in Chapter 4 and ULASJ2315+0143, suggesting scattered light may play a significant role in producing the blue photometric colours of all HRQs. The analysis of further SALT spectra is deferred to future work.
- We employ the Kocevski *et al.* (2024) LRD selection criteria to determine which of our HRQs are LRD-like. While 46/50 HRQs host a sufficiently red optical continuum, just 4/50 host a sufficiently blue UV continuum blue-ward of the Balmer Break. This implies that the average UV-to-optical SED shape differs between the two samples. We largely attribute this difference to the $(i-K)_{AB}$ colour selection applied to the HRQ sample, however, it may also imply that the source of the UV excess is different between the HRQ and LRD samples.
- We find that a single-component SED model which utilises the Orion Nebula dust-extinction law, successfully used by Li et al. (2025) to fit the SEDs of LRDs, is **not** favoured over the multi-component SED model used in this work across the entire HRQ sample. We find that the Orion dust-extinction law is too flat to reproduce the the rest-optical continuum emission of HRQs, even for those HRQs which satisfy the Kocevski et al. (2024) LRD selection criteria.
- We find that descriptions of the UV excess that invoke some intrinsic property of the SED as the primary cause such as Balmer Absorption blue-ward of the Balmer Break are inconsistent with the SEDs of HRQs. We find that the rest-UV/optical inflection points in the HRQ population are diverse, with a mean inflection point wavelength, $\langle \lambda_{\rm rest} \rangle = 2156 \pm 493 \mbox{Å}$. We interpret the diversity in the SED inflection point wavelength as evidence that a multi-component SED model is the best description of the UV excess in HRQs. Given that the Balmer Break is $\gtrsim 3.0\sigma$ from the sample mean, Balmer Absorption is unlikely the primary origin of the "V-shaped" continuum in HRQs.
- We explore the effects of our infrared selection on the sublimation temperature dust emission and find that the $(J-K)_{AB}$ colour is insensitive to the sublimation temperature dust amplitude at redshifts $z_{\rm sys} \geq 1.5$. Below this redshift, the distribution of the sublimation temperature dust amplitudes is largely shaped by NIR selection effects with only the highest sublimation temperature dust amplitudes yielding sufficiently red continua for our selection criteria. In addition, we find a systematic dependence of the (W1-W2) colour on the

5.6. Conclusions 147

sublimation temperature dust amplitudes as a function of redshift, biasing the HRQ sample to **higher** dust amplitudes.

- When restricting the HRQ sample to systemic redshifts, $z_{\rm sys} \geq 1.5$, we find that the distribution of sublimation-temperature dust amplitudes in the HRQ sample is biased towards lower amplitudes than that of blue SDSS quasars with a Kolmogorov-Smirnov (KS) test yielding a p-value = 2×10^{-5} . Given that our mid-infrared selection criteria biases the HRQ sample to higher dust amplitudes, we would expect the HRQ population to host even lower sublimation temperature dust amplitudes than observed in this sample. Hence, HRQs host intrinsically weaker sublimation temperature dust emission than their blue SDSS counterparts. We interpret this as evidence of a more extended obscuring medium amongst HRQs vs blue SDSS quasars, resulting from a merger-induced "blow-out" phase.
- Finally, we detect weak correlations connecting the rest-UV continuum to the
 dust properties of HRQs. More heavily extincted HRQs host lower scattering
 fractions. Additionally, HRQs whose sublimation temperature dust amplitudes
 are highest host the strongest UV continuum luminosities. Given that the
 sublimation temperature dust amplitude is a probe for the amount of torus-scale
 dust present in the system, this result implies that HRQs whose obscuring
 medium is located closer to the sublimation radius host higher scattering
 fractions.

Chapter 6

Final remarks and future prospects

"Trust me.... I'm a doctor"

Matthew Stepney

6.1 Introduction

In this thesis, we take a multi-faceted approach to understanding the co-evolution of supermassive black holes (SMBHs) and their host galaxies via AGN feedback throughout cosmic time - leveraging multi-wavelength spectroscopic **and** photometric datasets to study the evolution of blue and red quasars at cosmic noon and beyond. We demonstrate that the analysis of large survey datasets as well as detailed single-object investigations are powerful tools in understanding the evolution of quasars. Our study finds that only by analysing diverse populations of quasars - at various redshifts - can we gain a holistic view of galaxy evolution across cosmic time and that selection effects can significantly shape the distributions of quasar properties. In this chapter, we discuss our results in the context of the wider research themes and suggest how the current and upcoming generation of both ground- and space-based instruments can be utilised to further the research in this field.

6.2 The evolution of blue quasars across cosmic time

Many studies of AGN feedback at $z_{\rm sys}=5-7$ suggest that broad-line region winds are far stronger in early quasar populations than at cosmic noon (e.g. Mortlock *et al.*, 2011; Man *et al.*, 2019; Schindler *et al.*, 2020). Through robust statistical analysis of the rest-UV line properties of high-redshift SDSS quasars, we investigate the redshift evolution of broad-line region winds in luminous blue populations. We confirm that the same trends linking broad-line region outflow velocities to black-hole mass and accretion rate (e.g. Temple *et al.*, 2023) persist from $z_{\rm sys}=1.5$ to $z_{\rm sys}=4$. However, it remains unclear whether they hold in the Super-Eddington regime, particularly given that the structure of the accretion disk may fundamentally change at high accretion rates (Giustini & Proga, 2019). We hence conclude that reports of extreme quasar wind velocities in the high-redshift Universe (e.g. XQR30; Schindler *et al.*, 2020; Farina *et al.*, 2022) are most likely a result of luminosity bias, since the relatively small samples of optically-selected $z_{\rm sys}\sim 5-7$ quasars have a tendency to be super-Eddington.

Extending similar population studies to increasingly higher redshifts and more diverse black-hole masses and accretion rates is crucial for our understanding of how AGN and their SMBHs evolve in the early Universe. The Chilean AGN/Galaxy Extragalactic Survey (ChANGES) will utilise the 4-metre Multi-Object Spectroscopic Telescope (4MOST; Merloni *et al.* 2019) to target $\sim\!12000$ quasar candidates at $z_{sys}>4$. Given that 4MOST is integrated with Vera Rubin's Legacy Survey of Space and Time (LSST), ChANGES will utilise variability **and** multi-wavelength SED selection to build more complete samples of high-redshift quasars (Bauer *et al.*, 2023). ChANGES will therefore sample a broader dynamic range in both black-hole mass and accretion rate

at $z_{sys} \sim 4-5$, making comparisons between quasar outflow properties at cosmic noon and $z_{sys} \sim 5$ more robust. Furthermore, the Dark Energy Spectroscopic Instrument (DESI; Villar Martín *et al.*, 2020) has also begun pushing large statistical samples of luminous blue quasars to the Epoch of Reionisation (e.g. $z_{sys} \sim 5$ Yang *et al.*, 2023), hence our understanding of high-redshift quasar evolution is set to dramatically transform in the coming years.

6.3 AGN feedback in the red quasar phase

The role of a red quasar phase in advancing the evolution of massive galaxies remains a topic of hot debate. In this thesis, we investigate the role of dust in driving outflows which subsequently can trigger the "blow-out" phase predicted by galaxy evolution models (e.g. Di Matteo *et al.*, 2005; Hopkins *et al.*, 2008) in obscured quasar populations. In the heavily reddened quasar (HRQ) - ULASJ2315+0143 - we detect outflows signatures in the ionised gas on multiple scales and in multiple gas phases. We find that the kinetic power of the winds in the ionised gas of ULASJ2315+0143 is comparable to that of luminous blue SDSS quasars (e.g. Shen *et al.*, 2011). Therefore, strong feedback processes are most likely active in the system - although a systematic study of the effects of dust extinction on outflow velocity across large statistical samples is still required to verify these results.

To date, studies investigating the relationship between outflows and dust-extinction explore only moderately reddened samples with a relatively narrow dynamic range in E(B-V) (e.g. Calistro Rivera *et al.*, 2021; Fawcett *et al.*, 2022). The Very Large Telescope's Multi-Object Optical/Near-infrared Spectrograph (VLT-MOONS) will dramatically increase the number of spectroscopically confirmed red quasars at cosmic noon (Maiolino *et al.*, 2020). Hence, VLT-MOONS will facilitate a more robust analysis of the effects of dust-extinction on outflow velocity through large statistical samples that push redder than the current generation of optically-selected surveys. Furthermore, with H β -derived estimates of the black-hole mass, it will be possible to isolate the effects of dust-reddening on outflow velocity from the trends discussed in Chapter 3 between outflows, black-hole mass and accretion rate. Consequently, a more robust investigation of the "blow-out" phase framework will become viable in the era of VLT-MOONS.

6.4 Excess ultra-violet emission in red AGN populations

We have shown that excess blue photometric colours at rest-UV wavelengths are ubiquitous amongst HRQs. Given that similar UV continua are observed in both hot

dust obscured galaxies and JWST's little red dots, excess UV emission seems to be a defining characteristic of obscured accretion across all mass scales. Even so, the origin of the UV continuum is still uncertain. In the HRQ - ULASJ2315+0143 - SED fitting confirms a degeneracy between the star-forming galaxy and scattered AGN emission descriptions of the UV excess - both yielding equally good fits to the continuum. Furthermore, we observe signatures of both host galaxy emission - e.g. narrow $Ly\alpha$ and [O II] - and AGN emission - e.g. broad N V, Si IV and C IV - in the spectroscopic data at rest-UV wavelengths. However, since the 4000Å break was unobservable due to the telluric absorption between the J and H-bands, it was impossible to constrain the stellar mass of the host and break the degeneracy between the two components.

To discern the true nature of the UV excess in obscured AGN, future campaigns should focus on a number of key areas. First, the detection of broad emission lines at rest-UV wavelengths will confirm the presence of quasar emission. Second, polarisation studies similar to those conducted on hot dust obscured galaxies (e.g. Assef *et al.*, 2022) will confirm whether the rest-UV emission has been scattered by some obscuring medium. Finally, by observing the 4000Å break, we can determine the relative contribution of the star-forming host galaxy to the rest-UV continuum.

6.4.1 Scattered light in red AGN populations

Our analysis of the Southern African Large Telescope (SALT) spectrum of ULASJ2200+ 0056 has already confirmed the presence of broad rest-UV emission lines in another HRQ. With short-exposure rest-UV spectroscopic data available for an additional 11 HRQs via SALT, confirmation of broad emission lines in the rest-UV continuum will yield further insight into the source of the UV excess in the HRQ population. Preliminary results suggest that scattered AGN emission is contributing to the rest-UV in at least 5/13 HRQs - inclusive of ULASJ2315+0143 and ULASJ2200+0056 - with the remaining 8 HRQs proving inconclusive. Furthermore, by utilising diagnostic line ratios between the C IV λ 1550, He II λ 1640 and [C III] λ 1908 emission lines, we can probe the source of the gas photo-ionisation (e.g. Figure 5; Feltre *et al.*, 2016). The degree to which strong narrow components from the host galaxy bias the line ratios away from the AGN characteristic region will help determine whether the UV continuum originates purely from scattered AGN emission.

6.4.2 Host galaxy signatures in red AGN populations

The European Space Agency's Euclid mission is a space-based telescope with high-angular resolution imaging capabilities in the optical to near-infrared as well as a \sim 1.2-1.9 μ m spectroscopic wavelength coverage (Euclid Collaboration *et al.*, 2025b,c,d). With the large statistical samples available from both Euclid and VLT-MOONS, it will

be possible to confirm the presence of a UV excess in thousands of new red quasars (e.g. Euclid Collaboration *et al.*, 2025a). Furthermore, the 4000Å break will also be observable in cosmic noon sources, meaning that it will be possible to infer the relative contribution of the star-forming host to any UV continua detected. The high sensitivity of JWST also provides an opportunity to extend the study of the red AGN phase to lower-mass systems. With the power of space-based NIRCam imaging, separation of the AGN emission from the stellar continuum is viable for JWST-detected sources at $z_{\rm sys} \gtrsim 5$ (Ding *et al.*, 2023). Given that LRDs may host over-massive black holes (e.g. Rusakov *et al.*, 2025), studying the host galaxy AGN emission simultaneously could lend new insight into the role of obscured accretion in the formation of galaxies.

6.5 Sublimation temperature dust in red quasars

Dust reprocessing of the UV/optical emission is what dominates the near-infrared emission of a quasar - with the hottest components defined by the sublimation temperature of the dust grains, i.e. $\sim 1200 \, K$. There have been many studies aimed at linking the full ultra-violet to near-infrared SED properties of quasars, suggesting that torus-scale dust can provide the opacity to launch outflows and that sublimation-temperature dust-poor quasars are a relic of rapid accretion events (e.g. Jiang et al., 2010; Jun & Im, 2013; Temple et al., 2021a). While previous studies have largely focused on blue populations, we show that dust-reddened quasars may also host weak near-infrared emission. We find that the sublimation-temperature dust amplitudes of HRQs are generally weaker than that of blue SDSS quasars of comparable luminosity and redshift - which we interpret as evidence for the "blow-out" phase framework. In addition, we find that \sim 20 per cent of HRQs are formally considered dust poor when using the Jiang et al. (2010) criteria. However, this is most likely an underestimate given that the distribution of sublimation-temperature dust amplitudes in the HRQ population is largely shaped by selection effects as the dust amplitudes become more modest. Future campaigns should therefore focus on a more inclusive selection of dust-poor quasars. Hence, we propose that a more relaxed mid-infrared colour constraint - i.e. (W1 - W2) > 0.4 mag - should be applied to HRQs, potentially facilitating the detection of many more sublimation-temperature dust-poor objects.

6.6 Conclusions

The goal of this thesis is to further our understanding of SMBH and host galaxy co-evolution - through the lens of AGN feedback. In particular, we focus on the impact of multi-scale outflows launched in the vicinity of the black-hole as they propagate through the interstellar medium of the quasar host. This research finds that the primary drivers of outflows are the mass and accretion rate of the central SMBH, in both blue and red quasar populations (Chapters 3 & 4). While it is clear that cosmological redshift is not a fundamental driver of outflows at redshifts $1.5 < z_{sys} < 4.0$, it remains unclear to what extent dust extinction plays a role.

Our detailed analysis of the heavily reddened quasar - ULASJ2315+0143 - uncovers evidence of significant wind velocities on both parsec and kiloparsec scales, however, these winds are not uncharacteristically strong given the mass and accretion rate of the quasar. Similarly, the kinetic power of the winds in the ionised gas phase are equivalent to similarly luminous blue quasars at cosmic noon (Chapter 4). Conversely, a population study of heavily reddened quasar SEDs reveals that their sublimation-temperature dust emission is suppressed with respect to their blue SDSS counterparts - implying that dust-enhanced feedback processes can clear the inner regions of dust and ultimately change the quasar geometry (Chapter 5).

One explanation for these seemingly conflicting results could be the different time-scales at play in each region of the quasar. Should the red AGN phase be short-lived, the broad-line region and torus-scale dust are likely to respond quicker to enhanced AGN feedback processes than the more extended narrow-line region. Furthermore, for the impact of strong quasar-driven winds to be felt by the wider host high coupling efficiencies are required, which are likely to vary from source to source and between individual accretion events. This means that the limited evidence for the dust enhancement of quasar-driven winds in ULASJ2315+0143 may not be representative of the entire HRQ population.

There still remain several open questions regarding the role of AGN feedback in galaxy evolution. Over the next decade, transformative imaging and spectroscopic facilities are set to expand our census of AGN and quasars, exploring more diverse populations. Hence, by building on the work presented in this thesis, we can expect to further our understanding of how red and blue quasars evolve across cosmic time. Future work should explore whether the trends identified in this thesis between SMBH mass, accretion rate, SED properties, and the prevalence of outflows extend into the super-Eddington regime as well as the Epoch of Reionisation. Additionally, this thesis highlights the need for large statistical studies of red quasar populations to more robustly determine the role of dust in facilitating enhanced AGN feedback.

Appendix A

The heavily reddened quasar photometric catalogue

"I do not know any reading more easy, more fascinating, more *delightful* than a **catalogue**"

Anatole France

TABLE A.1: The HRQ photometry for each of the 60 sources selected in Banerji *et al.* (2012), Banerji *et al.* (2013), Banerji *et al.* (2015) and Temple *et al.* (2019). Photometric bands whose uncertainties are set by the 10 per cent floor (see Section 5.2) are presented in **bold face**.

$F_{\lambda} \ [10^{-19} \ { m erg \ s^{-1} \ cm^{-2} \ \AA^{-1}}]$											
Object	и	g	r	i	z	Υ	J	Н	K	W1	W2
ULASJ0016-0038	_	28±1	49±2	54±3	84±3	86±2	84±9	97±9	126±8	43± 4	41± 4
ULASJ0041-0021	_	13±1	6±1	8±3	16±2	26±1	49±10	93±9	109±5	54± 5	32±3
ULASJ0123+1525	_	43±5	44±7	44 ± 2^a	-	_	_	32±4	83± 8	128± 13	170± 17
ULASJ0141+0101	_	34±2	49±10	51±3	57±7	38±6	68±7 ^a	72±7	25±2	20±2	17±3
ULASJ0114-0014	_	21±2	16±1	16±5	23±1	38±1	81±8	113±7	125±5	74±7	63± 6
ULASJ0144-0114	_	21±3	16±1	16±1	23±2	38±4	81±9	114±10	125±9	74±7	63± 6
ULASJ0144+0036	_	4±1	4±1	13±2	27±2	36±1	69±12	100±10	113±9	53± 5	39±4
ULASJ0221-0019	_	12± 1	9± 1	19± 2	33± 3	47±5	85±21	85±16	105±11	49± 5	48± 5
ULASJ1002+0137	17±2	8±1	9±1	15±1	23±2	36±4	78±9	95±8	_	50± 5	43± 4
ULASJ1234+0907	_	_	_	_	-	_	_	28±6	136± 14	124± 12	156± 16
ULASJ1415-0836	_	_	_	_	_	_	_	39±4	86± 9	151± 15	187± 19
ULASJ1539+0557	_	_	_	_	_	_	_	87±7	179± 18	176± 18	159± 16
ULASJ2200+0056	_	72±2	71±4	78±1	125±4	170±7	201±13	274±11	304±1	124± 12	87± 9
ULASJ2224-0015	_	15±1	18±1	32±2	52±6	51±1	77±9	109±9	147±8	58± 6	51± 5
ULASJ2312+0454	_	35±1	36±1	53±3	50±8	47±5	23±8 ^a	39±6	80± 8	155± 16	184± 18

^a These bands were removed before fitting - see Section 5.3.2.1 for details.

Continued on next page

Table A.1 – continued from previous page

Object	и	8	r	i	z	Υ	J	Н	K	W1	W2
ULASJ2315+0143	_	37±2	26±1	18±1	17±1	13±2	_	38±5	101± 10	79± 7	87±9
VHSJ1117-1528	_	_	_	_	_	_	_	48±7	79±8	48± 5	39± 4
VHSJ1122-1919	_	_	_	_	_	_	52±14	_	174± 17	79±8	55± 6
VHSJ1301-1624	_	_	_	_	_	30±7	48±11	_	119± 12	99± 10	101± 10
VHSJ1350-0503	_	39±10	43±7	48±7	70±11	81±15	99±16	164± 16	193± 19	88± 9	68±7
VHSJ1409-0830	_	_	_	_	_	_	58±16	56±16	104±10	57± 6	62±6
VHSJ1556-0835	_	-	_	41±2	40±7	65±13	71±13	95±18	68±7	105±15	50± 5
VHSJ2024-5623	_	-	_	_	_	_	_	33±10	56±10	27±3	16±2
VHSJ2028-4631	_	76± 8	60± 36	58± 6	74±7	77±8	48 ± 12^{a}	64±15	78±14	27±3	23± 2
VHSJ2028-5740	_	11±2	13±1	17± 2	26±3	23±6	57±12	$144 {\pm} 15$	296±30	186± 19	191± 19
VHSJ2048-4644	_	6±2	5±1	15±2	16±2	24±4	33±7	37±9	70±7	43± 4	51± 5
VHSJ2100-5820	_	3±1	4±1	6±2	14±2	43±8	93±13	101±13	48± 5	42± 4	34±3
VHSJ2101-5943	_	15±2	32±3	82± 8	151± 15	169± 17	184±18	259± 26	489± 50	155± 16	123± 12
VHSJ2109-0026	_	16±2	20±4	23±5	30±13	34±6	57±10	67±10	78±7	38± 4	27±2
VHSJ2115-5913	_	45±5	34± 3	32±3	40± 4	39±6	109±15	164± 16	212± 21	132± 13	105± 11
VHSJ2130-4930	_	22±2	11±1	16±1	21± 2	20±4	33±11	59±15	101±10	55± 5	55± 5
VHSJ2141-4816	_	22± 2	18± 2	18± 2	23± 2	23±4	53±12	71±11	92±9	70±7	51± 5
VHSJ2143-0643	_	_	_	_	_	42±13	44±13	67±12	91±10	41± 4	36± 4
Continued on next nece											

Continued on next page

^a These bands were removed before fitting - see Section 5.3.2.1 for details.

Table A.1 – continued from previous page

	1		1	ı		T	Г	Г	Г	T	
Object	и	g	r	i	z	Υ	J	Н	K	W1	W2
VHSJ2144-0523	_	_	_	_	_	_	55±17	69±12	77±8	42± 4	44± 4
VHSJ2212-4624	_	_	_	_	_	_	30±6	_	79±9	38± 4	52± 5
VHSJ2220-5618	_	25±3	24±2	41± 4	79±8	102± 10	237±24	391±150	476± 50	247± 25	246± 25
VHSJ2227-5203	_	13±1	15±1	20± 2	37± 4	34±5	31±7	48±9	53±12	70±7	71± 7
VHSJ2256-4800	_	36±4	31± 3	23± 2	47±5	78± 8	110±11	146±15	167± 17	100± 10	106± 11
VHSJ2257-4700	_	_	8±1	18± 2	31± 3	36±4	44±7	62±8	91± 9	37± 4	38± 4
VHSJ2306-5447	_	12±1	6±1	14±1	27±3	36±4	39±8	79±8	121± 12	49±5	34± 3
VHSJ2332-5240	_	21±2	16± 2	14±1	18±2	28±5	41±11	65±9	46±6	28±3	21±2
VHSJ2355-0011	_	46±1	23±1	20±4	26±1	39±1	58±15	107±14	129±9	70±7	72±7
VIKJ2205-3132	_	6±1	8±1 ^a	5±1	16±2	22±3	32±3	47±4	54± 5	17±2	12±2
VIKJ2214-3100	_	_	8±1	_	19±2	22±4	20±3	39± 4	81± 8	130± 13	147± 15
VIKJ2228-3205	_	_	4± 1	_	7±2	11±3	12±2	15±2	19± 2	8±1	7±1
VIKJ2230-2956	39±7	16±2	13±2	_	13±2	14±2	_	37± 4	48± 5	68±7	96± 10
VIKJ2232-2844	_	_	_	_	9±2	20±4	29±3	43± 4	74± 7	32±3	32±3
VIKJ2238-2836	_	_	_	_	35± 4	40±4	45±5	63± 6	68±7	97± 10	137± 14
VIKJ2241-3006	30±7	17±2	30± 3	44±2	46±4	36±4	43± 4	53± 5	80± 8	141± 14	166± 17
VIKJ2243-3504	_	63±9	42±7	25±6	31±2	37±3	37±3	72±7	119± 12	85± 9	100± 10
VIKJ2245-3516	_	_	_	_	12±2	16±3	23±3	34±3	59± 6	112± 11	163± 16

Continued on next page

^a These bands were removed before fitting - see Section 5.3.2.1 for details.

Table A.1 – continued from previous page

Object	и	8	r	i	Z	Υ	J	Н	K	W1	W2
VIKJ2251-3433	_	15±2	8±1	_	13±2	16±3	9±3 ^a	33±3	27±3	41± 4	40± 4
VIKJ2256-3114	33±8	33± 3	22± 2	20±4	18±2	19±3	30±3	44± 4	55± 6	31± 3	26±3
VIKJ2258-3219	_	23±2	26±3	50±2	52±3	56±4	78± 8	96± 10	115± 12	163± 16	172± 17
VIKJ2306-3050	_	_	4±1	_	10±2	19±3	15±3	23±2	26±3	31± 3	36± 4
VIKJ2309-3433	19±4	19± 2	12±1	7±2	17±2	16±3	18±3	19±2	22± 2	11±1	11±2
VIKJ2313-2904	40±7	23±3	17±2	_	25±2	30±4	24±3	29±3	40± 4	40± 4	38± 4
VIKJ2314-3459	_	25±3	19±2	_	17±3	25±4	33±3	45±5	50± 5	22± 2	20±2
VIKJ2323-3222	18±6	5±1	7±1	6±2	18±2	17±3	27±3	48± 5	81± 8	44±5	35± 4
VIKJ2350-3019	_	-	7±1	_	14±2	15±3	26±3	34±3	41± 4	20± 2	15±2
VIKJ2357-3024	_	6±2	9±2	_	18±2	27±3	22±3	36± 4	41± 4	58± 6	80± 8

^a These bands were removed before fitting - see Section 5.3.2.1 for details.

Appendix B

The heavily reddened quasar "best-fit" SEDs

"Story
telling is about two things; it's about character and
 ${\bf plot[s]}"$

George Lucas

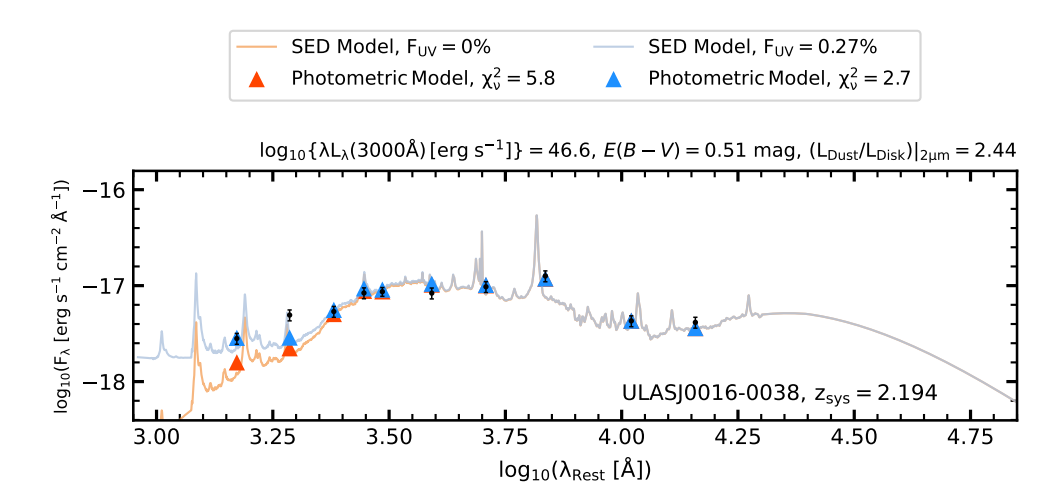


FIGURE B.1: The "best-fit" SED for the HRQ ULASJ0016-0038. The photometric data and associated uncertainties are presented in black. The best-fit multi-component SED model and photometry are presented by the blue line and triangles. The dust attenuated quasar component and photometry are presented by the orange line and triangles.

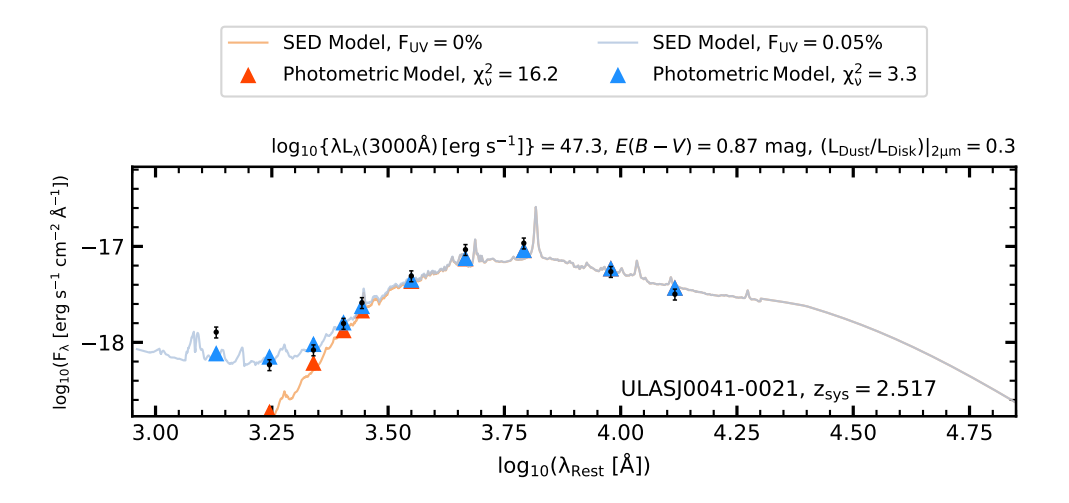


FIGURE B.2: Same as Fig. B.1 but for the HRQ - ULASJ0041-0021.

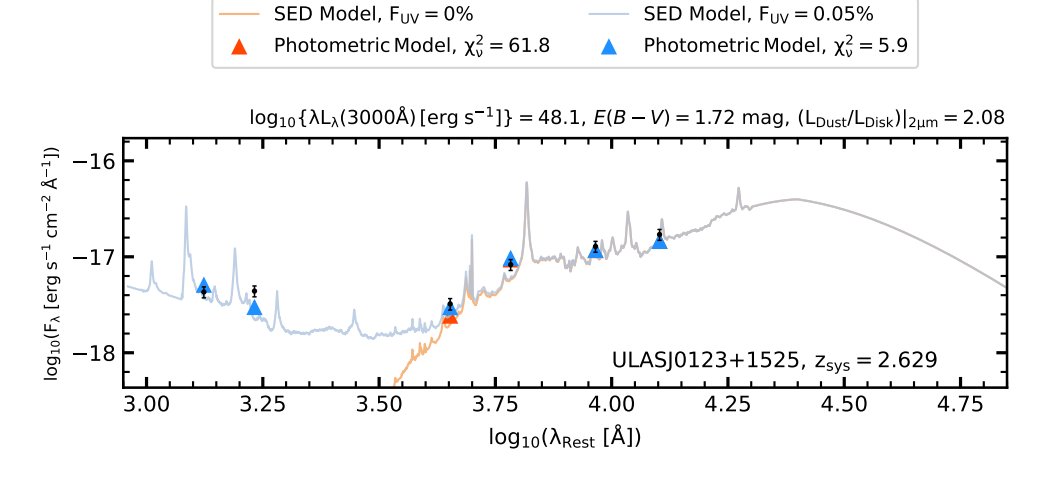


FIGURE B.3: Same as Fig. B.1 but for the HRQ - ULASJ0123+1525.

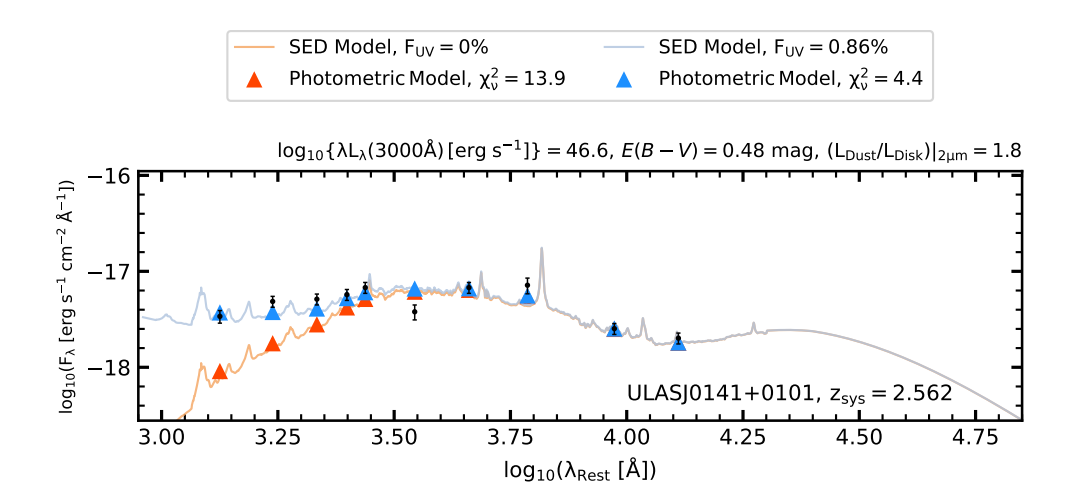


FIGURE B.4: Same as Fig. B.1 but for the HRQ - ULASJ0141+0101.

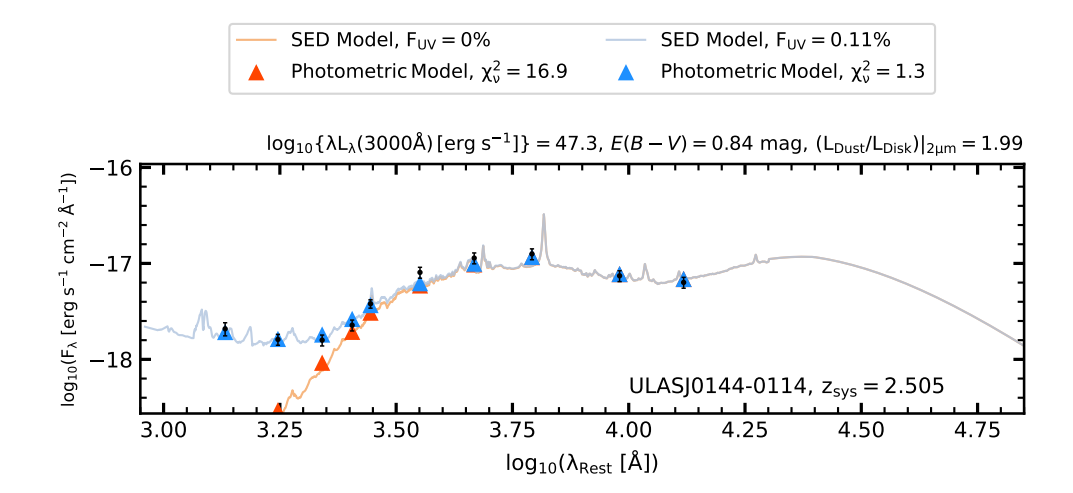


FIGURE B.5: Same as Fig. B.1 but for the HRQ - ULASJ0144-0114.

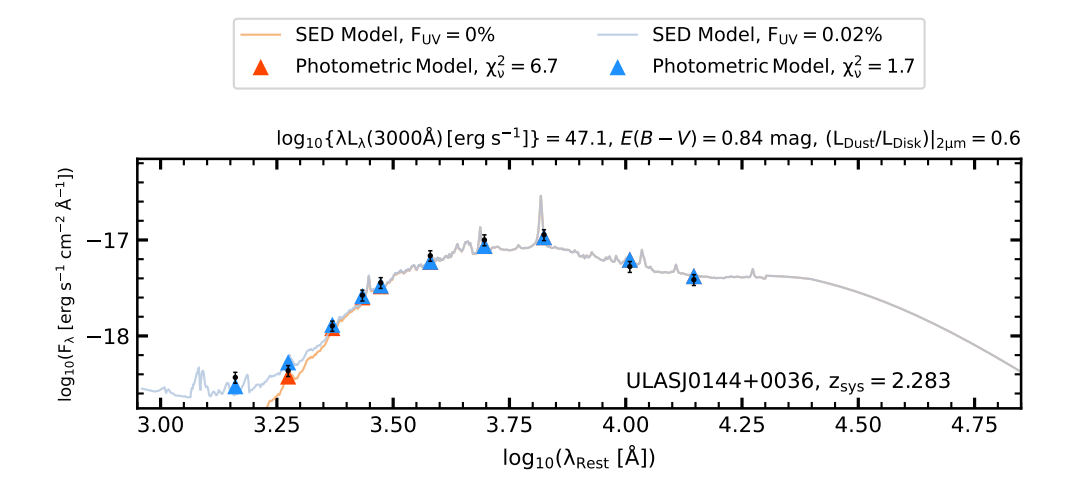


FIGURE B.6: Same as Fig. B.1 but for the HRQ - ULASJ0144+0036.

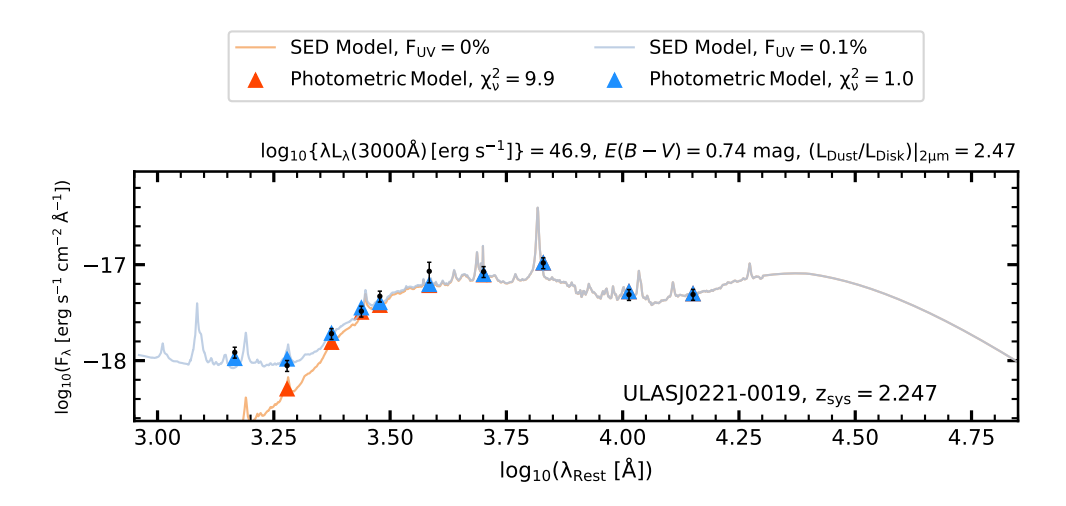


FIGURE B.7: Same as Fig. B.1 but for the HRQ - ULASJ0221-0019.

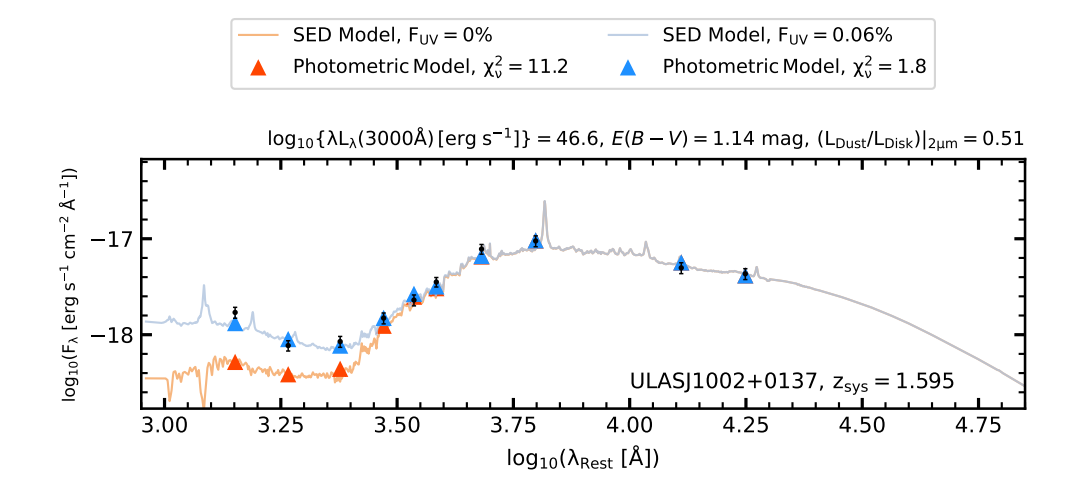


FIGURE B.8: Same as Fig. B.1 but for the HRQ - ULASJ1002+0137.

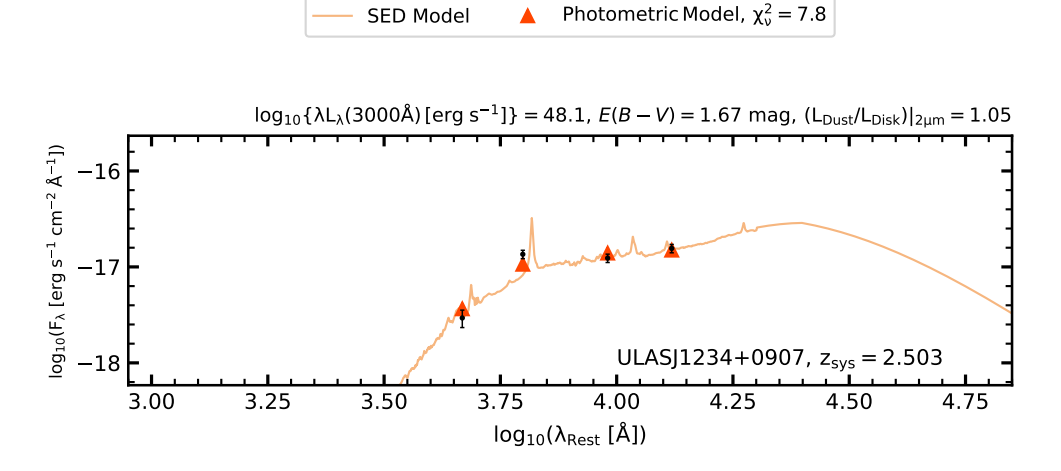


FIGURE B.9: The "best-fit" SED for the HRQ ULASJ1234+0907. The photometric data and associated uncertainties are presented in black. The best-fit single-component SED model and photometry are represented by the orange line and triangles.

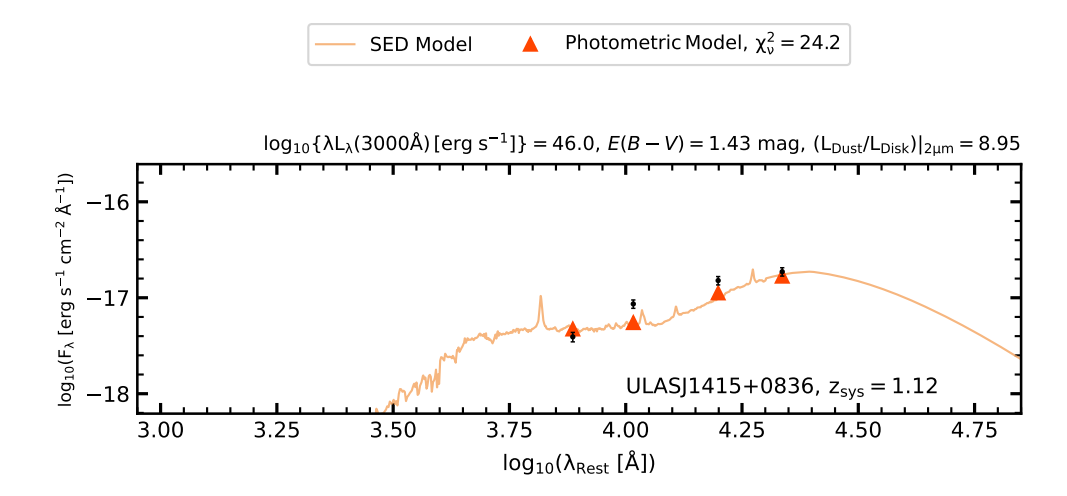


FIGURE B.10: Same as Fig. B.9 but for the HRQ - ULASJ1415+0836.

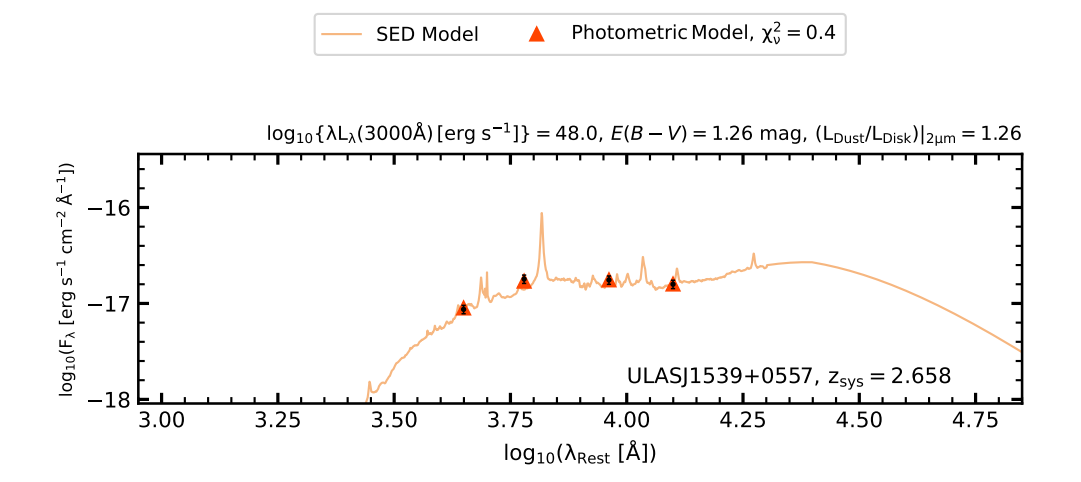


FIGURE B.11: Same as Fig. B.9 but for the HRQ - ULASJ1539+0557.

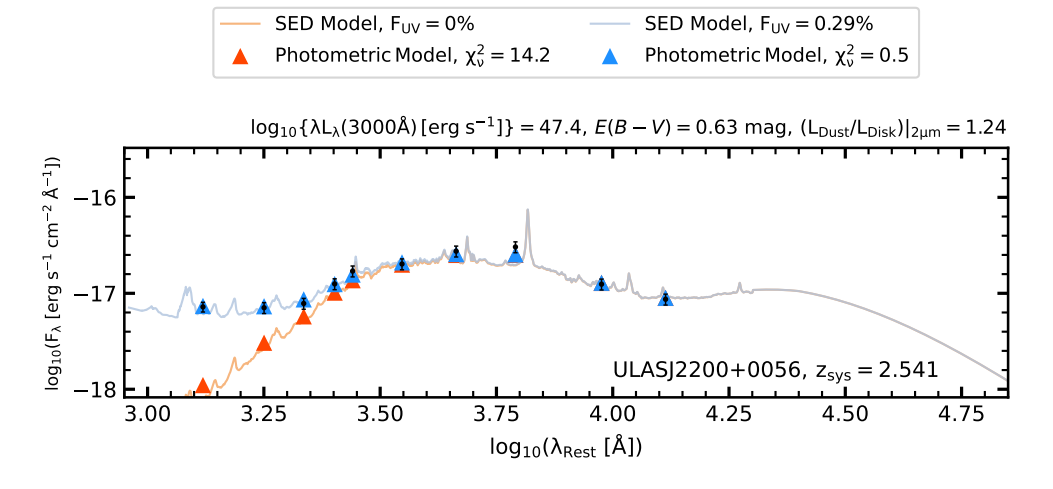


FIGURE B.12: Same as Fig. B.1 but for the HRQ - ULASJ2200+0056.

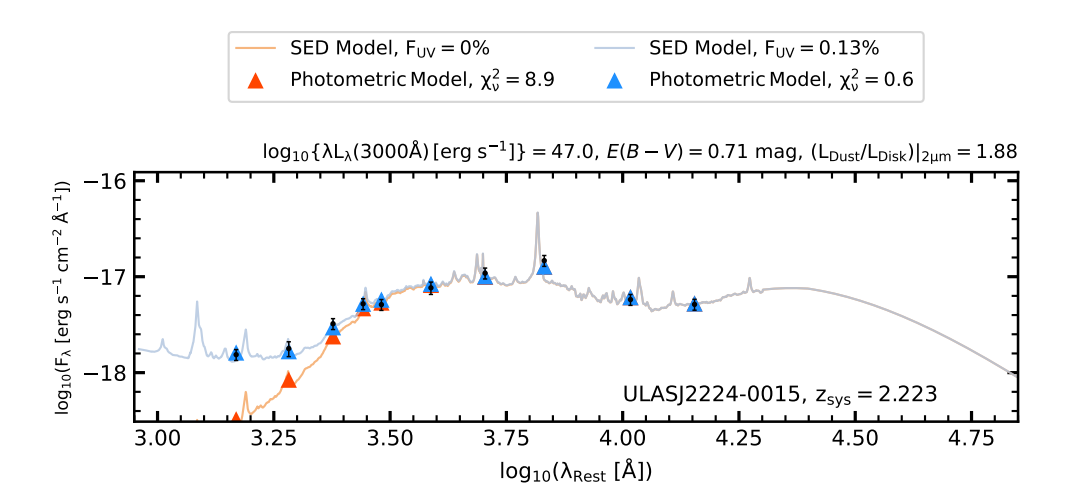


FIGURE B.13: Same as Fig. B.1 but for the HRQ - ULASJ2224-0015.

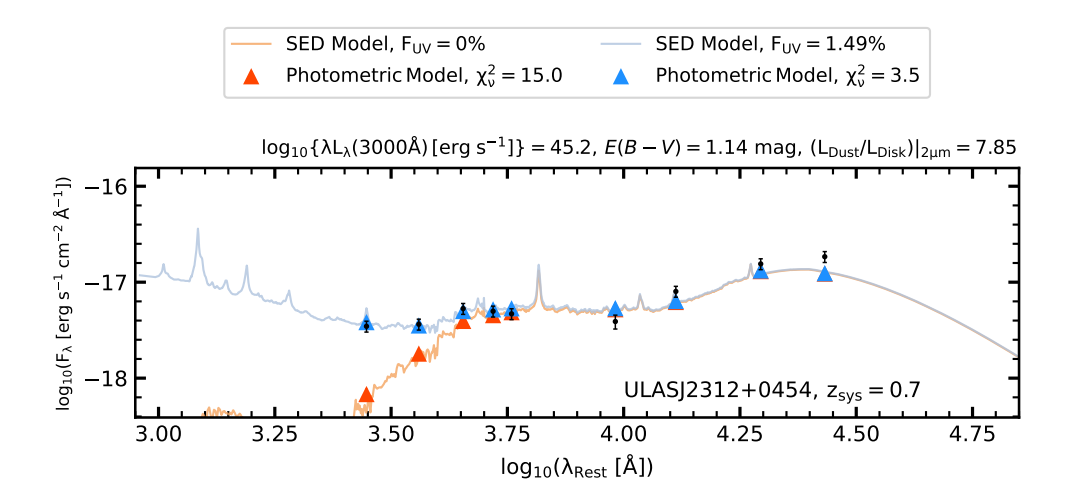


FIGURE B.14: Same as Fig. B.1 but for the HRQ - ULASJ2312+0454.

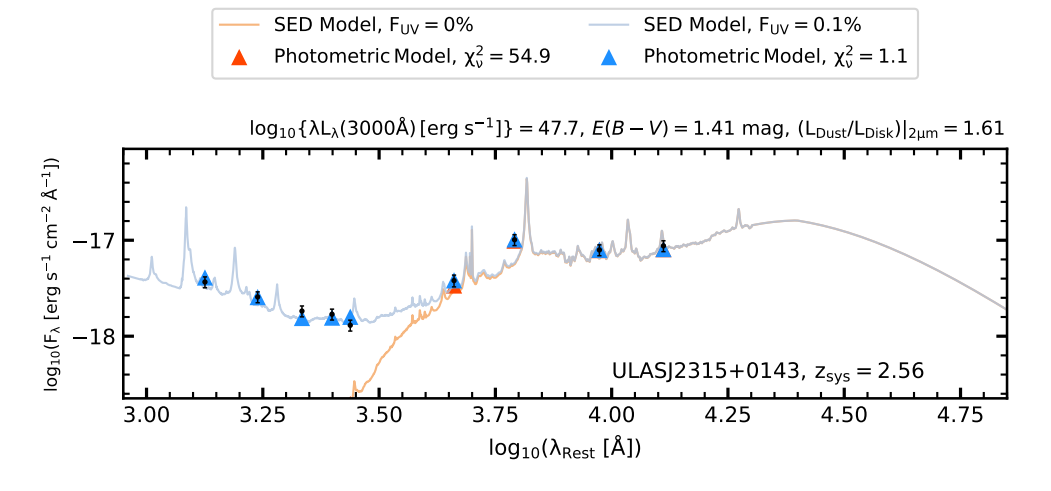


FIGURE B.15: Same as Fig. B.1 but for the HRQ - ULASJ2315+0143.

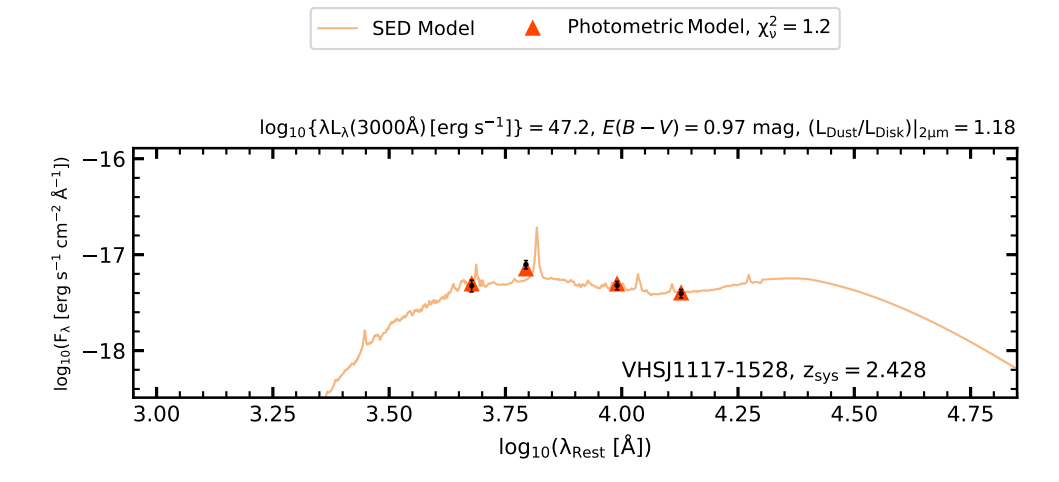


FIGURE B.16: Same as Fig. B.9 but for the HRQ - VHSJ1117-1528.

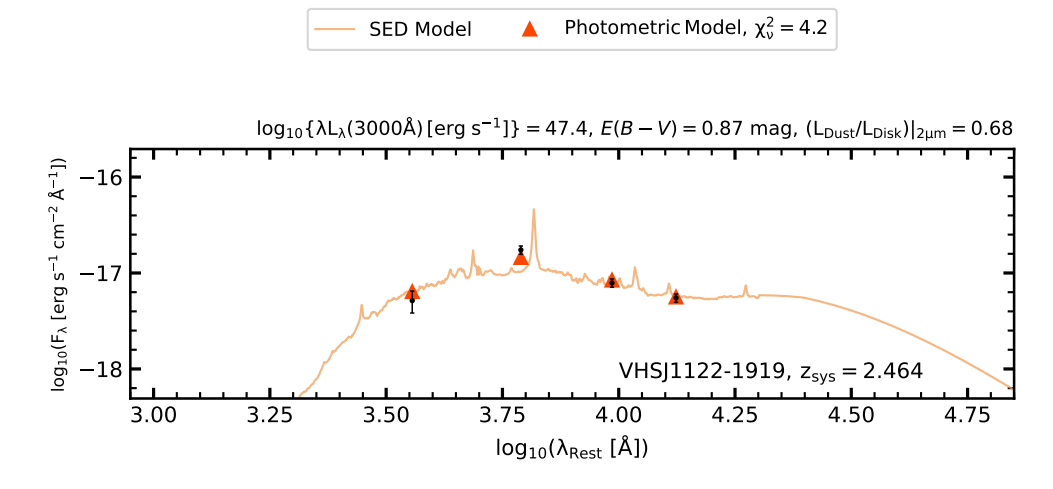


FIGURE B.17: Same as Fig. B.9 but for the HRQ - VHSJ1122-1919.

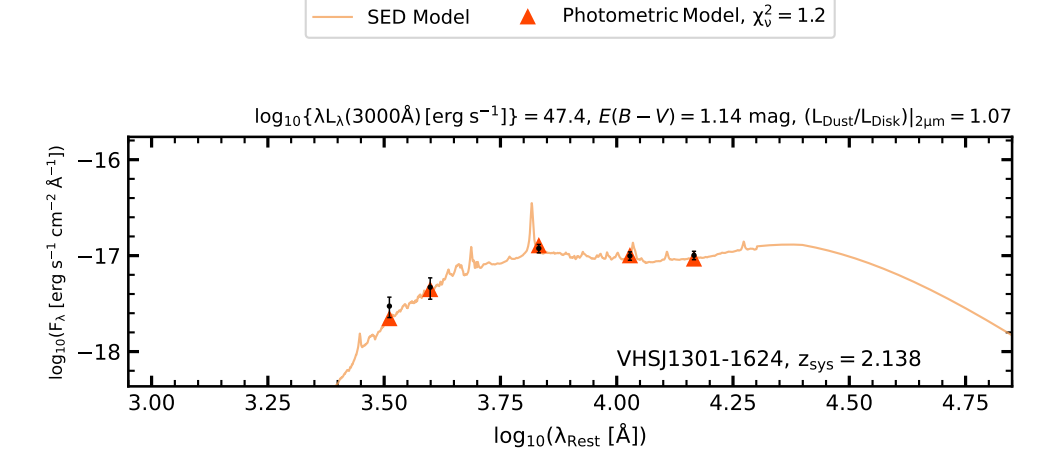


FIGURE B.18: Same as Fig. B.9 but for the HRQ - VHSJ1301-1624.

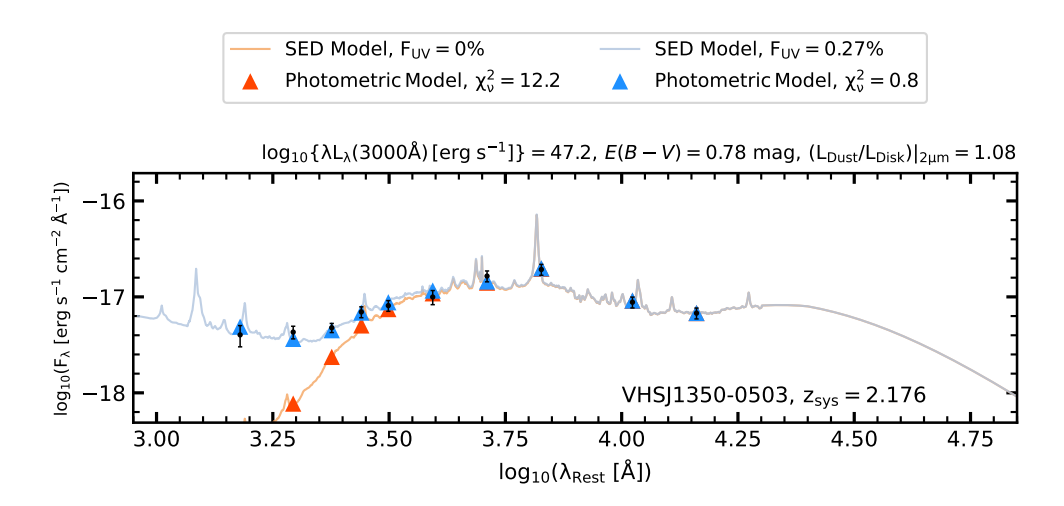


FIGURE B.19: Same as Fig. B.1 but for the HRQ - VHSJ1350-0503.

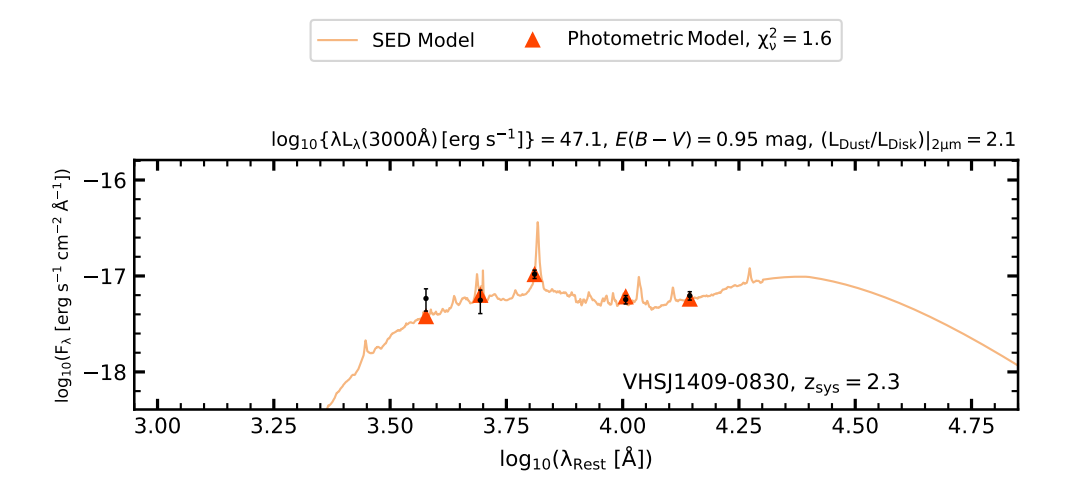


FIGURE B.20: Same as Fig. B.9 but for the HRQ - VHSJ1409-0830.

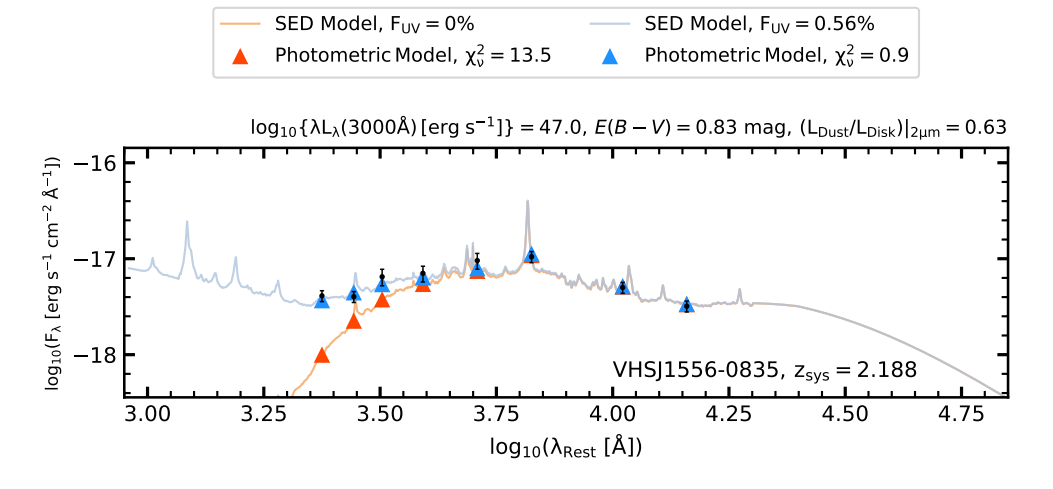


FIGURE B.21: Same as Fig. B.1 but for the HRQ - VHSJ1556-0835.

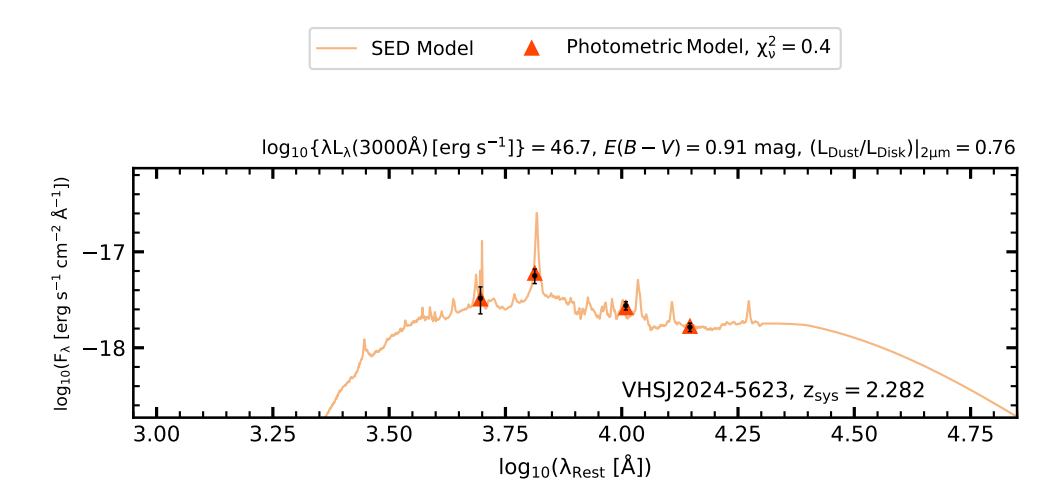


FIGURE B.22: Same as Fig. B.9 but for the HRQ - VHSJ2024-5623.

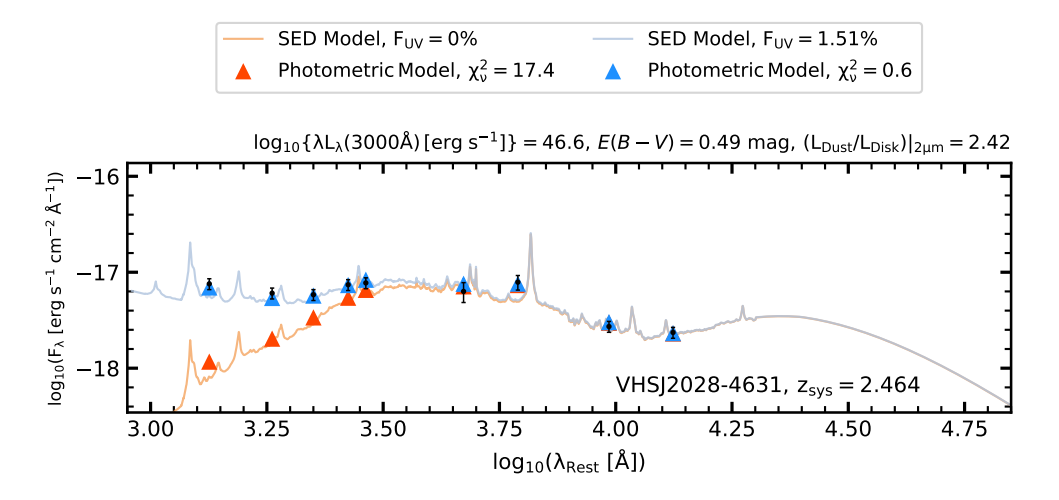


FIGURE B.23: Same as Fig. B.1 but for the HRQ - VHSJ2028-4631.

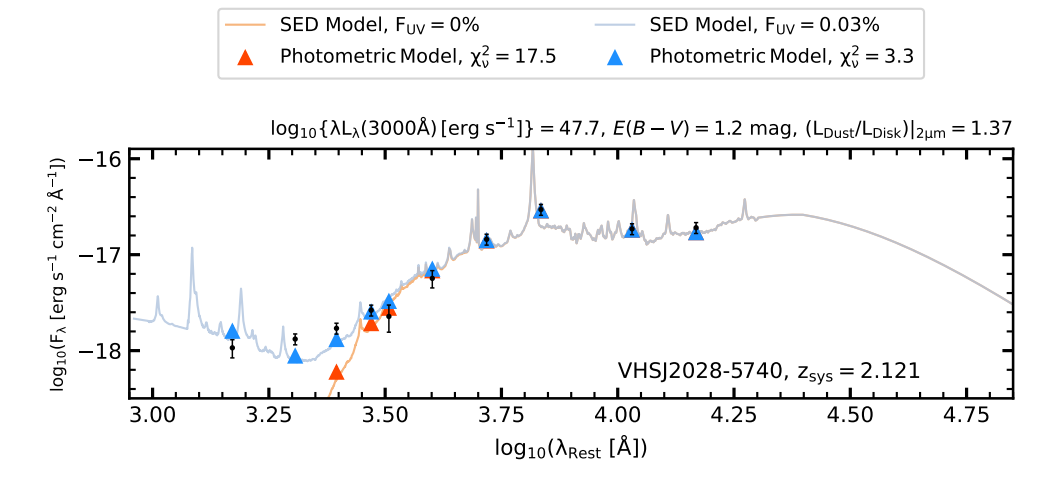


FIGURE B.24: Same as Fig. B.1 but for the HRQ - VHSJ2028-5740.

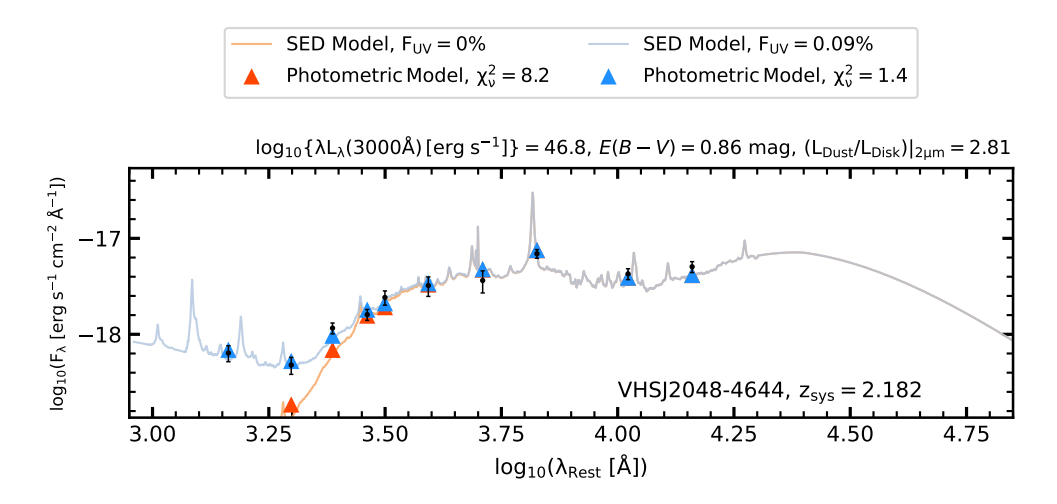


FIGURE B.25: Same as Fig. B.1 but for the HRQ - VHSJ2048-4644.

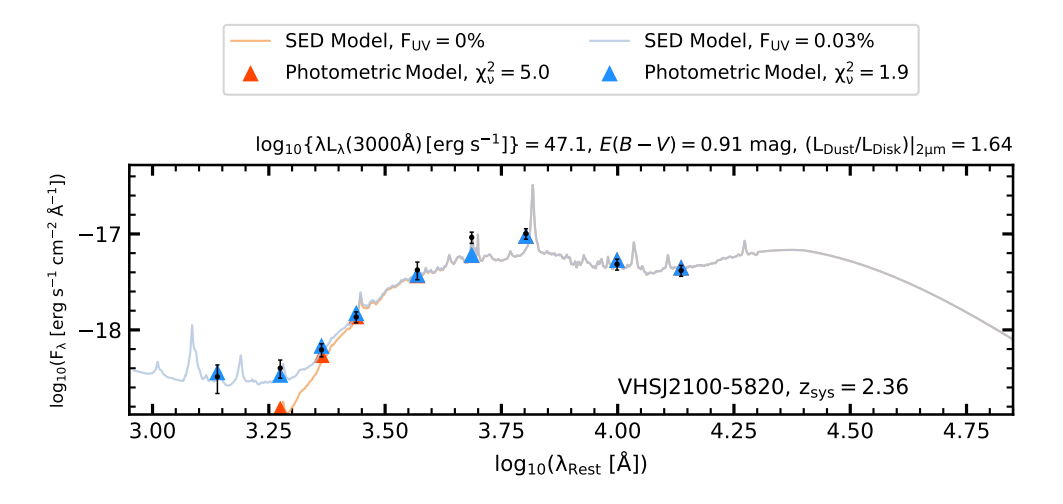


FIGURE B.26: Same as Fig. B.1 but for the HRQ - VHSJ2100-5820.

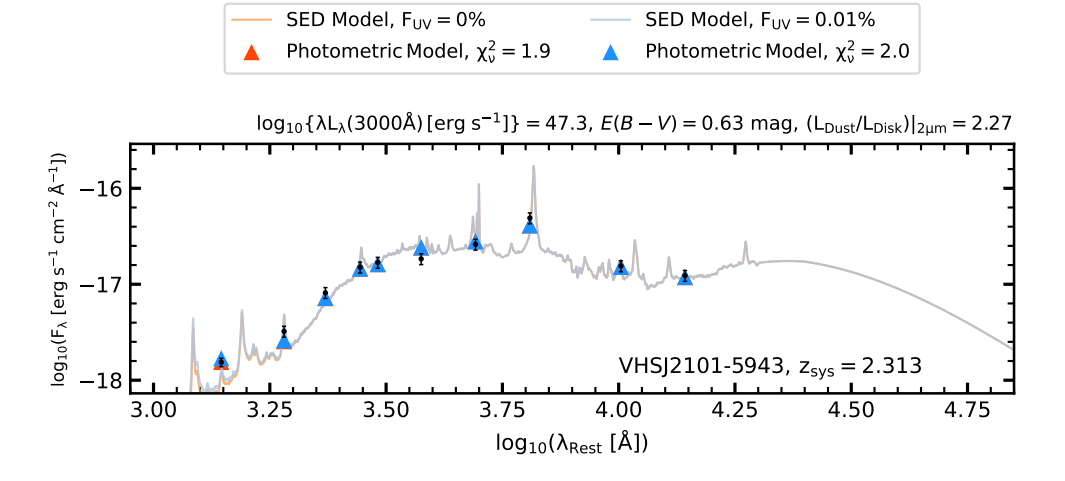


FIGURE B.27: Same as Fig. B.1 but for the HRQ - VHSJ2101-5943.

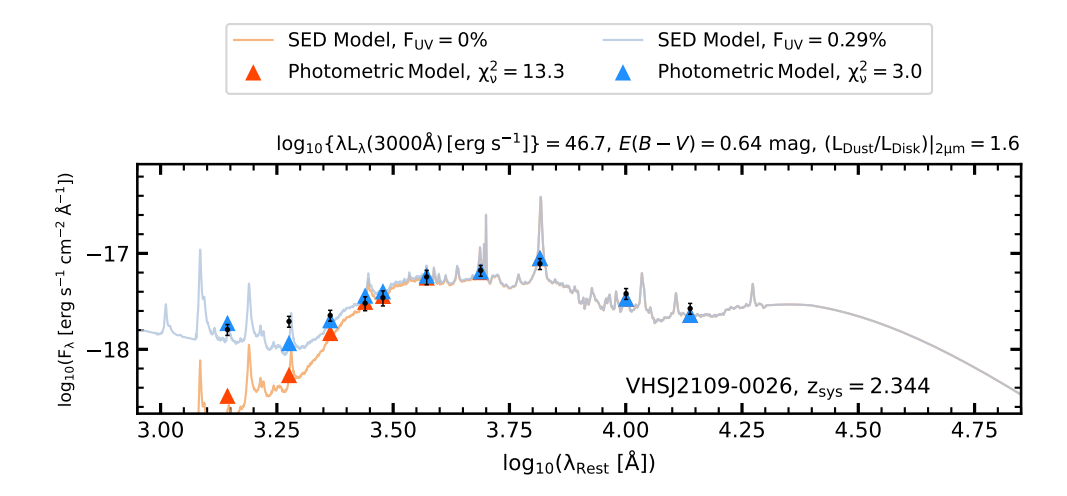


FIGURE B.28: Same as Fig. B.1 but for the HRQ - VHSJ2109-0026.

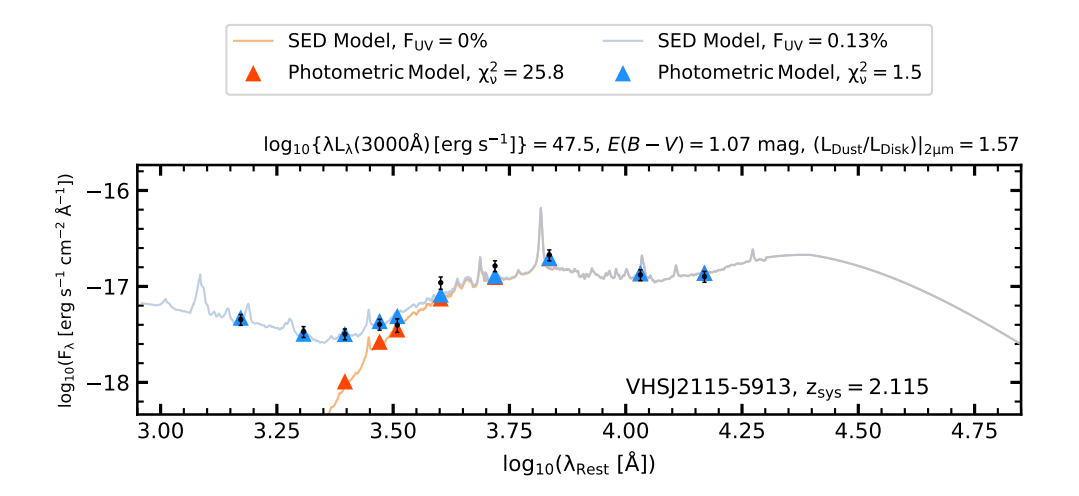


FIGURE B.29: Same as Fig. B.1 but for the HRQ - VHSJ2115-5913.

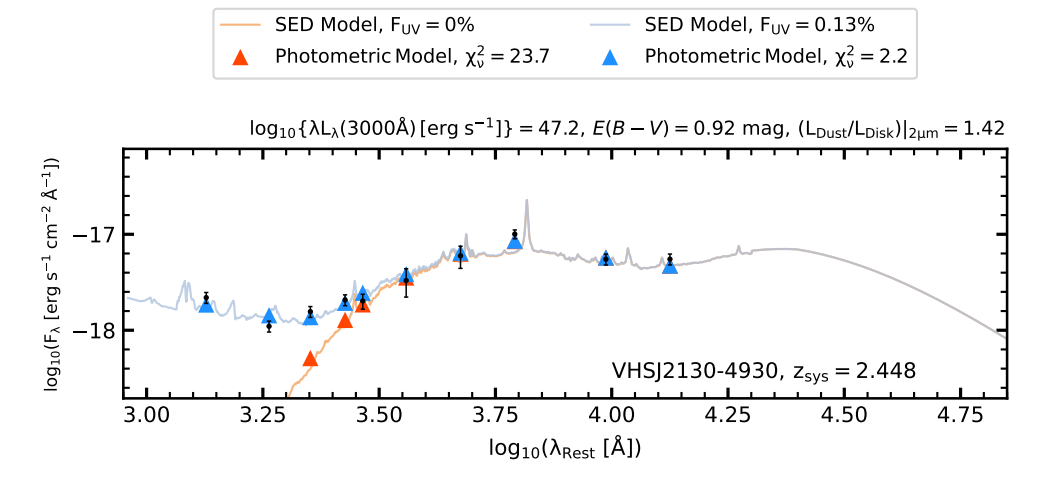


FIGURE B.30: Same as Fig. B.1 but for the HRQ - VHSJ2130-4930.

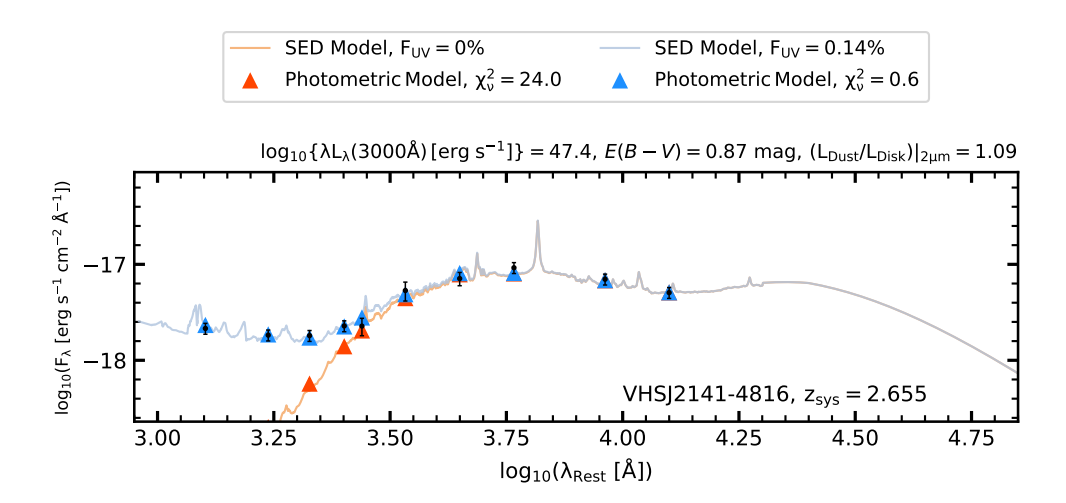


FIGURE B.31: Same as Fig. B.1 but for the HRQ - VHSJ2141-4816.

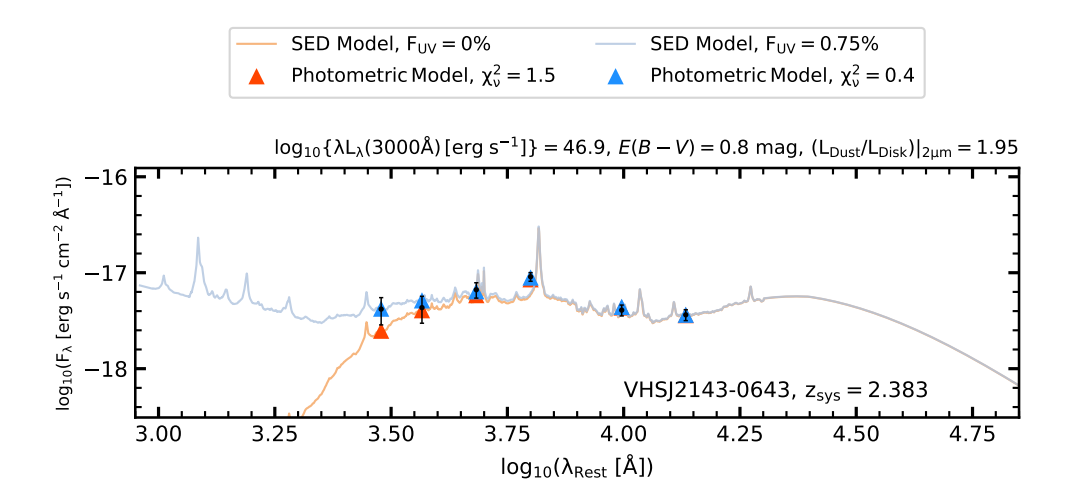


FIGURE B.32: Same as Fig. B.1 but for the HRQ - VHSJ2143-0643.

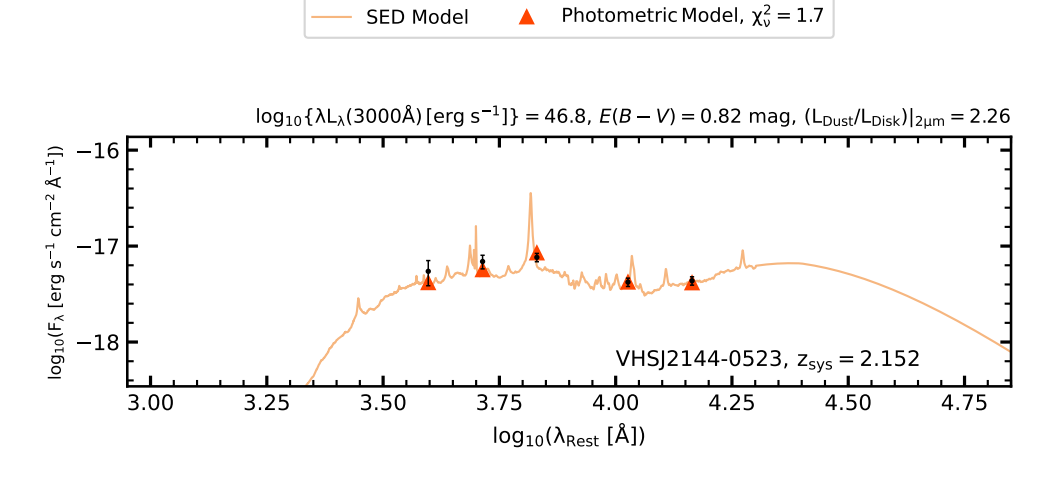


FIGURE B.33: Same as Fig. B.9 but for the HRQ - VHSJ2144-0523.

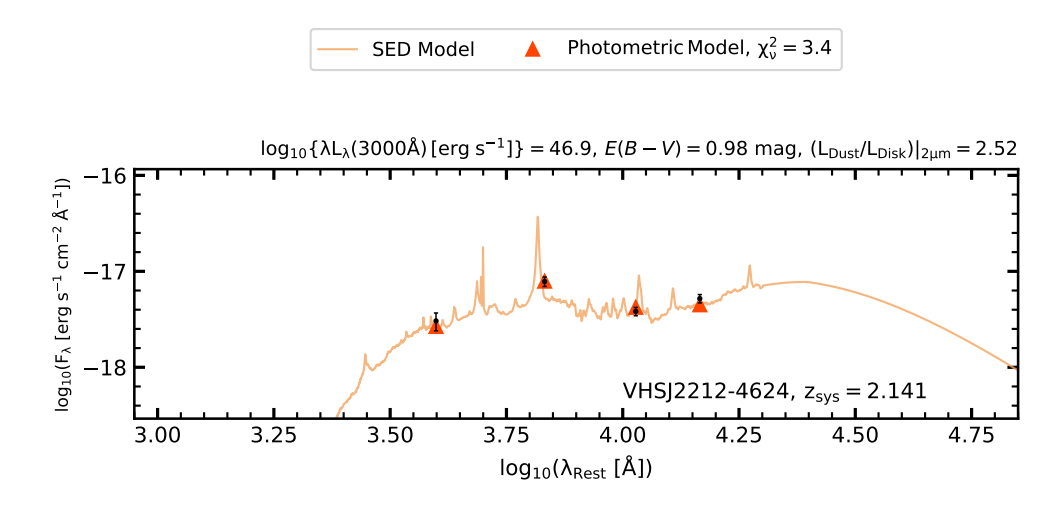


FIGURE B.34: Same as Fig. B.9 but for the HRQ - VHSJ2212-4624.

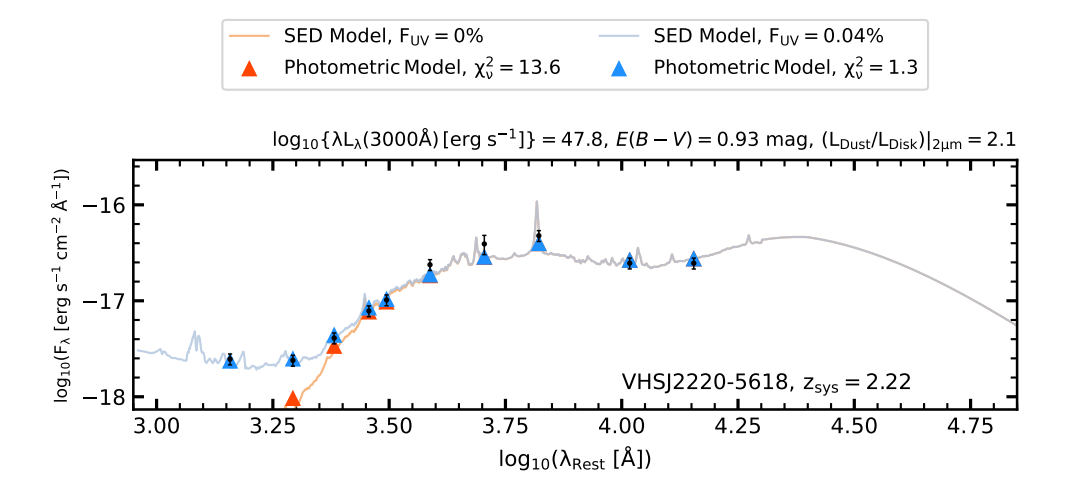


FIGURE B.35: Same as Fig. B.1 but for the HRQ - VHSJ2220-5618.

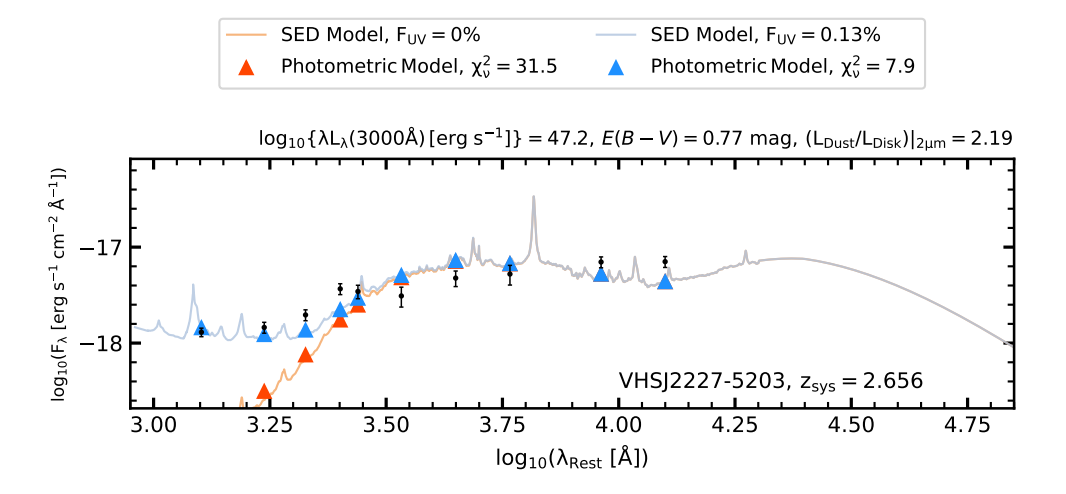


FIGURE B.36: Same as Fig. B.1 but for the HRQ - VHSJ2227-5203.

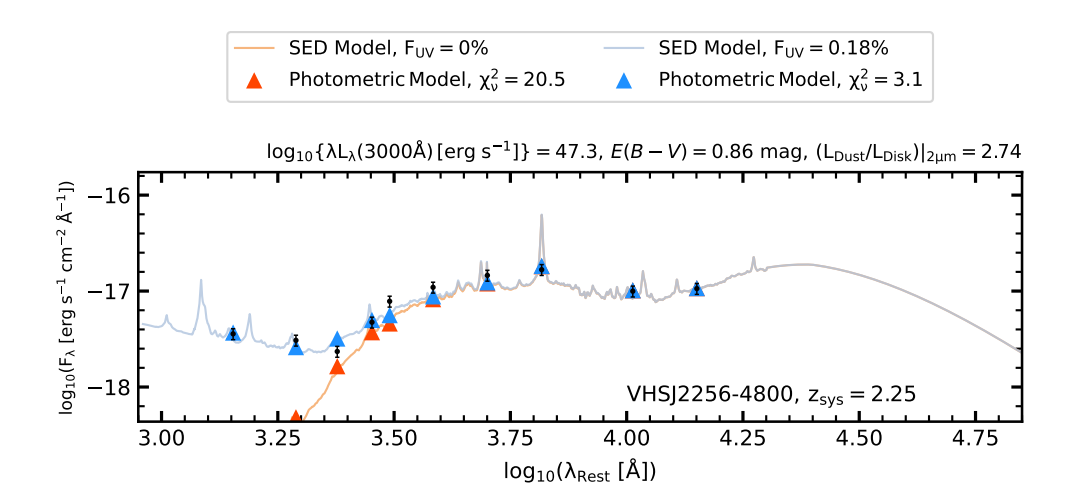


FIGURE B.37: Same as Fig. B.1 but for the HRQ - VHSJ2256-4800.

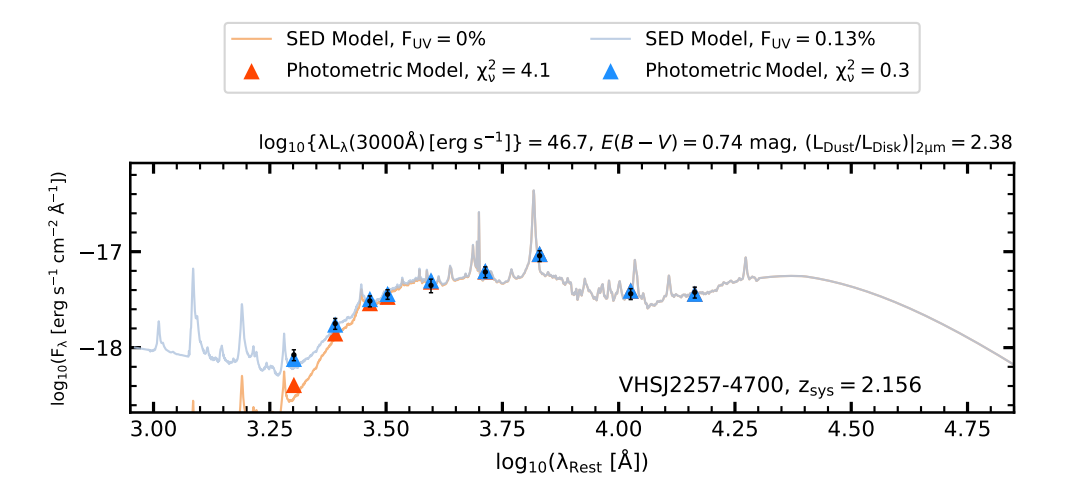


FIGURE B.38: Same as Fig. B.1 but for the HRQ - VHSJ2257-4700.

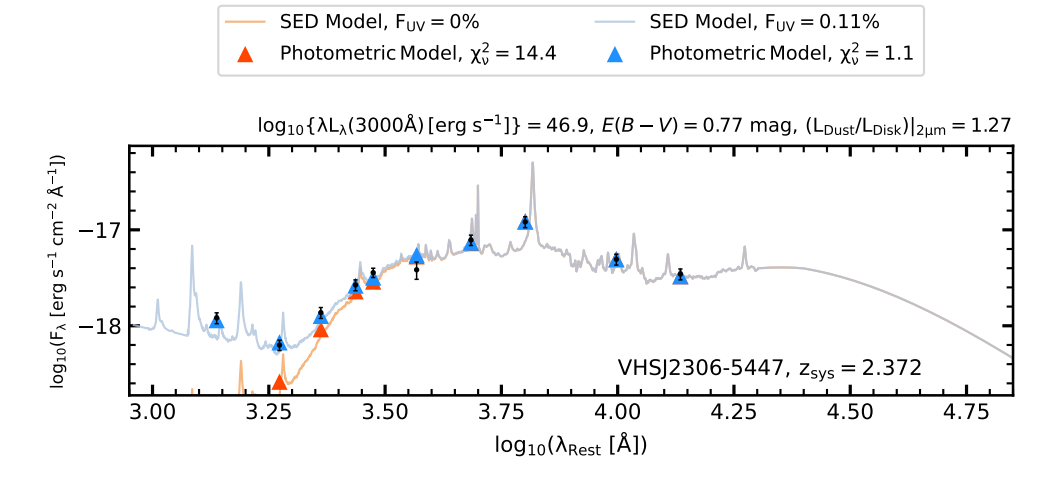


FIGURE B.39: Same as Fig. B.1 but for the HRQ - VHSJ2306-5447.

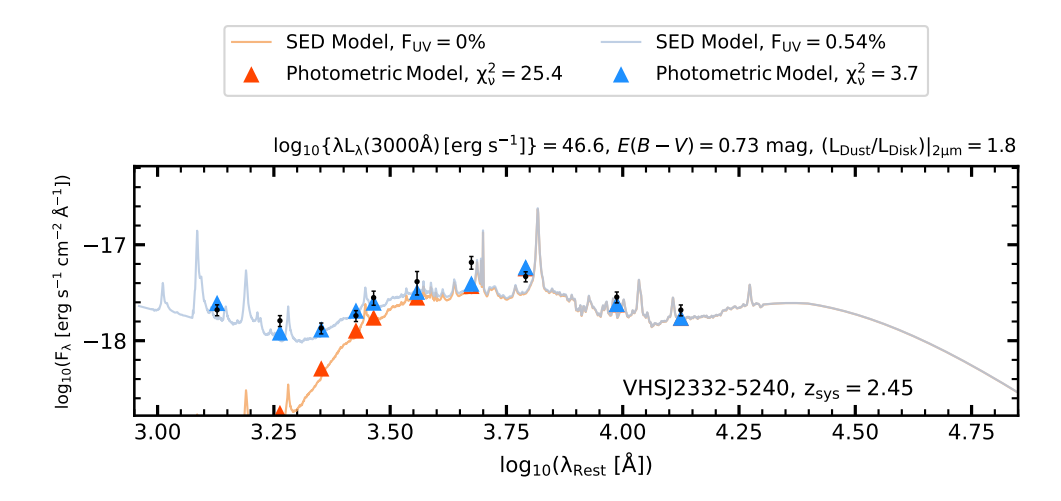


FIGURE B.40: Same as Fig. B.1 but for the HRQ - VHSJ2332-5240.

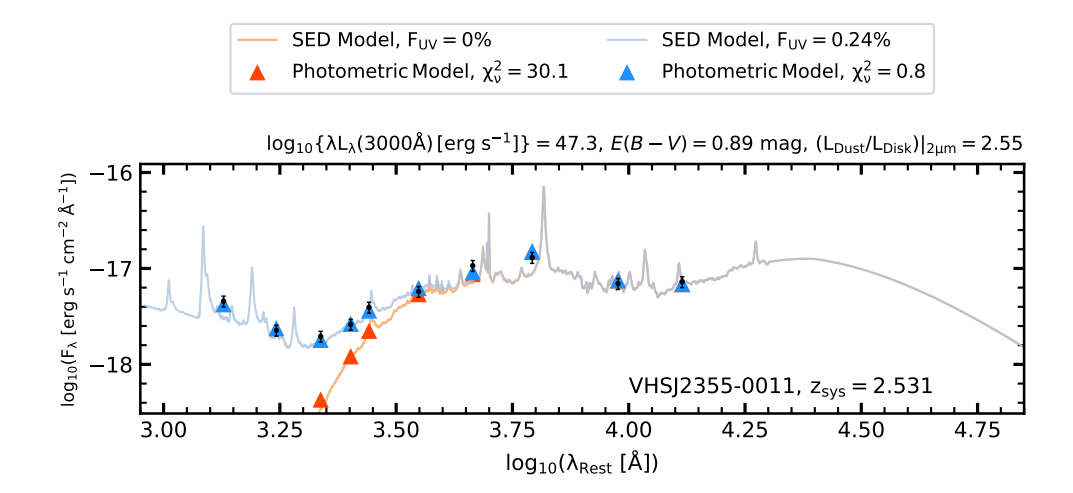


FIGURE B.41: Same as Fig. B.1 but for the HRQ - VHSJ2355-0011.

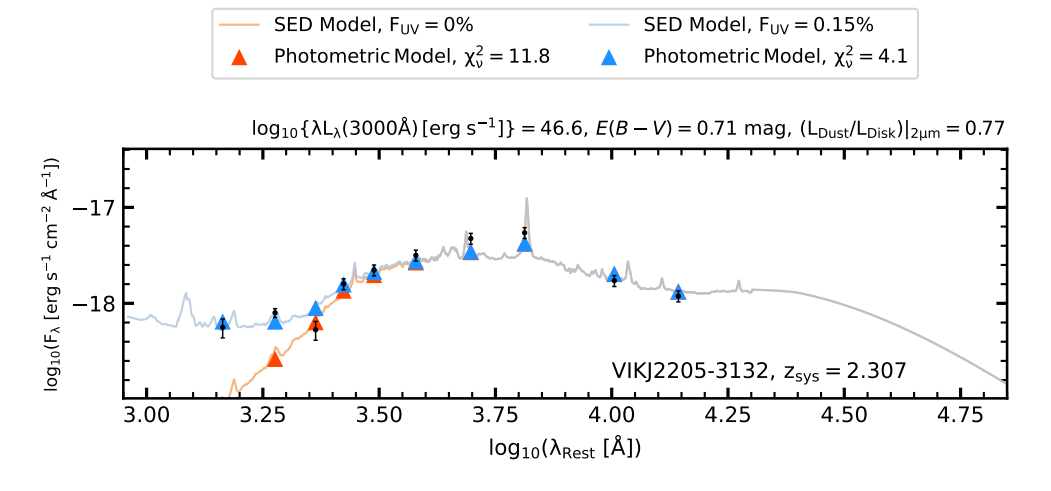


FIGURE B.42: Same as Fig. B.1 but for the HRQ - VIKJ2205-3132.

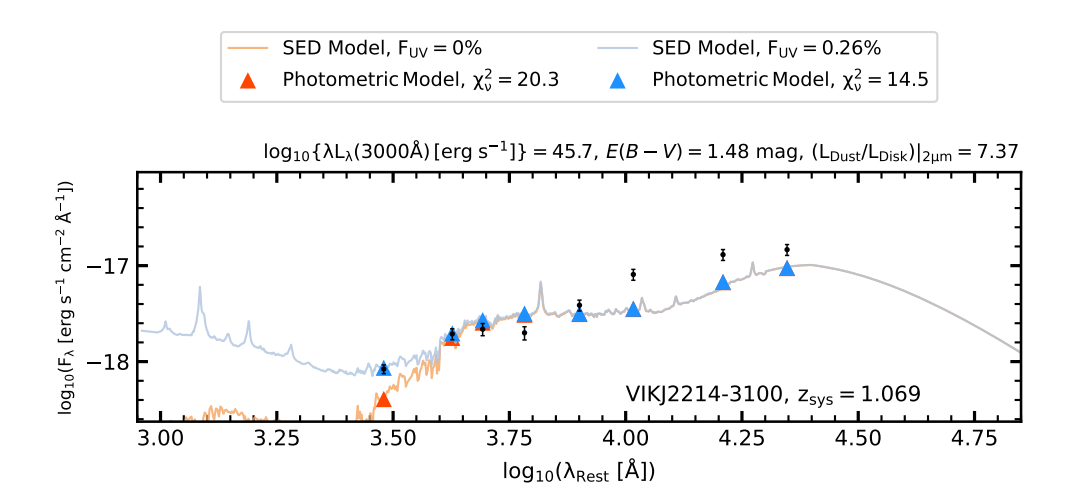


FIGURE B.43: Same as Fig. B.1 but for the HRQ - VIKJ2214-3100.

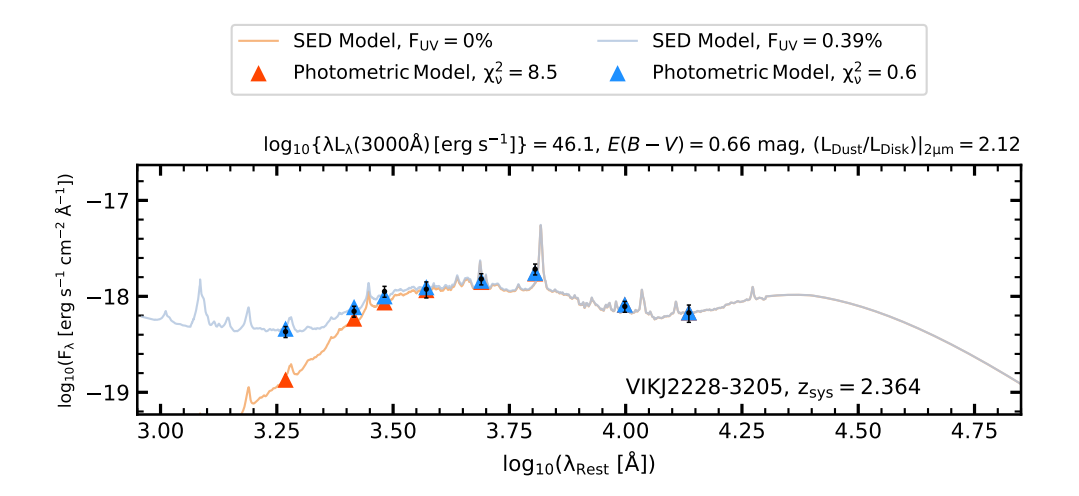


FIGURE B.44: Same as Fig. B.1 but for the HRQ - VIKJ2228-3205.

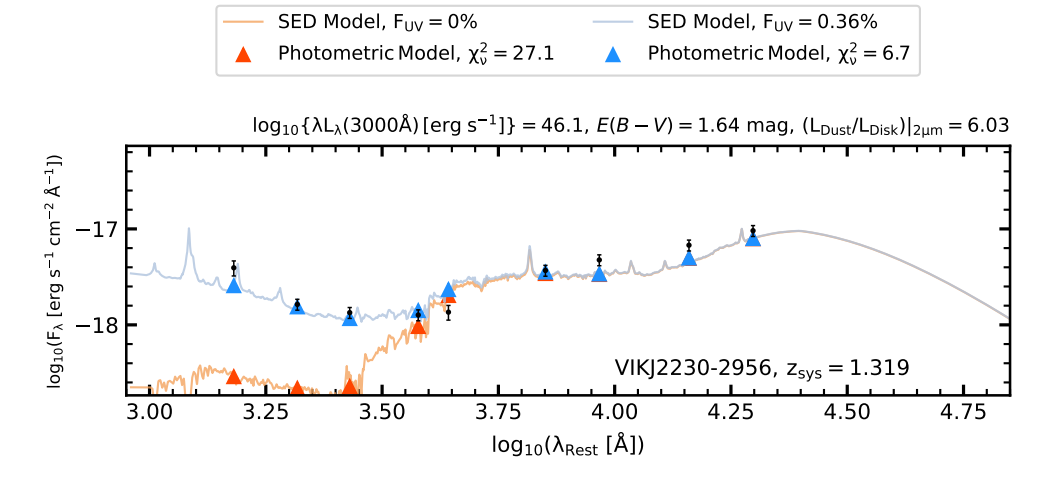


FIGURE B.45: Same as Fig. B.1 but for the HRQ - VIKJ2230-2956.

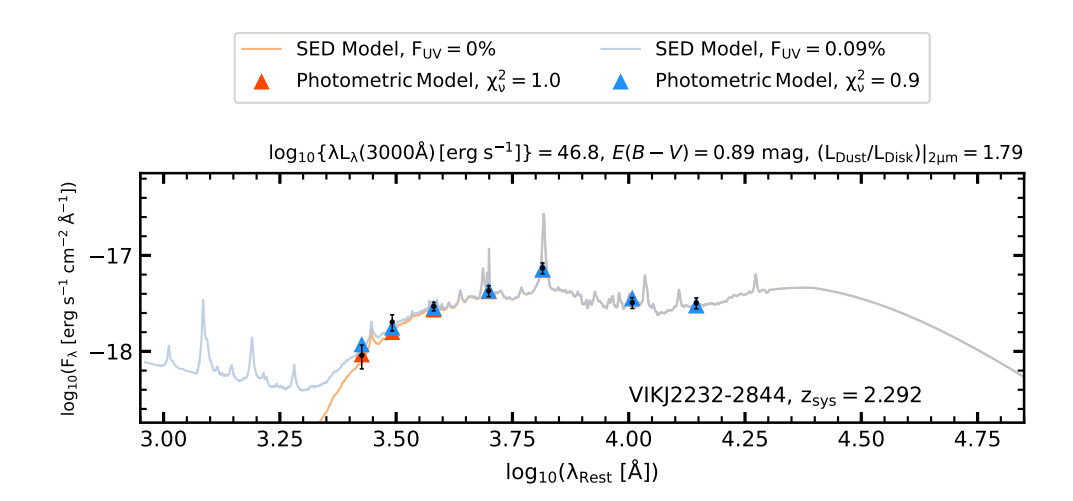


Figure B.46: Same as Fig. B.1 but for the HRQ - VIKJ2232-2844.

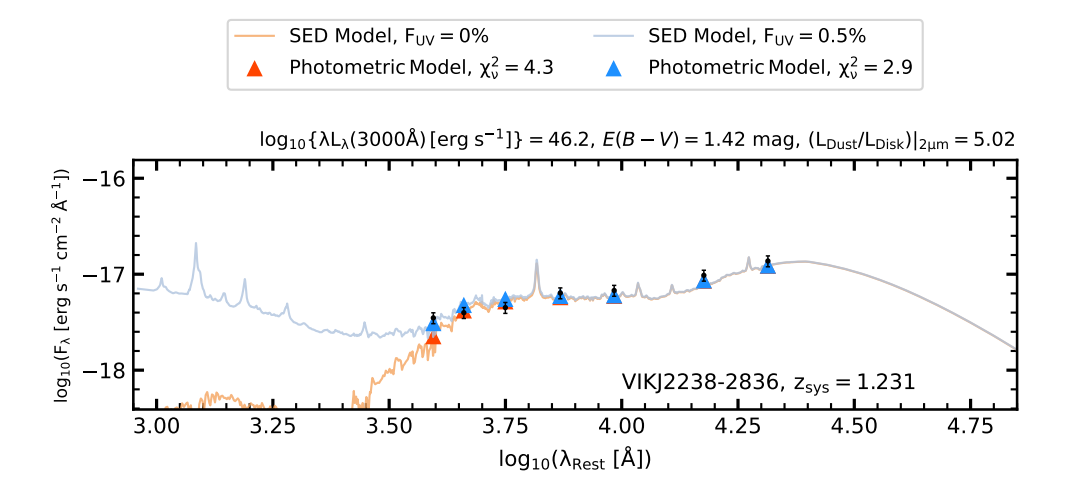


FIGURE B.47: Same as Fig. B.1 but for the HRQ - VIKJ2238-2836.

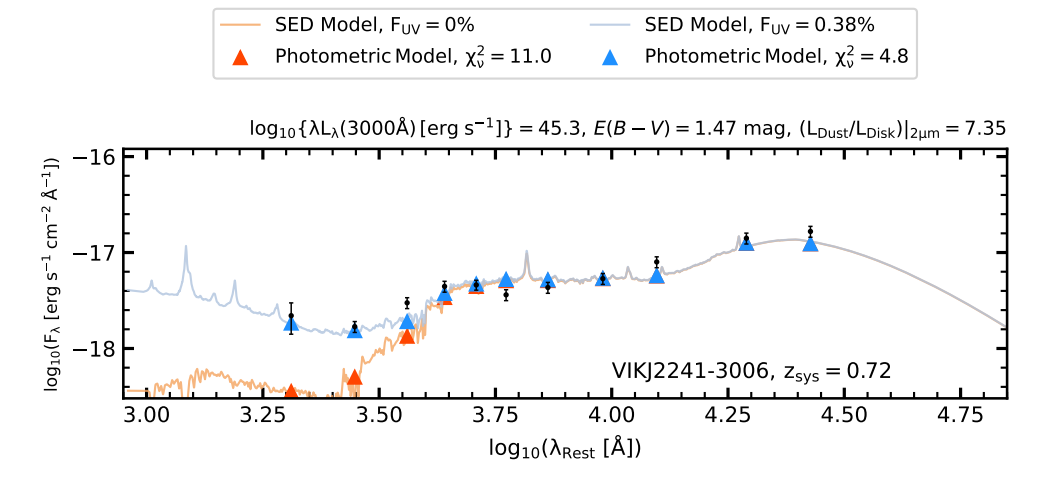


FIGURE B.48: Same as Fig. B.1 but for the HRQ - VIKJ2241-3006.

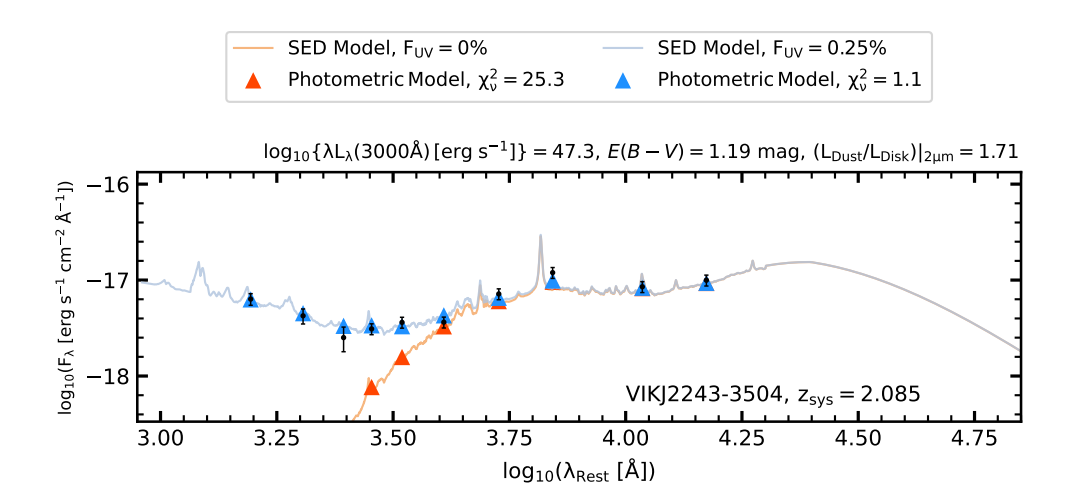


FIGURE B.49: Same as Fig. B.1 but for the HRQ - VIKJ2243-3504.

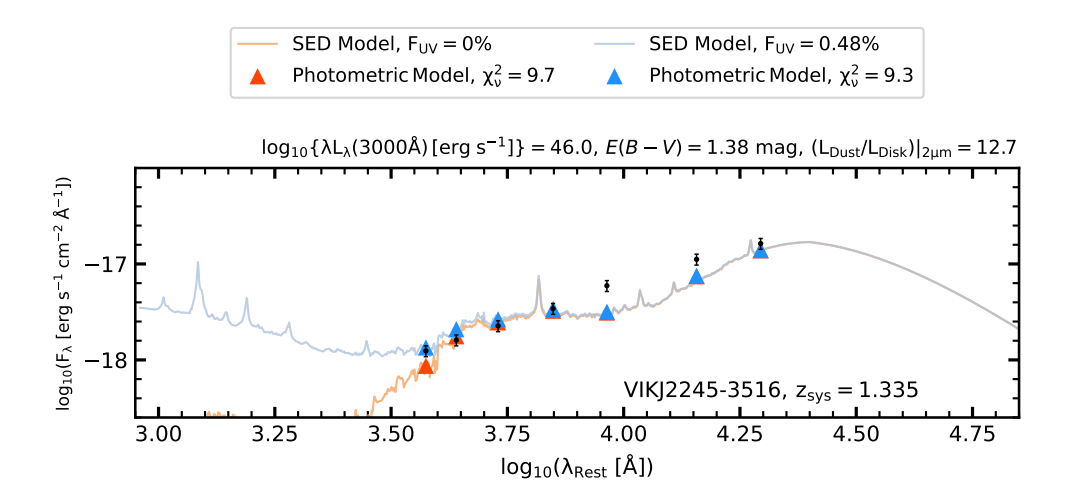


FIGURE B.50: Same as Fig. B.1 but for the HRQ - VIKJ2245-3516.

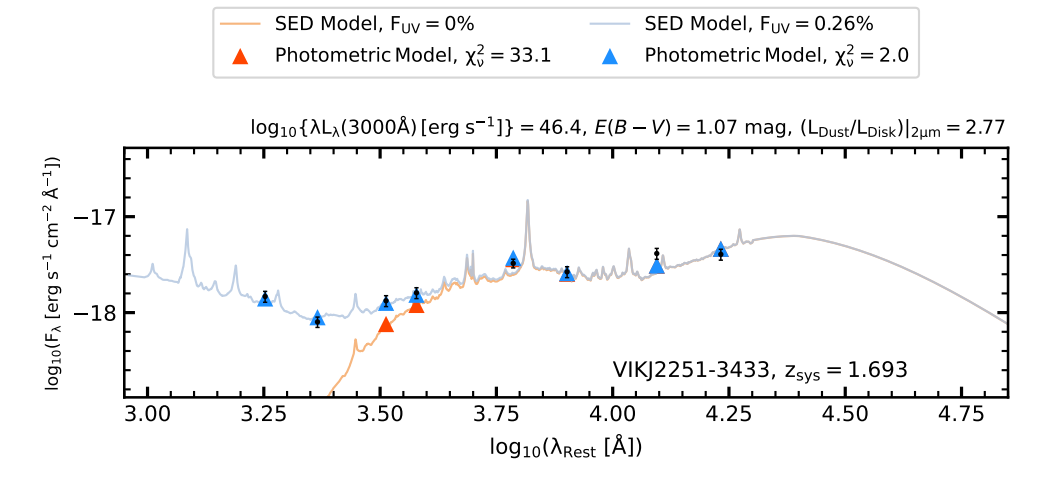


FIGURE B.51: Same as Fig. B.1 but for the HRQ - VIKJ2251-3433.

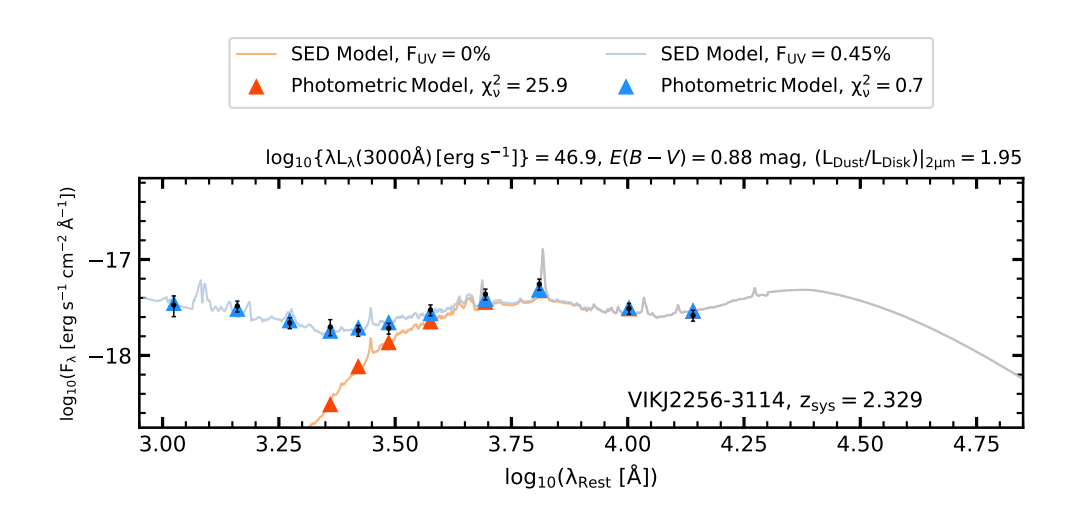


FIGURE B.52: Same as Fig. B.1 but for the HRQ - VIKJ2256-3114.

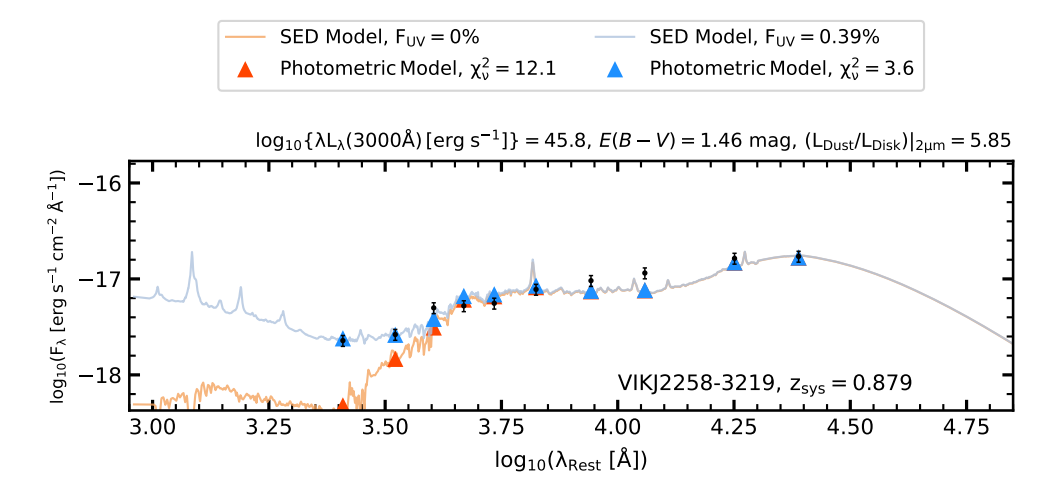


FIGURE B.53: Same as Fig. B.1 but for the HRQ - VIKJ2258-3219.

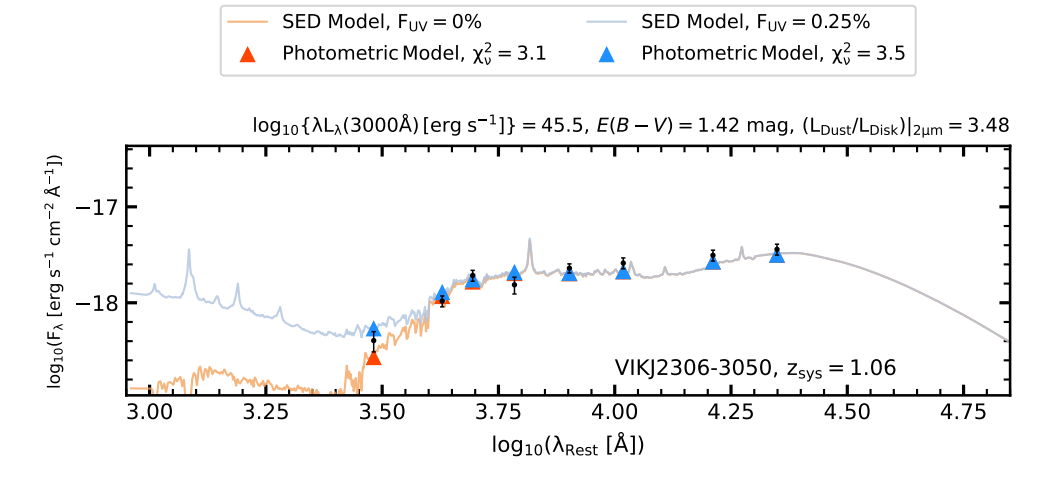


FIGURE B.54: Same as Fig. B.1 but for the HRQ - VIKJ2306-3050.

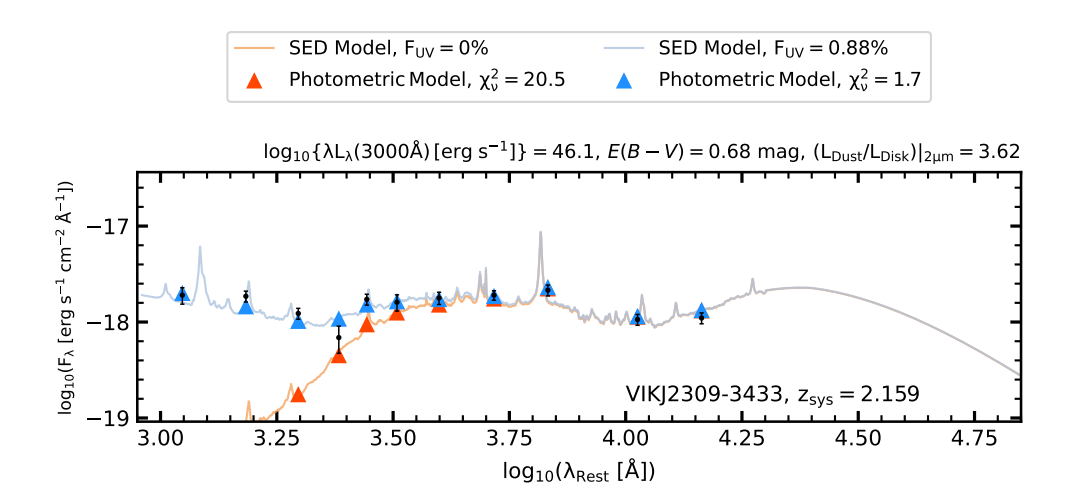


FIGURE B.55: Same as Fig. B.1 but for the HRQ - VIKJ2309-3433.

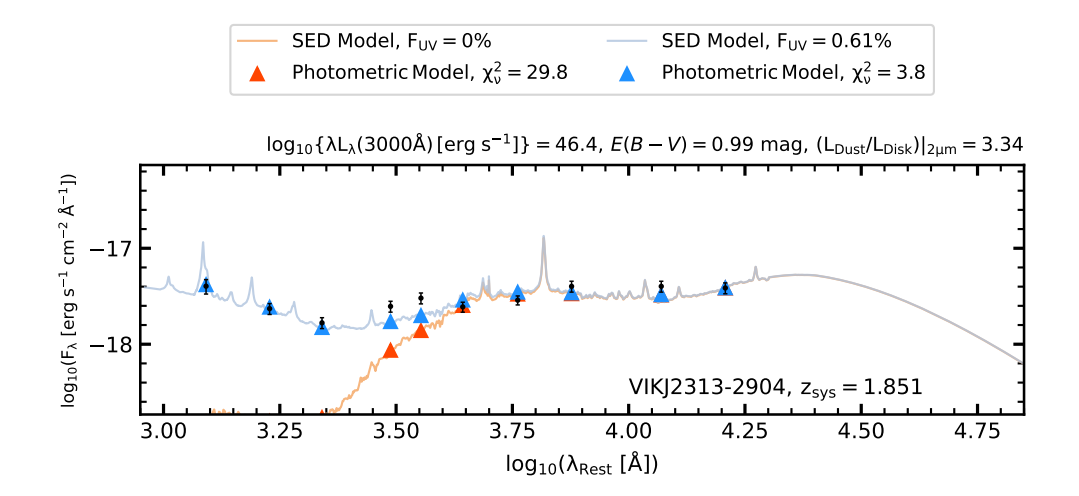


FIGURE B.56: Same as Fig. B.1 but for the HRQ - VIKJ2313-2904.

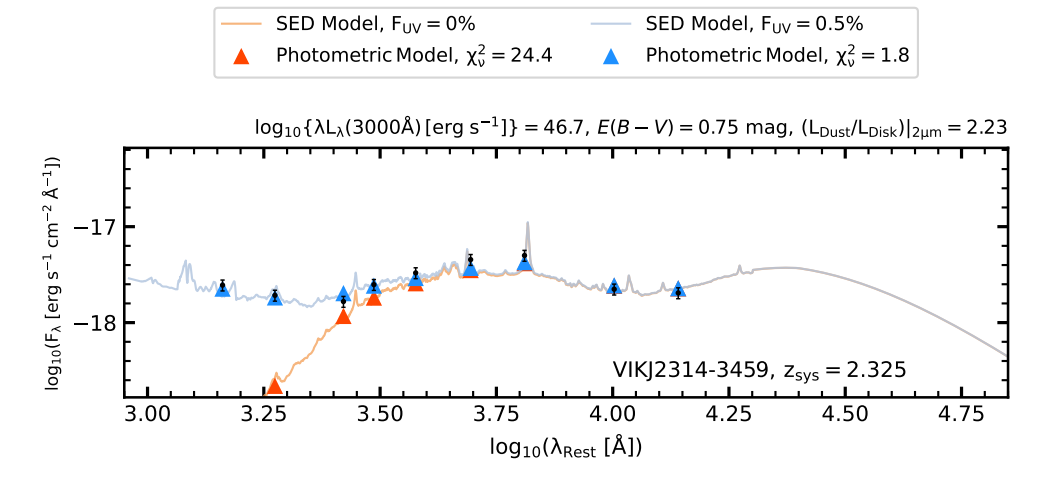


FIGURE B.57: Same as Fig. B.1 but for the HRQ - VIKJ2314-3459.

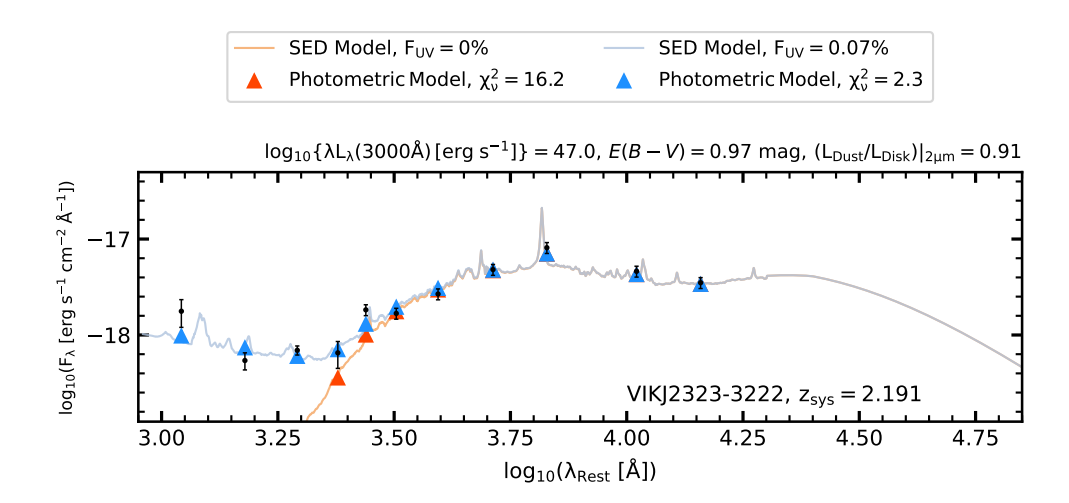


Figure B.58: Same as Fig. B.1 but for the HRQ - VIKJ2323-3222.

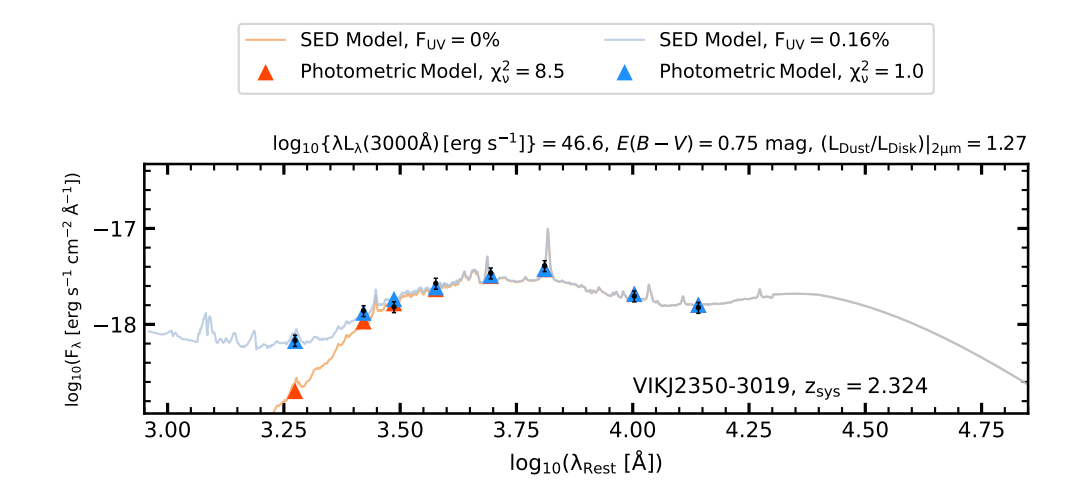


FIGURE B.59: Same as Fig. B.1 but for the HRQ - VIKJ2350-3019.

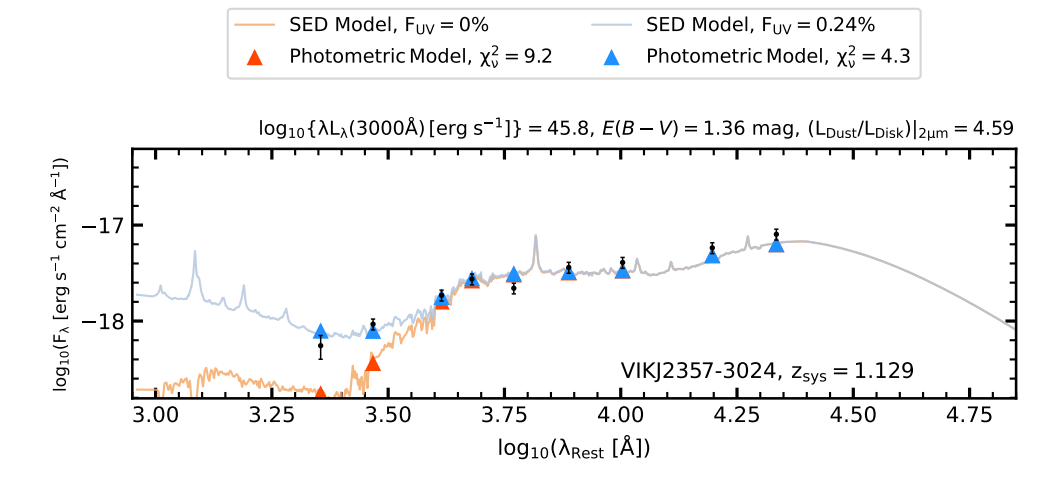


FIGURE B.60: Same as Fig. B.1 but for the HRQ - VIKJ2357-3024.

References

- **Abbott, T. M. C., Adamów, M., Aguena, M., et al.** (2021): The Dark Energy Survey Data Release 2
 - The Astrophysical Journal Supplement Series, Volume 255, Issue 2, Page 20 [DOI] [ADS] [arXiv]
- **Abuter, R., Allouche, F., Amorim, A., et al.** (2024): A dynamical measure of the black hole mass in a quasar 11 billion years ago
 - Nature, Volume 627, Issue 8003, Pages 281–285 [DOI] [ADS] [arXiv]
- **Ahumada, R., Allende Prieto, C., Almeida, A., et al.** (2020): The 16th Data Release of the Sloan Digital Sky Surveys: First Release from the APOGEE-2 Southern Survey and Full Release of eBOSS Spectra
 - The Astrophysical Journal Supplement Series, Volume 249, Issue 1, Page 3 [DOI] [ADS] [arXiv]
- Aihara, H., AlSayyad, Y., Ando, M., et al. (2022): Third data release of the Hyper Suprime-Cam Subaru Strategic Program

 Publications of the Astronomical Society of Japan, Volume 74, Issue 2, Pages 247–272 [DOI] [ADS] [arXiv]
- Akins, H. B., Casey, C. M., Lambrides, E., et al. (2024): COSMOS-Web: The over-abundance and physical nature of "little red dots"—Implications for early galaxy and SMBH assembly arXiv e-prints (2406.10341), Page arXiv:2406.10341 [DOI] [ADS] [arXiv]
- **Alexander, D. & Hickox, R. (2012)**: *What drives the growth of black holes?* New Astronomy Reviews, Volume 56, Issue 4, Pages 93–121 [DOI]
- **Alexander, D. M., Davis, T. M., Chaussidon, E., et al.** (2022): The DESI Survey Validation: Results from Visual Inspection of the Quasar Survey Spectra arXiv e-prints (2208.08517), Page arXiv:2208.08517 [DOI] [ADS] [arXiv]
- Alexander, D. M., Davis, T. M., Chaussidon, E., et al. (2023): The DESI Survey Validation: Results from Visual Inspection of the Quasar Survey Spectra

 The Astronomical Journal, Volume 165, Issue 3, Page 124 [DOI] [ADS] [arXiv]

184 REFERENCES

Alexandroff, R. M., Zakamska, N. L., Barth, A. J., et al. (2018): Spectropolarimetry of high-redshift obscured and red quasars
Monthly Notices of the Royal Astronomical Society, Volume 479, Issue 4, Pages 4936–4957 [DOI] [ADS] [arXiv]

- Allen, J. T., Hewett, P. C., Richardson, C. T., et al. (2013): Classification and analysis of emission-line galaxies using mean field independent component analysis
 Monthly Notices of the Royal Astronomical Society, Volume 430, Issue 4, Pages 3510–3536 [DOI] [ADS] [arXiv]
- Antonucci, R. (1993): Unified models for active galactic nuclei and quasars.

 Annual Review of Astronomy & Astrophysics, Volume 31, Pages 473–521 [DOI]

 [ADS]
- **Antonucci, R. R. J. & Miller, J. S.** (1985): *Spectropolarimetry and the nature of NGC 1068.* The Astrophysical Journal, Volume 297, Pages 621–632 [DOI] [ADS]
- **Aoki, K., Kawaguchi, T., & Ohta, K.** (2005): The Largest Blueshifts of the [O III] Emission Line in Two Narrow-Line Quasars

 The Astrophysical Journal, Volume 618, Issue 2, Pages 601–608 [DOI] [ADS] [arXiv]
- Assef, R. J., Bauer, F. E., Blain, A. W., et al. (2022): Imaging Polarization of the Blue-excess Hot Dust-obscured Galaxy WISE J011601.41-050504.0

 The Astrophysical Journal, Volume 934, Issue 2, Page 101 [DOI] [ADS] [arXiv]
- Assef, R. J., Brightman, M., Walton, D. J., et al. (2020): Hot Dust-obscured Galaxies with Excess Blue Light
 - The Astrophysical Journal, Volume 897, Issue 2, Page 112 [DOI] [ADS] [arXiv]
- **Assef, R. J., Eisenhardt, P. R. M., Stern, D., et al.** (2015): Half of the Most Luminous Quasars May Be Obscured: Investigating the Nature of WISE-Selected Hot Dust-Obscured Galaxies
 - The Astrophysical Journal, Volume 804, Issue 1, Page 27 [DOI] [ADS] [arXiv]
- **Bañados, E., Venemans, B. P., Decarli, R.,** *et al.* (2016): The Pan-STARRS1 Distant z > 5.6 Quasar Survey: More than 100 Quasars within the First Gyr of the Universe The Astrophysical Journal Supplement Series, Volume 227, Issue 1, Page 11 [DOI] [ADS] [arXiv]
- **Baker, J. G. & Menzel, D. H. (1938)**: Physical Processes in Gaseous Nebulae. III. The Balmer Decrement.
 - The Astrophysical Journal, Volume 88, Page 52 [DOI] [ADS]
- Baldwin, J. A., Ferland, G. J., Martin, P. G., et al. (1991): Physical Conditions in the Orion Nebula and an Assessment of Its Helium Abundance

 The Astrophysical Journal, Volume 374, Page 580 [DOI] [ADS]

Banerji, M., Alaghband-Zadeh, S., Hewett, P. C., et al. (2015): Heavily reddened type 1 quasars at z > 2 - I. Evidence for significant obscured black hole growth at the highest quasar luminosities

- Monthly Notices of the Royal Astronomical Society, Volume 447, Issue 4, Pages 3368–3389 [DOI] [ADS] [arXiv]
- **Banerji, M., Carilli, C. L., Jones, G.,** *et al.* (2017): The discovery of gas-rich, dusty starbursts in luminous reddened quasars at $z \sim 2.5$ with ALMA Monthly Notices of the Royal Astronomical Society, Volume 465, Issue 4, Pages 4390–4405 [DOI] [ADS] [arXiv]
- **Banerji, M., Fabian, A. C., & McMahon, R. G.** (**2014**): *ULASJ1234+0907: the reddest type 1 quasar at z* = 2.5 *revealed in the X-ray and far-infrared.*Monthly Notices of the Royal Astronomical Society, Volume 439, Pages L51–L55 [DOI] [ADS] [arXiv]
- **Banerji, M., Jones, G. C., Carniani, S., et al.** (2021): Resolving discs and mergers in $z \sim 2$ heavily reddened quasars and their companion galaxies with ALMA Monthly Notices of the Royal Astronomical Society, Volume 503, Issue 4, Pages 5583–5599 [DOI] [ADS] [arXiv]
- **Banerji, M., Jones, G. C., Wagg, J.,** *et al.* (2018): The interstellar medium properties of heavily reddened quasarsand companions at $z \sim 2.5$ with ALMA and JVLA Monthly Notices of the Royal Astronomical Society, Volume 479, Issue 1, Pages 1154–1169 [DOI] [ADS] [arXiv]
- **Banerji, M., McMahon, R. G., Hewett, P. C.,** *et al.* (2012): Heavily reddened quasars at *z* ∼ 2 in the UKIDSS Large Area Survey: a transitional phase in AGN evolution Monthly Notices of the Royal Astronomical Society, Volume 427, Issue 3, Pages 2275–2291 [DOI] [ADS] [arXiv]
- Banerji, M., McMahon, R. G., Hewett, P. C., et al. (2013): Hyperluminous reddened broad-line quasars at z -2 from the VISTA hemisphere survey and WISE all-sky survey. Monthly Notices of the Royal Astronomical Society, Volume 429, Pages L55–L59 [DOI] [ADS] [arXiv]
- **Barlow-Hall, C., Delaney, J., Aird, J., et al.** (2023): Constraints on the X-ray luminosity function of AGN at z = 5.7-6.4 with the Extragalactic Serendipitous Swift Survey Monthly Notices of the Royal Astronomical Society, Volume 519, Issue 4, Pages 6055–6064 [DOI]
- **Barvainis**, **R.** (1987): Hot Dust and the Near-Infrared Bump in the Continuum Spectra of Quasars and Active Galactic Nuclei

 The Astrophysical Journal, Volume 320, Page 537 [DOI] [ADS]

Baskin, A. & Laor, A. (2005): What controls the [OIII] λ 5007 line strength in active galactic nuclei?

Monthly Notices of the Royal Astronomical Society, Volume 358, Issue 3, Pages 1043–1054 [DOI] [ADS] [arXiv]

Baskin, A., Laor, A., & Hamann, F. (2015): On the origins of C IV absorption profile diversity in broad absorption line quasars

Monthly Notices of the Royal Astronomical Society, Volume 449, Issue 2, Pages 1593–1604 [DOI] [ADS] [arXiv]

Baskin, A., Laor, A., & Stern, J. (2013): Radiation pressure confinement – II. Application to the broad-line region in active galactic nuclei

Monthly Notices of the Royal Astronomical Society, Volume 438, Issue 1, Pages 604–619 [DOI] [arXiv]

Bauer, F. E., Lira, P., Anguita, T., et al. (2023): Chilean AGN/Galaxy Extragalactic Survey (ChANGES)

The Messenger, Volume 190, Pages 34–37 [DOI] [ADS]

Beckmann, V. & Shrader, C. (2012): The AGN phenomenon: open issues
In Proceedings of "An INTEGRAL view of the high-energy sky (the first 10 years)" - 9th
INTEGRAL Workshop and celebration of the 10th anniversary of the launch (INTEGRAL
2012). 15-19 October 2012. Bibliotheque Nationale de France [DOI] [ADS] [arXiv]

Begelman, M. C., Blandford, R. D., & Rees, M. J. (1980): Massive black hole binaries in active galactic nuclei

Nature, Volume 287, Issue 5780, Pages 307-309

Begelman, M. C., McKee, C. F., & Shields, G. A. (1983): Compton heated winds and coronae above accretion disks. I. Dynamics.

The Astrophysical Journal, Volume 271, Pages 70–88 [DOI] [ADS]

Benson, A. J., Bower, R. G., Frenk, C. S., et al. (2003): What Shapes the Luminosity Function of Galaxies?

The Astrophysical Journal, Volume 599, Issue 1, Page 38 [DOI]

- Bentz, M. C., Peterson, B. M., Netzer, H., et al. (2009): The Radius-Luminosity Relationship for Active Galactic Nuclei: The Effect of Host-Galaxy Starlight on Luminosity Measurements. II. The Full Sample of Reverberation-Mapped AGNs

 The Astrophysical Journal, Volume 697, Issue 1, Pages 160–181 [DOI] [ADS] [arXiv]
- Bentz, M. C., Walsh, J. L., Barth, A. J., et al. (2008): First Results from the Lick AGN Monitoring Project: The Mass of the Black Hole in Arp 151

 The Astrophysical Journal Letters, Volume 689, Issue 1, Page L21 [DOI] [ADS]

 [arXiv]

Bernstein, R. A., Freedman, W. L., & Madore, B. F. (2002): The First Detections of the Extragalactic Background Light at 3000, 5500, and 8000 Å. III. Cosmological Implications The Astrophysical Journal, Volume 571, Issue 1, Page 107 [DOI]

- Binney, J. & Tabor, G. (1995): Evolving cooling flows.

 Monthly Notices of the Royal Astronomical Society, Volume 276, Pages 663–678

 [DOI] [ADS]
- **Birrer, S., Shajib, A., Gilman, D., et al.** (2021): lenstronomy II: A gravitational lensing software ecosystem

 The Journal of Open Source Software, Volume 6, Issue 62, Page 3283 [DOI] [ADS]
 - [arXiv]
- **Bischetti, M., Feruglio, C., D'Odorico, V., et al.** (2022): Suppression of black-hole growth by strong outflows at redshifts 5.8-6.6

 Nature, Volume 605, Issue 7909, Pages 244–247 [DOI] [ADS]
- **Bischetti, M., Fiore, F., Feruglio, C.,** *et al.* (2023): The fraction and kinematics of broad absorption line quasars across cosmic time arXiv e-prints (2301.09731), Page arXiv:2301.09731 [DOI] [ADS] [arXiv]
- **Bischetti, M., Piconcelli, E., Vietri, G., et al.** (2017): The WISSH quasars project. I. Powerful ionised outflows in hyper-luminous quasars

 Astronomy & Astrophysics, Volume 598, Page A122 [DOI] [ADS] [arXiv]
- Blandford, R. D. & Znajek, R. L. (1977): Electromagnetic extraction of energy from Kerr black holes.

 Monthly Notices of the Royal Astronomical Society, Volume 179, Pages 433–456
 - Monthly Notices of the Royal Astronomical Society, Volume 179, Pages 433–456 [DOI] [ADS]
- **Bluck, A. F. L., Conselice, C. J., Bouwens, R. J.,** *et al.* (2009): A surprisingly high pair fraction for extremely massive galaxies at z ~3 in the GOODS NICMOS survey

 Monthly Notices of the Royal Astronomical Society, Volume 394, Issue 1, Pages L51–L55 [DOI] [ADS] [arXiv]
- **Bohren, C. F. & Huffman, D. R.** (1983): Absorption and scattering of light by small particles [ADS]
- **Boroson, T. (2005)**: Blueshifted [O III] Emission: Indications of a Dynamic Narrow-Line Region
 - The Astronomical Journal, Volume 130, Issue 2, Pages 381–386 [DOI] [ADS] [arXiv]
- **Bowen, I. S.** (1927): *The Origin of the Nebulium Spectrum* Nature, Volume 120, Issue 3022, Page 473 [DOI] [ADS]

Brodzeller, A. & Dawson, K. (2022): *Modeling the Spectral Diversity of Quasars in the Sixteenth Data Release from the Sloan Digital Sky Survey*The Astronomical Journal, Volume 163, Issue 3, Page 110 [DOI] [ADS] [arXiv]

- Buckley, D. A. H., Swart, G. P., & Meiring, J. G. (2006): Completion and commissioning of the Southern African Large Telescope
 In Stepp, L. M. (ed.): Ground-based and Airborne Telescopes. Society of Photo-Optical Instrumentation Engineers (SPIE) Conference Series [DOI] [ADS]
- Burgh, E. B., Nordsieck, K. H., Kobulnicky, H. A., et al. (2003): Prime Focus Imaging Spectrograph for the Southern African Large Telescope: optical design
 In Iye, M. & Moorwood, A. F. M. (eds.): Instrument Design and Performance for Optical/Infrared Ground-based Telescopes. Society of Photo-Optical Instrumentation Engineers (SPIE) Conference Series [DOI] [ADS]
- Calistro Rivera, G., Alexander, D. M., Rosario, D. J., et al. (2021): The multiwavelength properties of red QSOs: Evidence for dusty winds as the origin of QSO reddening Astronomy & Astrophysics, Volume 649, Page A102 [DOI] [ADS] [arXiv]
- Calzetti, D., Armus, L., Bohlin, R. C., et al. (2000): The Dust Content and Opacity of Actively Star-forming Galaxies

 The Astrophysical Journal, Volume 533, Issue 2, Pages 682–695 [DOI] [ADS] [arXiv]
- Cano-Díaz, M., Maiolino, R., Marconi, A., et al. (2012): Observational evidence of quasar feedback quenching star formation at high redshift
 Astronomy & Astrophysics, Volume 537, Page L8 [DOI] [ADS] [arXiv]
- Cardelli, J. A., Clayton, G. C., & Mathis, J. S. (1989): The Relationship between Infrared, Optical, and Ultraviolet Extinction

 The Astrophysical Journal, Volume 345, Page 245 [DOI] [ADS]
- Chambers, K. C., Magnier, E. A., Metcalfe, N., et al. (2016): The Pan-STARRS1 Surveys arXiv e-prints (1612.05560), Page arXiv:1612.05560 [DOI] [ADS] [arXiv]
- **Chandrasekhar, S.** (1950): *Radiative transfer.* Oxford University Press [ADS]
- Chen, C., Hamann, F., Simon, L., et al. (2018): The gaseous environments of quasars: associate absorption lines with density and distance constraints

 Monthly Notices of the Royal Astronomical Society, Volume 481, Issue 3, Pages 3865–3886 [DOI] [ADS] [arXiv]
- Cheney, J. E. & Rowan-Robinson, M. (1981): The average quasar spectrum in the wavelength range 0.1-0.6 micronMonthly Notices of the Royal Astronomical Society, Volume 195, Pages 831–837 [DOI] [ADS]

Ching, J. H. Y., Sadler, E. M., Croom, S. M., et al. (2017): The Large Area Radio Galaxy Evolution Spectroscopic Survey (LARGESS): survey design, data catalogue and GAMA/WiggleZ spectroscopy

Monthly Notices of the Royal Astronomical Society, Volume 464, Issue 2, Pages 1306–1332 [DOI] [ADS] [arXiv]

- Churazov, E., Forman, W., Jones, C., et al. (2000): Asymmetric, arc minute scale structures around NGC 1275

 Astronomy & Astrophysics, Volume 356, Pages 788–794 [DOI] [ADS] [arXiv]
- **Cicone, C., Maiolino, R., Sturm, E., et al.** (2014): Massive molecular outflows and evidence for AGN feedback from CO observations

 Astronomy & Astrophysics, Volume 562, Page A21 [DOI] [ADS] [arXiv]
- Clavel, J., Reichert, G. A., Alloin, D., et al. (1991): Steps toward Determination of the Size and Structure of the Broad-Line Region in Active Galactic Nuclei. I. an 8 Month Campaign of Monitoring NGC 5548 with IUE

 The Astrophysical Journal, Volume 366, Page 64 [DOI] [ADS]
- Coatman, L., Hewett, P. C., Banerji, M., et al. (2016): C IV emission-line properties and systematic trends in quasar black hole mass estimates

 Monthly Notices of the Royal Astronomical Society, Volume 461, Issue 1, Pages 647–665 [DOI] [ADS] [arXiv]
- Coatman, L., Hewett, P. C., Banerji, M., et al. (2017): Correcting C IV-based virial black hole masses
 Monthly Notices of the Royal Astronomical Society, Volume 465, Issue 2, Pages 2120–2142 [DOI] [ADS] [arXiv]
- Coatman, L., Hewett, P. C., Banerji, M., et al. (2019): Kinematics of C IV and [O III] emission in luminous high-redshift quasars

 Monthly Notices of the Royal Astronomical Society, Volume 486, Issue 4, Pages 5335–5348 [DOI] [ADS] [arXiv]
- Cole, S., Norberg, P., Baugh, C. M., et al. (2001): The 2dF galaxy redshift survey: near-infrared galaxy luminosity functions

 Monthly Notices of the Royal Astronomical Society, Volume 326, Issue 1, Pages 255–273 [DOI] [ADS] [arXiv]
- **Compton, A. H.** (1923): *A Quantum Theory of the Scattering of X-rays by Light Elements* Physical Review, Volume 21, Issue 5, Pages 483–502 [DOI] [ADS]
- Conselice, C. J., Bershady, M. A., Dickinson, M., et al. (2003): A Direct Measurement of Major Galaxy Mergers at z≤3
 The Astronomical Journal, Volume 126, Issue 3, Pages 1183–1207 [DOI] [ADS]
 [arXiv]

Costa, T., Rosdahl, J., Sijacki, D., et al. (2018): Quenching star formation with quasar outflows launched by trapped IR radiation

Monthly Notices of the Royal Astronomical Society, Volume 479, Issue 2, Pages 2079–2111 [DOI] [ADS] [arXiv]

- Crenshaw, D. M., Kraemer, S. B., & George, I. M. (2003): Mass Loss from the Nuclei of Active Galaxies
 - Annual Review of Astronomy & Astrophysics, Volume 41, Pages 117–167 [DOI] [ADS]
- Czerny, B., Li, J., Loska, Z., et al. (2004): Extinction due to amorphous carbon grains in red quasars from the Sloan Digital Sky Survey

 Monthly Notices of the Royal Astronomical Society, Volume 348, Issue 3, Pages
 L54–L57 [DOI] [ADS] [arXiv]
- Dai, X., Griffin, R. D., Kochanek, C. S., et al. (2015): The SWIFT AGN and Cluster Survey. I. Number Counts of AGNs and Galaxy ClustersThe Astrophysical Journal Supplement Series, Volume 218, Issue 1, Page 8 [DOI] [ADS] [arXiv]
- **Davis, S. W., Woo, J.-H., & Blaes, O. M.** (2007): *The UV Continuum of Quasars: Models and SDSS Spectral Slopes*The Astrophysical Journal, Volume 668, Issue 2, Pages 682–698 [DOI] [ADS] [arXiv]
- **Dawson, K. S., Kneib, J.-P., Percival, W. J., et al.** (2016): THE SDSS-IV EXTENDED BARYON OSCILLATION SPECTROSCOPIC SURVEY: OVERVIEW AND EARLY

The Astronomical Journal, Volume 151, Issue 2, Page 44 [DOI]

DATA

- **Dawson, K. S., Schlegel, D. J., Ahn, C. P., et al.** (2012): THE BARYON OSCILLATION SPECTROSCOPIC SURVEY OF SDSS-III
 - The Astronomical Journal, Volume 145, Issue 1, Page 10 [DOI]
- de Graaff, A., Rix, H.-W., Naidu, R. P., et al. (2025): A remarkable Ruby: Absorption in dense gas, rather than evolved stars, drives the extreme Balmer break of a Little Red Dot at z=3.5
 - arXiv e-prints (2503.16600), Page arXiv:2503.16600 [DOI] [ADS] [arXiv]
- **De Rosa, G., Venemans, B. P., Decarli, R.,** *et al.* (2014): Black Hole Mass Estimates and Emission-line Properties of a Sample of Redshift z > 6.5 Quasars

 The Astrophysical Journal, Volume 790, Issue 2, Page 145 [DOI] [ADS] [arXiv]
- **Di Matteo, T., Springel, V., & Hernquist, L.** (2005): Energy input from quasars regulates the growth and activity of black holes and their host galaxies

 Nature, Volume 433, Issue 7026, Pages 604–607 [DOI] [ADS] [arXiv]

Ding, X., Onoue, M., Silverman, J. D., et al. (2023): Detection of stellar light from quasar host galaxies at redshifts above 6

- Nature, Volume 621, Issue 7977, Pages 51–55 [DOI] [ADS] [arXiv]
- **Ding, X., Silverman, J., Birrer, S., et al.** (2022): *GaLight: 2D modeling of galaxy images* Astrophysics Source Code Library, record ascl:2209.011 [ADS]
- Draine, B. (2003): Interstellar Dust Grains
 Annual Review of Astronomy and Astrophysics, Volume 41, Issue Volume 41, 2003,
 Pages 241–289 [DOI]
- Dubois, Y., Peirani, S., Pichon, C., et al. (2016): The HORIZON-AGN simulation: morphological diversity of galaxies promoted by AGN feedback
 Monthly Notices of the Royal Astronomical Society, Volume 463, Issue 4, Pages 3948–3964 [DOI] [ADS] [arXiv]
- **Eddington, A. S.** (1925): A limiting case in the theory of radiative equilibrium Monthly Notices of the Royal Astronomical Society, Volume 85, Page 408 [DOI] [ADS]
- **Edge, A., Sutherland, W., Kuijken, K., et al.** (2013): The VISTA Kilo-degree Infrared Galaxy (VIKING) Survey: Bridging the Gap between Low and High Redshift The Messenger, Volume 154, Pages 32–34 [ADS]
- Edge, D. O., Shakeshaft, J. R., McAdam, W. B., et al. (1959): A survey of radio sources at a frequency of 159 Mc/s.
 - Memoirs of the Royal Astronomical Society, Volume 68, Pages 37–60 [ADS]
- **Einstein, A.** (1905a): Ist die Trägheit eines Körpers von seinem Energieinhalt abhängig? Annalen der Physik, Volume 323, Issue 13, Pages 639–641 [DOI] [ADS]
- **Einstein, A.** (1905b): Über einen die Erzeugung und Verwandlung des Lichtes betreffenden heuristischen Gesichtspunkt
 - Annalen der Physik, Volume 322, Issue 6, Pages 132–148 [DOI] [ADS]
- **Einstein, A.** (1905c): Zur Elektrodynamik bewegter Körper Annalen der Physik, Volume 322, Issue 10, Pages 891–921 [DOI] [ADS]
- Einstein, A. (1915): Die Feldgleichungen der Gravitation Sitzungsberichte der Königlich Preussischen Akademie der Wissenschaften, Pages 844–847 [ADS]
- **Einstein, A.** (**1916a**): *Die Grundlage der allgemeinen Relativitätstheorie* Annalen der Physik, Volume 354, Issue 7, Pages 769–822 [DOI] [ADS]
- **Einstein, A.** (1916b): *Strahlungs-Emission und Absorption nach der Quantentheorie* Deutsche Physikalische Gesellschaft, Volume 18, Pages 318–323 [ADS]

Eisenhardt, P. R. M., Wu, J., Tsai, C.-W., *et al.* (2012): THE FIRST HYPER-LUMINOUS INFRARED GALAXY DISCOVERED BY WISE

The Astrophysical Journal, Volume 755, Issue 2, Page 173 [DOI]

- **Euclid Collaboration, Bisigello, L., Rodighiero, G.,** *et al.* (2025a): Euclid Quick Data Release (Q1). Extending the quest for little red dots to z_i 4 arXiv e-prints (2503.15323), Page arXiv:2503.15323 [DOI] [ADS] [arXiv]
- Euclid Collaboration, Cropper, M. S., Al-Bahlawan, A., et al. (2025b): Euclid: II. The VIS instrument

Astronomy & Astrophysics, Volume 697, Page A2 [DOI] [ADS] [arXiv]

Euclid Collaboration, Jahnke, K., Gillard, W., et al. (2025c): Euclid: III. The NISP Instrument

Astronomy & Astrophysics, Volume 697, Page A3 [DOI] [ADS] [arXiv]

Euclid Collaboration, Mellier, Y., Abdurro'uf, et al. (2025d): Euclid: I. Overview of the Euclid mission

Astronomy & Astrophysics, Volume 697, Page A1 [DOI] [ADS] [arXiv]

- Event Horizon Telescope Collaboration, Akiyama, K., Alberdi, A., et al. (2019): First M87 Event Horizon Telescope Results. I. The Shadow of the Supermassive Black Hole The Astrophysical Journal Letters, Volume 875, Issue 1, Page L1 [DOI] [ADS] [arXiv]
- **Event Horizon Telescope Collaboration, Akiyama, K., Alberdi, A., et al.** (2022): First Sagittarius A* Event Horizon Telescope Results. I. The Shadow of the Supermassive Black Hole in the Center of the Milky Way

The Astrophysical Journal Letters, Volume 930, Issue 2, Page L12 [DOI] [ADS]

- **Fabian, A. C.** (1999): *The obscured growth of massive black holes*Monthly Notices of the Royal Astronomical Society, Volume 308, Issue 4, Pages L39–L43 [DOI] [ADS] [arXiv]
- **Fabian, A. C.** (2012): Observational Evidence of Active Galactic Nuclei Feedback
 Annual Review of Astronomy & Astrophysics, Volume 50, Pages 455–489 [DOI]
 [ADS] [arXiv]
- **Fabian, A. C., Lohfink, A., Kara, E., et al. (2015)**: Properties of AGN coronae in the NuSTAR era

Monthly Notices of the Royal Astronomical Society, Volume 451, Issue 4, Pages 4375–4383 [DOI] [ADS] [arXiv]

Fabian, A. C., Sanders, J. S., Allen, S. W., et al. (2003): A deep Chandra observation of the Perseus cluster: shocks and ripples

Monthly Notices of the Royal Astronomical Society, Volume 344, Issue 3, Pages L43–L47 [DOI] [ADS] [arXiv]

Fan, X., Banados, E., & Simcoe, R. A. (2022): Quasars and the Intergalactic Medium at Cosmic Dawn arXiv e-prints (2212.06907), Page arXiv:2212.06907 [DOI] [ADS] [arXiv]

- **Farina, E. P., Schindler, J.-T., Walter, F., et al.** (2022): The X-shooter/ALMA Sample of Quasars in the Epoch of Reionization. II. Black Hole Masses, Eddington Ratios, and the Formation of the First Quasars
 - The Astrophysical Journal, Volume 941, Issue 2, Page 106 [DOI] [ADS] [arXiv]
- **Fawcett, V. A., Alexander, D. M., Brodzeller, A., et al.** (2023): A striking relationship between dust extinction and radio detection in DESI QSOs: evidence for a dusty blow-out phase in red QSOs
 - Monthly Notices of the Royal Astronomical Society, Volume 525, Issue 4, Pages 5575–5596 [DOI] [ADS] [arXiv]
- **Fawcett, V. A., Alexander, D. M., Rosario, D. J., et al.** (2020): Fundamental differences in the radio properties of red and blue quasars: enhanced compact AGN emission in red quasars
 - Monthly Notices of the Royal Astronomical Society, Volume 494, Issue 4, Pages 4802–4818 [DOI] [ADS] [arXiv]
- **Fawcett, V. A., Alexander, D. M., Rosario, D. J., et al.** (2022): Fundamental differences in the properties of red and blue quasars: measuring the reddening and accretion properties with X-shooter
 - Monthly Notices of the Royal Astronomical Society, Volume 513, Issue 1, Pages 1254–1274 [DOI] [ADS] [arXiv]
- **Fawcett, V. A., Harrison, C. M., Alexander, D. M., et al.** (2025): Connection between steep radio spectral slopes and dust extinction in QSOs: evidence for outflow-driven shocks in dusty QSOs
 - Monthly Notices of the Royal Astronomical Society, Volume 537, Issue 2, Pages 2003–2023 [DOI] [ADS] [arXiv]
- Feltre, A., Charlot, S., & Gutkin, J. (2016): Nuclear activity versus star formation: emission-line diagnostics at ultraviolet and optical wavelengths

 Monthly Notices of the Royal Astronomical Society, Volume 456, Issue 3, Pages 3354–3374 [DOI] [ADS] [arXiv]
- **Ferrarese, L. & Merritt, D. (2000)**: A Fundamental Relation between Supermassive Black Holes and Their Host Galaxies
 - The Astrophysical Journal, Volume 539, Issue 1, Page L9 [DOI]
- **Finkelstein, D.** (1958): Past-Future Asymmetry of the Gravitational Field of a Point Particle Phys. Rev., Volume 110, Pages 965–967 [DOI]

Fluetsch, A., Maiolino, R., Carniani, S., et al. (2021): Properties of the multiphase outflows in local (ultra)luminous infrared galaxies

Monthly Notices of the Royal Astronomical Society, Volume 505, Issue 4, Pages 5753–5783 [DOI] [ADS] [arXiv]

- **Foltz, C. B., Weymann, R. J., Peterson, B. M., et al.** (1986): C IV Absorption Systems in QSO Spectra: Is the Character of Systems with $Z \simeq Z$ EM Different from Those with Z < Z em?
 - The Astrophysical Journal, Volume 307, Page 504 [DOI] [ADS]
- Foreman-Mackey, D., Hogg, D. W., Lang, D., et al. (2013): emcee: The MCMC Hammer PASP, Volume 125, Pages 306–312 [DOI] [arXiv]
- Gallerani, S., Maiolino, R., Juarez, Y., et al. (2010): The extinction law at high redshift and its implications
 - Astronomy & Astrophysics, Volume 523, Page A85 [DOI] [ADS] [arXiv]
- García-Burillo, S., Alonso-Herrero, A., Ramos Almeida, C., et al. (2021): The Galaxy Activity, Torus, and Outflow Survey (GATOS). I. ALMA images of dusty molecular tori in Seyfert galaxies
 - Astronomy & Astrophysics, Volume 652, Page A98 [DOI] [ADS] [arXiv]
- Gebhardt, K., Bender, R., Bower, G., et al. (2001): Erratum: "A Relationship between Nuclear Black Hole Mass and Galaxy Velocity Dispersion" (ApJ, 539, L13 [2000])
 The Astrophysical Journal, Volume 555, Issue 1, Page L75 [DOI]
- **Gillette, J., Hamann, F., Lau, M. W., et al.** (2024): Accurate systemic redshifts and outflow speeds for extremely red quasars (ERQs)
 - Monthly Notices of the Royal Astronomical Society, Volume 527, Issue 1, Pages 950–958 [DOI] [ADS] [arXiv]
- Girardi, L., Bertelli, G., Bressan, A., et al. (2002): Theoretical isochrones in several photometric systems. I. Johnson-Cousins-Glass, HST/WFPC2, HST/NICMOS, Washington, and ESO Imaging Survey filter sets

 Astronomy & Astrophysics, Volume 391, Pages 195–212 [DOI] [ADS] [arXiv]
- **Giustini, M. & Proga, D. (2019)**: A global view of the inner accretion and ejection flow around super massive black holes. Radiation-driven accretion disk winds in a physical context
 - Astronomy & Astrophysics, Volume 630, Page A94 [DOI] [ADS] [arXiv]
- **Glikman, E., Simmons, B., Mailly, M., et al.** (2015): Major Mergers Host the Most-luminous Red Quasars at $z \sim 2$: A Hubble Space Telescope WFC3/IR Study The Astrophysical Journal, Volume 806, Issue 2, Page 218 [DOI] [ADS] [arXiv]

Glikman, E., Urrutia, T., Lacy, M., et al. (2012): FIRST-2MASS Red Quasars:

Transitional Objects Emerging from the Dust

The Astrophysical Journal, Volume 757, Issue 1, Page 51 [DOI] [ADS] [arXiv]

- Goodman, J. & Weare, J. (2010): Ensemble samplers with affine invariance

 Communications in Applied Mathematics and Computational Science, Volume 5,

 Issue 1, Pages 65–80 [DOI] [ADS]
- Goulding, A. D., Zakamska, N. L., Alexandroff, R. M., et al. (2018): High-redshift Extremely Red Quasars in X-Rays

 The Astrophysical Journal, Volume 856, Issue 1, Page 4 [DOI]
- **Granato, G. L., Zotti, G. D., Silva, L., et al.** (2004): A Physical Model for the Coevolution of QSOs and Their Spheroidal Hosts

 The Astrophysical Journal, Volume 600, Issue 2, Page 580 [DOI]
- GRAVITY Collaboration, Abuter, R., Aimar, N., et al. (2022): Mass distribution in the Galactic Center based on interferometric astrometry of multiple stellar orbits

 Astronomy & Astrophysics, Volume 657, Page L12 [DOI] [ADS] [arXiv]
- GRAVITY Collaboration, Amorim, A., Bauböck, M., et al. (2020): The spatially resolved broad line region of IRAS 09149-6206
 Astronomy & Astrophysics, Volume 643, Page A154 [DOI] [ADS] [arXiv]
- Greene, J. E. & Ho, L. C. (2005): Estimating Black Hole Masses in Active Galaxies Using the Hα Emission Line

 The Astrophysical Journal, Volume 630, Issue 1, Pages 122–129 [DOI] [ADS] [arXiv]
- **Greene, J. E., Labbe, I., Goulding, A. D.,** *et al.* (2024): *UNCOVER Spectroscopy Confirms the Surprising Ubiquity of Active Galactic Nuclei in Red Sources at* z > 5 The Astrophysical Journal, Volume 964, Issue 1, Page 39 [DOI] [ADS] [arXiv]
- **Greenstein, J. L.** (1963): *Red-Shift of the Unusual Radio Source: 3C 48* Nature, Volume 197, Issue 4872, Pages 1041–1042 [DOI] [ADS]
- **Guo, H., Shen, Y., & Wang, S.** (2018): *PyQSOFit: Python code to fit the spectrum of quasars*Astrophysics Source Code Library [ADS] [arXiv]
- **Haardt, F. & Maraschi, L. (1991)**: A Two-Phase Model for the X-Ray Emission from Seyfert Galaxies

 The Astrophysical Journal Letters, Volume 380, Page L51 [DOI] [ADS]
- Hamann, F., Kanekar, N., Prochaska, J. X., et al. (2011): A high-velocity narrow absorption line outflow in the quasar J212329.46 005052.9
 Monthly Notices of the Royal Astronomical Society, Volume 410, Issue 3, Pages 1957–1974 [DOI] [ADS] [arXiv]

Hamann, F., Zakamska, N. L., Ross, N., et al. (2017): Extremely red quasars in BOSS Monthly Notices of the Royal Astronomical Society, Volume 464, Issue 3, Pages 3431–3463 [DOI] [ADS] [arXiv]

- **Hao, C.-N., Kennicutt, R. C., Johnson, B. D., et al.** (2011): Dust-corrected Star Formation Rates of Galaxies. II. Combinations of Ultraviolet and Infrared Tracers

 The Astrophysical Journal, Volume 741, Issue 2, Page 124 [DOI] [ADS] [arXiv]
- Hardcastle, M. J., Pierce, J. C. S., Duncan, K. J., et al. (2025): Radio AGN selection in LoTSS DR2
 - Monthly Notices of the Royal Astronomical Society, Volume 539, Issue 2 [DOI]
- **Harrison, C.** (2014): Observational constraints on the influence of active galactic nuclei on the evolution of galaxies
 - Ph.D. thesis, Durham University, UK [ADS]
- **Harrison, C. M.** (2017): *Impact of supermassive black hole growth on star formation* Nature Astronomy, Volume 1, Page 0165 [DOI] [ADS] [arXiv]
- **Harrison, C. M., Alexander, D. M., Mullaney, J. R., et al.** (2014): Kiloparsec-scale outflows are prevalent among luminous AGN: outflows and feedback in the context of the overall AGN population
 - Monthly Notices of the Royal Astronomical Society, Volume 441, Issue 4, Pages 3306–3347 [DOI] [ADS] [arXiv]
- Harrison, C. M. & Ramos Almeida, C. (2024): Observational Tests of Active Galactic Nuclei Feedback: An Overview of Approaches and Interpretation
 Galaxies, Volume 12, Issue 2, Page 17 [DOI] [ADS] [arXiv]
- Heckman, T. M. & Best, P. N. (2014): The Coevolution of Galaxies and Supermassive Black Holes: Insights from Surveys of the Contemporary Universe
 Annual Review of Astronomy & Astrophysics, Volume 52, Pages 589–660 [DOI]
 [ADS] [arXiv]
- **Herrera-Camus, R., Tacconi, L., Genzel, R., et al.** (2019): Molecular and Ionized Gas *Phases of an AGN-driven Outflow in a Typical Massive Galaxy at z* \approx 2 The Astrophysical Journal, Volume 871, Issue 1, Page 37 [DOI] [ADS] [arXiv]
- **Hertz, H.** (1887): *Ueber einen Einfluss des ultravioletten Lichtes auf die electrische Entladung*
 - Annalen der Physik, Volume 267, Issue 8, Pages 983–1000 [DOI] [ADS]
- **Hewett, P. C. & Wild, V. (2010)**: *Improved redshifts for SDSS quasar spectra*Monthly Notices of the Royal Astronomical Society, Volume 405, Issue 4, Pages 2302–2316 [DOI] [arXiv]

Hewett, P. C. & Wild, V. (2010): VizieR Online Data Catalog: Improved redshifts for SDSS quasar spectra (Hewett+, 2010)

VizieR On-line Data Catalog: J/MNRAS/405/2302. Originally published in: 2010MNRAS.405.2302H [ADS]

- **Hickox, R. C., Mullaney, J. R., Alexander, D. M., et al.** (2014): Black Hole Variability and the Star Formation-Active Galactic Nucleus Connection: Do All Star-forming Galaxies Host an Active Galactic Nucleus?
 - The Astrophysical Journal, Volume 782, Issue 1, Page 9 [DOI] [ADS] [arXiv]
- **Hönig, S. F. (2019)**: Redefining the Torus: A Unifying View of AGNs in the Infrared and Submillimeter
 - The Astrophysical Journal, Volume 884, Issue 2, Page 171 [DOI] [ADS] [arXiv]
- Hook, I. M., McMahon, R. G., Boyle, B. J., et al. (1994): The variability of optically selected quasars.
 - Monthly Notices of the Royal Astronomical Society, Volume 268, Pages 305–320 [DOI] [ADS]
- **Hopkins, P. F. & Elvis, M.** (2009): *Quasar feedback: more bang for your buck*Monthly Notices of the Royal Astronomical Society, Volume 401, Issue 1, Pages 7–14
 [DOI] [arXiv]
- Hopkins, P. F., Hernquist, L., Cox, T. J., et al. (2005): Black Holes in Galaxy Mergers: Evolution of Quasars
 - The Astrophysical Journal, Volume 630, Issue 2, Pages 705–715 [DOI] [ADS] [arXiv]
- Hopkins, P. F., Hernquist, L., Cox, T. J., et al. (2008): A Cosmological Framework for the Co-Evolution of Quasars, Supermassive Black Holes, and Elliptical Galaxies. I. Galaxy Mergers and Quasar Activity
 - The Astrophysical Journal Supplement Series, Volume 175, Issue 2, Page 356 [DOI]
- Horne, K. (1986): An optimal extraction algorithm for CCD spectroscopy.Publications of the Astronomical Society of the Pacific, Volume 98, Pages 609–617[DOI] [ADS]
- Huang, J. S., Glazebrook, K., Cowie, L. L., et al. (2003): The Hawaii+Anglo-Australian Observatory K-Band Galaxy Redshift Survey. I. The Local K-Band Luminosity Function The Astrophysical Journal, Volume 584, Issue 1, Pages 203–209 [DOI] [ADS] [arXiv]
- **Hund, F. (1925)**: Zur Deutung verwickelter Spektren, insbesondere der Elemente Scandium bis Nickel
 - Zeitschrift fur Physik, Volume 33, Issue 1, Pages 345–371 [DOI] [ADS]
- Højen-Sørensen, P. A., Winther, O., & Hansen, L. K. (2002): Mean-Field Approaches to Independent Component Analysis
 - Neural Computation, Volume 14, Issue 4, Pages 889–918 [DOI]

Inayoshi, K. & Maiolino, R. (2025): Extremely Dense Gas around Little Red Dots and High-redshift Active Galactic Nuclei: A Nonstellar Origin of the Balmer Break and Absorption Features

- The Astrophysical Journal Letters, Volume 980, Issue 2, Page L27 [DOI] [ADS] [arXiv]
- Ishibashi, W., Banerji, M., & Fabian, A. C. (2017): AGN radiative feedback in dusty quasar populations
 - Monthly Notices of the Royal Astronomical Society, Volume 469, Issue 2, Pages 1496–1501 [DOI] [ADS] [arXiv]
- Ishibashi, W. & Fabian, A. C. (2022): What powers galactic outflows: nuclear starbursts or AGN?
 - Monthly Notices of the Royal Astronomical Society, Volume 516, Issue 4, Pages 4963–4970 [DOI] [ADS] [arXiv]
- Ivezić, Ž., Kahn, S. M., Tyson, J. A., et al. (2019): LSST: From Science Drivers to Reference Design and Anticipated Data Products The Astrophysical Journal, Volume 873, Issue 2, Page 111 [DOI] [ADS] [arXiv]
- Jennison, R. C. & Das Gupta, M. K. (1953): Fine Structure of the Extra-terrestrial Radio Source Cygnus I Nature, Volume 172, Issue 4387, Pages 996–997 [DOI] [ADS]
- Jiang, L., Fan, X., Brandt, W. N., et al. (2010): Dust-free quasars in the early Universe
- Nature, Volume 464, Issue 7287, Pages 380–383 [DOI] [ADS] [arXiv]
- Jiang, L., McGreer, I. D., Fan, X., et al. (2016): The Final SDSS High-redshift Quasar Sample of 52 Quasars at z>5.7
 - The Astrophysical Journal, Volume 833, Issue 2, Page 222 [DOI] [ADS] [arXiv]
- Jun, H. D. & Im, M. (2013): Physical Properties of Luminous Dust-poor Quasars The Astrophysical Journal, Volume 779, Issue 2, Page 104 [DOI] [ADS] [arXiv]
- Kaspi, S., Maoz, D., Netzer, H., et al. (2005): The Relationship between Luminosity and Broad-Line Region Size in Active Galactic Nuclei
 - The Astrophysical Journal, Volume 629, Issue 1, Pages 61–71 [DOI] [ADS] [arXiv]
- Kaspi, S., Smith, P. S., Netzer, H., et al. (2000): Reverberation Measurements for 17 Quasars and the Size-Mass-Luminosity Relations in Active Galactic Nuclei The Astrophysical Journal, Volume 533, Issue 2, Pages 631–649 [DOI] [ADS] [arXiv]
- Kawanomoto, S., Uraguchi, F., Komiyama, Y., et al. (2018): Hyper Suprime-Cam: Filters
 - Publications of the Astronomical Society of Japan, Volume 70, Issue 4, Page 66

Kelly, B. C., Vestergaard, M., Fan, X., et al. (2010): Constraints on Black Hole Growth, Quasar Lifetimes, and Eddington Ratio Distributions from the SDSS Broad-line Quasar Black Hole Mass Function

The Astrophysical Journal, Volume 719, Issue 2, Pages 1315–1334 [DOI] [ADS]

[arXiv]

- Kennicutt, J., Robert C. (1998): Star Formation in Galaxies Along the Hubble Sequence Annual Review of Astronomy & Astrophysics, Volume 36, Pages 189–232 [DOI] [ADS] [arXiv]
- **Kennicutt, R. C. & Evans, N. J.** (2012): *Star Formation in the Milky Way and Nearby Galaxies*
 - Annual Review of Astronomy & Astrophysics, Volume 50, Pages 531–608 [DOI] [ADS] [arXiv]
- **Kerr, R. P. (1963)**: Gravitational Field of a Spinning Mass as an Example of Algebraically Special Metrics
 - Phys. Rev. Lett., Volume 11, Pages 237–238 [DOI]
- **King, A.** (2003): Black Holes, Galaxy Formation, and the M_{BH} - σ Relation The Astrophysical Journal Letters, Volume 596, Issue 1, Pages L27–L29 [DOI] [ADS] [arXiv]
- Klindt, L., Alexander, D. M., Rosario, D. J., et al. (2019): Fundamental differences in the radio properties of red and blue quasars: evolution strongly favoured over orientation Monthly Notices of the Royal Astronomical Society, Volume 488, Issue 3, Pages 3109–3128 [DOI] [ADS] [arXiv]
- Kobulnicky, H. A., Nordsieck, K. H., Burgh, E. B., et al. (2003): Prime focus imaging spectrograph for the Southern African large telescope: operational modes
 In Iye, M. & Moorwood, A. F. M. (eds.): Instrument Design and Performance for Optical/Infrared Ground-based Telescopes. Society of Photo-Optical Instrumentation Engineers (SPIE) Conference Series [DOI] [ADS]
- **Kocevski, D. D., Barro, G., McGrath, E. J.,** *et al.* (2023): CEERS Key Paper. II. A First Look at the Resolved Host Properties of AGN at 3 < z < 5 with JWST The Astrophysical Journal Letters, Volume 946, Issue 1, Page L14 [DOI] [ADS] [arXiv]
- **Kocevski, D. D., Finkelstein, S. L., Barro, G., et al.** (2024): The Rise of Faint, Red AGN at z > 4: A Sample of Little Red Dots in the JWST Extragalactic Legacy Fields arXiv e-prints (2404.03576), Page arXiv:2404.03576 [DOI] [ADS] [arXiv]
- **Kocevski, D. D., Onoue, M., Inayoshi, K.,** *et al.* **(2023)**: *Hidden Little Monsters: Spectroscopic Identification of Low-mass, Broad-line AGNs at* $z \gtrsim 5$ *with CEERS* The Astrophysical Journal Letters, Volume 954, Issue 1, Page L4 [DOI]

Kormendy, J. & Ho, L. C. (2013): Coevolution (Or Not) of Supermassive Black Holes and Host Galaxies

Annual Review of Astronomy & Astrophysics, Volume 51, Issue 1, Pages 511–653 [DOI] [ADS] [arXiv]

- **Koss, M. J., Treister, E., Kakkad, D., et al.** (2023): *Ugc* 4211: A confirmed dual active galactic nucleus in the local universe at 230 pc nuclear separation

 The Astrophysical Journal Letters, Volume 942, Issue 1, Page L24
- Kulkarni, G., Worseck, G., & Hennawi, J. F. (2019): Evolution of the AGN UV luminosity function from redshift 7.5
 Monthly Notices of the Royal Astronomical Society, Volume 488, Issue 1, Pages 1035–1065 [DOI] [ADS] [arXiv]
- **Lansbury, G. B., Banerji, M., Fabian, A. C.,** *et al.* (2020): *X-ray observations of luminous dusty quasars at* z > 2 Monthly Notices of the Royal Astronomical Society, Volume 495, Issue 3, Pages
- Lawrence, A., Warren, S. J., Almaini, O., et al. (2007): The UKIRT Infrared Deep Sky

Monthly Notices of the Royal Astronomical Society, Volume 379, Issue 4, Pages 1599–1617 [DOI] [ADS] [arXiv]

- Lenard, P. (1902): *Ueber die lichtelektrische Wirkung*Annalen der Physik, Volume 313, Issue 5, Pages 149–198 [DOI] [ADS]
- Lewis, G. N. (1926): *The Conservation of Photons*Nature, Volume 118, Issue 2981, Pages 874–875 [DOI] [ADS]

2652–2663 [DOI] [ADS] [arXiv]

Survey (UKIDSS)

- **Li, A.** (2008): *Optical Properties of Dust* arXiv e-prints (0808.4123), Page arXiv:0808.4123 [DOI] [ADS] [arXiv]
- **Li, L.-X., Zimmerman, E. R., Narayan, R., et al.** (2005): Multitemperature Blackbody Spectrum of a Thin Accretion Disk around a Kerr Black Hole: Model Computations and Comparison with Observations

The Astrophysical Journal Supplement Series, Volume 157, Issue 2, Pages 335–370 [DOI] [ADS] [arXiv]

- **Li, Z., Inayoshi, K., Chen, K.,** *et al.* (2025): Little Red Dots: Rapidly Growing Black Holes Reddened by Extended Dusty Flows

 The Astrophysical Journal, Volume 980, Issue 1, Page 36 [DOI] [ADS] [arXiv]
- Lilly, S. J., Le Fevre, O., Hammer, F., et al. (1996): The Canada-France Redshift Survey: The Luminosity Density and Star Formation History of the Universe to Z approximately 1 The Astrophysical Journal Letters, Volume 460, Page L1 [DOI] [ADS] [arXiv]

López-Sanjuan, C., Le Fèvre, O., Ilbert, O., et al. (2012): The dominant role of mergers in the size evolution of massive early-type galaxies since $z \sim 1$ Astronomy & Astrophysics, Volume 548, Page A7 [DOI] [ADS] [arXiv]

- Luo, B., Brandt, W. N., Xue, Y. Q., et al. (2017): The Chandra Deep Field-South Survey: 7

 Ms Source Catalogs
 - The Astrophysical Journal Supplement Series, Volume 228, Issue 1, Page 2 [DOI] [ADS] [arXiv]
- Lyke, B. W., Higley, A. N., McLane, J. N., et al. (2020): The Sloan Digital Sky Survey Quasar Catalog: Sixteenth Data Release

 The Astrophysical Journal Supplement Series, Volume 250, Issue 1, Page 8 [DOI] [ADS] [arXiv]
- Lynden-Bell, D. (1969): Galactic Nuclei as Collapsed Old Quasars Nature, Volume 223, Issue 5207, Pages 690–694 [DOI] [ADS]
- Madau, P. & Dickinson, M. (2014): Cosmic Star-Formation History

 Annual Review of Astronomy & Astrophysics, Volume 52, Pages 415–486 [DOI]

 [ADS] [arXiv]
- Madau, P., Ferguson, H. C., Dickinson, M. E., et al. (1996): High-redshift galaxies in the Hubble Deep Field: colour selection and star formation history to z-4

 Monthly Notices of the Royal Astronomical Society, Volume 283, Issue 4, Pages 1388–1404 [DOI] [ADS] [arXiv]
- Madau, P., Pozzetti, L., & Dickinson, M. (1998): The Star Formation History of Field Galaxies
 - The Astrophysical Journal, Volume 498, Issue 1, Pages 106–116 [DOI] [ADS] [arXiv]
- Maddox, N. (2018): [O II] as a proxy for star formation in AGN host galaxies: beware of extended emission line regions

 Manthly Nations of the Boxel Astronomical Society Volume 480, James 4, Barrel
 - Monthly Notices of the Royal Astronomical Society, Volume 480, Issue 4, Pages 5203–5210 [DOI] [ADS] [arXiv]
- Maddox, N., Hewett, P. C., Péroux, C., et al. (2012): The large area KX quasar catalogue I. Analysis of the photometric redshift selection and the complete quasar catalogue Monthly Notices of the Royal Astronomical Society, Volume 424, Issue 4, Pages 2876–2895 [DOI] [ADS] [arXiv]
- Magliocchetti, M., Popesso, P., Brusa, M., et al. (2018): A census of radio-selected AGNs on the COSMOS field and of their FIR properties

 Monthly Notices of the Royal Astronomical Society, Volume 473, Issue 2, Pages 2493–2505 [DOI] [ADS] [arXiv]

Magorrian, J., Tremaine, S., Richstone, D., et al. (1998): The Demography of Massive Dark Objects in Galaxy Centers

The Astronomical Journal, Volume 115, Issue 6, Page 2285 [DOI]

Maiolino, R., Cirasuolo, M., Afonso, J., et al. (2020): MOONRISE: The Main MOONS GTO Extragalactic Survey

The Messenger, Volume 180, Pages 24–29 [DOI] [ADS] [arXiv]

- Man, A. W. S., Lehnert, M. D., Vernet, J. D. R., et al. (2019): Quenching by gas compression and consumption. A case study of a massive radio galaxy at z = 2.57 Astronomy & Astrophysics, Volume 624, Page A81 [DOI] [ADS] [arXiv]
- **Man, A. W. S., Toft, S., Zirm, A. W., et al.** (2012): The Pair Fraction of Massive Galaxies at $0 \le z \le 3$

The Astrophysical Journal, Volume 744, Issue 2, Page 85 [DOI] [ADS] [arXiv]

- Martocchia, S., Piconcelli, E., Zappacosta, L., et al. (2017): The WISSH quasars project. III. X-ray properties of hyper-luminous quasars Astronomy & Astrophysics, Volume 608, Page A51 [DOI] [ADS] [arXiv]
- Mathews, W. G. & Ferland, G. J. (1987): What Heats the Hot Phase in Active Nuclei? The Astrophysical Journal, Volume 323, Page 456 [DOI] [ADS]
- **Matthee, J., Naidu, R. P., Brammer, G., et al.** (2024): Little Red Dots: An Abundant Population of Faint Active Galactic Nuclei at $z \sim 5$ Revealed by the EIGER and FRESCO JWST Surveys

The Astrophysical Journal, Volume 963, Issue 2, Page 129 [DOI] [ADS] [arXiv]

- Maxwell, J. C. (1865): A Dynamical Theory of the Electromagnetic Field
 Philosophical Transactions of the Royal Society of London, Volume 155, Pages
 459–512
- Mazzucchelli, C., Bañados, E., Venemans, B. P., et al. (2017): Physical Properties of 15 Quasars at $z \gtrsim 6.5$

The Astrophysical Journal, Volume 849, Issue 2, Page 91 [DOI] [ADS] [arXiv]

McMahon, R. G., Banerji, M., Gonzalez, E., et al. (2013): First Scientific Results from the VISTA Hemisphere Survey (VHS)

The Messenger, Volume 154, Pages 35–37 [ADS]

Merloni, A., Alexander, D. A., Banerji, M., et al. (2019): 4MOST Consortium Survey 6: Active Galactic Nuclei

The Messenger, Volume 175, Pages 42–45 [DOI] [ADS] [arXiv]

Merloni, A., Lamer, G., Liu, T., *et al.* (2024): The SRG/eROSITA all-sky survey. First X-ray catalogues and data release of the western Galactic hemisphere
Astronomy & Astrophysics, Volume 682, Page A34 [DOI] [ADS] [arXiv]

Meyer, R. A., Bosman, S. E. I., & Ellis, R. S. (2019): *New constraints on quasar evolution: broad-line velocity shifts over* $1.5 \lesssim z \lesssim 7.5$ Monthly Notices of the Royal Astronomical Society, Volume 487, Issue 3, Pages

3305–3323 [DOI] [ADS] [arXiv]

Millikan, R. A. (1914): A Direct Determination of "h." Phys. Rev., Volume 4, Pages 73–75 [DOI]

- Morganti, R., Fogasy, J., Paragi, Z., et al. (2013): Radio Jets Clearing the Way Through a Galaxy: Watching Feedback in Action
 Science, Volume 341, Issue 6150, Pages 1082–1085 [DOI] [ADS] [arXiv]
- Mortlock, D. J., Warren, S. J., Venemans, B. P., et al. (2011): A luminous quasar at a redshift of z = 7.085Nature, Volume 474, Issue 7353, Pages 616–619 [DOI] [ADS] [arXiv]
- Murphy, E. J., Condon, J. J., Schinnerer, E., et al. (2011): Calibrating Extinction-free Star Formation Rate Diagnostics with 33 GHz Free-free Emission in NGC 6946

 The Astrophysical Journal, Volume 737, Issue 2, Page 67 [DOI] [ADS] [arXiv]
- Murray, N. & Chiang, J. (1995): Active Galactic Nuclei Disk Winds, Absorption Lines, and Warm Absorbers

The Astrophysical Journal, Volume 454, Issue 2, Page L105 [DOI]

- Murray, N., Chiang, J., Grossman, S. A., et al. (1995): Accretion Disk Winds from Active Galactic Nuclei

 The Astrophysical Journal, Volume 451, Page 498 [DOI] [ADS]
- Murray, N., Quataert, E., & Thompson, T. A. (2005): On the Maximum Luminosity of Galaxies and Their Central Black Holes: Feedback from Momentum-driven Winds

 The Astrophysical Journal, Volume 618, Issue 2, Pages 569–585 [DOI] [ADS] [arXiv]
- Naidu, R. P., Matthee, J., Katz, H., et al. (2025): A "Black Hole Star" Reveals the Remarkable Gas-Enshrouded Hearts of the Little Red Dots arXiv e-prints (2503.16596), Page arXiv:2503.16596 [DOI] [ADS] [arXiv]
- **Nanni, R., Vignali, C., Gilli, R., et al.** (2017): The X-ray properties of z > 6 luminous quasars

Astronomy & Astrophysics, Volume 603, Page A128 [DOI] [ADS] [arXiv]

- Nestor, D., Hamann, F., & Rodriguez Hidalgo, P. (2008): The quasar-frame velocity distribution of narrow CIV absorbers

 Monthly Notices of the Royal Astronomical Society, Volume 386, Issue 4, Pages 2055–2064 [DOI] [ADS] [arXiv]
- Netzer, H. (2019): Bolometric correction factors for active galactic nuclei
 Monthly Notices of the Royal Astronomical Society, Volume 488, Issue 4, Pages
 5185–5191 [DOI] [ADS] [arXiv]

Noboriguchi, A., Nagao, T., Toba, Y., et al. (2019): Optical Properties of Infrared-bright Dust-obscured Galaxies Viewed with Subaru Hyper Suprime-Cam

The Astrophysical Journal, Volume 876, Issue 2, Page 132 [DOI] [ADS] [arXiv]

- **Onoue, M., Inayoshi, K., Ding, X., et al.** (2023): A Candidate for the Least-massive Black Hole in the First 1.1 Billion Years of the Universe

 The Astrophysical Journal Letters, Volume 942, Issue 1, Page L17 [DOI]
- Oppenheimer, J. R. & Volkoff, G. M. (1939): On Massive Neutron Cores Physical Review, Volume 55, Issue 4, Pages 374–381 [DOI] [ADS]
- **Pâris, I., Petitjean, P., Aubourg, É., et al.** (2012): The Sloan Digital Sky Survey quasar catalog: ninth data release
 Astronomy & Astrophysics, Volume 548, Page A66 [DOI] [ADS] [arXiv]
- **Pensabene, A., Carniani, S., Perna, M., et al.** (2020): The ALMA view of the high-redshift relation between supermassive black holes and their host galaxies

 Astronomy & Astrophysics, Volume 637, Page A84 [DOI] [ADS] [arXiv]
- **Pérez-González, P. G., Barro, G., Rieke, G. H., et al.** (2024): What Is the Nature of Little Red Dots and what Is Not, MIRI SMILES Edition

 The Astrophysical Journal, Volume 968, Issue 1, Page 4 [DOI] [ADS] [arXiv]
- Perrotta, S., Hamann, F., Zakamska, N. L., et al. (2019): ERQs are the BOSS of quasar samples: the highest velocity [O III] quasar outflows
 Monthly Notices of the Royal Astronomical Society, Volume 488, Issue 3, Pages 4126–4148 [DOI] [ADS] [arXiv]
- **Peterson, B.** (2006): *The Broad-Line Region in Active Galactic Nuclei* Springer Berlin Heidelberg, Berlin, Heidelberg [DOI]
- Peterson, B. M. (1993): Reverberation Mapping of Active Galactic Nuclei

 Publications of the Astronomical Society of the Pacific, Volume 105, Page 247 [DOI]

 [ADS]
- Pillepich, A., Springel, V., Nelson, D., et al. (2017): Simulating galaxy formation with the IllustrisTNG model
 Monthly Notices of the Royal Astronomical Society, Volume 473, Issue 3, Pages 4077–4106 [DOI] [arXiv]
- **Planck, M.** (1901): *Ueber das Gesetz der Energieverteilung im Normalspectrum* Annalen der Physik, Volume 309, Issue 3, Pages 553–563 [DOI] [ADS]

[ADS]

Pogson, N. (1856): Magnitudes of Thirty-six of the Minor Planets for the first day of each month of the year 1857Monthly Notices of the Royal Astronomical Society, Volume 17, Pages 12–15 [DOI]

Polletta, M., Tajer, M., Maraschi, L., et al. (2007): Spectral Energy Distributions of Hard X-Ray Selected Active Galactic Nuclei in the XMM-Newton Medium Deep Survey The Astrophysical Journal, Volume 663, Issue 1, Pages 81–102 [DOI] [ADS] [arXiv]

- **Pons, E., McMahon, R. G., Banerji, M.,** *et al.* (2020): *X-ray properties of z* \gtrsim 6.5 quasars Monthly Notices of the Royal Astronomical Society, Volume 491, Issue 3, Pages 3884–3890 [DOI] [ADS] [arXiv]
- Prochaska, J. X., Hennawi, J., Cooke, R., et al. (2020): pypeit/PypeIt: Release 1.0.0 Zenodo [DOI] [ADS]
- Prochaska, J. X., Hennawi, J. F., Westfall, K. B., et al. (2020): Pypelt: The Python Spectroscopic Data Reduction Pipeline
 Journal of Open Source Software, Volume 5, Issue 56, Page 2308 [DOI]
- **Proga, D., Stone, J. M., & Kallman, T. R.** (2000): Dynamics of Line-driven Disk Winds in Active Galactic Nuclei

 The Astrophysical Journal, Volume 543, Issue 2, Pages 686–696 [DOI] [ADS] [arXiv]
- Puglisi, A., Daddi, E., Renzini, A., et al. (2017): The Bright and Dark Sides of High-redshift Starburst Galaxies from Herschel and Subaru ObservationsThe Astrophysical Journal Letters, Volume 838, Issue 2, Page L18 [DOI] [ADS] [arXiv]
- Rakshit, S., Stalin, C. S., & Kotilainen, J. (2020): Spectral Properties of Quasars from Sloan Digital Sky Survey Data Release 14: The Catalog

 The Astrophysical Journal Supplement Series, Volume 249, Issue 1, Page 17 [DOI]

 [ADS] [arXiv]
- Rangwala, N., Williams, T. B., Pietraszewski, C., et al. (2008): An Imaging

 FABRY-PÉROT System for the Robert Stobie Spectrograph on the Southern African Large

 Telescope

 The Astronomical Journal, Volume 135, Issue 5, Pages 1825–1836 [DOI] [ADS]

 [arXiv]
- Rankine, A. L., Hewett, P. C., Banerji, M., et al. (2020): BAL and non-BAL quasars: continuum, emission, and absorption properties establish a common parent sample Monthly Notices of the Royal Astronomical Society, Volume 492, Issue 3, Pages 4553–4575 [DOI] [ADS] [arXiv]
- **Reed, S. L., Banerji, M., Becker, G. D.,** *et al.* (2019): *Three new VHS-DES quasars at 6.7* < z < 6.9 and emission line properties at z > 6.5 Monthly Notices of the Royal Astronomical Society, Volume 487, Issue 2, Pages 1874–1885 [DOI] [ADS] [arXiv]

Richards, G. T., Hall, P. B., Vanden Berk, D. E., et al. (2003): Red and Reddened Quasars in the Sloan Digital Sky Survey

The Astronomical Journal, Volume 126, Issue 3, Pages 1131–1147 [DOI] [ADS]

[arXiv]

- Richards, G. T., Kruczek, N. E., Gallagher, S. C., et al. (2011): UNIFICATION OF LUMINOUS TYPE 1 QUASARS THROUGH C IV EMISSION

 The Astronomical Journal, Volume 141, Issue 5, Page 167 [DOI]
- Rivera, A. B., Richards, G. T., Gallagher, S. C., et al. (2022): Exploring Changes in Quasar Spectral Energy Distributions across C iv Parameter Space

 The Astrophysical Journal, Volume 931, Issue 2, Page 154 [DOI]
- **Rodrigo, C. & Solano, E. (2020)**: The SVO Filter Profile Service In XIV.0 Scientific Meeting (virtual) of the Spanish Astronomical Society [ADS]
- Rodrigo, C., Solano, E., & Bayo, A. (2012): SVO Filter Profile Service Version 1.0 IVOA Working Draft 15 October 2012, Page 1015 [DOI] [ADS]
- **Rosa, G., Venemans, B., Decarli, R., et al.** (2013): Black hole mass estimates and emission line properties of a sample of redshift Z > 6:5 quasars

 The Astrophysical Journal, Volume 790 [DOI]
- Rosas-Guevara, Y. M., Bower, R. G., McAlpine, S., et al. (2019): The abundances and properties of Dual AGN and their host galaxies in the EAGLE simulations

 Monthly Notices of the Royal Astronomical Society, Volume 483, Issue 2, Pages 2712–2720
- Rupke, D. S. N. & Veilleux, S. (2011): Integral Field Spectroscopy of Massive,
 Kiloparsec-scale Outflows in the Infrared-luminous QSO Mrk 231
 The Astrophysical Journal Letters, Volume 729, Issue 2, Page L27 [DOI] [ADS]
 [arXiv]
- **Rusakov, V., Watson, D., Nikopoulos, G. P., et al.** (2025): *JWST's little red dots: an emerging population of young, low-mass AGN cocooned in dense ionized gas* arXiv e-prints (2503.16595), Page arXiv:2503.16595 [DOI] [ADS] [arXiv]
- **Salpeter, E. E. (1964)**: Accretion of Interstellar Matter by Massive Objects. The Astrophysical Journal, Volume 140, Pages 796–800 [DOI] [ADS]
- **Sandage, A.** (1965): The Existence of a Major New Constituent of the Universe: the Quasistellar Galaxies.
 - The Astrophysical Journal, Volume 141, Page 1560 [DOI] [ADS]
- **Sawicki, M.** (2002): *The 1.6 Micron Bump as a Photometric Redshift Indicator*The Astronomical Journal, Volume 124, Issue 6, Pages 3050–3060 [DOI] [ADS]
 [arXiv]

Schawinski, K., Koss, M., Berney, S., et al. (2015): Active galactic nuclei flicker: an observational estimate of the duration of black hole growth phases of ~10⁵ yr Monthly Notices of the Royal Astronomical Society, Volume 451, Issue 3, Pages 2517–2523 [DOI] [ADS] [arXiv]

- Schaye, J., Crain, R. A., Bower, R. G., et al. (2015): The EAGLE project: simulating the evolution and assembly of galaxies and their environments

 Monthly Notices of the Royal Astronomical Society, Volume 446, Issue 1, Pages 521–554 [DOI] [ADS] [arXiv]
- Schindler, J.-T., Farina, E. P., Bañ ados, E., et al. (2020): The X-SHOOTER/ALMA Sample of Quasars in the Epoch of Reionization. I. NIR Spectral Modeling, Iron Enrichment, and Broad Emission Line Properties

 The Astrophysical Journal, Volume 905, Issue 1, Page 51 [DOI]
- Schlafly, E. F. & Finkbeiner, D. P. (2011): Measuring Reddening with Sloan Digital Sky Survey Stellar Spectra and Recalibrating SFD

 The Astrophysical Journal, Volume 737, Issue 2, Page 103 [DOI] [ADS] [arXiv]
- **Schmidt, M.** (1963): *3C 273 : A Star-Like Object with Large Red-Shift* Nature, Volume 197, Issue 4872, Page 1040 [DOI] [ADS]
- Schneider, D. P., Richards, G. T., Hall, P. B., et al. (2010): The Sloan Digital Sky Survey Quasar Catalog. V. Seventh Data Release

 The Astronomical Journal, Volume 139, Issue 6, Page 2360 [DOI] [ADS] [arXiv]
- Schwarzschild, K. (1916): Über das Gravitationsfeld eines Massenpunktes nach der Einsteinschen Theorie
 Sitzungsberichte der Königlich Preussischen Akademie der Wissenschaften, Pages 189–196 [ADS]
- **Science Software Branch at STScI** (2012): *PyRAF: Python alternative for IRAF* Astrophysics Source Code Library, record ascl:1207.011 [ADS]
- **Seyfert, C. K.** (1943): *Nuclear Emission in Spiral Nebulae*.

 The Astrophysical Journal, Volume 97, Page 28 [DOI] [ADS]
- **Shakura, N. I. & Sunyaev, R. A.** (1973): Black holes in binary systems. Observational appearance.

Astronomy & Astrophysics, Volume 24, Pages 337–355 [ADS]

- **Shankar, F., Weinberg, D. H., & Miralda-Escudé, J. (2009)**: Self-Consistent Models of the AGN and Black Hole Populations: Duty Cycles, Accretion Rates, and the Mean Radiative Efficiency
 - The Astrophysical Journal, Volume 690, Issue 1, Pages 20–41 [DOI] [ADS] [arXiv]

Shen, Y. (2016): Rest-frame Optical Properties of Luminous 1.5 < Z < 3.5 Quasars: The $H\beta$ -[O III] Region

- The Astrophysical Journal, Volume 817, Issue 1, Page 55 [DOI] [ADS] [arXiv]
- Shen, Y., Brandt, W. N., Dawson, K. S., et al. (2015): The Sloan Digital Sky Survey
 Reverberation Mapping Project: Technical Overview
 The Astrophysical Journal Supplement Series, Volume 216, Issue 1, Page 4 [DOI]
 [ADS] [arXiv]
- **Shen, Y. & Ménard, B.** (2012): On the Link between Associated Mg II Absorbers and Star Formation in Quasar Hosts

 The Astrophysical Journal, Volume 748, Issue 2, Page 131 [DOI] [ADS] [arXiv]
- Shen, Y., Richards, G. T., Strauss, M. A., et al. (2011): A CATALOG OF QUASAR PROPERTIES FROM SLOAN DIGITAL SKY SURVEY DATA RELEASE 7

 The Astrophysical Journal Supplement Series, Volume 194, Issue 2, Page 45 [DOI]
- Silk, J. & Rees, M. J. (1998): Quasars and galaxy formation
 Astronomy & Astrophysics, Volume 331, Pages L1–L4 [DOI] [ADS] [arXiv]
- **Silverman, J. D., Tang, S., Lee, K.-G.,** *et al.* (2020): Dual supermassive black holes at close separation revealed by the Hyper Suprime-Cam Subaru Strategic Program

 The Astrophysical Journal, Volume 899, Issue 2, Page 154
- Simpson, J. M., Swinbank, A. M., Smail, I., et al. (2014): An ALMA Survey of Submillimeter Galaxies in the Extended Chandra Deep Field South: The Redshift Distribution and Evolution of Submillimeter Galaxies

 The Astrophysical Journal, Volume 788, Issue 2, Page 125 [DOI] [ADS] [arXiv]
- Soltan, A. (1982): *Masses of quasars*.

 Monthly Notices of the Royal Astronomical Society, Volume 200, Pages 115–122

 [DOI] [ADS]
- Somerville, R. S., Hopkins, P. F., Cox, T. J., et al. (2008): A semi-analytic model for the co-evolution of galaxies, black holes and active galactic nuclei

 Monthly Notices of the Royal Astronomical Society, Volume 391, Issue 2, Pages 481–506 [DOI] [arXiv]
- **Stecher, T. P. & Donn, B.** (1965): *On Graphite and Interstellar Extinction* The Astrophysical Journal, Volume 142, Page 1681 [DOI] [ADS]
- **Steinborn, L. K., Dolag, K., Comerford, J. M., et al.** (**2016**): Origin and properties of dual and offset active galactic nuclei in a cosmological simulation at z=2 Monthly Notices of the Royal Astronomical Society, Volume 458, Issue 1, Pages 1013–1028 [DOI] [ADS] [arXiv]

Stepney, M., Banerji, M., Hewett, P. C., *et al.* (2023): *No redshift evolution in the rest-frame ultraviolet emission line properties of quasars from* z = 1.5 *to* z = 4.0 Monthly Notices of the Royal Astronomical Society, Volume 524, Issue 4, Pages 5497–5513 [DOI] [ADS] [arXiv]

- **Stepney, M., Banerji, M., Tang, S., et al.** (2024): A big red dot: scattered light, host galaxy signatures, and multiphase gas flows in a luminous, heavily reddened quasar at cosmic noon Monthly Notices of the Royal Astronomical Society, Volume 533, Issue 3, Pages 2948–2965 [DOI] [ADS] [arXiv]
- **Stevens, I. R. & Kallman, T. R. (1990)**: *X-Ray Illuminated Stellar Winds: Ionization Effects in the Radiative Driving of Stellar Winds in Massive X-Ray Binary Systems*The Astrophysical Journal, Volume 365, Page 321 [DOI] [ADS]
- **Sulentic, J. W., Bachev, R., Marziani, P., et al.** (2007): C IV λ1549 as an Eigenvector 1 Parameter for Active Galactic Nuclei

 The Astrophysical Journal, Volume 666, Issue 2, Pages 757–777 [DOI] [ADS] [arXiv]
- Swann, E., Sullivan, M., Carrick, J., et al. (2019): 4MOST Consortium Survey 10: The Time-Domain Extragalactic Survey (TiDES)

 The Messenger, Volume 175, Pages 58–61 [DOI] [ADS] [arXiv]
- **Tang, S., Silverman, J. D., Ding, X., et al.** (2021): Optical spectroscopy of dual quasar candidates from the Subaru HSC-SSP program

 The Astrophysical Journal, Volume 922, Issue 1, Page 83
- **Temple, M. J., Banerji, M., Hewett, P. C., et al.** (2019): [O III] Emission line properties in a new sample of heavily reddened quasars at z ¿ 2 Monthly Notices of the Royal Astronomical Society, Volume 487, Issue 2, Pages 2594–2613 [DOI] [ADS] [arXiv]
- **Temple, M. J., Banerji, M., Hewett, P. C., et al.** (2021a): Exploring the link between C IV outflow kinematics and sublimation-temperature dust in quasars

 Monthly Notices of the Royal Astronomical Society, Volume 501, Issue 2, Pages 3061–3073 [DOI] [ADS] [arXiv]
- **Temple, M. J., Hewett, P. C., & Banerji, M.** (2021b): *Modelling type 1 quasar colours in the era of Rubin and Euclid*Monthly Notices of the Royal Astronomical Society, Volume 508, Issue 1, Pages 737–754 [DOI] [ADS] [arXiv]
- **Temple, M. J., Matthews, J. H., Hewett, P. C., et al.** (2023): Testing AGN outflow and accretion models with C IV and He II emission line demographics in $z \approx 2$ quasars Monthly Notices of the Royal Astronomical Society, Volume 523, Issue 1, Pages 646–666 [DOI] [ADS] [arXiv]

Temple, M. J., Rankine, A. L., Banerji, M., *et al.* (2024): [O III] emission in $z \approx 2$ quasars with and without broad absorption lines

Monthly Notices of the Royal Astronomical Society, Volume 532, Issue 1, Pages 424–437 [DOI] [ADS] [arXiv]

- **Thomson, J.** (1906): *Conduction of Electricity through Gases*Cambridge University Press
- Timlin, I., John D., Brandt, W. N., & Laor, A. (2021): What controls the UV-to-X-ray continuum shape in quasars?

 Monthly Notices of the Royal Astronomical Society, Volume 504, Issue 4, Pages 5556–5574 [DOI] [ADS] [arXiv]
- **Trakhtenbrot, B., Netzer, H., Lira, P., et al.** (2011): Black Hole Mass and Growth Rate at $z \simeq 4.8$: A Short Episode of Fast Growth Followed by Short Duty Cycle Activity

 The Astrophysical Journal, Volume 730, Issue 1, Page 7 [DOI] [ADS] [arXiv]
- **Tripp, T. M., Lu, L., & Savage, B. D.** (1998): The Relationship between Galaxies and Low-Redshift Weak Lyα Absorbers in the Directions of H1821+643 and PG 1116+215 The Astrophysical Journal, Volume 508, Issue 1, Pages 200–231 [DOI] [ADS] [arXiv]
- **Trumpler, R. J.** (1930): ABSORPTION OF LIGHT IN THE GALACTIC SYSTEM
 Publications of the Astronomical Society of the Pacific, Volume 42, Issue 248, Page 214 [DOI]
- Urrutia, T., Becker, R. H., White, R. L., et al. (2009): The FIRST-2MASS Red Quasar Survey. II. An Anomalously High Fraction of LoBALs in Searches for Dust-Reddened Quasars

 The Astrophysical Journal, Volume 698, Issue 2, Pages 1095–1109 [DOI] [ADS]
 - The Astrophysical Journal, Volume 698, Issue 2, Pages 1095–1109 [DOI] [ADS] [arXiv]
- **Urrutia, T., Lacy, M., & Becker, R. H.** (2008): Evidence for Quasar Activity Triggered by Galaxy Mergers in HST Observations of Dust-reddened Quasars

 The Astrophysical Journal, Volume 674, Issue 1, Pages 80–96 [DOI] [ADS] [arXiv]
- Urry, C. M. & Padovani, P. (1995): Unified Schemes for Radio-Loud Active Galactic Nuclei Publications of the Astronomical Society of the Pacific, Volume 107, Page 803 [DOI]
- **Vanden Berk, D., Khare, P., York, D. G.,** *et al.* **(2008)**: Average Properties of a Large Sample of $z_{abs} \sim z_{em}$ Associated Mg II Absorption Line Systems

 The Astrophysical Journal, Volume 679, Issue 1, Pages 239–259 [DOI] [ADS] [arXiv]
- Vanden Berk, D. E., Richards, G. T., Bauer, A., et al. (2001): Composite Quasar Spectra from the Sloan Digital Sky Survey

 The Astronomical Journal, Volume 122, Issue 2, Pages 549–564 [DOI] [ADS] [arXiv]

Veilleux, S., Liu, W., Vayner, A., et al. (2023): First Results from the JWST Early Release Science Program Q3D: The Warm Ionized Gas Outflow in $z \simeq 1.6$ Quasar XID 2028 and Its Impact on the Host Galaxy

- The Astrophysical Journal, Volume 953, Issue 1, Page 56 [DOI] [ADS] [arXiv]
- Veilleux, S., Rupke, D. S. N., Kim, D.-C., et al. (2009): SPITZER QUASAR AND ULIRG EVOLUTION STUDY (QUEST). IV. COMPARISON OF 1 Jy ULTRALUMINOUS INFRARED GALAXIES WITH PALOMAR-GREEN QUASARS The Astrophysical Journal Supplement Series, Volume 182, Issue 2, Page 628 [DOI]
- **Vernet, J., Dekker, H., D'Odorico, S., et al.** (2011): *X-shooter, the new wide band intermediate resolution spectrograph at the ESO Very Large Telescope*Astronomy & Astrophysics, Volume 536, Page A105 [DOI] [ADS] [arXiv]
- **Vestergaard, M. & Peterson, B. M.** (2006): Determining Central Black Hole Masses in Distant Active Galaxies and Quasars. II. Improved Optical and UV Scaling Relationships The Astrophysical Journal, Volume 641, Issue 2, Pages 689–709 [DOI] [ADS] [arXiv]
- **Vignali, C., Bauer, F. E., Alexander, D. M.,** *et al.* (2002): The Chandra Deep Field-North Survey. XVI. The X-Ray Properties of Moderate-Luminosity Active Galaxies at z ¿ 4

 The Astrophysical Journal Letters, Volume 580, Issue 2, Pages L105–L109 [DOI]

 [ADS] [arXiv]
- **Villar Martín, M., Perna, M., Humphrey, A., et al.** (2020): Peculiar emission line spectra of core extremely red BOSS quasars at $z\sim2$ -3: orientation and/or evolution? Astronomy & Astrophysics, Volume 634, Page A116 [DOI] [ADS] [arXiv]
- Volonteri, M., Dubois, Y., Pichon, C., et al. (2016): The cosmic evolution of massive black holes in the Horizon-AGN simulation Monthly Notices of the Royal Astronomical Society, Volume 460, Issue 3, Pages 2979–2996
- **Wang, F., Yang, J., Fan, X., et al.** (2019): Exploring Reionization-era Quasars. III. Discovery of 16 Quasars at $6.4 \lesssim z \lesssim 6.9$ with DESI Legacy Imaging Surveys and the UKIRT Hemisphere Survey and Quasar Luminosity Function at $z \sim 6.7$ The Astrophysical Journal, Volume 884, Issue 1, Page 30 [DOI] [ADS] [arXiv]
- Weedman, D., Sargsyan, L., Lebouteiller, V., et al. (2012): Infrared Classification and Luminosities for Dusty Active Galactic Nuclei and the Most Luminous Quasars

 The Astrophysical Journal, Volume 761, Issue 2, Page 184 [DOI] [ADS] [arXiv]
- Wethers, C. F., Banerji, M., Hewett, P. C., et al. (2018): UV-luminous, star-forming hosts of $z \sim 2$ reddened quasars in the Dark Energy Survey

 Monthly Notices of the Royal Astronomical Society, Volume 475, Issue 3, Pages 3682–3699 [DOI] [ADS] [arXiv]

Wild, V., Kauffmann, G., White, S., et al. (2008): Narrow associated quasi-stellar object absorbers: clustering, outflows and the line-of-sight proximity effect

Monthly Notices of the Royal Astronomical Society, Volume 388, Issue 1, Pages 227–241 [DOI] [ADS] [arXiv]

- **Williams, C. C., Alberts, S., Ji, Z.,** *et al.* (2024): The Galaxies Missed by Hubble and ALMA: The Contribution of Extremely Red Galaxies to the Cosmic Census at 3 < z < 8 The Astrophysical Journal, Volume 968, Issue 1, Page 34 [DOI] [ADS] [arXiv]
- **Wright, A. H., Kuijken, K., Hildebrandt, H., et al.** (2024): The fifth data release of the Kilo Degree Survey: Multi-epoch optical/NIR imaging covering wide and legacy-calibration fields
 - Astronomy & Astrophysics, Volume 686, Page A170 [DOI] [ADS] [arXiv]
- Wright, E. L., Eisenhardt, P. R. M., Mainzer, A. K., et al. (2010): The Wide-field Infrared Survey Explorer (WISE): Mission Description and Initial On-orbit Performance

 The Astronomical Journal, Volume 140, Issue 6, Pages 1868–1881 [DOI] [ADS]

 [arXiv]
- **Wu, Q. & Shen, Y. (2022)**: A Catalog of Quasar Properties from Sloan Digital Sky Survey Data Release 16
 - The Astrophysical Journal Supplement Series, Volume 263, Issue 2, Page 42 [DOI] [ADS] [arXiv]
- **Wylezalek, D., Vayner, A., Rupke, D. S. N., et al.** (2022): First Results from the JWST Early Release Science Program Q3D: Turbulent Times in the Life of a $z \sim 3$ Extremely Red Quasar Revealed by NIRSpec IFU
 - The Astrophysical Journal Letters, Volume 940, Issue 1, Page L7 [DOI] [ADS] [arXiv]
- **Yang, J., Fan, X., Gupta, A., et al.** (2023): DESI $z \gtrsim 5$ Quasar Survey. I. A First Sample of 400 New Quasars at z 4.7-6.6
 - The Astrophysical Journal Supplement Series, Volume 269, Issue 1, Page 27 [DOI] [ADS] [arXiv]
- **Yang, J., Wang, F., Fan, X., et al.** (2021): Probing Early Supermassive Black Hole Growth and Quasar Evolution with Near-infrared Spectroscopy of 37 Reionization-era Quasars at $6.3 < z \le 7.64$
 - The Astrophysical Journal, Volume 923, Issue 2, Page 262 [DOI] [ADS] [arXiv]
- Yèche, C., Palanque-Delabrouille, N., Claveau, C.-A., et al. (2020): Preliminary Target Selection for the DESI Quasar (QSO) Sample
 Research Notes of the American Astronomical Society, Volume 4, Issue 10, Page 179
 [DOI] [ADS] [arXiv]
- York, D. G., Adelman, J., Anderson, J. E., Jr., et al. (2000): The Sloan Digital Sky Survey: Technical Summary
 - The Astronomical Journal, Volume 120, Issue 3, Page 1579 [DOI]

Yu, Q. & Tremaine, S. (2002): Observational constraints on growth of massive black holes Monthly Notices of the Royal Astronomical Society, Volume 335, Issue 4, Pages 965–976 [DOI] [ADS] [arXiv]

- Yu, Z., Martini, P., Penton, A., et al. (2021): OzDES Reverberation Mapping Programme: the first Mg II lags from 5 yr of monitoring

 Monthly Notices of the Royal Astronomical Society, Volume 507, Issue 3, Pages
 3771–3788 [DOI] [ADS] [arXiv]
- **Yue, M., Fan, X., Yang, J.,** *et al.* (2021): A candidate kiloparsec-scale quasar pair at z = 5.66 The Astrophysical Journal Letters, Volume 921, Issue 2, Page L27
- Zakamska, N. L. & Greene, J. E. (2014): Quasar feedback and the origin of radio emission in radio-quiet quasars

Monthly Notices of the Royal Astronomical Society, Volume 442, Issue 1, Pages 784–804 [DOI] [ADS] [arXiv]

- **Zakamska, N. L., Hamann, F., Pâris, I.,** *et al.* (**2016**): Discovery of extreme [O III] λ5007 Å outflows in high-redshift red quasars

 Monthly Notices of the Royal Astronomical Society, Volume 459, Issue 3, Pages 3144–3160 [DOI] [ADS] [arXiv]
- **Zel'dovich, Y. B.** (1964): The Fate of a Star and the Evolution of Gravitational Energy Upon Accretion
 Soviet Physics Doklady, Volume 9, Page 195 [ADS]
- **Zimmerman, E. R., Narayan, R., McClintock, J. E., et al.** (2005): Multitemperature Blackbody Spectra of Thin Accretion Disks with and without a Zero-Torque Inner Boundary Condition

The Astrophysical Journal, Volume 618, Issue 2, Pages 832–844 [DOI] [ADS] [arXiv]